Dynamic process modelling of the HPS2 solar thermal molten salt parabolic trough test facility

Prepared by:

Robert Temlett

TMLROB001

Department of Mechanical Engineering

University of Cape Town

Supervisor:

Prof Pieter Rousseau

December 2018

Submitted to the Department of Mechanical Engineering at the University of Cape Town in partial fulfilment of the academic requirements for a Masters of Science degree in Mechanical Engineering

Key Words: CSP, Molten Salt, Parabolic Trough, HTF, Helical Coil Steam Generator, Dynamic Modelling.

Abstract

In recent years power generation from renewable energy has grown substantially both in South Africa and around the world. This growth is set to continue as there is more pressure to reduce the burning of fossil fuels. However, renewable energy power generation suffers from unpredictability, which causes problems when it comes to managing power grids. Concentrated Solar Power (CSP) plants offer a practical solution to store power in the form of thermal energy storage (TES). Thus, the plant can run when there is no solar energy available, leading to a more stable power supply. Unfortunately, CSP plants cost more than other renewables such as photovoltaic and wind power. Thus, there is a need for research into how to bring down the cost of CSP plants. One of the most proven types of CSP is the parabolic trough plant. The most recent innovation is to try and use molten salt as the heat transfer fluid which would reduce the cost of the plant. However, this new technology has not been implemented on a full scale CSP plant and little testing has been done to prove the technology.

The HPS2 is a test facility aimed at testing the use of molten salt as a heat transfer fluid (HTF). This test facility, located in Evora Portugal, is being developed by an international consortium led by the German DLR institute of Solar Research. It is one of the first test facilities of its kind where experiments will be conducted to demonstrate the validity of using molten salt as a HTF and a storage medium in a parabolic trough CSP plant. The HPS2 test facility is not yet operational and there is a need for a dynamic thermofluid process model to better understand and predict both its steady state and transient operational behaviour.

This dissertation reports on the development of such a dynamic thermofluid process model and the results obtained from it. The process model developed primarily focuses on the steam cycle with the TES incorporated into the model. The physical geometry of each of the components are employed to construct discretized elements for which the conservation of mass, energy, and momentum are applied in a one-dimensional network approach. The economizer and evaporator combined has a helical coil geometry and uses molten salt as a heat transfer fluid, which is unique. Thus, correlations had to be adjusted for the flow characteristics found in the economizer/evaporator.

Results from the steady state simulations of the steam cycle show that the molten salt mass flowrate through the steam generation system will have to be reduced from the initially expected value to meet operational requirements. Results of the dynamic simulations show that the test facility will be able to produce a constant power supply despite transient solar conditions and highlights key dynamic responses for operators to be aware of.

Declaration

I, Robert Temlett, hereby declare the work contained in this dissertation to be my own. All information which has been gained from various journal articles, text books or other sources has been referenced accordingly. I have not allowed, and will not allow, anyone to copy my work with the intention of passing it off as their own work or part thereof.

Signed by candidate

Robert Temlett

Acknowledgements

I would like to acknowledge and thank my supervisor, Professor Pieter Rousseau, for being an excellent supervisor as he provided the right amount of input and guidance but left me with enough freedom to approach problems in my own way. Also, I must thank him for his guidance and advice given to me in other aspects of my life outside of this project.

I would like to thank my amazing wife, Kirstie Temlett, for being by my side throughout this project, supporting and encouraging me during the more stressful times over the past two years.

I would like to thank my parents and sister who have provided an amazing amount of support and encouragement throughout my six years of studying at UCT, and without them I would not be where I am today.

I am incredibly grateful to Eskom, EPPEI and ATProM who provided me the opportunity and financial support to do this Master's degree. I would also like to thank ATProM again for providing the opportunities and funding to present at several conferences over the project's life span.

I would like to thank Priyesh Gosai who was always available and happy to provide advice on the project and other ATProM related activities.

My gratitude also to Mr Gary de Klerk and Prof Louis Jestin of Eskom, Dr Michael Wittmann of DLR and Ralph Ernst of Steinmüller who facilitated the exchange of information about the HPS2 design and provided valuable information for the project.

I would like to acknowledge my fellow peers who I have had the pleasure of working alongside for the duration of this project. These peers include Patrick Akpan, John Clark, Gerto Prinsloo, Pieter Rosslee, Rendi Khobo, Excellent Gwebu, Geoff Raikes, Willie le Grange, Cheriska Polton and Rushavya Naidu.

Last, but not least, I would like to thank God for opening the right doors, guiding me and providing me with the opportunity to study a Master's degree and for my personal growth by being involved in this research group.

Table of Contents

List of Figures

List of Tables

List of Nomenclature

General symbols

f	Friction factor	G	Mass flow per unit area $[kg/m^2]$
D	Diameter [m]	h	Enthalpy [kJ/kg]
L	Length [m]	Q , $\dot{P}$	Power [kW]
V	Volume [m^3]	$Q^{"}$	Power per unit volume [kW/m^3]
v	Velocity [m/s]	x	Thermodynamic quality
ν	Specific volume [m^3/kg]	N	Number
$\dot{Q}$	Heat transfer [kW]	Ω	Characteristic frequency of phase change (reaction frequency)
T	Temperature [K]	F	Force [N]
$\dot{q}$	Heat transfer per area [kW/m^2]	$\vec{T}$	Stress tensor $[N/m^2]$
A	Area $[m^2]$	$\vec{B}$	Body force [N]
t	Time [s]	g	Gravitational acceleration $[m/s^2]$
Cp	Heat capacity [kJ/kgK]	x,y,z	Cartesian coordinate system
κ	Thermal conductivity [W/mK]	K	Loss coefficients
μ	Dynamic viscosity $[m^2/s]$	M	Mach number
θ	Helix Angle [degrees]	$q^{"}$	Heat flux [W/m^2]
H	Helical coil pitch [m]	H	Heat vaporization
Re	Reynolds number	C_v	Valve flow coefficient
De	Dean number	K_p	Proportional term
Nu	Nusselt number	T_i	Integral time constant
Pr	Prandtl number	T_d	Derivative time constant
S	Tube bank pitch [m]	s	Laplace operator
ς	S / D_{pipe}	d	Decay time of the derivative
F	Flow factor	$\dot{V}$	Volume flowrate $[m^3/s]$
Wo	Oscillation frequency number	p	Pressure [Pa]
Wp	Oscillatory amplitude number	$\dot{m}$	Mass flowrate [kg/s]

Greek symbols

α	Crank Nicolson factor
χ	Tank fill factor
λ	Heat transfer coefficient [W/m^2K]
δ	Curvature ratio [D_{pipe} / D_{Coil}]
ε	Material roughness[μm]
ρ	Density [kg/ m^3]
ϕ	Two-phase friction multiplier
Δ	Change
m	Mass [kg]
λ	Fluid conductivity
σ	Surface tension

Acronyms and Abbreviations

HPS2	High Performance Solar Two
CSP	Concentrated Solar Power
PV	Photovoltaic
TES	Thermal Energy Storage
HTF	Heat Transfer Fluid
LCoE	Levelized Cost of Electricity
PDO	Pressure Drop Oscillations
ONB	Onset of Nucleate Boiling
DWO	Density Wave Oscillations
DNI	Direct Normal Irradiance
C	Controller
CV	Control Valve
V	Valve
SE	Simulation Environment
CHF	Critical heat flux
MHF	Minimum heat flux
NPSH	Net Positive Suction Head

Subscripts

ms	Molten salt
0	Fluid Temperature, total
a	Ambient
c	Coil
C	Convection
L	Longitudinal
T	Transversal
w	Wall
crit	Critical
LM	Lockhart Martinelli
l	Liquid only
g	Gas only
fg	Mixture of gas and liquid
in	Inlet
ex	Exit
pch	Phase change
sub	Subcooling
H	Homogeneous solution
S	Sum
R	Orifice losses
surf	surface
film	Film boiling
h	Hydraulic
m	Motor
e	Electrical

1. Introduction

1.1 Background and motivation

Power generation in South Africa is primarily provided by coal fired power plants. However, there is currently pressure both locally and internationally to increase the amount of renewable energy being provided to the South African power grid. The motivation to have more renewable energy is primarily driven by the need to reduce the consumption of fossil fuels worldwide. The contribution from renewable energy sources to the South African power grid has already begun, as shown in Figure 1.1, and will continue to increase and play an important role in the ongoing transformation of the power system.

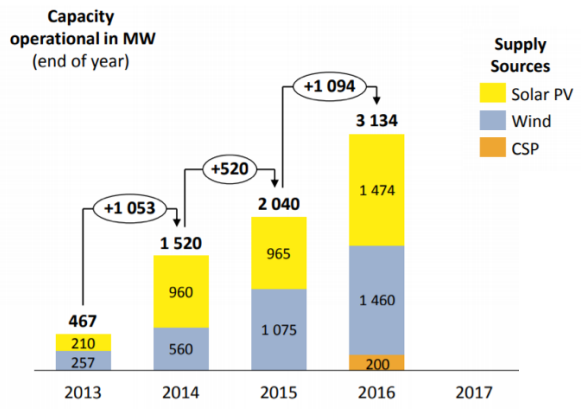

Figure 1.1 South African renewable energy capacity [1]

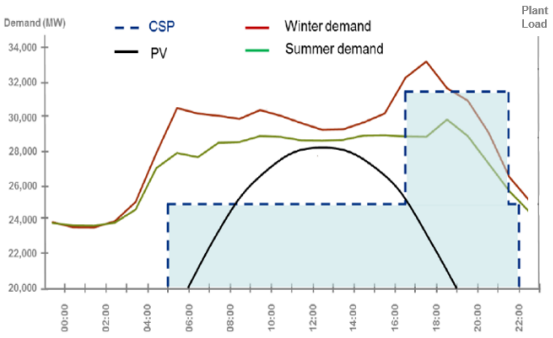

Figure 1.2 Dispatchability of CSP vs PV [2]

Renewable energy typically suffers from two characteristics which make energy utility companies resist implementing it. These are unpredictable power generation, such as wind power, and non-dispatchability, such as power produced by photovoltaics (PV) [3]. This is due to their dependence on weather conditions and not yet having any economically viable way to store power. Modern Concentrated Solar Power (CSP) plants however offer a practical solution for dispatchable power generation. This is achieved by directly storing thermal energy in a thermal energy storage (TES) system. Currently almost all CSP plants being built have a TES system. This gives them the ability to generate power on demand and continue to generate power during peak hours after the sun has set, as shown in Figure 1.2. South Africa has direct normal irradiance (DNI) values as high as 3000kWh/m^2, which is considered ideal for operating CSP plants [4]. Hence, there is motivation for stakeholders such as Eskom to stay abreast with developments in this area.

All CSP plants work by focusing DNI, also referred to as direct sunlight, onto a focal point or focal line with the use of mirrors [5]. The two most common types of CSP plants are central receiver tower

plants and parabolic trough plants. For these two types of CSP plants, heat transfer fluid (HTF) is heated at the focal point/line. The HTF is then transported to the power block. In the power block, the HTF is used either to boil water for a normal Rankine cycle and/or is used to store its thermal energy in the TES system. Central receiver tower plants use one receiver located at the top of a tower, where the DNI is focused by mirrors in the solar field as shown in Figure 1.3. Parabolic trough plants use long parabolic mirror troughs to focus the sunlight onto receiver tubes as shown in Figure 1.4. There are typically thousands of individual parabolic troughs making up a solar field.

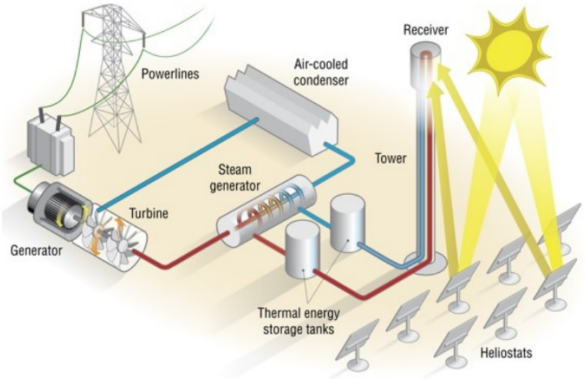

Figure 1.3 Central Receiver tower plant [6]

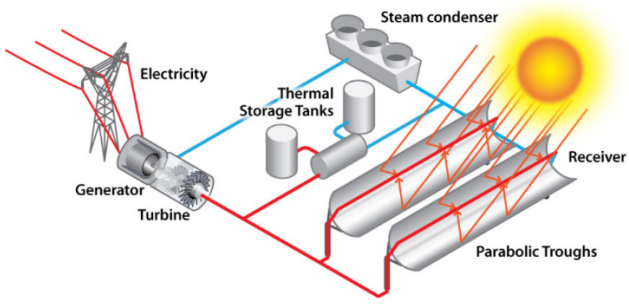

Figure 1.4 Parabolic trough plant [7]

Currently, parabolic trough plants with TES systems operate with a three-fluid setup. Synthetic oil is used as the HTF, molten salt as the storage medium and water as the fluid used in the Rankine cycle. One of the recent advancements in the CSP field is to use a two-fluid system. This is achieved by using molten salt as the HTF and storage medium, therefore removing the synthetic oil from the system. Using molten salt as the HTF leads to the following potential advantages: higher temperatures can be reached by molten salt, therefore improving the efficiency of the steam cycle; the transient conditions within the solar field have minimal impact on the steam cycle; there are fewer components in the plant; the volume of salt needed to store the same amount of energy in the TES is reduced; and molten salt is less expensive than synthetic oil. Also, molten salt doesn't degrade, has a lower vapour pressure and is non-flammable. These potential advantages will lead to a lower LCoE for parabolic trough CSP plants. However, the major risk with molten salt is the possibility of freezing in the plant as the melting point is usually around 220 ℃, depending on the salt used [8]. Table 1.1 shows the differences between conventional three-fluid plants and the two-fluid molten salt plants.

Table 1.1 Conventional three fluid vs two fluid CSP plants

	Solar energy available (Charging TES)	Solar energy unavailable (Discharging TES)
Three fluid CSP plant	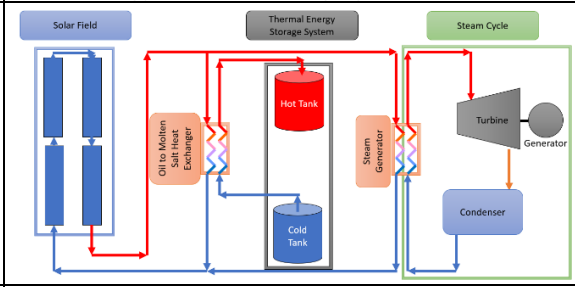	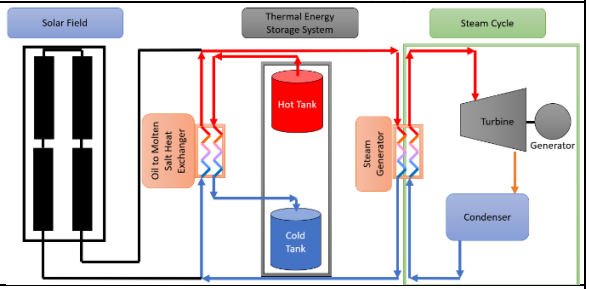
Two fluid CSP plant	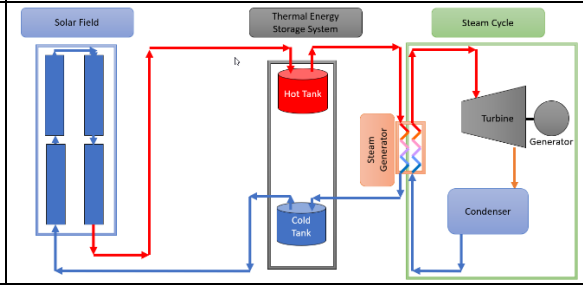	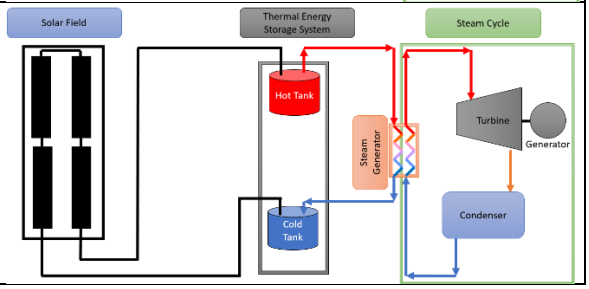

Using molten salt as a HTF has already been implemented on a very limited number of plants including a commercial 110 MW central receiver tower, namely “Crescent Dunes” [9], which is situated near Tonopah in the USA. Almost all future central receiver tower plants will implement this two-fluid design. However, there are still no full scale CSP parabolic trough plants that use molten salt as a HTF, even though the parabolic trough plants are the most mature and proven CSP technology [10]. The main reason why molten salt has not been implemented on parabolic trough plants is due to the risk of having the salt freeze within the plant. This risk is higher for a parabolic trough plant, compared to a central receiver tower plant. This is due to the longer length of piping that the salt runs through in the parabolic trough solar field, compared to the minimal piping in the central receiver tower plants.

Hence, there is motivation to test the suitability of using molten salt in a parabolic trough plant as a HTF and storage medium. Eskom initially formed part of an international consortium led by the German DLR Institute of Solar Research that is developing an innovative solar thermal molten salt parabolic trough test facility, called the High Performance Solar Two (HPS2) test facility. The test facility will be built and operated at the University of Evora, in Portugal. The objective is to test the validity of using molten salt as a HTF and storage medium. The test facility consists of a solar field, molten salt storage tanks and a steam cycle. Eskom’s membership of the consortium has since been withdrawn but its role in the project would have been to review the design and then, once constructed, to operate the plant for one year. This project was conceived to support Eskom in this role to better understand the steady state and transient operational behaviour of the test facility.

1.2 Research problem

The HPS2 test facility has yet to be commissioned, which is due to start in the first half of 2019. One of the major unknowns is how the steam cycle will behave and how to optimize its operation. The steam cycle consists of a helical coil economizer and evaporator, two superheaters, a valve section to expand and cool the superheated steam (to emulate the operation of a turbine), condenser, condensate tank and pump, and a feedwater tank and pump.

The unique component is the once-through economizer and evaporator which is a helical coil heat exchanger. In this type of heat exchanger, the water is evaporated in the helical coil tubes while the molten salt flows over the helical tube bundle. This type of heat exchanger differs from conventional straight tube heat exchangers due to the flow characteristics that develop within the helical coil tubes. These flow characteristics influence the heat transfer and friction factors. This type of heat exchanger was installed to test if faster start-up, shut down and load ramp times could be achieved, compared to kettle type boilers typically installed on CSP plants. This is to increase the dispatchability of CSP plants, making them a more attractive renewable energy source for energy utility companies to implement. In addition, one of the HPS2 project's aims is to test different molten salt compounds to find a compound that will be most suited for the use in parabolic trough CSP plants.

Developing a thermofluid process model capable of both steady state and transient simulations of the complete steam cycle and molten salt storage tanks will provide insight into the thermofluid processes that will occur in the system. This can lead to optimizing its operation, being able to predict operating conditions and provide transient simulations to show how the test facility will react to load changes and weather conditions, as well as identify possible problems before the system is commissioned.

1.3 Objectives

The main objectives of the study are to:

I. Do a comprehensive literature review of CSP technology, characteristics of components that are used in the test facility and other relevant literature about phenomena that may occur in the test facility.
II. Create a dynamic thermofluid process model of the HPS2 steam cycle and TES system using the Flownex software. This model must consider the unique flow characteristics that exist in the helical coil economizer and evaporator.
III. Conduct steady state simulations to predict and check operating conditions for the steam cycle.

IV. Conduct transient simulations to provide an understanding of how the test facility will respond to transient conditions.
V. Tune controllers from transient responses to correctly control the test facility.
VI. Provide operators with insight into how the test facility will respond during transient conditions.

1.4 Scope

The main outcome for this project is to develop a dynamic process model which can model the transient responses of the HPS2 steam cycle. The model will be developed using the Flownex software because it uses a one-dimensional modelling approach that has been extensively validated and verified as well as been developed within the ISO 9001 and ASME NQA1 accredited quality system. The developed model of the steam cycle must emulate with reasonable accuracy each of the heat exchangers where the molten salt and water/steam are exchanging heat, this being the economizer, evaporator and the two superheaters. The actual physical geometry of the remaining components of the steam cycle must be accounted for in the model. The start-up processes of the test facility will not be modelled.

Furthermore, due to delays in the HPS2 project rollout, the model will not be validated against data from the test facility. However, the model will be verified where possible, against the original design documents for the HPS2 project, provided by Steinmüller. It is not possible to reference these design documents as they are not publicly accessible and are confidential. The specific solar field data for the HPS2 test facility will also be unavailable as an input into the model and the simulation of the solar field itself is not included in the project scope.

2. Literature review

2.1 General principles of concentrated solar power plants

Concentrated Solar Power (CSP) plants differ considerably from photovoltaic systems that are more commonly known as a power generation source from solar energy. CSP plants are relatively simple when looking at the operation of the plant at a basic level. CSP plants use the DNI/direct light from the sun to produce thermal heat as opposed to the photon energy that photovoltaic systems use [5]. CSP systems are able to generate high amounts of thermal heat by concentrating the sunlight through the use of mirrors. This heat that has been concentrated by the mirrors then heats up HTF which gets used to generate power in the power block and/or the thermal energy is stored [11]. Most large scale CSP plants use the heat energy to drive steam turbines to generate the electrical power. Thus, the operating principle of a CSP power plant remains very similar to that of conventional power plants that use fossil fuels, except that the heat energy is now being provided to the system from the sun. Since a CSP plant most commonly uses a steam turbine system to generate the electricity, a CSP plant can be coupled with conventional fuels, making it highly dispatchable [12]. However, a steam turbine isn't the only way a CSP plant can generate electricity. Stirling engines can also be used [13]. These differ substantially from the technology used in steam turbines. When there is no sunlight like at night or if it's cloudy, the power output of a CSP plant would reduce or completely stop if there wasn't some form of energy storage system to keep the plant running. Unlike a photovoltaic system where electricity is generated directly, thus a storage system would have to store electricity, a CSP system would store thermal energy and there are various technologies and systems that do this effectively and at an economical cost. This means that a CSP plant with thermal storage can provide dispatchable energy and provide electricity for hours even after the sun has set.

2.2 Types of concentrated solar power plant technologies

There are four major types of CSP technologies: Parabolic troughs, central receiver towers, parabolic dish Stirling engine systems and linear Fresnel reflectors [13]. These four designs all use mirrors to focus the sunlight to a focal point or focal line. However, they differ slightly in design each having various advantages and disadvantages.

2.2.1 Parabolic troughs

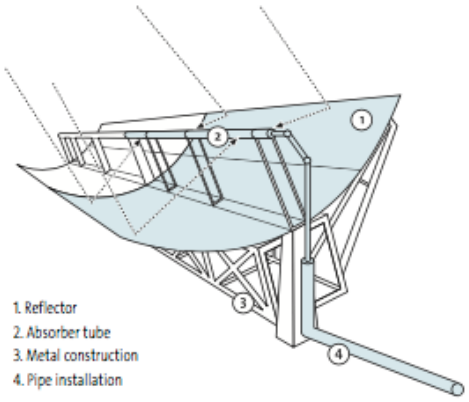

Figure 2.1 Parabolic Trough [14]

As shown in Figure 2.1 trough shape mirrors are used to focus the sun's rays by a factor of typically 80 onto an absorption pipe [14]. The absorption pipe is a stainless-steel tube that has a sunlight absorbing surface. The steel tube is mounted inside an anti-reflective outer glass tube with a vacuum separating the two tubes [5][15]. The troughs are arranged in long parallel lines. They are arranged in such a way that by tilting the troughs they can follow the sun throughout the day, which is achieved using a tracking system, which is classified as a single axis tracking system. The absorption pipe carries a heat transfer fluid that gets heated up and pumped into a centrally located power block.

2.2.2 Central receiver towers

This type of CSP technology uses hundreds or thousands of mirrors called heliostats to concentrate the sunlight onto one common focal point. These heliostats track the sun to keep the sunlight focused on the common focal point [16], using a multi axis tracking system. A diagram of a typical layout of one of these plants is shown in Figure 2.2. These Central Receiver Tower designs allow for higher operating temperatures, which leads to higher efficiencies [11]. The Heliostat field is also very flexible which means that it can be built around the natural contours of the land rather than over almost perfectly flat ground [5]. The common focal point heats the heat transfer fluid from where it goes to the power block. Since these CSP plants have the ability to operate at a higher efficiency it is expected that they will be more cost effective than other CSP systems [15], providing a heat transfer fluid can be used that can handle the high temperatures.

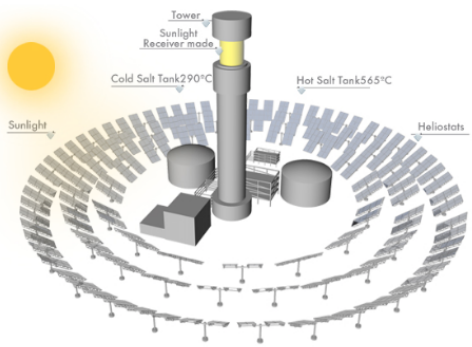

Figure 2.2 Central Tower CSP [16]

2.2.3 Dish Stirling engine systems

Parabolic Dish systems use a mirror dish that looks much like a satellite dish to concentrate the sunlight onto a focal point [15]. A picture of a typical Dish Stirling Engine system is shown in Figure 2.3. Unlike other forms of CSP plants that mostly use the heat generated to drive conventional steam turbines, the heat generated by the parabolic dish drives a Stirling engine to generate electricity [5]. The parabolic dish also tracks the sun, using multi axis tracking, to optimize the heat generated. Incorporating a thermal storage system into this CSP system is possible but requires a specialized design, and the storage capacity isn't over a long period of time [13][17]. Even though this CSP system is highly efficient at up to 32% efficiency, the cost is higher when compared to other CSP systems [17]. However, like the Central Receiver CSP system, the dishes don't have to be installed on flat ground [5]. Also, the design is highly modular meaning that one doesn't have to install and pay for an entire solar field before a return on investment is seen [17].

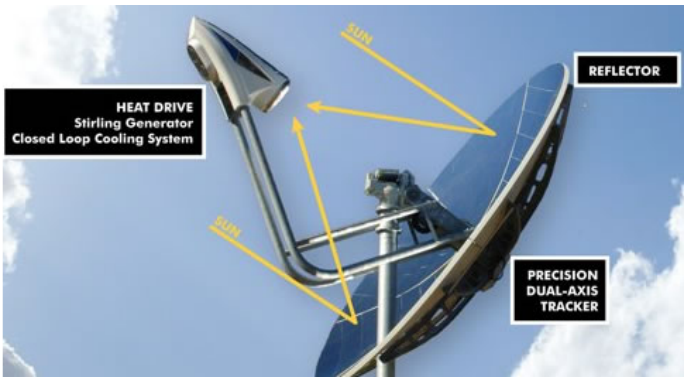

Figure 2.3 Dish Stirling engine [17]

2.2.4 Linear Fresnel reflector

This system is very similar to the parabolic trough system. However, instead of using a parabolic trough, a series of flat mirrors are used to focus the sunlight on the absorber tube [18] as shown in Figure 2.4. The advantage of this is that it is a simpler design than the parabolic troughs, and doesn't need expensive curved mirrors [11]. Most existing designs use a direct steam generation system. This means that the heat transfer fluid that runs through the absorber pipe is water, which is being heated up directly, turning into steam to drive a turbine. However, the company Frenell has tested and produced Fresnel reflector plants that use molten salt as a HTF and storage medium [19].

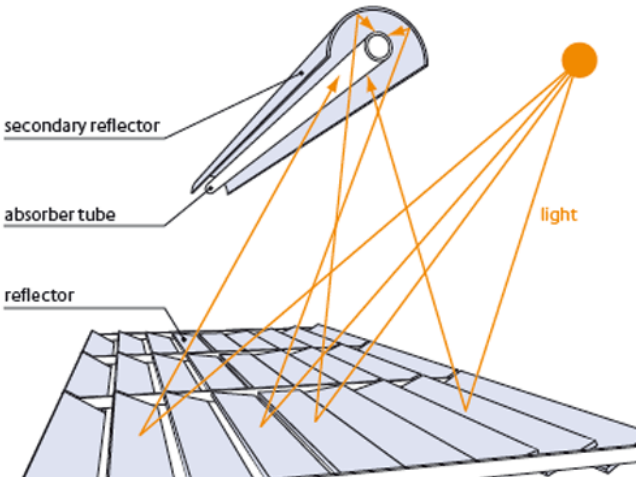

Figure 2.4 Linear Fresnel reflector [18]

2.3 Thermal Energy Storage (TES)

2.3.1 General principle of a TES system

TES systems when compared to other energy storage systems store thermal energy as opposed to electrical energy in the case of battery storage or potential energy in the case of pumped storage. Compared to other storage technologies TES generally have lower capital costs as well as very high operating efficiencies [13]. A thermal storage system generally consists of three components, namely a storage medium, heat transfer fluid and a containment system. Currently molten salt is the most commonly used storage medium in large scale CSP plants [13]. There are various types of TES systems each with its own advantages and some are integrated more easily with certain CSP plants. However, in general there are several requirements that must be considered to ensure optimal storage dynamics and longevity [13].

1. High energy density in the storage material.
2. Good heat transfer between the heat transfer fluid and the storage medium.
3. Mechanical and chemical stability of the storage material.
4. Chemical compatibility between the heat transfer fluid, heat exchanger, and storage medium.
5. Complete reversibility for many charging/discharging cycles.
6. Low thermal losses.
7. Low cost.
8. Low environmental impact.

The basic operating principle of a TES system is that a heat transfer fluid is heated by the CSP, or the storage medium is heated directly. In the first case, the heat transfer fluid then heats the storage medium via a heat exchanger. The heat is then stored and preserved in the storage medium for later use when the CSP plant can't generate more heat due to a lack of sunlight.

2.3.2 Heat storage forms

The heat can be stored in three forms, namely sensible heat, latent heat and thermo-chemical reactions [20]. Sensible heat storage is achieved by simply raising the temperature of the storage medium. The storage medium does not undergo any phase changes and can be either a solid or a liquid. Latent heat storage is achieved by using the heat from the CSP plant to cause a phase change of the material at a temperature that falls within the upper and lower limit of the solar field. The most common phase change used in this form of storage is liquid to solid transitions. This is due to its low volumetric expansion compared to other phase changes. Given that this process is nearly

isothermal it can provide significantly enhanced storage quantities when compared to sensible heat storage in the same temperature range. Thermal-chemical storage uses the heat from the CSP plant to drive a reversible chemical reaction. Thus, the forward reaction is endothermic absorbing the heat of the CSP plant to drive the reaction. The reverse reaction is exothermic which will be used to generate the electricity at a later stage, this is the least investigated way to store thermal energy. However, it has the potential to be more effective than both sensible and latent heat storage since the chemical components after the endothermic reaction can be stored indefinitely at ambient temperatures thus reducing thermal losses. However, due to the cost and complexity of this energy storage, they are currently not in use on large CSP plants [13].

2.3.3 Common types of TES systems

The design of a TES storage system depends on multiple factors, the major ones being the type of CSP plant and the type of storage medium being used. TES systems can be defined as either an active or passive system. In an active system, the storage material circulates between heat exchangers in the plant. Where the storage medium is also used as the heat transfer fluid it is referred to as a direct-active system [13]. Where the storage medium is a solid or does not flow the system is referred to as a passive system.

Active Storage

There are various designs for active storage. Two-tank systems shown in Figure 2.5 are commonly used for higher temperature CSP plants where molten salts are used [13], a basic two tank diagram is. In a two-tank system, the plant has a hot tank and a cold tank. The storage medium is pumped from the cold tank and gets heated up by the CSP plant and then gets pumped to the hot tank for storage. Due to the insulation of the tank and the properties of the storage medium the heat is retained in the storage medium for long periods of time. When the stored heated fluid is needed it is pumped out of the hot storage tank and the heat is used to generate steam and then returned to the cold tank [20][21].

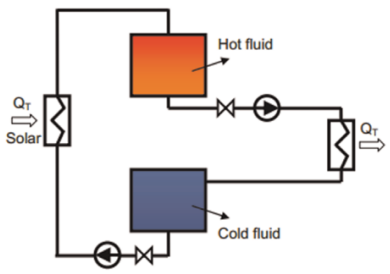

Figure 2.5 Two tank active storage [22]

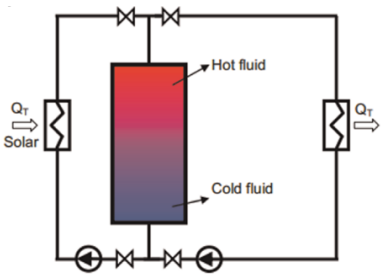

Figure 2.6 Single tank/thermocline active system [22]

A single active storage system shown in Figure 2.6 essentially combines the hot and cold tank into one storage volume. This removes the need for a second tank thus reducing capital costs [21]. A single tank system in this sense is also referred to as a thermocline system [13]. This system works by pumping the hot fluid into the top of the tank, which gradually displaces the cold fluid at the bottom of the tank during charging mode. Buoyancy effects preserve the thermal gradient that is created inside the tank. However, it is difficult to separate the hot and cold fluid. Single tank designs are more commonly used when the storage medium is solid [20].

Passive Storage

In a passive system shown in Figure 2.7, the heat transfer fluid is used to heat up a storage material which does not flow through heat exchangers. The major advantage is that this storage material is often inexpensive in the form of rocks, sand or concrete for storing sensible heat storage or phase change materials for storing the thermal energy [13].

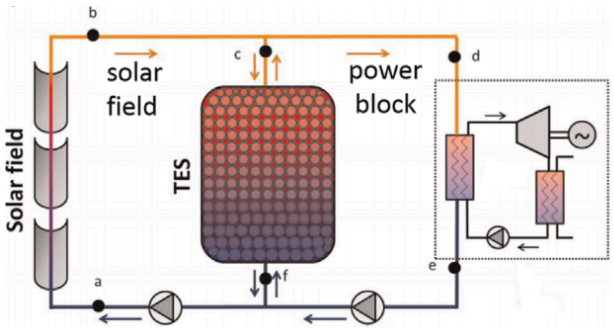

Figure 2.7 Packed bed passive storage [22]

2.4 CSP Parabolic trough power plant behaviour during strongly cloudy days

The following information was taken from reference [12]. The paper uses both measured data from a CSP plant and a simulation model to observe the dynamic behaviour of the plant on strongly cloudy days. The software used to simulate the CSP plant is called APROS and uses a finite volume solution method to solve the one-dimensional partial differential equations. The power plant modeled is the "Andasol II" in Guadix, Grandada, Spain. This CSP plant is a parabolic trough power plant, consisting of 156 collector loops. This plant uses a heat transfer fluid that runs through the heat absorbers in the solar field which either gets used directly via a heat exchanger to generate steam or when there

is excess heat, to heat the storage medium. In this case the storage medium is molten salt. The TES system in this power plant uses a two tank design for storing the molten salt.

The measured data shown in the results were taken from Andasol II on 29 June 2010 and on 8 July 2010. For these days using more than one weather station at the power plant's location, typical meteorological year data was used to obtain the direct normal irradiation (DNI) for the power plant. The DNI for these days is the input for the model. The model was validated versus the actual measured data from the plant. The results of the simulated model are shown against the actual reading in the graphs shown in Figure 2.8.

The differences that can be seen between the simulated and measured heat transfer fluid flow rates show that the operational procedures in the real power plant were different to those implemented by the model. In general, as expected the thermal power generated has a direct correlation to the DNI (a) and the mass flow rate of the heat transfer fluid (c). However, the results point out some operational limitations such as that at t = 15:41 there was a substantial amount of DNI available (a), but the simulated heat transfer fluid flow rate (c) could not be increased above 1179 kg/s due to the limited capacity of the pumps. Thus, in this case, in a real power plant, some collectors are deviated from the sun track to keep the temperature of the fluid (b) at the design maximum outlet temperature, which is this case is 393 ℃. Another factor that limits the mass flow rate is that for maximum heat transfer between the absorber tubes and the heat transfer fluid a turbulent flow with a minimum Reynolds number of 200,000 should be used. Thus, the mass flow rate of the heat transfer fluid has an upper limit due to the pumps and a lower limit due to the optimal heat exchanger properties. At t = 20:38 there is no thermal storage (e) even though there is an increase in DNI (a), but not sufficient to achieve the required mass flow rates (c) and design temperatures (b) of the plant. Thus, heat energy available from the sun was not used, due to limitations of the plant. The other factor that made the power plant less efficient compared to the simulation model is that the model strategy increased the operating hours of the plant compared with the operator's decisions.

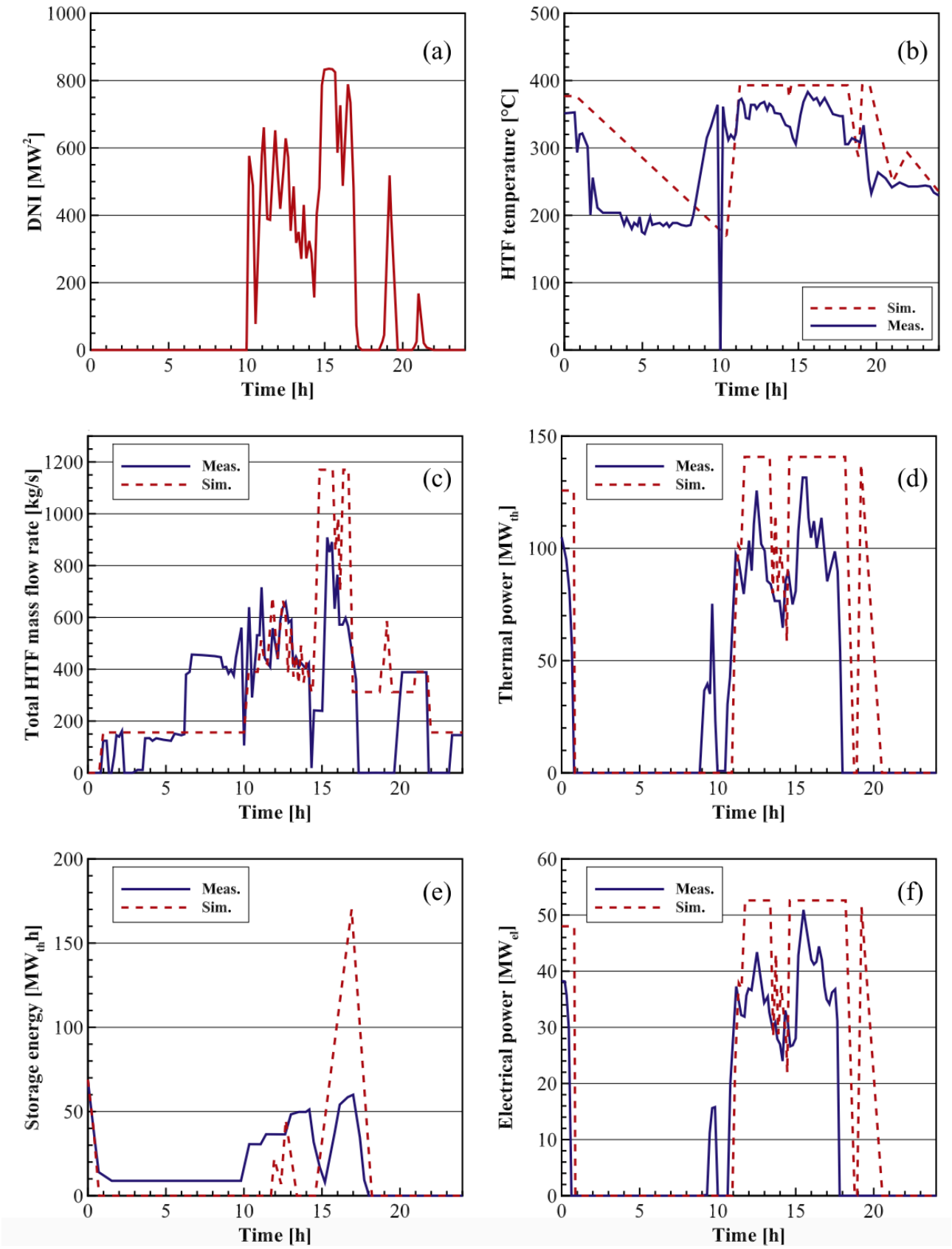

Figure 2.8 Simulated vs actual data for Andasol II [12]

2.5 Using molten salts as a heat transfer fluid in a parabolic trough Plant

Using molten salt as the heat transfer fluid in a parabolic trough designed CSP plant has its risks as opposed to using synthetic oil, which is the most mature and fully commercial technology [23]. The major risks/challenges associated with molten salt is having the molten salt freeze in the system and the additional operational complexities.

2.5.1 Testing molten salt in a parabolic trough test facility

The use of molten salt as a heat transfer fluid in a parabolic trough plant has been demonstrated by Archimede Solar Energy and Chiyoda [24], [25]. This test facility is located in Massa Martana (Italy) and first started operating in July 2013. This test facility consists of one solar loop, two molten salt storage tanks and an air-cooled heat exchanger to cool the molten salt. From the tests that were conducted Maccari et al. [26] concluded that using molten salt as a HTF in a parabolic trough plant is feasible for large scale commercial applications. The test facility showed no problems in either normal or extraordinary operating scenarios, which indicate that the molten salt can readily be managed, even during an emergency. No freezing problems were reported in a complete year while being in a location that is not best suited for a CSP plant. Draining and filling of the solar field also did not pose serious problems.

To test what would happen if the salt were to freeze in a parabolic trough solar field, a test facility was constructed consisting of the same components used in the Archimede Solar Energy test facility, including the same heating system. The test consisted of letting the molten salt freeze and then the heating system is switched on. In all the tests the heating system successfully thawed the molten salt. More than ten tests were completed without damage to any of the components. This showed that it is feasible to recover the solar field even if the molten salt freezes in the system.

There are at least two other parabolic trough molten salt test facilities that are known of by the author. However, due to the confidentiality around these projects, there are no results found in available literature and therefore they cannot be reported on.

2.5.2 Advantages to using molten salt as a heat transfer fluid

The major advantage to using molten salt as the HTF compared to the synthetic oil is that the molten salt can be heated to a higher temperature. The chemical stability of the synthetic oil limits its temperature to typically below 400 ℃ [27], while molten salt has a broader temperature range. For example, a mixture consisting of 60% $NaNO_3$ and 40% KNO_3 has a melting point of 220 ℃ and a

stability limit at roughly 600 ℃, although the practical limit is around 565 ℃ [8]. This increase in the maximum temperature means that the outlet temperature of the solar field is higher, thus increasing plant efficiency when compared to oil being used as the HTF [28]. Nitrate salts have been shown to be favourable for heat transfer fluids and thermal storage mediums. Other than the higher heat capacity, nitrate salts also exhibit low corrosion rates with common piping materials, good heat transfer properties, very low vapour pressures, are widely available, have a low environmental impact and are relatively inexpensive [28]. By directly using molten salt as the HTF there are fewer components in the system when using a TES system. The oil to molten salt heat exchanger is no longer needed and the size of the salt storage tanks can decrease to store the same amount of thermal energy due to the higher temperature limit of the salt. In addition, the expansion vessels and fire systems needed for the synthetic oil is no longer needed. Using molten salt as the HTF also is more efficient when the stored thermal energy is used. Thus, there could be a significant advantage to both plant efficiency and overall cost when using molten salt as a HTF if the difficulties associated with molten salt are correctly dealt with.

2.6 Future of heat transfer fluids

Even though using molten salt as the HTF has significant advantages when compared to synthetic oil. There are still other alternatives that can be used as heat transfer fluids. These alternatives can have more advantages than the typical solar salt used (60% $NaNO_3$ and 40% KNO_3). The main objectives for finding other heat transfer fluids is to decrease the melting temperature which reduces the risk of freezing in the plant, to increase the maximum operating temperature which will increase plant efficiency, and to have a high heat capacity which will reduce the overall cost of the storage system.

2.6.1 Development of new molten salts

Changing the typical solar salt mixture of 60 wt% $NaNO_3$ and 40% wt% KNO_3 by adding in various additions of $Ca(NO_3)_2$ and/or $LiNO_3$ has been investigated to try and further optimise molten salts. Fernández [29] briefly mentions different variations that have been tried in the past. All the variations mentioned showed that the melting point had reduced but other property changes were not beneficial. Fernandez [29] further investigates different additions of $Ca(NO_3)_2$ and/or $LiNO_3$ to the standard solar salt. The melting points, maximum stability temperature, heat capacity as well as the viscosity of the fluid close to the melting point are obtained. The results are shown in Table 2.1.

Table 2.1 Physicochemical results obtained in new molten salts developed [29]

Molten Salt	Melting Point (℃)	Thermal-Stability (℃)	Heat Capacity (J/g℃)
$60\%NaNO_3 + 40\%KNO_3$	221.04	588.51	1.498
$48\%Ca(NO_3)_2 + 7\%NaNO_3 + 45\%KNO_3$	130.61	554.39	1.272
$20\%LiNO_3 + 52\%KNO_3 + 28\%NaNO_3$	130.15	600.05	1.091
$30\%LiNO_3 + 60\%KNO_3 + 10\%Ca(NO_3)_2$	132.15	567.18	1.395

The viscosity results are represented in Figure 2.9 where Solution 1 represents $48\%Ca(NO_3)_2 + 7\%NaNO_3 + 45\%KNO_3$, solution 2 represents $20\%LiNO_3 + 52\%KNO_3 + 28\%NaNO_3$, and solution 3 represents $30\%LiNO_3 + 60\%KNO_3 + 10\%Ca(NO_3)_2$. Viscosity is an important factor to consider as the salt must flow properly through the plant at the lowest possible temperature.

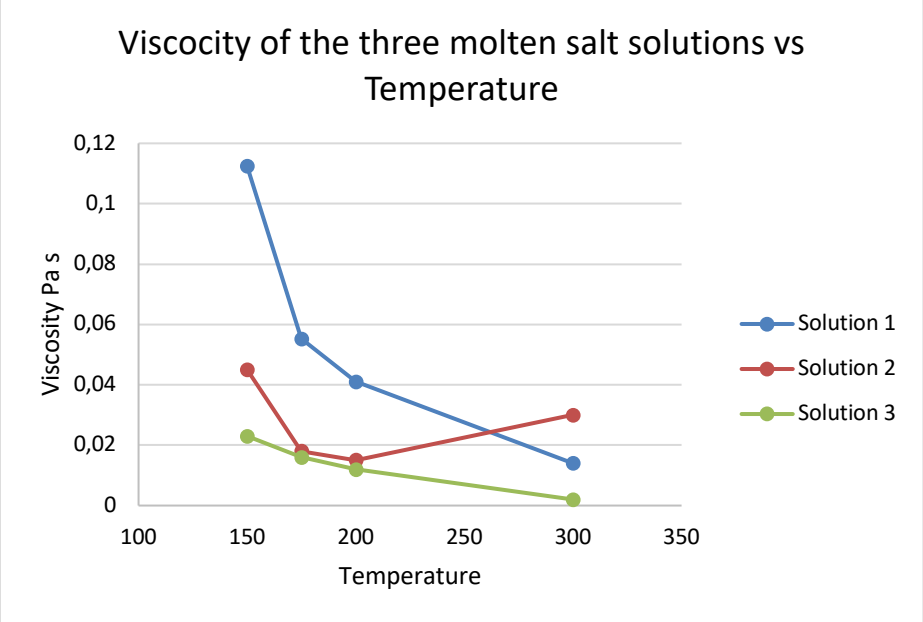

Figure 2.9 Graph of Viscosity if the molten salt solutions

Van der Merwe et al. [30] showed another composition made up of $10\%LiNO_3 + 10\%Ca(NO_3)_2 + 60\%KNO_3 + 20\%NaNO_3$ where its melting point is 132.08 ℃, thermal stability 580.36 ℃ and a heat capacity of 1.517 J/g℃. This paper however did not show the fluids viscosity characteristics.

Cost of the salt solution is also a major factor in the feasibility of the additions. It has been found that the general cost of each component can be arranged against each other as follows: Li>K>Na>Ca [30]. Thus, Calcium nitrate is a promising additive as it would reduce the cost of the salt solution.

However, adding Ca reduces the heat capacity of the solution, which impacts the thermal storage of the plant, the mass flowrates through the solar field and heat exchangers, and has a lower maximum temperature. Based on the results of Fernández [29] one can conclude the thermal stability temperature did not change much when compared to the standard solar salt. The viscosity of the new salt solutions showed that they flowed properly over the range of the temperatures studied. However, the biggest advantage is the decrease in the melting point, when compared to the standard solar salt. This decrease will significantly reduce the risk of unintended freezing of the salt in the pipes.

2.6.2 Using liquid metals as heat transfer fluids

Pacio et al. [8] investigates the thermodynamic properties of liquid metals as heat transfer fluids. Liquid metals are chemically stable over their entire temperature range. This means they have a larger operating temperature range and the upper temperature limit may be around 1000 ℃. This would significantly increase the efficiency of the power plant. The first metal investigated is sodium (Na) in various compositions like sodium-potassium alloys (NaK) which is a liquid at room temperature. This would be extremely beneficial for a CSP trough designed power plant. The other metal is lead-bismuth eutectic (LBE) alloy, which has a higher boiling point. Table 2.2 shows the physical properties of the metals together with standard solar salt.

Table 2.2 Physical Properties of Solar Salt and Liquid metals

Physical Property	Solar Salt	Liquid Na	Liquid LBE
Lower temperature limit ℃	220	98	125
Upper temperature limit ℃	600	883	1670
Heat capacity J/g℃	1.52	1.27	0.143
Thermal conductivity $Wm^{-1}K^{-1}$	0.53	69.8	13.7
Density kgm^{-3}	1804	850	10,139
Dynamic viscosity mPa s	1.69	0.27	1.44
Prandtl number	4.85	0.005	0.015

The study showed that the liquid metals had higher heat transfer coefficients and operating temperatures, which can improve receiver efficiency and higher receiver fluid outlet temperature. For solar salts, the optimum heat-flux density in view of receiver efficiency lies below 1 MW/m^2. With the use of liquid metals, this can be increased up to 5 MW/m^2. This would result in significant investment cost reductions. However due to the relatively low heat capacity of metals, they can't be used as a storage medium, thus making a direct TES system using liquid metals economically unattractive. Since molten salts cannot accommodate the higher temperature of the liquid metals a different type of thermal storage system would have to be used, such as a solid storage medium.

Other issues associated with liquid metals is that liquid sodium reacts violently with water, and LBE is lead based which has health risks associated with it.

2.7 Dynamic modelling

Various research has been done to create dynamic models of CSP plants. These dynamic models are used to optimise plant design and running conditions for both current plant designs and future designs. These dynamic models also give an insight into each component within the plant and will help in future research and development of CSP technology. For a CSP plant with TES capabilities, there are three main sections that need to be modelled. The solar field, the TES system, and the steam cycle of the power plant. Since this paper primarily focuses on the TES system and steam cycle, the literature review focuses on these topics.

2.7.1 One-dimensional modelling compared to two-dimensional modelling for a CSP plant

Research by L.Migliari et al. [31] compared the results from a non-stationary one-dimensional model developed in Matlab, to a sophisticated dynamic 2D numerical model developed using Comsol. The purpose of using a 1D model instead of a 2D model is that the 1D model is simpler and therefore computationally less demanding. However, one dimensional modelling can potentially be less accurate than two dimensional modelling especially for highly detailed results such as flow distributions within a cross section of a pipe or container. The solar field modelled in this research is the Ottana power plant which is composed of six lines of Linear Fresnel collectors, each 200 meters long. The solar field, in this case, uses synthetic oil as the heat transfer fluid with an inlet temperature of 150 ℃ and an outlet temperature of 260 ℃. The comparison between the models was carried out under the following conditions of the solar field:

a) The warm-up phase, obtained by simplifying the increasing power coming from the sun with ramps of different duration.
b) The full operation transients, applying different steps and pulses of the sun power.
c) The shut-down phase, realized through a ramp with negative slopes.

The results for condition (b) are shown in Figure 2.10 below. The results for (b) are shown in preference to conditions (a) and (c), as condition (b) represents the most dynamic and transient conditions. For the full results of all the conditions refer to [31]. The two models showed very similar results when modelling the solar field in all three test cases, the only slight difference can be observed either at or just after the 240 second mark. This research shows that a simplified one-dimensional model can be used when simulating a CSP power plant and a more sophisticated 2D

model is not necessary. The results were also validated against actual measurements from the Ottana Solar power plant. The current research found in [23], [27], [28], [31]–[33] have dynamically modelled a CSP plant or components of a CSP plant using a one-dimensional approach based on the mass, momentum and energy conservation equations applied to control volumes. These models have been experimentally validated against actual readings from the CSP plant investigated in each case. This shows that one-dimensional models have been frequently used for modelling CSP power plants, obtaining accurate and useable results while keeping the computational intensity low.

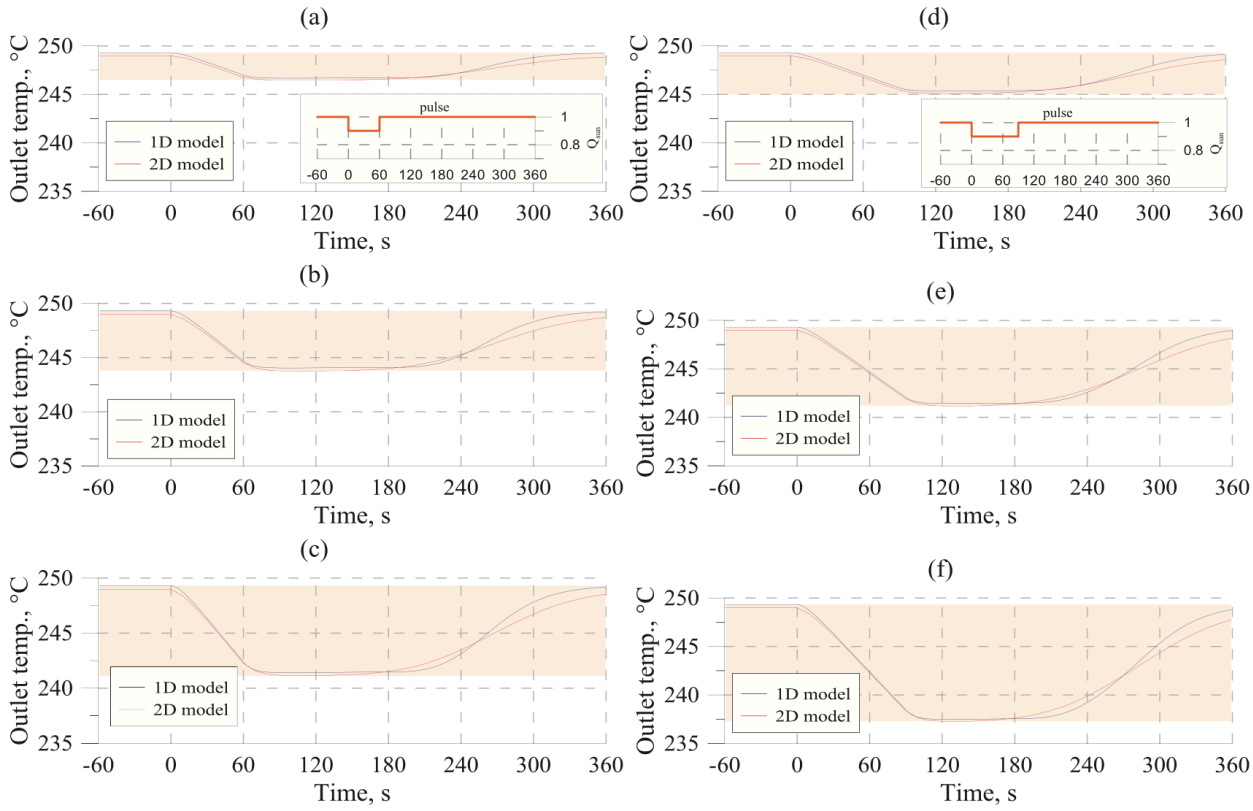

Outlet temperature of the SF: system responses to pulses. (a) $Q_{sun,f}$= 0.9 $Q_{sun,i}$, t=60s; (b) $Q_{sun,f}$= 0.8 $Q_{sun,i}$, t=60s; (c) $Q_{sun,f}$= 0.7 $Q_{sun,i}$, t=60s; (d) $Q_{sun,f}$= 0.9 $Q_{sun,i}$, t=90s; (e) $Q_{sun,f}$= 0.8 $Q_{sun,i}$, t=90s; (f) $Q_{sun,f}$= 0.7 $Q_{sun,i}$, t=90s.

Figure 2.10 Results of SF response to pulses [31]

2.7.2 Transient modelling of two tank thermal storage system

Since two tank molten salt thermal storage systems are the most common commercially used thermal storage systems in CSP plants, it is important to understand the characteristics of these systems to accurately model them. Research has been done to investigate the flow, which creates the temperature distribution in the storage tanks. Zaversky et al. [34] describes the natural convection flow profile as follows; In regions close to the tank walls the molten salt cools down, its density increases and starts to move towards the tank bottom. Close to the bottom corner, it reaches its maximum velocity. Then it is decelerated and moves towards the tank bottom centre.

Its temperature rises again, and it moves towards the molten salt surface. This leads to good mixing of the relatively cool and hot salt, ensuring a homogeneous temperature distribution. Suárez et al. [35] employed a two dimensional CFD analysis that confirms these findings but states that minimum temperatures are reached near the tank surfaces, especially near the free surface and the bottom. This is also confirmed by Rodríguez [36] which showed that after an initial transient period the process occurs in a quasi-steady state in which the heat is exchanged at almost a constant rate. Good storage tank design will avoid local cold spots in the tank to reduce the risk of local freezing of the salt [34]. These results indicate that the molten salt in a storage tank can be modelled as a homogeneously mixed volume, with one representative fluid temperature. The results of the temperature distribution from Suárez et al. [35] are shown in Figure 2.11.

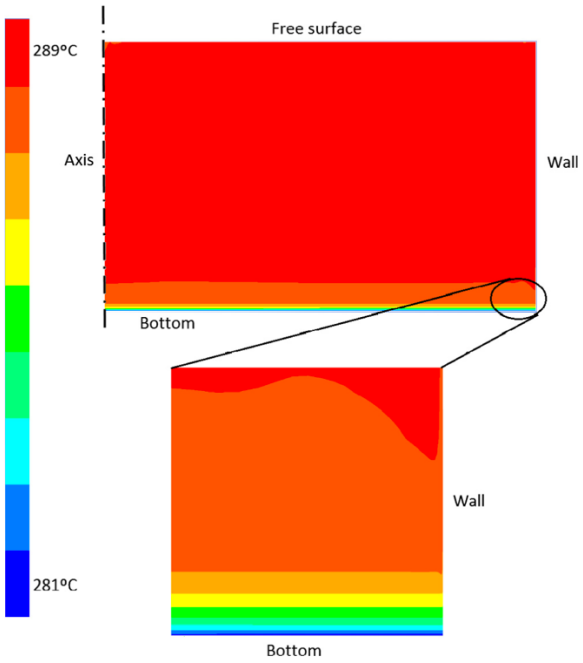

Figure 2.11 Temperature distribution for maximum charging level [35]

Heat loss through the walls depends largely on the salt level in the storage tank [22]-[23]-[25]. The higher the tank level the greater the wetted area is, thus the heat loss through the walls is higher. However, when there is less molten salt in the tank the temperature decrease per day is faster than when the tank is full, due to the overall volume of molten salt in the tank. Rovira et al. [37] showed that for the CSP plant Andasol I, when the tank was full it was subject to roughly 1 ℃ in temperature loss per day. With the tank at the minimum height it showed a temperature loss of 5-6 ℃ per day. Suárez etal. [35] shows that the heat loss trends in the hot and cold tank are similar, but there are higher thermal losses in the hot tank.

Taking data from the Andasol CSP plant, Equation (2.1) was developed through dimensionless analysis [37]. The heat loss occurring in the storage tanks depends on the tank fill factor χ as well

as the characteristic diameter D of the tank. The purpose of the research was to look at the energy efficiency of a standard double tank storage system versus a subdivided solar field approach. This equation uses values from the Andasol CSP plant being the $\dot{Q}_{losses\ full}$, $\dot{Q}_{losses\ empty}$, h_{max}, and h_{min}. Using the known tank geometry, the characteristic diameter can be calculated. However, the assumptions when using equation (2.1) is that the same thermal insulation, the same geometrical design as well as the same operating temperature differences are used [34].

$$\dot{Q}_{Losses} = \left[\chi \dot{Q}_{losses\ full} + (1-\chi)\dot{Q}_{losses\ empty} \right] D_{\text{tank}} / D_{ref} \tag{2.1}$$

$$\chi = (h - h_{min}) / (h_{max} - h_{min})$$

Zaversky et al. [34] presents two other equations for heat loss. Equation (2.2) was developed using data from the Solar Two project where T_{salt} is the molten salt temperature in ℃, and $\dot{q}_{loss}$ is the specific heat loss in kW per area (valid for both cold and hot tanks). Equation (2.3) is developed using an overall heat transfer coefficient ($\lambda_{overall}$) correlation for taking the storage tank heat losses into account. Where T_0 represents the temperature of the containing medium, T_a the ambient temperature, A the reference surface area (m^2).

$$\dot{q}_{loss} = 0.00017 T_{salt} + 0.012 \frac{kW}{m^2} \tag{2.2}$$

$$\dot{Q}_{loss} = \lambda_{overall} A (T_0 - T_a) \tag{2.3}$$

Torras et al. [38] conducted a 2D CFD parametric study to investigate the influence of the meteorological data, insulation thickness of the storage tank and configuration of the foundation. The study was conducted using a dynamic numerical model by varying one parameter at a time and studying the effect on the storage tank performance. The meteorological data not only affects the hot salt input on molten salt into the tank but also the thermal losses to the environment. As a point of interest, one of the meteorological data points was from Upington in South Africa, which showed that in both winter and summer months the DNI was higher than that of Sevilla Spain, Antofagasta Chile, and Las Vagas USA. The results show that higher DNI values, result in higher plant capacity factors. The insulation result was as expected with increased insulation results in a decrease in heat loss. The different configurations of the foundation had almost no impact on the performance characteristics of the tank.

Suarez et al. [35] also conducted 2D CFD calculations on both hot and cold storage tanks to evaluate the transient cooling down processes. The purpose of this study was to understand the cooling process and the risk of freezing in the storage tanks when the plant is on standby or maintenance is being conducted. The calculations were done using commercial software called ANSYS FLUENT.

Since there was not enough information to validate this model with an actual molten salt thermal storage tank, the model was validated against the turbulent natural convection in a differently heated square cavity, which is very similar to the conditions found inside a molten salt thermal storage tank. The results of the research are best represented in Figure 2.12, where different durations of standby time is shown and if there is a risk of freezing a safe charging level is shown. It compares these simulated results to a linear equation (2.4) that can be used to estimate the onset of freezing. The results for the simulation and linear equation are shown in Figure 2.13. Their results were also compared to other simulated results with other research and showed good correlation.

	Cold tank (T_o = 292 °C)		Hot tank (T_o = 386 °C)	
Standby duration (days)	Risk	Safe charging level (%)	Risk	Safe charging level (%)
<3	No	Any	No	Any
4	Yes	5	No	Any
5	Yes	7	No	Any
6	Yes	9	No	Any
7	Yes	11	No	Any
14	Yes	24	Yes	8
30	Yes	55	Yes	19
60	Yes	None	Yes	40

Figure 2.12 Risk of crystallization during standby periods (worst-case scenario conditions) [35]

$$T_{ms}(t) = T_0 - \frac{\dot{Q}_{total}}{h_{ms} \cdot Cp_{ms}} \cdot t \tag{2.4}$$

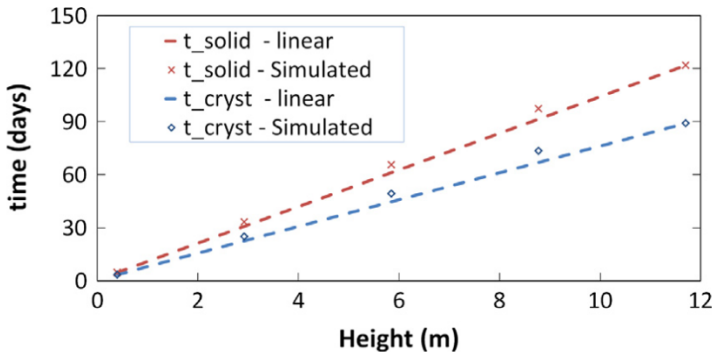

Figure 2.13 Onset of crystallization and solidification for intermediate charging level (red hot tank, blue cold tank) [35]

Research done by Zaversky et al. [34] took a more in-depth approach to look at the different heat losses found in a molten salt thermal storage tank. It goes as far as to consider the absorbed solar irradiation at the outer surface of the tank, as well as wind speed. It features a degree of physical modelling which is able to provide more accurate results but is still suitable for solar thermal power plant simulations. For this modelling it is also assumed that the gas atmosphere above the molten salt in the tank also has a homogeneous temperature distribution. A detailed diagram shown in Figure 2.14 shows the heat transfers that a tank has.

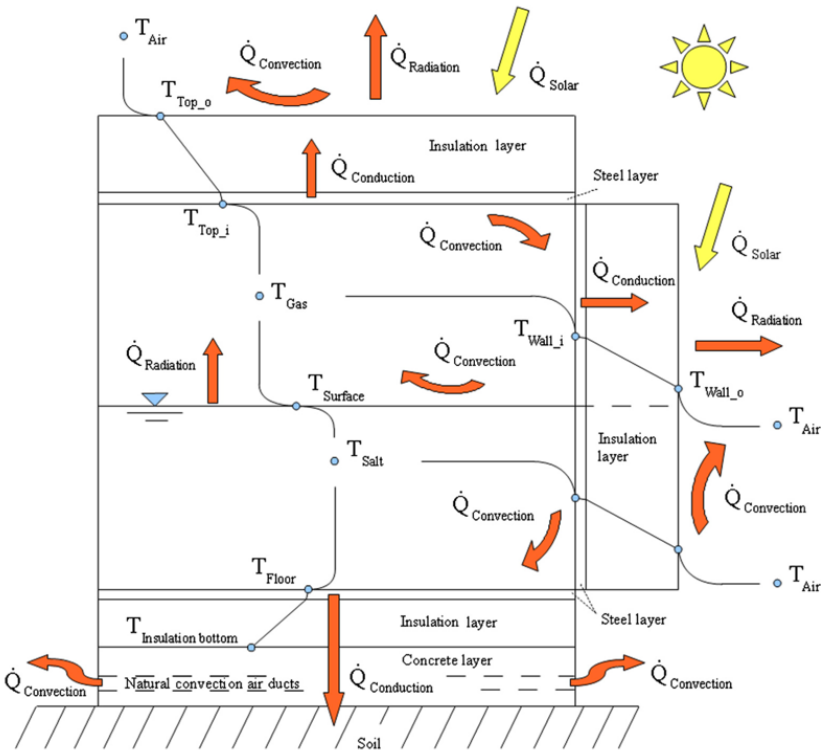

Figure 2.14 Molten salt thermal storage tank model scheme - temperature distributions and heat flows [34]

The paper also presents equations used for thermal conductivity of the various materials that make up a storage tank, as well as density and specific heat capacity for the insulation materials. Modelica modelling language was used for the study. The storage tank walls, roof and floor are modelled as one-dimensional multilayer conduction models. The molten salt is treated as an incompressible fluid. Also, molten salts are nearly transparent to infrared radiation, thus was modelled as a quasi-black body. This means that its emissivity is close to one and almost all the incoming radiation is absorbed by the liquid. Thus, the emissivity if the molten salt was set to 0.95. The heat exchange between the tank's outer surface and the ambient happens via convection and radiation. The convection part can be further divided into heat transfer via natural convection and forced convection. This is determined by the relationship between the Grashof number and the square of the Reynolds number. The results are shown in Figure 2.15.

With the results obtained from the research, the following simplifications to the model can be made. The convective heat transfer between the molten surface and the gas atmosphere can be neglected. The gas exchange between the hot and the cold tank can be neglected. The major heat exchanges are the convective heat transfer at the wetted inner surfaces of the tank jacket and the radiative heat transfer between the molten salt surface and the non-wetted inner surfaces of the tank jacket.

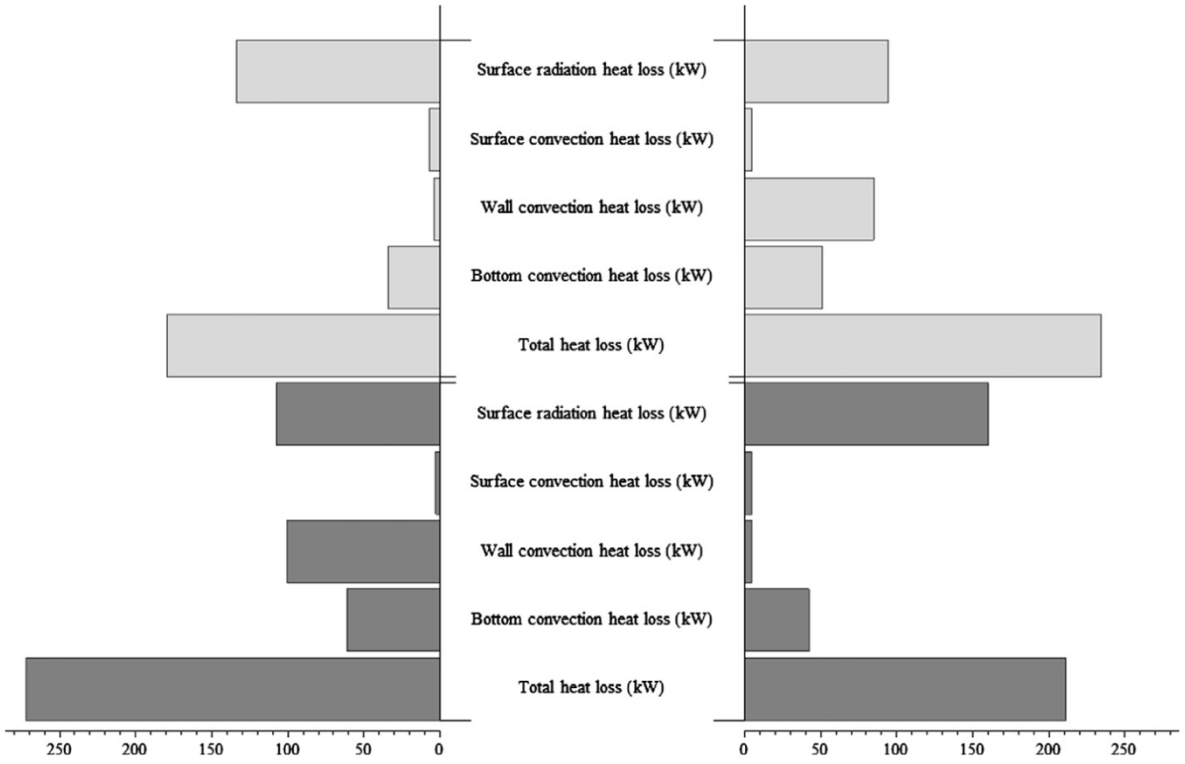

Figure 2.15 Storage tank heat loss fractions at temperature levels 386 ℃/292 ℃ - on the left: fully charged storage system on the right: fully discharged storage system - hot tank grey - cold tank grey [34]

2.7.3 Two-phase flow

In steam generators, there is a region where there will be two-phase flow present in the pipes, typically where flow boiling is occurring. There are two modelling techniques to model two-phase flow. A homogeneous model, where both phases of the fluid are assumed to exist at the same conditions, travelling at the same velocity and have the same properties. This approach takes less computing power but can have inaccuracies in certain conditions. In contrast to this, the two-fluid model treats the two-phases as separate fluids. This is a more complex approach and increases the computing power needed, but should provide higher fidelity for a wider range of operating conditions.

Cilliers [39] investigated how a homogeneous model for two-phase flow compares with a two-fluid model when applied to a u-tube steam generator of a typical pressurized water reactor used in the nuclear power plant industry. For this type of U-Tube steam generator, the tube side is where the hot water from the reactor goes through to boil the water in the shell side. Thus, the research aimed at clarifying under which conditions it is acceptable to use the homogeneous model over the two-fluid model. Flownex was used to model the U-tube steam generator with the homogeneous approach while RELAP5 was used for the two-fluid approach. Due to different heat transfer

correlations being used in the two different programs it was decided to modify Flownex to use the Chen correlation as opposed to the Stienberg and Tamorek correlation already present in Flownex. The models were validated against the plant operating data from Koeberg NPP, with the plant running at 100%, 80%, and 60% power output. After comparing the model results it was concluded that the homogeneous model for two-phase flow produces reliable results when compared to both the plant data and the two-fluid model, in the context of normal operating conditions of the steam generator. Further, it was shown that the homogeneous model can be used when performing operational analysis. However, where detailed results are required, for example in safety analysis, the homogeneous model may not be appropriate. However, this was not studied in detail as it was outside of the scope of the study.

Botha [40] also developed a model in Flownex to simulate the transient conditions that occur in a once-through helical coil steam generator, also using the homogeneous two-phase approach. The results from the study compared well with experiments done on the IRIS OTHSG and therefore supports the use of the homogeneous modelling approach.

2.8 Helical coil steam generators

Shell and tube heat exchangers are common in the power plant industry. The tube side of the heat exchanger is normally made up of multiple tubes. Steam generators typically transfer heat from the shell side to the tube side, thus the steam gets generated in the tubes. There are variations in design for shell and tube heat exchangers. One of these variations is a helical-coil heat exchanger. This design is where the tubes are run in a helix and the fluid in the shell side runs over the helical bundle. These helical-coil heat exchangers can have a 16% to 45% higher heat transfer coefficient than straight pipe heat exchangers [41], due to the flow characteristics in the helical tube. The geometric variables are shown in the Figure 2.16 below.

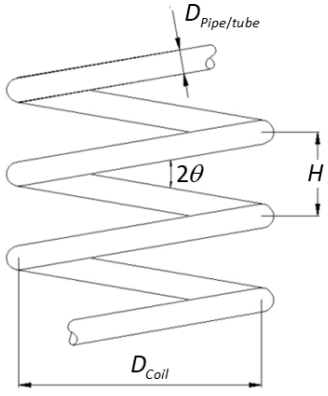

Figure 2.16 Helical Coil Geometry [41]

2.8.1 Flow characteristics

Jayakumar et al. [42] describes the fluid flow characteristics as follows. Due to the curved shape of the tube, the fluid in the tube experiences centrifugal force. The magnitude of this centrifugal force experienced by the fluid depends on the local axial velocity of the fluid and the radius of the curvature of the coil. In the core of the tube, the fluid velocities are higher than at the wall of the tube. Thus, the fluid particles closer to the wall of the tube experience less centrifugal force than the fluid in the tube core. This causes the fluid from the core region to be pushed towards the wall of the tube (away from the coil axis). The stream bifurcates at the wall, driving the fluid towards the inner wall along the tube periphery. This causes counter-rotating vortices called secondary flows as shown in Figure 2.17. These secondary flows produce additional transport of the fluid over the cross section of the pipe. This enhanced mixing from the secondary flow is more evident with laminar flow due to the limited fluid mixing in straight tube laminar flow [43]. The secondary flows reduce the thermal boundary layer and account for 16-20% of the mean fluid flow velocity [44]. Because of the enhanced mixing due to the secondary flow, both the heat transfer and the pressure drop increase when compared to straight tubes. Due to the geometry of the coil turbulent fluctuations are suppressed in the flowing fluid smoothing the emergence of turbulence. Thus, the critical Reynolds number that typically describes when the flow is turbulent is increased. This effect of turbulence suppression increases with the curvature ratio. Torsion effects in the coil tend to destabilize the flow and could theoretically decrease the critical Reynolds number, however in practical application the torsion value never reaches a high enough value to affect the destabilization of flow.

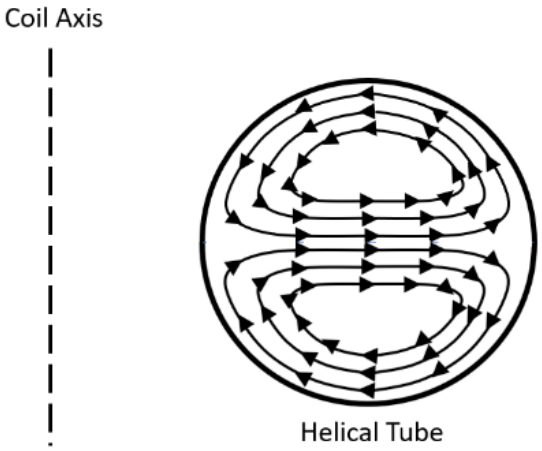

Figure 2.17 Secondary flows in a helical coil cross section

Since the helical coil geometry will generally lead to higher critical Reynolds numbers another phenomenon can also be present which is called relaminarization. This is when the fluid flow which was originally turbulent before entering the helical coil becomes laminar flow while passing through

the coil. The following critical Reynolds number correlations have been used in literature. Both equation (2.5) and equation (2.6) have been shown to produce similar results [45]. Equation (2.7) is also a well know critical Reynolds number correlation for curved tube and was used by Jayakumar [46] who conducted an experimental study and a CFD simulation of the heat transfer in a helically coiled heat exchanger. For curvature rations less than 1/860, the critical Reynolds number becomes to that of straight tubes [46].

$$Re_{cr} = 20{,}000\left(\frac{D_{Pipe}}{D_{Coil}}\right)^{0.32} \quad Ito \tag{2.5}$$

$$Re_{cr} = 2100\left(1 + 12\left(\frac{D_{Pipe}}{D_{Coil}}\right)^{0.5}\right) \quad Srinivan\,et\,al \tag{2.6}$$

$$Re_{cr} = 2300\left(1 + 8.6\left(\frac{D_{Pipe}}{D_{Coil}}\right)^{0.45}\right) \quad Schmidt \tag{2.7}$$

It is useful to understand what geometrical parameters affect the heat transfer on the fluid inside the helical coil and which have no effect. The coil diameter has a significant effect on the heat transfer. This is due to the fact that as the coil diameter increases the centrifugal forces present in the tube decreases. Thus, the secondary flow and the effects of the secondary flow decrease. The effect of the coil diameter on the ratio of the heat transfer coefficient between two-phase and single phase flow was also investigated by Jayakumar et al. [42]. It was observed that the ratio is almost independent of the curvature ratio of the coil. Thus, the effect of curvature on two-phase heat transfer is almost the same as single phase flow and is well predicted by the single-phase heat transfer correlation. From the experiments conducted it was shown that the influence of pitch on the heat transfer correlations are negligible. Therefore the effect that the pitch has on the overall heat transfer for design purposes need not be considered for most practical application with helical coils [42]. The Dean number shown in Equation (2.8) is commonly used to characterise the flow on a helical coil pipe, much like the Reynolds number. The Dean number is sometimes used in heat transfer correlations.

$$De = Re\sqrt{\frac{D_{Pipe}}{D_{Coil}}} \tag{2.8}$$

2.8.2 Heat transfer modelling on the tube side

The geometry of a helical coil steam generator proves to be complex to model. A common method that has been found in literature is to model the helical tubes as one straight pipe with a slight

inclination angle. This inclination angle is the same as the helix angle shown in Figure 2.16. This simplified modelling technique is shown by Hoffer et al. [41], who modelled a helical-coil steam generator in RELAP5-3D. The heat exchanger that was modelled is typically found in the nuclear power plant industry. The heat exchanger that was modelled has the following sections in one unit: the economizer, evaporator, and two superheater sections. The following simplifications were made to model the steam generator. The helical-coil bundle of this heat exchanger had 441 tubes and was modelled as a single tube with an equivalent flow area, heat transfer surface area, hydraulic diameter, and heated hydraulic diameter. The single tube was simplified again by unwrapping the coil tube to make an inclined pipe of the same length of the helical coil tubes but to only have an elevation corresponding to the outlet of the heat exchanger. A heat transfer multiplier was added to model the enhanced heat transfer.

As already stated the typical heat transfer correlation used in straight tubes must be modified to account for the enhanced heat transfer in a helical coil. It is noted by Fsadni et al. [43], that fewer studies have investigated the two-phase flow heat transfer characteristics in helically coiled tubes than in single phase flow. In the review, it is concluded that there are no comprehensive reviews on the heat transfer characteristics of two-phase flow in helically coiled tube heat exchangers. However, Jayakumar e al. [42] has shown that the quantitative dependence of coil parameters on heat transfer is the same for both single and two-phase flows.

The following studies that investigated the heat transfer characteristics in helical coils. Most of the studies apply a modified version of the trusted Dittus-Boelter correlation shown in Equation (2.9).

$$Nu = 0.023 Re^{0.8} Pr^{n} \tag{2.9}$$

Where n = 0.4 for heating fluids and n = 0.3 for cooling fluids.

Esch et al. [47] conducted a study of the influence of different heat transfer correlations for a helical coil tube steam generator using the system code TRACE. The helical coil for the steam generator was simplified into straight angular tubes for the model. The results were validated by comparing the simulated results to the experimental data from the THTR-300 steam generator. The results of the investigation showed the standard Nusselt number Equation (2.10) which is for fully turbulent flow does not model the steam generator as well as the modified Nusselt number shown in Equation (2.11). It is important to note though that in the THTR-300 helium flows in the shell side. Thus, the recommended Nusselt number correlation may not be applicable for the steam generator used in a CSP plant. However, it shows that the Nusselt number is an important consideration for the heat transfer correlation for a helical coil steam generator when modelling it.

$$Nu = \frac{F\left(Re - 1000\right)\cdot Pr}{1 - 12.7\cdot\sqrt{F}\left(Pr^{0.66} - 1\right)} \qquad (2.10)$$

Where:

$$F = \frac{0.5}{(1.58\cdot\log_e(\mathrm{Re}) - 3.28)^2}$$

$$Nu = 0.1135\cdot\left(F\cdot Re\right)^{0.714}\cdot Pr^{1/3} \qquad (2.11)$$

Where:

$$F = \frac{\varsigma_T - 1}{\varsigma_T\cdot\sqrt{1 + (\varsigma_L^2 / 16\varsigma_T^2) - 1}}$$

$$\varsigma_L = S_L / D_{Pipe}$$

$$\varsigma_T = S_L / D_{Pipe}$$

Botha [40] developed two computer models to simulate the transient conditions that occur in a once-through helical coil steam generator (OTHSG). The aim was to develop a dynamic model for an OTHSG tube, which modelled the transient response and the two-phase boiling phenomena in the helical coils. The transient scenario was the start-up to normal operating conditions. The first model that was developed was developed in Engineering Equation Solver (EES) in order to correctly understand the fundamentals. This model was compared to a model created in Flownex which is a commercial software package. The Flownex model was then further developed to model more complex transients. Both models developed use the homogeneous two-phase flow approach. For the Flownex model, the helical coil was simplified and represented by equivalent vertical pipes in parallel and an enhanced heat transfer coefficient was applied to take into account the influence of the coil geometry, the Dittus-Boelter equation was modified to achieve this as shown in Equation (2.12).

$$Nu_{enhanced} = 0.116 Re^{0.71} Pr^n \delta^{0.11} \qquad (2.12)$$

$$\left(14000 < Re < 70000\right)\ \left(3 < Pr < 5\right)\ \ (0.05 < \delta < 0.2)$$

The steady state results from the Flownex model compared well with experiments done on the IRIS reactor's OTHSG. The heat transfer rate resulting from the Flownex model only had an error of 0.48%.

Guo et al. [48] investigated the transient convective heat transfer of steam-water for two-phase flow in a helical coil tube. Most studies have investigated the heat transfer under steady state conditions, but the investigation into transient scenarios gives a better understanding of start-up scenarios. This paper conducted experiments for subcooled water flow and steam-water two-phase flow to investigate the effects of pulsations on the transient heat transfer characteristics in a closed-circulation helical coiled tubed steam generator. The test section was made of a 6448 mm long tube of 15 mm diameter tube, with a helix angle of 4.27°, coil diameter of 256mm and a pitch of 60mm. The paper presented results for turbulent heat transfer for single phase water flow. The data

obtained fitted in between a predicted curve based on a correlation by Seban and Mclaughlin and the Dittus-Boelter correlation. Thus, a new correlation was proposed for a wider range of Reynolds numbers shown in Equation (2.13).

$$Nu = 0.328 Re^{0.58} Pr^{0.4} \tag{2.13}$$

$$6000 < Re < 180,000$$

The data obtained for the transient heat transfer correlations for unsteady flow shows that the heat transfer coefficients were higher than that of steady flow. The oscillations in flow enhanced the effects of the single phase turbulent heat transfer. However, the results obtained showed that the correlations are unpredictable using typical Nusselt number correlations for helical coil tubes. Thus, two non-dimensional parameters were introduced, the oscillation frequency number $\overline{Wo}$ and the oscillatory amplitude $\overline{Wp}$. This lead to Equation (2.14), which uses a time averaged Dean number, and applicable for the range of oscillation $f = 0.05 - 0.003$, $\overline{Re} = 25,000 - 125,000$. This correlation reaches reasonable agreement with a 15% deviation between the calculated value and the experimental value.

$$\overline{Nu_{osc}} = 0.147 \overline{Wo}^{-0.31} Pr^{-4.4} \left(\frac{\overline{De}}{1000} \right)^{0.82} \tag{2.14}$$

Zhao [45] investigated the convective boiling heat transfer of two-phase flow characteristics inside a small horizontal helically coiled tubing once-through steam generator. The paper presented correlations already tested for helical tubes and concluded that the correlations found could only be used in specific ranges and there are some conflicts among their conclusions. Thus, the research experimentally investigates the effect of miniaturization on the two-phase flow and boiling characteristics inside a horizontal helically coiled once-through steam generator. For the single phase heat transfer the correlation presented by Seban and McLaughlin shown in Equation (2.15), had a $\pm 10\%$ agreement with experimental results. For the boiling heat transfer coefficient, the Chen's correlation was investigated. The results showed that the Chen correlation had a mean deviation of 23.4%.

$$Nu = 0.023 Re^{0.8} Pr^{0.4} \left(Re \left(\frac{D_{Pipe}}{D_{Coil}} \right)^2 \right)^{0.05} \quad (6000 < Re < 65,600) \tag{2.15}$$

Jayakumar [46] shows an experimental study and CFD estimation of heat transfer in helically coiled heat exchangers. Using multiple regression analysis, the correlation shown in Equation (2.16) was obtained. The method for estimation of heat transfer for a helically coiled heat exchanger has been validated against experiments.

$$Nu = 0.025De^{0.9112}Pr^{0.4} \quad (2000 < De < 12{,}000) \tag{2.16}$$

Jayakumar [42] Used multiple-regression analysis based on data from cases studies and found the Nusselt number correlation is shown in Equation (2.17). Another Nusselt number correlation was also obtained by looking at constant heat flux boundary conditions shown in Equation (2.18). This is applicable to heat flux controlled surfaces such as electrically heated pipes. Nuclear elements etc. These two correlations showed very little difference for a lower range of Reynolds numbers, however they showed marginal differences when Re>50000.

$$Nu = 0.166Re^{0.71}Pr^{0.4}\delta^{0.11} \tag{2.17}$$

$$Nu = 0.085Re^{0.74}Pr^{0.4}\delta^{0.1} \tag{2.18}$$

$$(14000 < Re < 70000)\ \ (3000 < De < 22000)\ \ (3.0 < Pr < 5.0)\ \ \ (0.05 < \delta < 0.2)$$

As can be seen from the literature presented little investigation has been done into the heat transfer correlations for higher Reynolds numbers. Guo [48] shows test data for the equation presented in Guo [49], these results are shown in Figure 2.18. The results show that with increasing Reynolds numbers the average heat transfer of the helical coil tends to match that of the standard Dittus-Boelter correlation for straight tubes. Thus, this implies that the heat transfer enhancement effect due to the secondary flow becomes less significant due to the thinning of the thermal boundary layer at much higher Reynolds numbers. Furthermore, an investigation done by Santini [50] showed that the curvature effects on the heat transfer during flow boiling were found to be negligible. Thus, for the boiling region the heat transfer correlations can be predicted using existing correlations for straight tubes. However, it is noted that standard straight tube correlations do tend to slightly under predict the heat transfer correlation. This is also shown by Jayakumar [42].

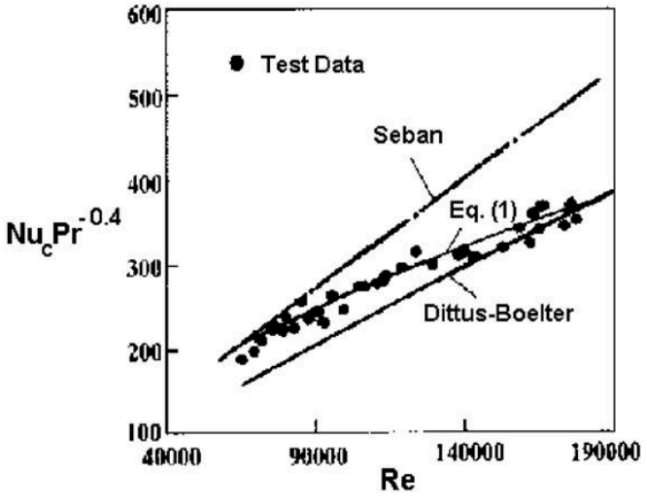

Figure 2.18 Heat transfer correlations vs test data [48]

2.8.3 Modelling principles on the shell side

The heat transfer and flow characteristics of the shell side of a helical coil heat exchanger also have to be understood and accounted for. Rivas [51] conducted research in order to obtain suitable heat transfer correlations on the molten salt side of a helical steam generator. The research was conducted as there is little literature that can be found on the topic. A CFD model was developed to model a 300 kWth MS prototype helical steam generator. This steam generator is integrated into the molten salt storage tank. The model was validated against the prototype that was erected in the Casaccia Research Centre of ENEA (Italy). The CFD model used the commercial code STAR-CCM+8.04.010 (based on finite volume method). The molten salt properties were modelled using the following assumptions; The Boussinesq approximation was applied since the density variations with temperature are considered small enough in the range of operating conditions to assume constant density in all momentum terms except in the buoyancy term. The thermo-physical properties were the heat capacity, thermal conductivity and dynamic viscosity, are considered to be dependent on temperature. The resultant heat transfer coefficients in all elements are comprised between 600 and 1200 W/m^2K. The Nusselt, Reynolds and Prandtl numbers are based on the outer diameter of the helical coils, the local heat transfer coefficients calculated, the maximum numerical velocities and the molten salt physical properties. The correlation developed is shown in Equation (2.19).

$$Nu = 0.314 Re^{0.54} Pr^{0.36} \tag{2.19}$$

This correlation is valid for Re between 400 up to 1200, Pr between 4 up to 11, an average winding angle of 2° and an outer diameter of the helical coil of 0.0127 m. As can be seen, this correlation is only valid for low Reynold numbers and this type of helical steam generator design relies on natural convection for the shell side. Unfortunately, to the best of the author's knowledge no other research has been conducted extensively to evaluate the molten salt heat transfer characteristics on the shell side of a helical coil steam generator.

However, since molten salt behaves in much the same way as water, existing correlations for flow over tube banks should be suitable for modelling the helical coil tube bank on the shell side of the heat exchanger. For the external flow over the helical tubes, there is a combination of cross and counter flow. The smaller the helix angle the greater the cross flow component and vice versa. In the model developed by Botha [40], the external flow over the tubes was modelled in the following way: Equation (2.20) was used for the external conductive heat transfer, which takes into account the geometry of the pipes [52]. The use of this correlation was validated by Botha [40].

$$Nu = C_1 Re^m Pr^{0.36} \left(\frac{Pr}{Pr_w}\right)^{0.25} \tag{2.20}$$

Where C_1 is obtained from Figure 2.19 and Table 2.3.

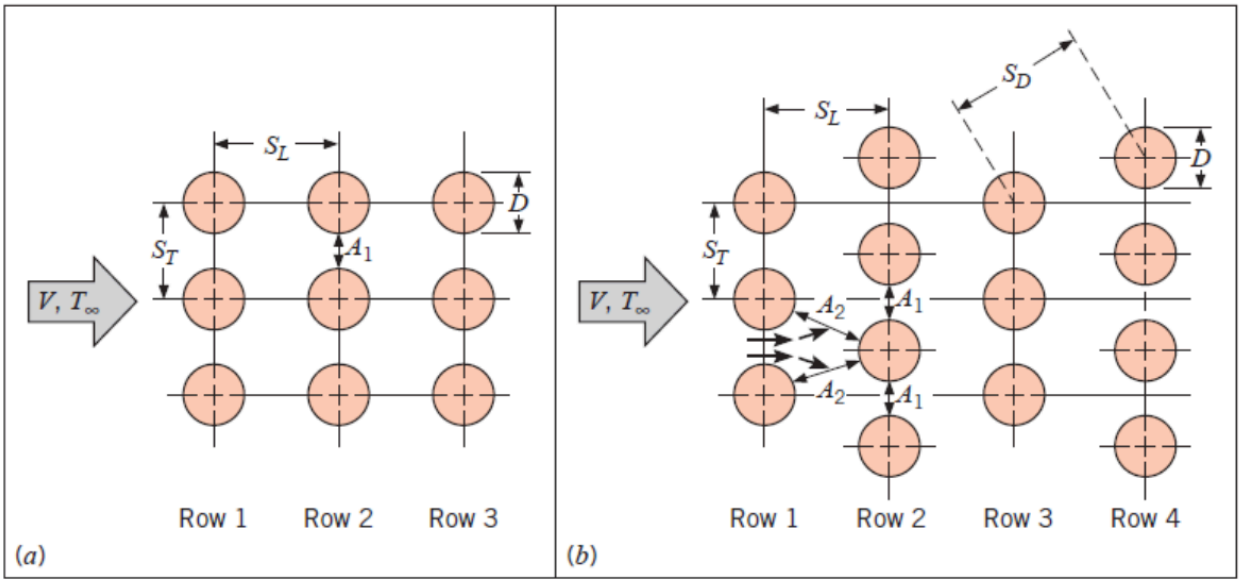

Figure 2.19 Cross flow heat transfer constants for tube layout

Table 2.3 Cross flow heat transfer constant for tube layout

Configuration	Re	C_1	m
Aligned	$10\text{-}10^2$	0.8	0.4
Staggered	$10\text{-}10^2$	0.9	0.4
Aligned	$10^2\text{-}10^3$	Approximate as a single cylinder	
Staggered	$10^2\text{-}10^3$		
Aligned (S_T/S_L >0.7)	$10^3\text{-}2x10^5$	0.27	0.63
Staggered (S_T/S_L <2)	$10^3\text{-}2x10^5$	$0.35(S_T/S_L)^{0.2}$	0.60
Staggered (S_T/S_L >2)	$10^3\text{-}2x10^5$	0.4	0.60
Aligned	$2x10^5\text{-}2x10^6$	0.021	0.84
Staggered	$2x10^5\text{-}2x10^6$	0.022	0.84

2.8.4 Friction factor correlations for helical coils

In addition to the effects on the heat transfer in a helically coiled pipe, the frictional pressure drop is also affected by the secondary flows that occur within the pipe. For single phase flow, the frictional pressure drop through a coiled or curved pipe is larger than that of the same flow conditions through a straight pipe [53]. For laminar flow, numerous studies have been done to obtain a friction factor that accounts for the increase in frictional pressure drop. Hart [53] found a more accurate correlation for laminar flow given by Equation (2.21), where the friction factor satisfies the boundary condition $f_c = f$ for $De \to 0$ and covers the whole laminar domain where $0 < Re < Re_{crit}$.

$$f_c = f\left\{1 + \left(\frac{0.09De^{1.5}}{70 + De}\right)\right\} \tag{2.21}$$

where f is the laminar friction factor for straight tubes in laminar flow

There are also various friction factor correlations for the turbulent region in a helical coiled tube. However, Hart et al. [53] found that their experimental results were in good agreement with Equation (2.22) by White [54].

$$f_c = f + 0.01\left(\frac{D_{Pipe}}{D_{Coil}}\right)^{1/2} \quad (Re_{crit} < Re < 2\times10^5) \tag{2.22}$$

where f is the normal straight tube friction factor in turbulent flow

Both of the friction factor correlations given by Hart et al. [53] are for the fanning friction factor (as opposed to the Darcy-Weisbach friction factor), therefore this must be taken into account when using these correlations.

Santini et al. [50] investigated the pressure drops for a helical coil to better predict the pressure drops seen in helical coil steam generators. Their review of the single phase friction factor correlations in turbulent flow showed that for Re<150000 Equation (2.23) given by Ito [55] can be used and for Re>150000 Equation (2.24) given by Ruffell can be used. From experimental data it was shown that Equation (2.23) starts to under predict the friction factor while Equation (2.24) tends to over predict as the Reynolds numbers increase. From their experimental results, they also derived a correlation for the friction factor that better fitted their data. However, in their proposed equation the coil diameter ratio was not taken into account and therefore the possibility of using it on other coils with different geometries is unknown.

$$f_c = 0.076Re^{-0.25} + 0.00725\left(D_{Coil} / D_{Pipe}\right)^{-0.5} \tag{2.23}$$

$$f_c = 0.00375 + 0.633\left(D_{Coil} / D_{Pipe}\right)^{-0.275} Re^{-0.4} \tag{2.24}$$

Ju et al. [56] conducted research on the hydraulic performance of small bending radius helical coil tubes used in the HRT-10 steam generator. From their experiments different single phase friction factors were obtained depending on the magnitude of the Reynolds number. Below are the friction factor correlations for each range of Reynolds numbers.

$$f = \frac{64}{Re};\ \ \frac{f_c}{f} = 1 \tag{2.25}$$

$$when\, De < 11.6 \left(Laminar\, Flow\right)$$

$$f = \frac{64}{Re}; \frac{f_c}{f} = 1 + 0.015 Re^{0.75}\left(D_{Pipe} / D_{Coil}\right)^{0.4} \tag{2.26}$$

$$when\, De > 11.6, Re < Re_{crit}\ \left(laminar\ flow\, with\, big\, vortex\right)$$

$$f = \frac{0.316}{Re^{0.25}} \qquad \left(Smooth\, pipe\right) \tag{2.27}$$

$$f = 0.1\left(\frac{1.46\varepsilon}{D_{Coil}} + \frac{100}{Re}\right)^{0.25} \qquad \left(\varepsilon : roughness\, of\, the\, pipe\right) \tag{2.28}$$

$$\frac{f_c}{f} = 1 + 0.11 Re^{0.23}\left(\frac{D_{Pipe}}{D_{Coil}}\right)^{0.14} \tag{2.29}$$

$$when\, De > 11.6, Re > Re_{crit}\ \left(Turbulent\, Flow\right)$$

Fsadi et al. [44] reviewed much of the current literature available on the two-phase pressure drop characteristics in helically coiled tubes. Their review covered multiple fluids other than just two-phase water and steam flow. However, only the conclusion for the water and steam two-phase flow was considered for this literature review. There is limited literature on the two-phase pressure drop characteristics in helically coiled tubes when compared to the single-phase pressure drop regions. This is due to the added complexity of the combination of the governing forces over the flow regime, being the inertia, gravity and centrifugal forces. From the literature that Fsadi et al. [44] reviewed, it was concluded that in open literature available at the time of writing the paper no comprehensive critical reviews on the pressure drop characteristics of the two-phase flow region in helical coil tubes existed. However, some conclusions can be drawn from the literature reviewed. There appears to be general agreement that the two-phase pressure drop increases with vapour quality and mass flux while it will decrease with increasing system pressure. This is shown in Figure 2.20 from Colombo et al. [57]. It would appear that there is no significant influence on the two-phase flow due

to the curvature ratio of the coil while there is some controversy surrounding the influence of the coil orientation and heat flux due to a paper by Guo et al. [58]. One of the earliest investigations by Owhadi et al. [59] roughly showed that the two-phase pressure drop can be predicted using the well-known Lockhart and Martinelli multiplier for straight tubes. However, it has been shown that the Lockhart and Martinelli approach will under predict the two-phase pressure drop when the system is at low pressure and high Reynolds numbers. Colombo et al. [57] developed a better two-phase correlation based off the well-known Lockhart and Martinelli approach. Their first proposed correlation is shown in Equation (2.30) and then further refined to give Equation (2.31). The modifications that were made essentially extend the range and validity of the Lockhart and Martinelli approach by considering the coil curvature and the liquid phase. The mixture-to-liquid density ratio accounts for the effect of the system pressure. The new correlation was validated with two databases containing more than 1000 experimental data points. The correlation gives a mean error of about 12.9%, which compared to other correlations shows the highest accuracy across the database.

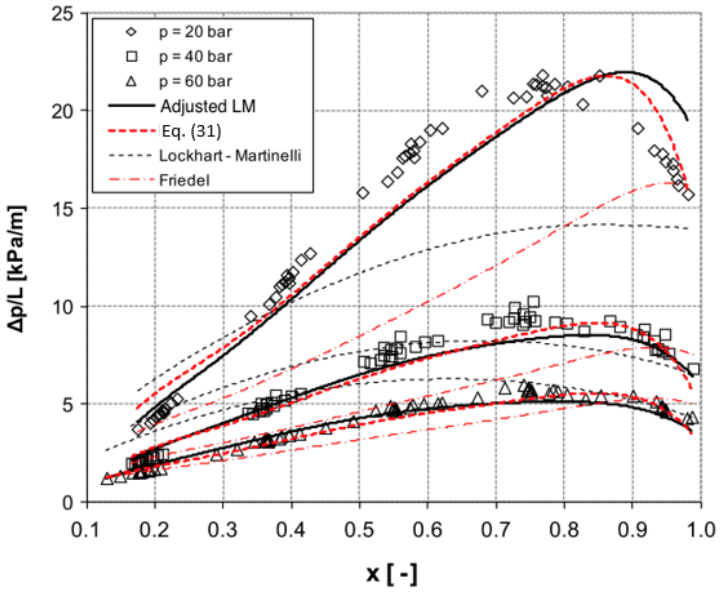

Figure 2.20 Two-Phase Pressure drop in helical coil tubes [57]

$$\phi_l^2 = 0.13\phi_{LM}^2 De_l^{0.15}\left(\frac{\rho_{fg}}{\rho_l}\right)^{-0.37} \tag{2.30}$$

$$\phi_l^2 = 0.0986\phi_{LM}^2 De_l^{0.19}\left(\frac{\rho_{fg}}{\rho_l}\right)^{-0.4} \tag{2.31}$$

2.9 Two-phase flow instabilities

Flow instabilities of two-phase flow is a complicated phenomenon to study as there are various types of two-phase flow instabilities that have been found. First Ruspini et al. [60] states that there are microscopic and macroscopic instabilities. Microscopic instabilities occur locally at the liquid-gas interface, while macroscopic instabilities influence the whole two-phase system and thus are more important to understand for industrial purposes, especially in steam generators. Within macroscopic instabilities, there are two main sections of instabilities defined as static and dynamic instabilities. Ruspini et al. [60] describes a static instability as a stability that can be predicted using steady state conservation laws. Kakac et al. [61] simply states that a static instability occurs when the operating point is not a stable equilibrium point, and the system will move to a different equilibrium point which is a stable one. For a dynamic instability, there is sufficient interaction and delay feedback between the inertia of flow and compressibility of the two-phase mixture, or it may result from multiple feedbacks between flow rate, pressure drop and the change in density as a result of the rate of vapour generation in a boiling channel [61].

2.9.1 Static instabilities

For static instabilities the pressure-drop vs flowrate curve shown in Figure 2.21 can be used to illustrate the phenomenon. It depicts two characteristic curves from two steady state systems. These two curves are classified as internal and external curves, where the internal curve is the boiling channel curve of the system that can take the form of an N-shape, while the external curve is an external component such as a pump for example. The operating point of the system is given by the points where these lines intersect. Thus, depending on the external characteristic curve, the operating points can be stable or unstable. For the stable operating condition, the internal characteristic curve must have a slope greater than the external characteristic curve. This is described by Equation (2.32) [60]. From Figure 2.21, one can see the in case 1 and 2 there is only one point of intersection between the external and internal curve giving a stable system. Where with case 3 and 4 there are multiple operating points making the system unstable.

$$\frac{\partial \Delta P}{\partial G} int \mid_w > \frac{\partial \Delta P}{\partial G} ext \mid_w \tag{2.32}$$

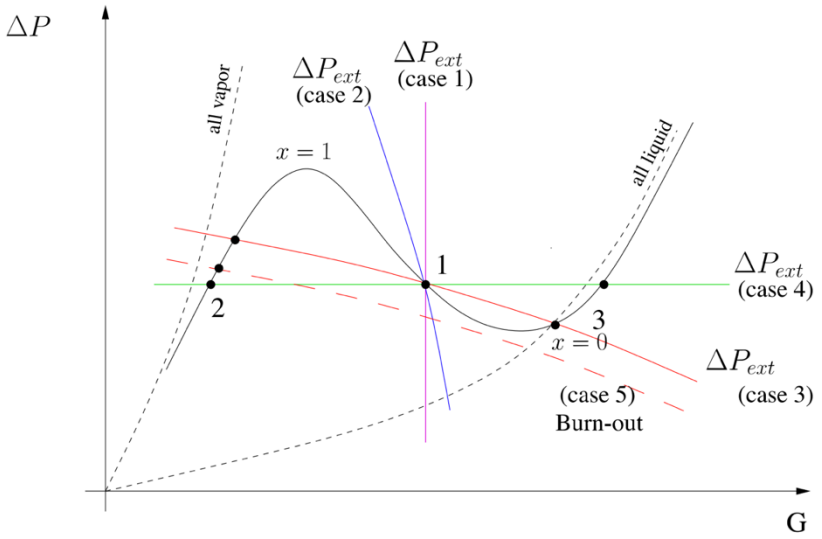

Figure 2.21 Pressure drop vs Flow rate curve for a boiling channel [60]

The N shape that is seen in Figure 2.21 is made up of three major pressure drop components. The main components are momentum, frictional and potential pressure drops. One can see from Figure 2.22 which components contribute to the N shape curve of the pressure-drop vs flowrate curve. The potential term is then said to be stabilizing, while the momentum and pressure terms are destabilizing the system [60].

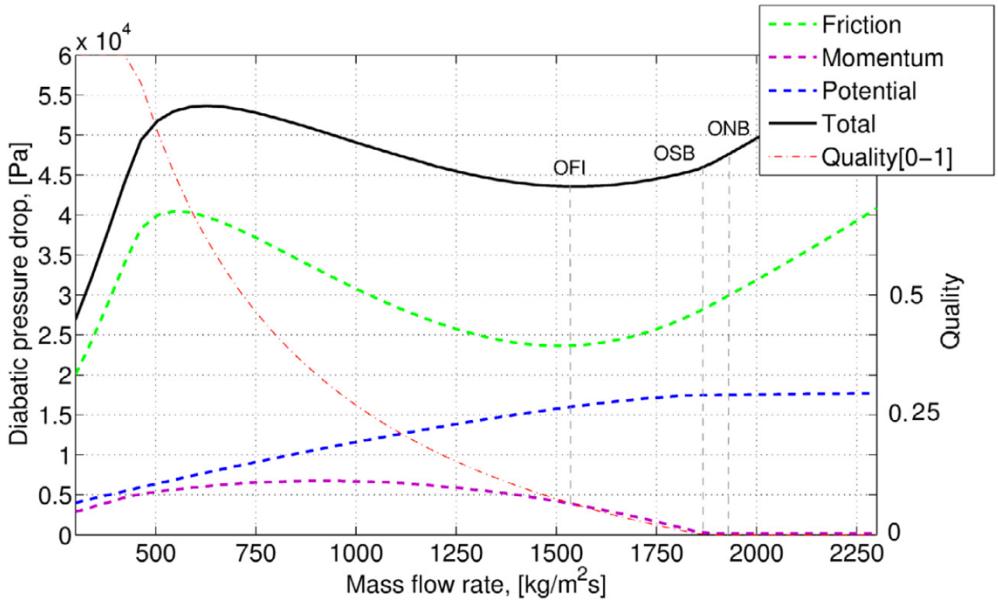

Figure 2.22 Pressure Drop Components [60]

One of the most studied static instabilities is called the Leginegg instability. The Leginegg instability is the basic phenomenon associated with the pressure-drop vs flowrate curve already described. The occurrence of the Ledinegg flow instability has been shown by Farhadi [62] to depend on the

length to diameter ratio of the heated channel, the inlet temperature, the exit pressure, and the surface heat flux. This Leginegg instability can further to complicated by having multiple tubes. If the parallel tubes have different characteristic curves, there can be several regions where there would be multiple solutions as shown in Figure 2.23 [60].

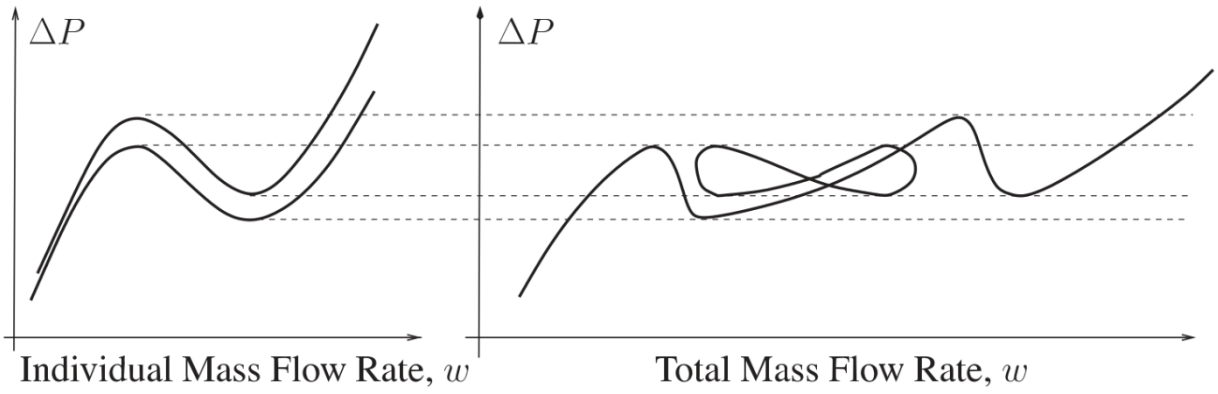

Figure 2.23 Parallel tube pressure drop vs flowrate [60]

The remainder of the static instabilities typically have a smaller amplitude than the Leginegg instability and usually occur under rare conditions, thus further discussion into static instabilities is not necessary.

2.9.2 Dynamic instabilities

This literature review focuses on three dynamic instabilities namely Pressure Drop Oscillations (PDO), Density Wave Oscillations (DWO) and thermal oscillations. Pressure Drop oscillations can be shown through Figure 2.24 where the typical N-shape for pressure-drop vs flowrate is shown. This type of instability occurs when there is a compressible volume placed upstream of the heated section [60]. Ruspini et al [60] reports on a controversial study which indicated that for very long test sections there can be sufficient compressibility inherent in the test section itself due to vapour generation to initialize the instability. However, no other work in the field supports this finding. Kakac et al. [61] does state that this compressible volume can be internal or external. Referring to Figure 2.24 to describe the pressure drop oscillation: Compression occurs in the compressible volume from C to D; flow excursion from a two-phase state to a liquid state from D to A; decompression in the compressible volume from A to B; and flow excursion from a low quality to a high quality two-phase state from B to C. For high power density systems it is shown that the compressible volume needed to sustain the oscillation is very small [60].

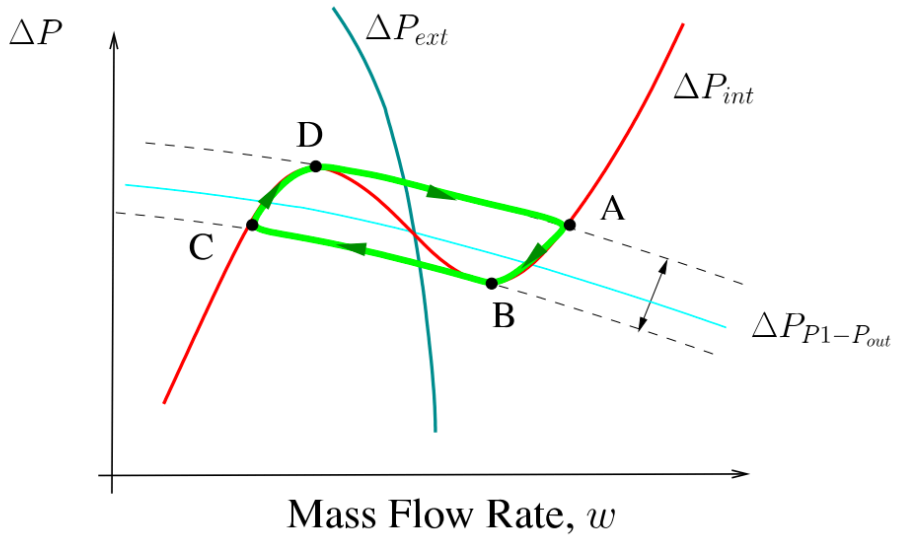

Figure 2.24 Pressure Drop Oscillation Description [60]

Density-wave oscillation (DWO) is arguably the most common type of instability in a vapour generation boiling system [63] and the most researched. However, there is still conflicting conclusions and being able to correctly predict the stability threshold remains a cumbersome task. Colombo et al [63] gives the following description of a DWO: DWOs are induced by delays in the transient distribution of pressure drops along the tube, which originate from the difference in density between the subcooled liquid entering the channel and the water-steam mixture exiting. If the pressure drop along the channel in imposed, a sudden pressure drop perturbation necessarily leads to a flow rate perturbation. An instantaneous perturbation of flow rate causes an enthalpy perturbation propagating throughout the channel, which affects both the boiling boundary position and the length of the single-phase and two-phase regions. The result is a perturbation in the single-phase pressure drop and a delayed two-phase pressure drop perturbation of the opposite sign. The latter creates a feedback pressure perturbation of the opposite sign in the single-phase region. With the correct timing, the single-phase region and two-phase region pressure terms oscillate in counter-phase, flow oscillation becomes self-sustained and waves of higher density and lower density fluid propagate through the channel. The time period for these oscillations is typically between 1.5 and 2 times the required time for the fluid to travel through the system or mixture transit times [60]. Mixture transit times are calculated with classical homogeneous flow theory, by adding single-phase region transit time and two-phase region transit time shown in Equation (2.33) [64].

$$t = t_1 + t_2 = \frac{\rho_{in}\Delta h_{in}}{Q''} + \frac{h_{fg}}{Q''\nu_{fg}}\ln\left(1 + \frac{\nu_{fg}}{\nu f}x_{ex}\right) \tag{2.33}$$

Rearranged:

$$t = \frac{A_{tube} L_{tube} h_{fg}}{Q} \left[-\rho_{in} x_{in} + \frac{1}{v_{fg}} \ln\left(1 + \frac{v_{fg}}{v_f} x_{ex} \right) \right] \tag{2.34}$$

The literature review by Ruspini et al [60] reports that the DWO's have been divided into three categories, DWO_I due to gravity, DWO_{II} due to friction and DWO_{III} due to momentum. DWO_I has been observed in upward vertical systems with a long adiabatic chimney section down-stream from the heated section. This type of oscillation is very important in natural convection loops but has been reported in forced convection loops. DWO_{II} is the most common type of density wave instability described in literature. The instability occurs due to the difference in propagation speed of the flow perturbations in the single and two-phase region. Pressure drop variations occur due to changes in flow or void fraction. These perturbations propagate rather slowly along the two-phase region, a significant delay marks the onset of perturbations in the two-phase region. Because of this phenomenon, the two-phase and single-phase pressure drop oscillate out of phase. DWO_{III} is the interaction between the inertia and momentum pressure-drop terms and the thermohydraulic propagation delays. However, this type of instability has received very little attention in literature. In parallel channels, the stability for the DWO type depends on the local stability for each channel.

Thermal oscillations are another type of instability that are primarily triggered by other types of instabilities. The term thermal oscillations are associated with large fluctuations in the heated channel wall temperature. Thermal oscillations have two types of instabilities, the first is associated with the movement of the dry out and nucleate boiling boundaries. When the instability is triggered by low frequency oscillations (PDO), the temperature fluctuations are simply the result of the boiling boundary movement. The oscillation frequency is equivalent to that of the primary oscillation. When the instability is triggered by DWO, the frequency in temperature fluctuations have two distinct modes, a high frequency and small amplitude that corresponds to the DWO and a low frequency and large amplitude mode. The low frequency mode is found to be a system mode which depends on the heated wall capacity, axial conduction and transition boiling characteristics. This is separate from the primary instability and is thus called a thermal oscillation [60].

Table 2.4 is provided from a review paper done by Kakac et al. [61], where the most common types of instabilities are reported. Some have not been reviewed in detail as they are either uncommon or shouldn't be a factor in the HPS2 test facility.

Table 2.4 Two-phase flow instabilities [61]

Class	Type	Mechanism	Characteristics
Static instabilities	Ledinegg instability	Internal characteristics are steeper than external characteristics in a negative slope region.	Flow undergoes sudden, large amplitude excursion to a new stable operating condition.
	Boiling crisis	Ineffective removal of heat from heated surface.	Wall temperature excursion and flow oscillation.
	Flow pattern transition instability	Bubbly flow has less void but high pressure-drop than annular flow.	Cyclic flow pattern transition and flow variations.
	Bumping Geysering Chugging	Periodic adjustment of metastable condition, usually due to lack of nucleation sites.	Periodic process of super-heated and violent evaporation with possible expulsion and refilling.
Dynamic instabilities	Acoustic oscillations	Resonance of pressure waves.	High frequencies (10-100Hz) related to time required for pressure wave propagation in the system.
	Density-wave oscillations	Delay and feedback effects in relationship between flow rate, density, and pressure-drop.	Frequencies related to transit time as a continuity wave.
	Pressure-drop oscillations	Dynamic interaction between channel and compressible volume.	Very low frequency periodic process.
	Thermal oscillations	Interaction of variable heat transfer coefficient with flow dynamics.	High magnitude temperature oscillations in the solid due to transitions between different boiling regimes.
	Boiling water reactor instability	Interaction of void reactivity coupling with flow dynamics and heat transfer.	Strong only for small fuel time constant and under low pressure.
	Parallel channel instability	Interaction amount parallel channels.	Various modes of flow redistribution or V-tube manometer oscillations.

2.9.3 Stability maps for DWOs

For DWOs no universal stability map exists, and different ones have been proposed over the years with the use of different non-dimensional numbers. However, a relatively successful stability map has been widely used using a phase change number N_{pch} (2.35) and subcooling number N_{sub} (2.36) . The phase change number scales the characteristic frequency of phase change Ω to the inverse of single-phase transit time in the system, the subcooling number measures the inlet subcooling [63].

$$N_{pch} = \frac{\Omega}{v_{in} / L_{channel}} = \frac{v_{fg} \cdot Q'' / h_{fg}}{v_{in} / L_{channel}} = \frac{Q}{\dot{m} \cdot h_{fg}} \cdot \frac{v_{fg}}{v_l} \tag{2.35}$$

$$N_{sub} = \frac{\Delta h_{in}}{h_{fg}} \cdot \frac{v_{fg}}{v_l} \tag{2.36}$$

The advantage of these non-dimensional numbers is that they include the effect the pressure variations through $\frac{v_{fg}}{v_l}$. The typical shape of this type of stability map is shown in Figure 2.25, one can see the L shape that forms the stability boundary. The region on the left hand side of the stability boundary is the stable region and the region on the right is the unstable region.

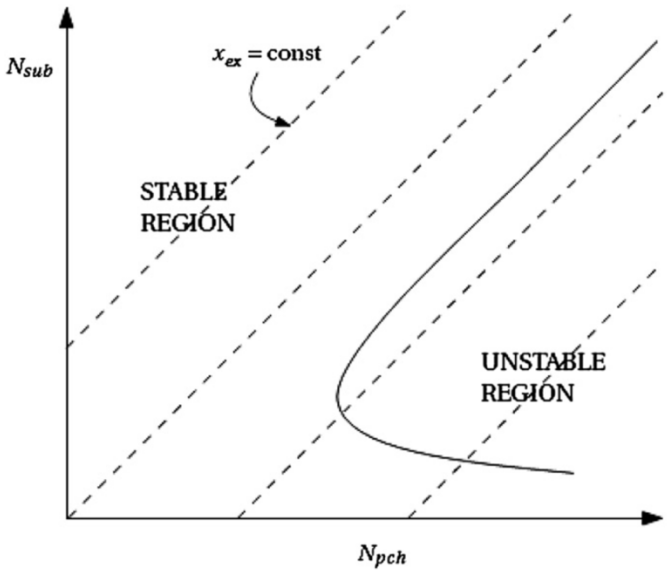

Figure 2.25 Typical Stability Map For DWOs [63]

From Figure 2.25 one can identify how the parameters of the system influence the stability. By increasing the thermal power the effect is a destabilizing effect and the same effect is had by decreasing the flow rate. By increasing the thermal power or decreasing the flow rate the exit quality is increased, which is a key parameter for system stability. When the subcooling increases the

system becomes more stable and will be destabilizing at low subcooling. An increase in operating pressure is also a stabilizing factor. The effect of inlet throttling is always a strong stabilizing effect and exit throttling is a destabilizing effect [63].

2.9.4 Experimental investigations DWOs

The following findings were presented in the review paper by Ruspini et al [60], regarding results for experimental investigations. Increasing the inlet throttling stabilises the system, while decreasing the system pressure proved to destabilize the system. When looking at parallel channels a 180◦ shift out of phase is observed for the DWO_{II} type. Furthermore, the parallel system configuration results in a more unstable system than a single channel system. An investigation was also conducted on a full scale nuclear reactor channel. Two different kinds of phenomena were reported. A high frequency random oscillation, which was probably associated with thermal-acoustic oscillations and DWO and high quality conditions DWO_{II}.

2.9.5 Analytical investigations DWOs

Ruspini et al [60] reviews numerical and analytical investigations. Four main types of models are presented, the two-fluid model, the drift-flux model, the slip-flow model, and the homogeneous model. The homogeneous model is shown to be the most common type of model for transient modelling in two-phase flow systems. Kakac et al. [61] shows the homogeneous assumption is found to be valid for rapid interfacial rates of heat and momentum transfer. Therefore, the model can be expected to be most applicable for those two-phase flow regimes where the phases are well-mixed, such as bubble, churn or mist flow regimes.

One of the interesting findings from the review by Ruspini et al [60] is that flow distribution instability was found in a parallel flow model where the flow did not split symmetrically even though there was symmetric heating. For asymmetric heating most liquid tend to flow in the pipe which absorbs less heat. Colombo et al [63] presents a study on density wave instabilities in single and two parallel channels using RELAP5/MOD3.3. Many of the studies have imposed a constant ΔP across the heated section, the study notes that this is not a realistic assumption with respect to typical experimental setup. Two RELAP5 models were investigated, the first that imposed a ΔP across. While the second investigate a model configured the way most experiments are setup for investigating DWOs. Figure 2.26 shows a typical experimental setup for DWO experiments. It features a large bypass tube to maintain the constant pressure drop boundary condition.

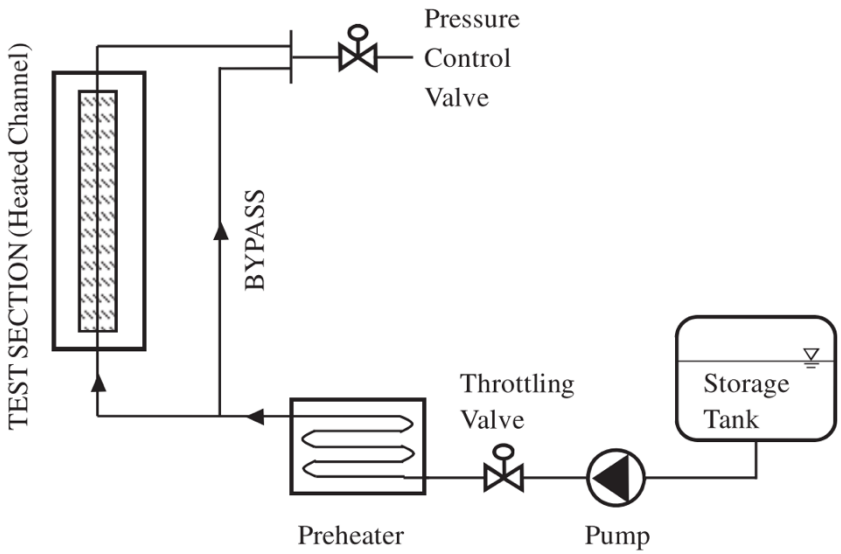

Figure 2.26 Typical Experimental Setup for two-phase flow instabilities experiments [63]

It is important to note that this setup with such a bypass is significantly different to actual flow boiling setups found in industry. From Figure 2.27 one can see that the stability maps generated by both the models compare well with each other, however comparing it to an actual experiment showed that at high subcooling conditions the models give a good prediction while at low subcooling conditions both models deviate from the experimental data. The model for the bypass experimental setup was also used to investigate the size of the bypass needed to give reliable results. It was found that for a bypass ratio greater than 50 there is little change in the results for the models.

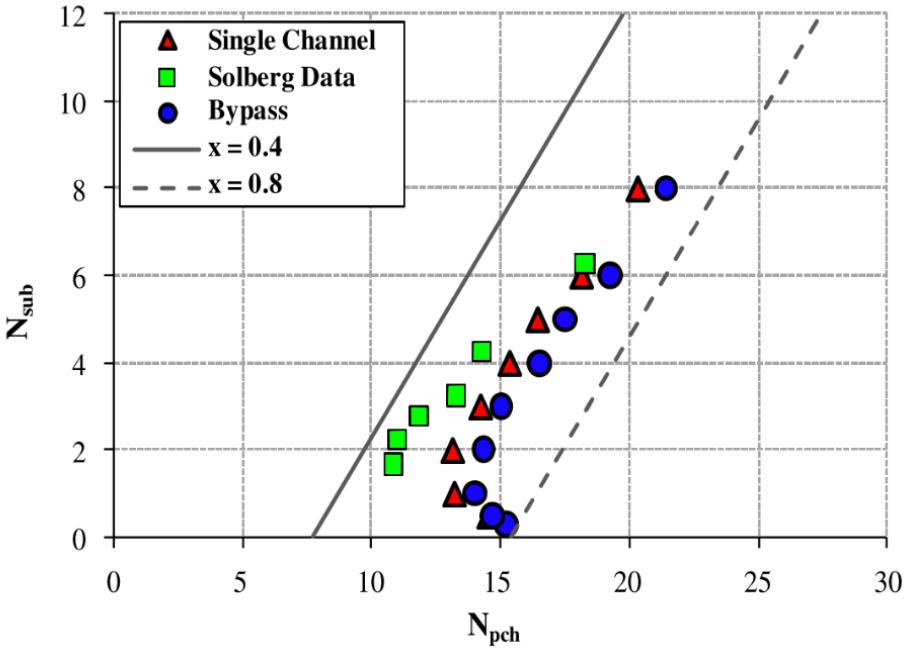

Figure 2.27 Stability map from Colombo et al [63]

2.9.6 DWOs in helical coil tubes

Papini et al [64] presents a paper on experimental and theoretical studies on density wave instabilities in helically coiled tubes. The experimental facility features two parallel helical coils for the boiling section with no bypass, which better represents boiler setups in industry. From the experiments conducted when creating the common N_{pch} vs N_{sub} stability maps. It was found that when comparing the stability maps for the helical coils to the straight tubes there was a difference in shape. Straight tube stability maps normally feature an L shape, while it was found that the shape resembles more of a J shape for helical coils as can be seen in Figure 2.28.

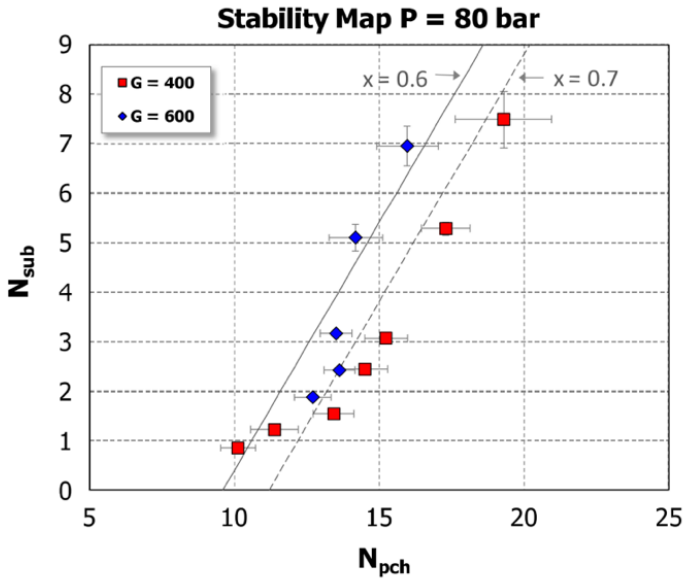

Figure 2.28 Stability Maps Generated from a Helical Coil [64]

It is found that by increasing the thermal power or decreasing the channel mass flow rate can cause an onset of DWOs, both these parameters affect the exit quality. The effects of thermal power, mass flow rate and pressure level do not show differences in the helical geometry when compared to the straight tube case. However, from the stability maps the following is found: The conventional L shape is found at medium to high subcooling, non-conventional shape is found at low subcooling, with marked destabilising effects as the inlet temperature increases and approaches the saturation level.

While the period of oscillations to transit time is usually around two, the experiments conducted showed a different trend. The period of oscillations to transit time ratio is found to be very low at high inlet subcooling. This can be seen in Figure 2.29.

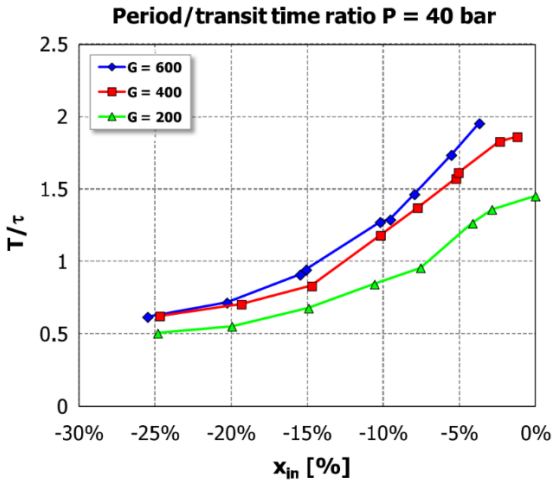

Figure 2.29 Transit Times [64]

They compare an analytical model where one-dimensional equations were used to solve for energy, mass and momentum conservation. The following friction factors were used in the analytical model; white correlation for laminar regime, Ito and Ruffell correlations for the turbulent regime for single phase friction factors. A tuned Lockhart-Martinelli multiplier was used for the friction factor in the two-phase region. For medium to high flowrates, the stability map generated by the model shows the classic L shape, as can be seen in Figure 2.30 and Figure 2.31. While the more unusual helical coil shape is only seen at a lower flow rate of 200 kg/m^2s shown in Figure 2.32. The analytical model underestimates the instability threshold conditions, hence the theoretical instabilities are predicted to occur at lower qualities. The experimental findings were better predicted at high pressure of 80 bar until subcooling conditions decrease below 1.5.

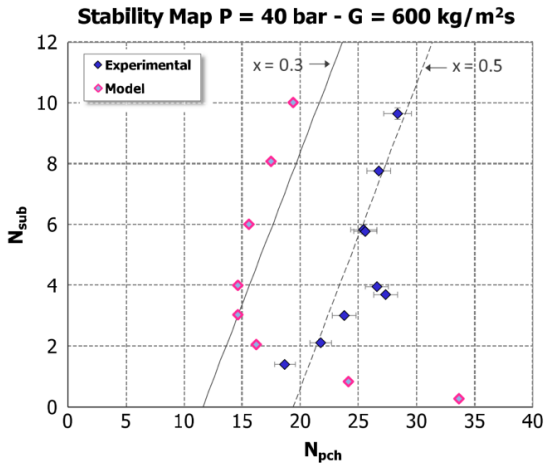

Figure 2.30 Stability Map for helical coils 40 bar and 600 kg/m2s [64]

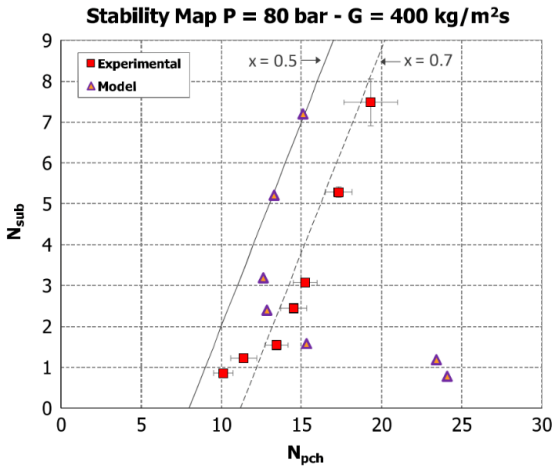

Figure 2.31 Stability Map for helical coils 80 bar and 400 kg/m2s [64]

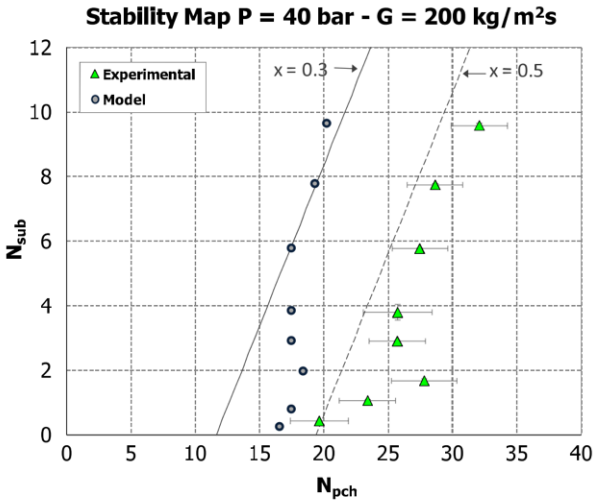

Figure 2.32 Stability Map for helical coils 40 bar and 200 kg/m2s [64]

A RELAP5/MOD3.3-p03 was also used and compared against experimental stability maps. It was concluded that the version of RELAP5 could not be used as a suitable tool to study DWOs within helical coiled tubes.

3. Methodology

3.1 Overview of the test facility

The HPS2 test facility can be split up into three main sections; the solar field, the thermal energy storage (TES) system, and the steam cycle. A basic diagram of the test facility is shown in Figure 3.1.

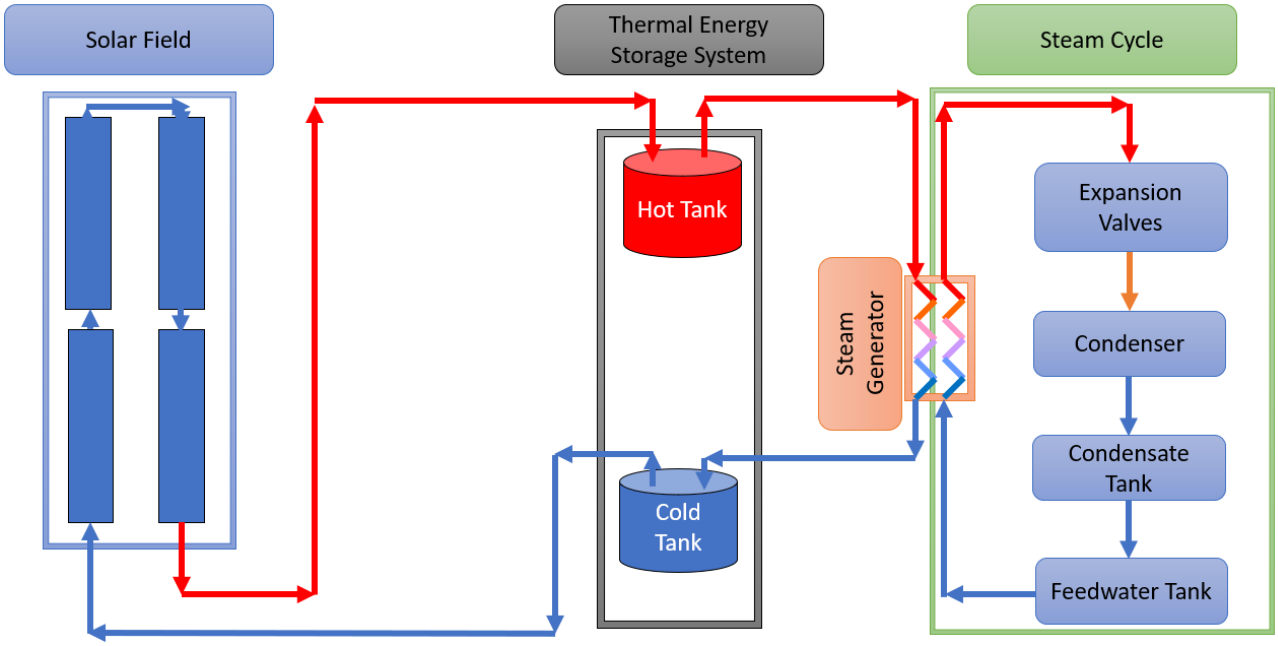

Figure 3.1 HPS2 Overview diagram of the test facility

3.1.1 Solar field

When the model was developed, the parabolic solar field was still being built. This means that little information is known about the solar field. What is stated in the design documentation is that the solar field will consist of one loop where a total of four parabolic troughs are installed. The control philosophy is to maintain a constant outlet temperature for the solar field. This control philosophy should ensure that the temperature in the hot tank doesn't have any major oscillations. The temperature at the outlet is controlled by varying the salt mass flowrate through the solar field. The variations of salt mass flow through the solar field will depend on the amount of DNI available. In cases where the hot tank is full, the flowrate entering it from the solar field will have to match the flowrate of molten salt entering the steam generation section. In this case to stop the salt in the solar field from overheating some of the parabolic troughs would have to be defocused, thus lowering the amount of heat absorbed.

3.1.2 Thermal Energy Storage system (TES)

The TES system consists of two tanks, the hot and cold tank. This is where the molten salt is stored. The two tanks are installed with electrical heaters to protect the salt from freezing during the commissioning time and long shut down periods. The salt tanks also have minimum level requirements to protect from unwanted freezing. Both the salt tanks are insulated in a similar way to full scale CSP plants.

3.1.3 Steam cycle

A diagram of the steam cycle is shown in Figure 3.2. The steam cycle consists of a steam generation section, a valve expansion section (to emulate the operation of a turbine), a condenser and tank and pump section. This includes a condensate tank with a water makeup tank attached, a centrifugal condensate pump, a feedwater tank, and the positive displacement feedwater pump.

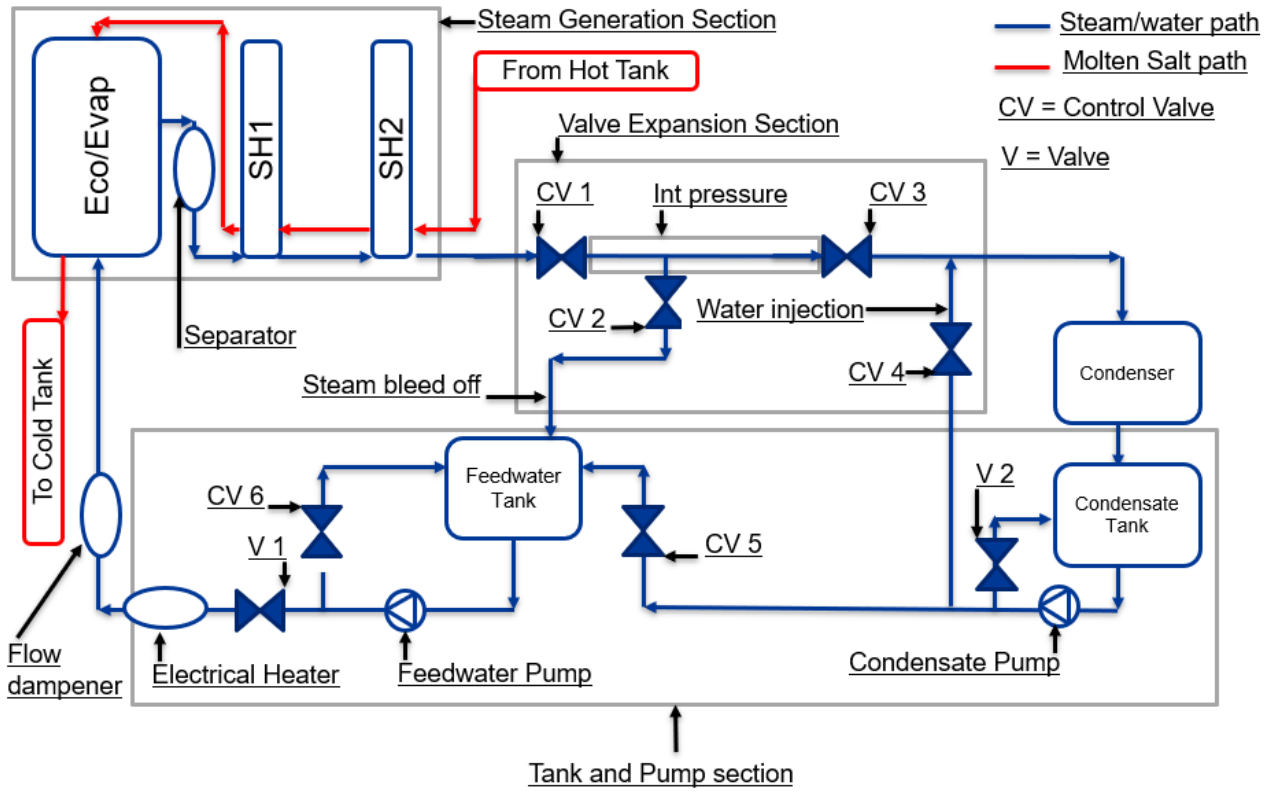

Figure 3.2 Diagram of the steam cycle

The steam generation section was designed and supplied by Steinmüller Engineering GmbH. It consists of a helical coil economizer and evaporator, a separator that was designed to only function under start-up conditions, and two U-tube superheaters. It's within these heat exchangers where the molten salt exchanges its heat with the water. The outlet of the second superheater has a control valve (CV1) to control the pressure, using a sliding pressure control methodology based on

plant load. After this first control valve, superheated steam is tapped off through a control valve (CV2) which controls pressure in the feedwater tank. The next control valve (CV3) controls the intermediate pressure, this is the pressure between CV1 and CV3. Subcooled water is added to the superheated steam at the intermediate pressure valve (CV3). The subcooled water is supplied from the condensate tank. The subcooled water is added to the superheated steam to control the temperature entering the condenser, which is achieved through control valve 4 (CV4). This series of valves is essentially replacing the turbine train on a full scale CSP plant.

The condenser is an air-cooled condenser, where the superheated steam is condensed to a subcooled liquid. There is a condensate tank that receives water from the condenser and if need be, a water make-up tank can supply water to the condensate tank. The condensate is then pumped via the condensate pump to the feedwater tank. There is a control valve (CV5) controlling the flow of water to the feedwater tank to maintain a constant level. The feedwater then gets extracted out of the feedwater tank with the feedwater pump. The feedwater mass flowrate is controlled by a bypass valve (CV6), where excess water is bypassed back to the feedwater tank. Just after the feedwater, pump there is an electrical start-up heater and a device that dampens any flow oscillations due to the positive displacement feedwater pump.

3.2 Flownex Simulation Environment modelling approach

The model for the steam cycle and TES system is developed using the software Flownex Simulation Environment (SE). Flownex is an integrated systems modelling software tool used for design, simulation and optimization of complete thermofluid systems [65].

3.2.1 Background to Flownex SE

A one-dimensional modelling approach is used, where the conservation equations for mass, momentum, and energy are solved. This is used to obtain mass flow, pressure and temperature distributions throughout a network [66]. Flownex has been extensively validated and verified as well as been developed within the ISO 9001 and ASME NQA1 accredited quality system. Flownex has been audited based on Nuclear standards and quality procedures [66].

3.2.2 Governing equations

The governing equations solved in Flownex are the one dimensional conservation equations for mass (3.1), momentum (3.2) and energy (3.3). These equations are defined in the Eulerian reference frame, where a stationary volume is defined, and fluid can cross the control surfaces of the volume.

$$\frac{\partial \rho}{\partial t} + \frac{\partial (\rho v)}{\partial x} = 0 \tag{3.1}$$

$$\rho \frac{\partial v}{\partial t} \rho v \frac{\partial v}{\partial x} = -\frac{\partial p}{\partial x} - \rho g \frac{\partial z}{\partial x} - \frac{f \rho |v| v}{2D} \tag{3.2}$$

$$\frac{\partial (\rho h_0)}{\partial t} - \frac{\partial p}{\partial t} + \frac{\partial (\rho v h_0)}{\partial x} + \rho v \frac{\partial (gz)}{\partial x} = \dot{Q}_H + \dot{W} \tag{3.3}$$

$$Where: h_0 = h + \frac{1}{2} v^2, h = u + pv$$

For the full derivation of the equations refer to Appendix A.

3.2.3 Implicit and explicit solving

For transient conditions, the differential equations can be integrated with respect to time either implicitly, explicitly or a mixture of the two. For the fully explicit solution, only the variables from the previous time step are used. For the fully implicit solution only the variables at the present time step are used. The advantages and disadvantages of using the implicit or explicit solutions are summarized in Table 3.1.

Table 3.1 Advantages and disadvantages for explicit and implicit solutions.

	Advantages	**Disadvantages**
Explicit Solution	• Easy to implement. • Fast solution time. • Accurate.	• Strict time step limitations. • Conditionally stable. • Difficult to solve networks with different fluids.
Implicit Solution	• Unconditionally stable. • Can solve networks with different types of fluids.	• Difficult to implement. • Potentially inaccurate when using large time steps. • Potentially slow.

For the model developed only the fully implicit solution is used. This decision was made as there are two fluids within the system. The time step limitation changes depending on the fluid properties, hence knowing the exact time step limitation for the explicit solution for all scenarios is not possible. Under transient conditions where the conditions are near steady state, it is advantageous to increase the time step. This is to reduce solving time for whole day transient simulations. This would not be possible with the explicit solution due to the time step limitation.

3.2.4 Homogeneous two-phase flow modelling

The basic two-phase flow model implemented in Flownex is referred to as the homogeneous two-phase modelling approach and is used for all the two-phase regions in the current model. This is

essentially a mixture model where the two-phase fluid properties, velocities, and temperatures are assumed to be homogeneous over the cross-sectional area. The equations for the fluid properties are shown in Appendix A.

Using the homogeneous approach is advantageous as it will reduce the computational intensity of the model, which is necessary as the complete model will consist of many elements. Also, the homogeneous approach has been proven to be valid by Cilliers [39] who compared it to the two fluid model for a U-tube steam generator. Cilliers found that the models compared well with each other and with plant data. A homogeneous flow helical coil steam generator model was also developed by Botha [40] using Flownex and it compared well to results from experiments done on the IRIS OTHSG.

3.2.5 Overview of the common Flownex components used

There are common components used in almost all sections of the model. Thus, instead of describing them in each section of the methodology, they are described below.

Pipe component

The symbol for the pipe component available in Flownex is shown in Figure 3.3. This component is used to model pipe sections in the model. It takes into account the pressure drop due to friction, elevations and secondary losses. These pressure drop equations are shown in Appendix A.

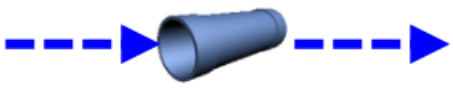

Figure 3.3 Pipe component

The pressure drop through the pipe component is calculated using the Darcy-Weisbach approach together with the Swamee and Jain friction factor correlations.

The inputs for the pipe component that are used for this model are shown in Table 3.2.

Table 3.2 Pipe component inputs

Input	Description
Wall thickness	Thickness of the pipe wall
Length	Total length of the pipe
Diameter	Diameter of the pipe can specify a different inlet and outlet diameter.
Friction factor	Can be calculated based on a correlation, constant or custom script.

K forward	Sum of loss coefficients.
Orifice diameter ratio	Can be used to model a valve within a pipe, is useful when little information is known about a valve.
Fixed mass flowrate option	If the flowrate through the pipe has to be specified.
Number of increments	This separates the pipe into a number of equal length elements as specified by the number.
Number in parallel	Models pipes in parallel, by solving one pipe and inferring the same conditions in the other parallel pipes.

Flow resistance component

The symbol for this component is shown in Figure 3.4. It is a custom loss component that was used to model the pressure drops through the shell side of the heat exchangers. This component was used as it simplifies the solving of the pressure drop.

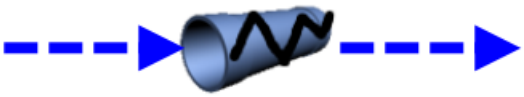

Figure 3.4 Flow Resistance component

For the model developed, all the pressure drops were calculated using equation (3.4). This is referred to as the quadratic resistance behaviour where density change is accounted for. This behaviour is valid for cases where the fluid flow is highly turbulent, leading to the friction factor remaining relatively constant.

$$\Delta p_0 = \frac{|\dot{m}|\dot{m}}{\rho \cdot A_f \cdot A_{sf} \cdot A_0} + \rho g \Delta z \tag{3.4}$$

The derivation of this simplified pressure drop equation (3.4) is shown in Appendix A.

The overall inputs for the flow resistance component are shown in Table 3.3.

Table 3.3 Inputs that can change for each flow resistance component used

Inputs	**Description**
Flow admittance A_f	This unitless input is what is used to adjust the pressure drop for the flow resistance component.
Admittance scaling factor A_{sf}	Always one for all flow resistance components used.
Opening A_O	Always one for all flow resistance components used.
Volume	Volume modelled by the component.

Composite heat transfer

The symbol for the composite heat transfer component is shown in Figure 3.5. This component is used to model the heat transfer in the heat exchangers. For the model developed only convection

and conduction heat transfer is considered. Thus, this component is modelling the convection on the salt side (shell side of the heat exchanger), the conduction through the pipe wall and the convection on the water/steam side (tube side of the heat exchanger).

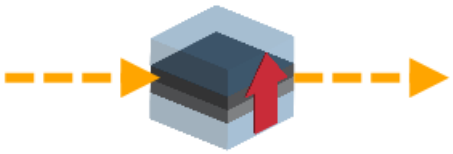

Figure 3.5 Heat transfer component

The description of how the heat transfer for the convection and the conduction is calculated is shown in Appendix A.

Table 3.4 shows the inputs that are provided to the model.

Table 3.4 Composite heat transfer inputs

Inputs	**Description**
Conduction thickness	Thickness of the tube wall in the heat exchangers.
Number of nodes in conduction layer	Discretisation of the conduction layer.
Material option	Selected stainless steel for all heat exchangers.
Flow configuration	For selecting between counter or parallel flow heat exchangers. For the model all the heat exchangers are counter flow heat exchangers.
Convection area	Specify the area where the convection takes place, this is specified for both shell and tube side of the heat exchanger.
Convection heat transfer correlation used	Select the form of heat transfer correlation used, for example the Dittus-Boelter equation can be used but all the constants within the equation can by changed.
Cross sectional area	This is the area that is used by Flownex to determine the fluid velocity.
Hydraulic Diameter	Used when handling flow of non-circular ducts, defined as four times the cross-sectional diameter over the wetted perimeter.
Zero Flow Nusselt number	In the case of no flow in the pipes the specified Nusselt number will be used. (Not applicable for the model developed)
Transition Reynolds number	The Reynolds number which defines the point at which turbulent flow starts.

Nodes and boundary conditions

The boundary component is used where the boundary conditions of a network can be specified and is shown in Figure 3.6. The boundary conditions that can be entered are pressure, temperature, quality (only for two-phase fluids), enthalpy and mass source.

Figure 3.6 Boundary component

Figure 3.7 Node component

Nodes are the end points of elements and they can also join multiple elements together. The node component is shown in Figure 3.7. It is at nodes where boundary conditions can be specified for a network. For the model developed, the elevation is always specified at the nodes, which allows the model to account for elevation pressure losses.

3.3 Economizer and evaporator

3.3.1 Overview of design

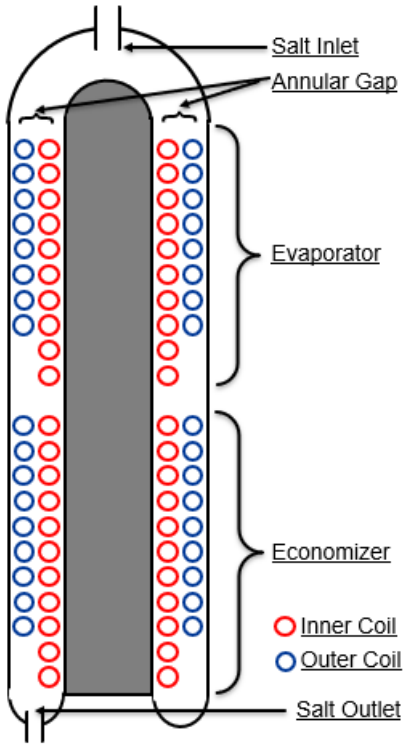

Figure 3.8 Basic cross-sectional diagram of economizer and evaporator

The economizer and evaporator heat exchanger is a helical coil design. The two sections being the economizer and evaporator are contained in the same vessel but are physically separated within the vessel as shown in Figure 3.8. The feedwater enters the heat exchanger from the bottom. The flow is split into two tubes, with both tubes having the same length and heating surface area. Since

they are the same length, the inner tube with the smaller coil diameter starts earlier than the outer tube coil as shown in Figure 3.8.

The economizer section of the heat exchanger is responsible for raising the temperature of the sub-cooled feedwater. The feedwater exiting the economizer should have a quality around zero. Thus, the entire economizer region should contain a single-phase fluid. The evaporator section is meant to receive the water still as a single-phase fluid and then evaporate the water. Steam at a quality of one or greater is meant to exit the evaporator under normal plant load conditions. Thus, it is in the evaporator where all the complex two-phase fluid flow is found. The configuration that the helical coil tube bank forms on the shell side is classified as an aligned bank of tubes. The molten salt enters from the top of the vessel and then runs down an annular gap in which the helical coil tube bank is located as shown in Figure 3.8.

This will be the first once-through helical coil economizer and evaporator that will use molten salt as a heat transfer fluid. This differs from the typical kettle type boiler found on current CSP plants. The reason why the once-through helical coil design was chosen, is to improve start-up times and the time it takes to change plant load. This would lead to a CSP plant being more dispatchable.

3.3.2 Simplifying the helical coil geometry

Flownex doesn't have a standard component to model the helical coil heat exchanger. However, it is possible to modify the standard pipe component for this purpose. This was done by essentially unwinding the helical coil pipe into one straight pipe. The inclination angle of the straight pipe is the same as the pitch angle of the helical coil that is modelled. This ensures that the overall length of the pipe as, well as the overall height difference from the inlet to the outlet, is the same. This modelling technique has been used by Hoffer et al. [41] and Botha [40] and is represented in Figure 3.9.

The heat transfer and pressure drop correlations were then adjusted to model the helical coil flow characteristics. These correlations differ from straight tube correlations due to the secondary flows that can develop within the helical coil due to the coil geometry as discussed in section 2.8.1.

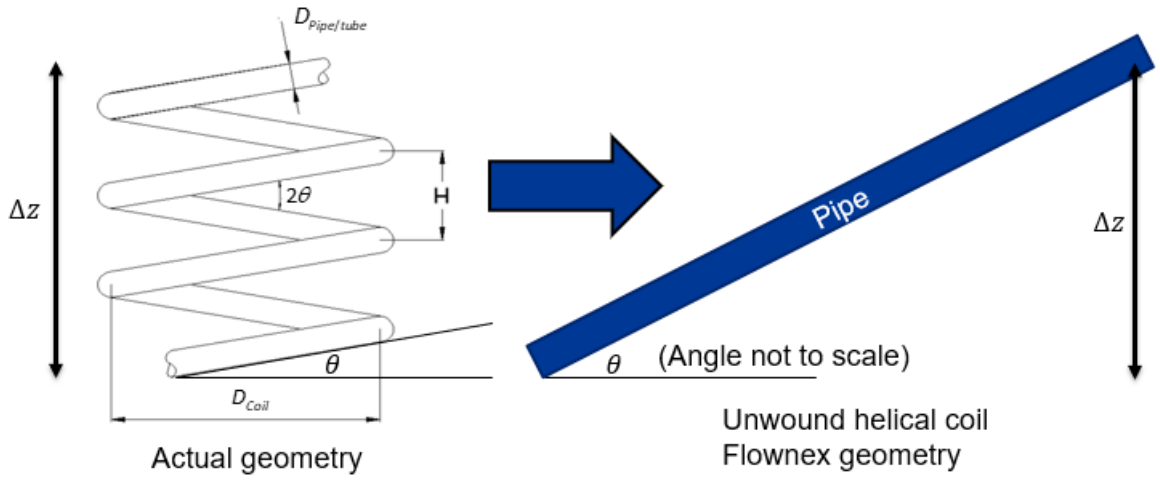

Figure 3.9 Helical coil simplification

Due to the flow characteristics the critical Reynolds number used in the model increases. This implies that the onset of turbulent flow is delayed when compared to straight pipes. The critical Reynolds number was adjusted based on a correlation developed by Schmidt [46] as shown in equation (3.5) which is well-known for use with curved tubes.

$$Re_{cr} = 2300\left(1 + 8.6\left(\frac{D_{pipe}}{D_{coil}}\right)^{0.45}\right) \tag{3.5}$$

3.3.3 Tube side heat transfer

Due to the tube diameter and the mass flowrate through the steam generation section, the flow is always highly turbulent for all loads. Thus, no adjustments to the heat transfer correlations for natural convection and laminar flow were applied. Only adjustments for forced convection were considered. Little work has been done on the heat transfer correlations for forced convection at high Reynolds numbers, with most of the correlations available in literature only being valid for Reynolds numbers up to 70,000. However, from the research done by Guo et al. [48] it was shown that at high Reynolds numbers, being greater than 180,000, the Nusselt number correlation tends towards the well know straight tube Dittus-Boelter correlation. Thus, for the model the Dittus-Boelter Nusselt number correlation is used as shown in equation (3.6).

$$Nu = 0.027\mathrm{Re}^{0.8}\,\mathrm{Pr}^{0.4} \tag{3.6}$$

For cases where the Reynolds number is lower than 180,000, due to the test facility operating at a lower load, a Nusselt number correlation developed by Guo et al. [48] is used shown in equation (3.7).

$$Nu = 0.328 Re^{0.58} Pr^{0.4} \tag{3.7}$$

$$6000 > \mathrm{Re} > 180,000$$

This correlation is implemented in the model with a script shown in Appendix B. This script is only implemented in the economizer section as the Reynolds numbers in the evaporator section are always greater than 180,000 for all loads. This is due to the high velocity steam found in the evaporator section.

For the two-phase regions in the helical coil economizer and evaporator, the solution scheme implemented in the Flownex software is used. This solution scheme uses straight tube correlations. No custom adjustments were made to this solution scheme, for two reasons: Firstly, very little conclusive research has been done on the two-phase heat transfer in helical coils, thus finding a well proven correlation was not possible. Secondly, Jayakumar et al. [42] showed that the quantitative dependence of coil parameters on heat transfer is the same for both single and two-phase flows. Therefore, it has been shown for the single-phase regions, when the Reynolds number is greater than 180,000, straight tube correlations can be used. This follows to say that when the two-phase region Reynolds number is greater than 180,000, the straight tube two-phase heat transfer solving approach can be used.

The two-phase flow boiling heat transfer is significantly more complicated than the single-phase heat transfer. This is because there are both convective and boiling heat transfer to consider, with the added complexity of the two-phases interacting with each other. For this reason, a solution scheme has been implemented in Flownex where it separates out the flow boiling conditions into different regions. These regions are shown in Figure 3.10, along with how the heat flux changes depending on the boiling region. Heat transfer modes are then assigned to each region. Thus, when the fluid is in a certain boiling region, the heat transfer mode for that region is solved.

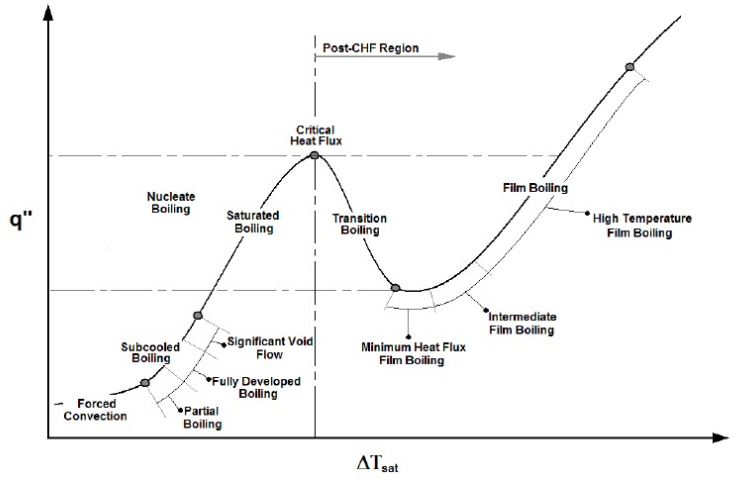

Figure 3.10 Boiling regions [66]

The heat transfer regions that are solved in Flownex are as follows: Forced convection heat transfer, which is assumed for both single-phase and two-phase regions when there is forced convection conditions. Subcooled boiling, which is assumed when the wall temperature exceeds the saturation temperature, although this mode of heat transfer is normally only found in very specialized systems. Saturated boiling is defined as the region where the quality is between zero and one, or between zero and where the CHF point is reached. The CHF point is when the heat flux is raised to such a level that the heated surface can no longer support continuous liquid contact. Transition boiling, when the fluid is between its CHF point and its minimum heat flux (MHF) point. Film boiling, when the fluid is between the MHF point and a quality of one. For a full description and equations solved for each of these regions refer to Appendix A.

Table 3.5 summarizes the heat transfer correlations used for the helical coil economizer and evaporator.

Table 3.5 Heat transfer correlations used for the economizer and evaporator

Flow Region	**Heat Transfer Correlation**
Single-phase forced convection	Dittus-Boelter (Re>180,000) Guo et al (Re<180,000 in economizer)
Two-phase forced convection	Dittus-Boelter
Subcooled boiling	Sato and Matsumara (1964)
Saturated Boiling	Sato and Matsumara (1964)
Transition Boiling	Linear interpellation between CHF and MHF
Film Boiling	2003 Groenveld film boiling tables
Critical Heat Flux (CHF) point	1995 Groenveld look-up tables [67]
Minimum Heat Flux (MHF) point	Max temperature calculated by Zuber or Simon.

3.3.4 Tube side pressure drop

The pressure drop typically increases in helical coils when compared to straight tubes. This was incorporated by adjusting the friction factor in the pressure drop equation that is solved in Flownex. The pressure drop characteristics have been well defined for the single-phase region. For the single-phase region the friction factors are based on correlations developed by Ju et al. [56]. These correlations were validated from experiments on the helical coil HRT-10 steam generator and vary based on three regions given by the Reynolds number, namely: laminar (3.8), laminar with big vortex (3.9) and turbulent flow (3.10).

Table 3.6 Single-phase friction factors for helical coils

Laminar	Laminar with big vortex	Turbulent
$\frac{f_c}{f} = 1$ (3.8)	$\frac{f_c}{f} = 1 + 0.015\,\mathrm{Re}^{0.75}(\frac{D_{Pipe}}{D_{Coil}})^{0.4}$ (3.9)	$\frac{f_c}{f} = 1 + 0.11\,\mathrm{Re}^{0.23}(\frac{D_{pipe}}{D_{coil}})^{0.14}$ (3.10)
Where:	Where:	Where:
$f = \frac{64}{\mathrm{Re}}$	$f = \frac{64}{\mathrm{Re}}$	$f = \frac{0.316}{\mathrm{Re}^{0.25}}$(smooth pipe)
$De < 11.6$	$De > 11.6, Re < Re_{crit}$	$f = 0.1(\frac{1.46\varepsilon}{D_{pipe}} + \frac{100}{\mathrm{Re}})^{0.25}$
		$De > 11.6, Re > Re_{crit}$

The friction factor for the turbulent region was further developed to include the Swamee and Jain friction factor correlation shown in equation (3.12) which is valid for $5000 \leq Re \leq 10^8$ and $10^{-6} \leq (\frac{\varepsilon}{d}) \leq 10^{-2}$. For regions where $2300 < Re < 5000$ a linear interpolation is used to calculate the straight pipe friction factor used in equation (3.10).

Thus the turbulent region friction factor is now defined by equation (3.11).

$$\frac{f_c}{f} = 1 + 0.11\,\mathrm{Re}^{0.23}(\frac{D_{pipe}}{D_{coil}})^{0.14} \tag{3.11}$$

where:

$$f = \frac{0.25}{[\log\{(\frac{\varepsilon}{3.7D_{pipe}}) + \frac{5.74}{\mathrm{Re}^{0.9}}\}]^2} \tag{3.12}$$

For the pressure drop in the two-phase flow region, correlations are not readily available, as shown by Fsadni et al. [44]. The two-phase pressure drop for the helical coil tubes is therefore predicted by the well-known Lockhart and Martinelli approach for straight tubes. Owhadi et al. [59] first suggested that the Lockhart and Martinelli approach can be used to predict the pressure drop in helical coil tubes. Colombo et al. [57] showed that the Lockhart and Martinelli approach becomes less accurate at low system pressures. However, for system pressures above 40 bar, the approach predicts the two-phase pressure drop well. Since under normal operating conditions the system pressure does not go below 75 bar, the Lockhart Martinelli approach is used in the current model.

The Lockheart-Martinelli multiplier is first defined as shown in equation (3.13). $(\frac{dp}{dz})_{fl}$ is the pressure drop of the liquid component and $(\frac{dp}{dz})_{fg}$ is the pressure drop of the gas component. Either the liquid (3.14) or gas (3.15) multiplier can be used in the Lockheart-Martinelli two-phase pressure drop equation (3.16).

$$X_{tt} = \sqrt{\frac{(\frac{dp}{dz})_{fl}}{(\frac{dp}{dz})_{fg}}} \tag{3.13}$$

$$\phi_l^2 = 1 + \frac{C}{X_{tt}} + \frac{1}{X_{tt}^2} \tag{3.14}$$

$$\phi_g^2 = X_{tt} + CX_{tt} + 1 \tag{3.15}$$

$$(\frac{dp}{dz})_f = \phi_l^2 (\frac{dp}{dz})_{fl} = \phi_g^2 (\frac{dp}{dz})_{fl} \tag{3.16}$$

However, since there are both single and two-phase regions within the helical coil heat exchanger a friction factor script was written to incorporate both regions. In the script, the single phase region friction factor was calculated using equations (3.8), (3.9) and (3.11). While the two-phase pressure drop given by equation (3.16) had to be converted into the friction factor equation (3.17). This script is shown in Appendix B**.**

$$f = \rho \left\{ \frac{f_l^{'}(1-x)^2}{\rho_l} + Cx(1-x)\left(\frac{f_l^{'}}{\rho_l}\frac{f_g^{'}}{\rho_g} \right)^{\frac{1}{2}} + \frac{f_g^{'}x^2}{\rho_g} \right\} \tag{3.17}$$

Where:

$$2 > C = -2 + F(G)T(\Lambda, G)$$

$$F(G) = 28 - 0.3\sqrt{G}$$

$$T(\Lambda, G) = e^{\left[-\frac{(\log_{10}\Lambda + 2.5)^2}{2.4 - G(10^{-4})} \right]}$$

$$\Lambda = \frac{\rho_g}{\rho_l}\left(\frac{\mu_l}{\mu_g} \right)^{0.2}$$

3.3.5 Shell side heat transfer

For the shell side, the molten salt passes over the helical coil tube bank. The external flow over the tubes would be made up of a combination of cross and counter flow. Due to the small helix angle of

the helical coil, the flow is mainly cross flow over the banks. Therefore, the counter flow component is not considered. For this reason, a well-known heat transfer correlation developed by Zhukauska [68] is used which is shown in equation (3.18) and Table 3.7 is used to determine the equation constants. This approach was also used by Botha [40] where a model for a once-through helical coil steam generator was developed.

$$Nu = C_1 \mathrm{Re}_D^m \mathrm{Pr}^{0.36} \left(\frac{\mathrm{Pr}}{\mathrm{Pr}_s}\right)^{0.25} \tag{3.18}$$

Table 3.7 Constants for equation (3.18)

Re_D	C_1	m
$10 - 10^2$	0.8	0.4
$10^2 - 10^3$	Approximate as a single cylinder	
$10^3 - 2 \times 10^5$ $(if \frac{S_T}{S_L} > 0.7)$	0.27	0.63
$2 \times 10^5 - 2 \times 10^6$	0.021	0.84

From equation (3.18) the Reynolds number used is not the normal Reynolds number defined. This Reynolds number is defined in equation (3.19), where the maximum velocity that occurs between the tubes is used, rather than the velocity in the vessel before the tubes. This is shown in Figure 3.11.

$$\mathrm{Re}_D = \frac{\rho v_{Max} D}{\mu} \tag{3.19}$$

where:

$$v_{Max} = v_\infty \left(\frac{S_T}{S_T - D}\right) \tag{3.20}$$

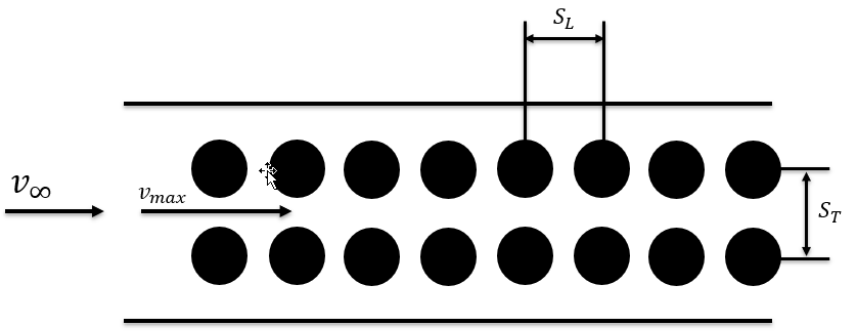

Figure 3.11 Flow over tube bank diagram

Thus, the cross sectional area that is entered into the composite heat transfer component was adjusted so that the correct velocity was used for the Reynolds number calculation (3.18). This adjusted area was calculated by using equation (3.21) which was derived as follows:

$$v_{\infty} = \frac{\dot{V}}{A_{Free}}$$

$$v_{Max} = v_{\infty}\left(\frac{S_T}{S_T - D}\right) = \frac{\dot{V}}{A_{Adjusted}}$$

$$\frac{\dot{V}}{A_{Adjusted}} = \frac{\dot{V}}{A_{Free}}\left(\frac{S_T}{S_T - D}\right)$$

$$A_{Adjusted} = \frac{A_{free}}{\frac{S_T}{S_T - D}} \tag{3.21}$$

The constants C_1 and m were selected as 0.27 and 0.63 respectively for the correlation given in equation (3.18). This is due to the Re_D numbers being 4,958 and 10,365 for the 35% and 100% load cases respectively. For the small regions within the heat exchanger where there is only one tube in cross flow, the heat transfer correlation shown in equation (3.18) is used. However, the constants for C_1 and m are now 0.193 and 0.618 respectively, since these are the constants used for a single cylinder in cross flow.

3.3.6 Shell side pressure drop

The flow resistance component was selected to model the shell side. This decision was based on two reasons: The geometry within the shell side of the heat exchanger is complex and the effect on the pressure drop is not fully known. Furthermore using a flow resistance component as opposed to a pipe, reduces the solving time in complex networks [65]. The pressure drop equation for the flow resistance component has been described in section 3.2.5 and the flow admittance factor was adjusted to give the desired pressure drop for the 100% load conditions. The desired pressure drop was determined from design documents provided by Steinmüller.

3.3.7 Helical coil economizer and evaporator Flownex model

Figure 3.12 shows the model of the helical coil economizer and evaporator that is used in the complete steam cycle model. The two pipes within the heat exchanger are modelled as two separate pipes. This will account for any flow differences between the two pipes due to the different coil diameters or other influences. Four flow resistance components were used on the shell side to more accurately model the heat transfer between the shell and tube side when only the single coil with the smaller coil diameter is exchanging heat with the salt.

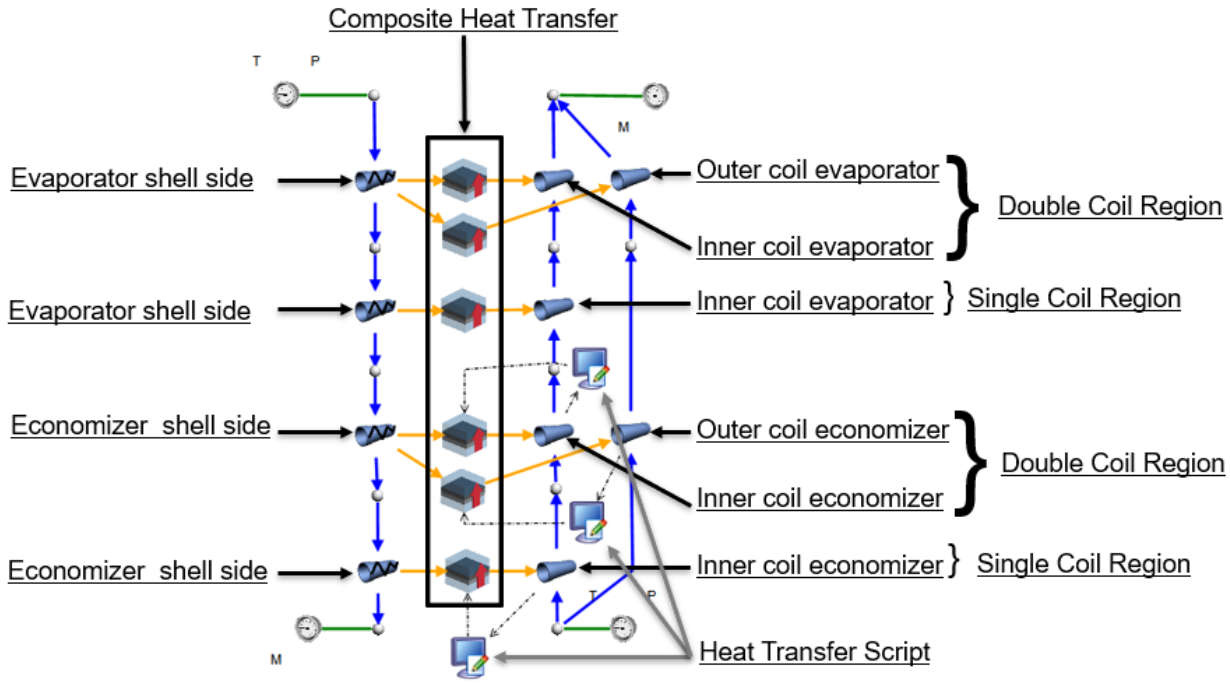

Figure 3.12 Final Flownex helical coil economizer and evaporator model

Mesh independence studies were done to determine the minimum number of increments required for the heat transfer solution to no longer be dependent on the number of increments in each of the four sections. These four sections were the single and double coil regions in the economizer and evaporator sections. The mesh independence studies can be found in Appendix C. From the results for the mesh independence studies 10 increments were selected for the single coil regions and 75 increments were selected for double coil regions.

All the inputs and correlations needed for the flow resistance, pipe and composite heat transfer components have now been defined for the helical coil economizer and evaporator and are summarized in the tables found in Appendix D.

3.3.8 Helical coil economizer and evaporator model verification

To verify the modelling methodology for the helical coil heat exchanger, the results were compared to the expected results from the design documents provided by Steinmüller. All the results in the design documents are from thermodynamic calculations that were performed by using Steinmüller's own software tool DimBo (Dimensioning of Boilers). The design documents show the expected results for each separate section which were the economizer and the evaporator. Thus, boundary conditions were placed across the economizer and evaporator sections as shown in Figure 3.13 and Figure 3.14.

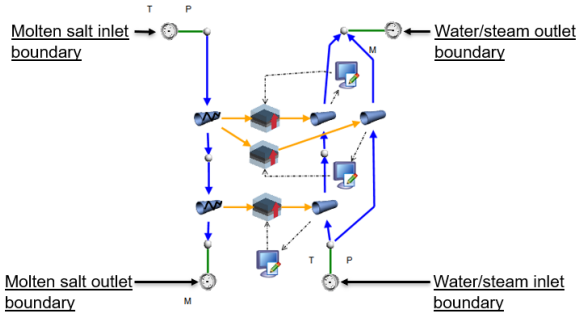

Figure 3.13 Economizer section

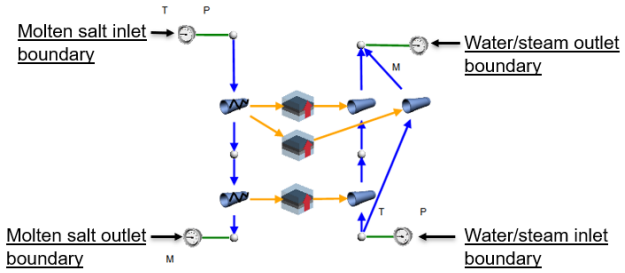

Figure 3.14 Evaporator section

These boundary values are the inlet temperature and pressure values for the feedwater and salt inlet boundaries, with the exit boundary values being the specified mass flowrate in the form of a mass sink. These boundary values are shown in Table 3.8.

Table 3.8 Boundary conditions for economizer and evaporator verification

Boundary	Properties specified for economizer	Properties specified for evaporator
Molten salt inlet	$Temperature = 345\ ℃$ $Pressure = 0.225\ MPa$	$Temperature = 345\ ℃$ $Pressure = 0.225\ MPa$
Molten salt outlet	$Mass\ flowrate = 3.8\ \frac{kg}{s}$	$Mass\ flowrate = 3.8\ \frac{kg}{s}$
Water/steam inlet	$Temperature = 260\ ℃$ $Pressure = 16\ MPa$	$Temperature = 337\ ℃$ $Pressure = 15.6\ MPa$
Water/steam outlet	$Mass\ flowrate = 0.7\ \frac{kg}{s}$	$Mass\ flowrate = 0.7\ \frac{kg}{s}$

The molten salt compound that is stated to be used in the design document is known as solar salt which is 60% $NaNO_3$ and 40% KNO_3. This fluid is entered into Flownex by creating a custom fluid, where the fluid properties are defined by Siemens, who were part of the original HPS1 project. The fluid properties that were defined are the density, viscosity, conductivity and Cp/Enthalpy. These properties are only dependent on temperature. To verify the model, the expected results from the design documentation for each component were compared to the results from the model, this is shown in Table 3.9.

Table 3.9 Expected results compared to model results for the economizer and evaporator

	Economizer			**Evaporator**		
Result	Expected	Result	Error	Expected	Result	Error
Salt Exit Temperature	291.0 ℃	292.6 ℃	0.56%	345.0 ℃	340.4 ℃	-1.33%
Salt Pressure Drop	0.250 MPa	0.259 MPa	3.7%	0.250 MPa	0.263 MPa	5.12%
Steam Outlet Temperature	337.0 ℃	341.9 ℃	1.46%	342.0 ℃	372.9 ℃	9%

Steam Outlet Pressure	15.600 MPa	15.408 MPa	-1.23%	14.700 MPa	14.836 MPa	0.92%

From the results shown, the pressure drops across both the salt side and the water/steam side are in good agreement with what is expected. Based on the final exit temperatures for both the salt side and the water/steam side, there is good agreement between the model and what is expected. However, there is a 9% error for the final exit temperature of the evaporator. This could be due to the different two-phase heat transfer solution schemes implemented in Flownex and Steinmüller's own software tool DimBo. From these results, the model of the economizer and evaporator is in good agreement with what is excepted thus the methodology used is considered to be verified.

3.4 Superheaters 1 and 2

3.4.1 Overview of design

Superheaters 1 and 2 have the same design, however superheater 2 has more heating surface area than superheater 1. The design of the superheaters is a counter flow U-tube heat exchanger shown in Figure 3.15, where the salt flows on the shell side and the steam is superheated in the tube side. On the tube side there are multiple tubes to increase the heat transfer area. This also increases the cross-sectional flow area which decreases the velocity within the tubes. This reduces the pressure drop across the component.

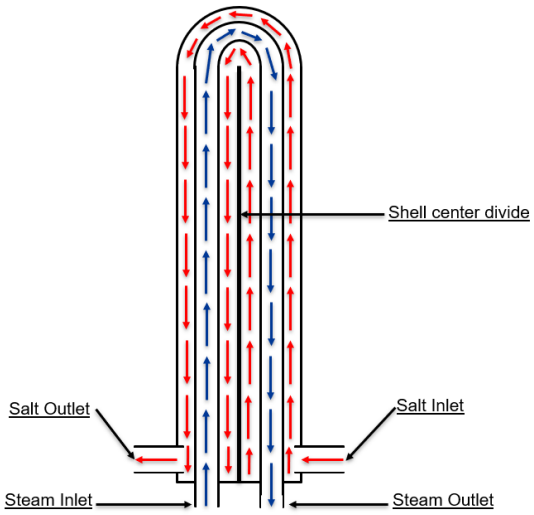

Figure 3.15 Diagram of superheater design

3.4.2 Tube side heat transfer and pressure drop

To model the tube side, two pipe components are used, one to model from the inlet to the bend at the top and one to model from the bend to the outlet. The pressure drop across the pipe

components is calculated as described in section 3.2.5. The friction factor correlation used is the Swamee and Jain correlation where the wall roughness is entered. The pressure loss due to the bend in the pipes is modelled using a calculated K loss coefficient. This is calculated using tables that are available in Flownex that calculates the K loss coefficient based on the diameter, bend radius and angle of bend. The heat transfer is calculated using the Dittus-Boelter Nusselt number correlation. Unlike the helical coil heat exchanger, the correlation did not need to be adjusted as the pipes are straight. There should only be single phase superheated steam in the superheaters. Thus, only single-phase pressure drop and heat transfer should be calculated. However, if there is a two-phase water and steam mixture in the pipes the solution scheme for two-phase heat transfer is used as described in section 3.3.3. For the two-phase pressure drop the Lockheart-Martinelli two-phase friction factor multiplier is used.

3.4.3 Shell side heat transfer and pressure drop

The shell side is modelled using the flow resistance component where the pressure drop equation in solved as described in section 3.2.5. The flow admittance factor is selected based on knowing the expected pressure drop across each superheater from the design documentation provided by Steinmüller. The heat transfer on the shell side is calculated with the correlation given by Grimison (3.22), which was developed for shell side single phase flow [65].

$$Nu = 0.2\mathrm{Re}^{0.6}\,\mathrm{Pr}^{0.33}\left(\frac{\mu}{\mu_w}\right)^{0.14} \tag{3.22}$$

3.4.4 Superheater 1 and 2 Flownex model

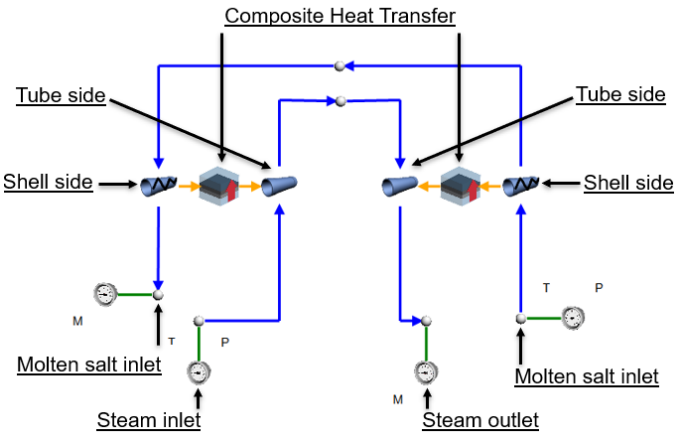

Figure 3.16 Flownex model of a superheater

Figure 3.16 shows the Flownex superheater model. From a visual perspective, there is no difference between the two Flownex superheater models. The physical differences between each of the superheaters have been accounted for in the inputs of the components used.

Mesh independent studies were done on the two superheater models to determine the number of increments necessary for the heat transfer to no longer depend on the number of increments. These independent studies can be found in Appendix C. From the results of the mesh independence studies four increments were selected for each of the pipes and flow resistance components in superheater 1 and eight increments were selected for each of the pipe and flow resistance components in superheater 2. There are significantly fewer increments needed in the superheaters when compared to the economizer and evaporator. This is because of the geometry differences and the fact that there is only single-phase flow in the superheaters.

The inputs for the components used for superheater one and two have now been defined and are shown in Appendix D.

3.4.5 Superheater 1 and 2 model verification

To verify the superheater models, the model results were compared to the expected results that are reported in the design documentation provided by Steinmüller. The same inlet conditions are applied to the model as to what is specified from the design documentation. This being the inlet pressure and temperature for both the steam and salt. The mass flowrate is specified for the outlet of the salt and steam sides of the heat exchanger. These boundaries are shown in Figure 3.17.

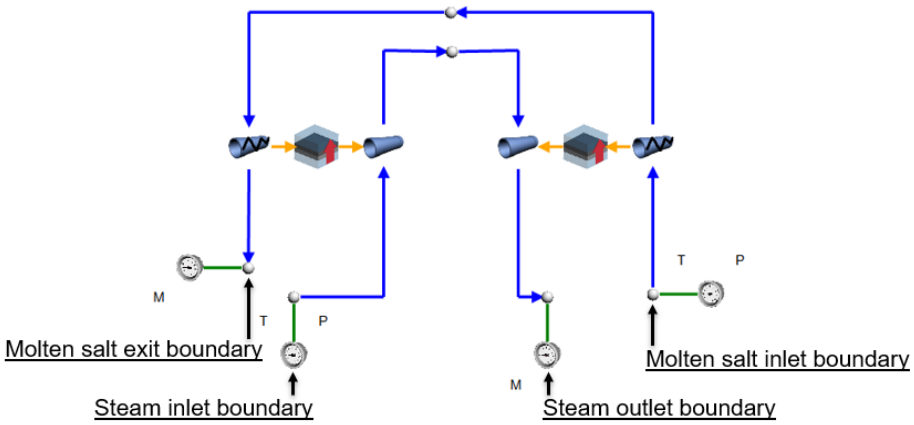

Figure 3.17 Superheater model boundaries

Table 3.10 shows the boundary conditions applied to the model as specified from the design documentation.

Table 3.10 Superheater boundary conditions

Boundary	Properties specified for superheater 1	Properties specified for superheater 2
Molten salt inlet	$Temperature = 540$ ℃ $Pressure = 0.275\ MPa$	$Temperature = 580$ ℃ $Pressure = 0.3\ MPa$
Molten salt outlet	$Mass\ flowrate = 3.8\ \frac{kg}{s}$	$Mass\ flowrate = 3.8\ \frac{kg}{s}$
Steam inlet	$Temperature = 342$ ℃ $Pressure = 14.5\ MPa$	$Temperature = 443$ ℃ $Pressure = 14.3\ MPa$
Steam outlet	$Mass\ flowrate = 0.7\ \frac{kg}{s}$	$Mass\ flowrate = 0.7\ \frac{kg}{s}$

The molten salt compound that is used is the same molten salt compound as described in the Helical coil economizer and evaporator model verification section. As can be seen from the steam inlet conditions in Table 3.10 the pressure decreases over superheater 1 due to frictional losses while the temperature increases by about 100℃. Thus, the results for the two superheater models are shown in Table 3.11.

Table 3.11 Superheater 1 and 2 model results

	Superheater 1			**Superheater 1**		
Result	Expected	Result	Error	Expected	Result	Error
Salt Exit Temperature	480.0 ℃	487.7 ℃	1.6%	540.0 ℃	544.9 ℃	0.9%
Salt Pressure Drop	0.025 MPa	0.025 MPa	1.24%	0.025 MPa	0.026 MPa	3.156%
Steam Outlet Temperature	443.0 ℃	444.4 ℃	0.32%	563.0 ℃	559.2 ℃	-0.67%
Steam Outlet Pressure	14.300 MPa	14.485 MPa	1.29%	14.000 MPa	14.267 MPa	1.9%

Table 3.11 shows that the results from the model are in good agreement with what is expected from the design documentation. This provides confidence in the modelling methodology for the two superheater models.

3.5 Piping

To model the piping in between components an approach was used which reduced the amount of Flownex components required. This approach still modelled the piping between components accurately and reduced the solving time. This was achieved by using a single pipe component between junctions rather than using multiple pipe and bend components. This single pipe had the total length equal to the total length of pipe between junctions. All the pressure losses due to pipe bends were accounted for by entering a total K loss factor for all the bends. The K loss factor is calculated using tables where the diameter of the pipe, bending radius and bend angle are used to select a K loss factor. The elevation losses were accounted for by entering the same elevations at

the inlet and outlet as specified in the pipe drawings. This was done for all pipe sections between components which were identified from pipe drawings or 3D models.

To prove that this technique is accurate in modelling the piping, a detailed piping model was developed as shown in Figure 3.18 and the same piping network was simplified using the technique described above and shown in Figure 3.19. The results of the two pipe networks with the same boundary conditions are then compared in Table 3.12.

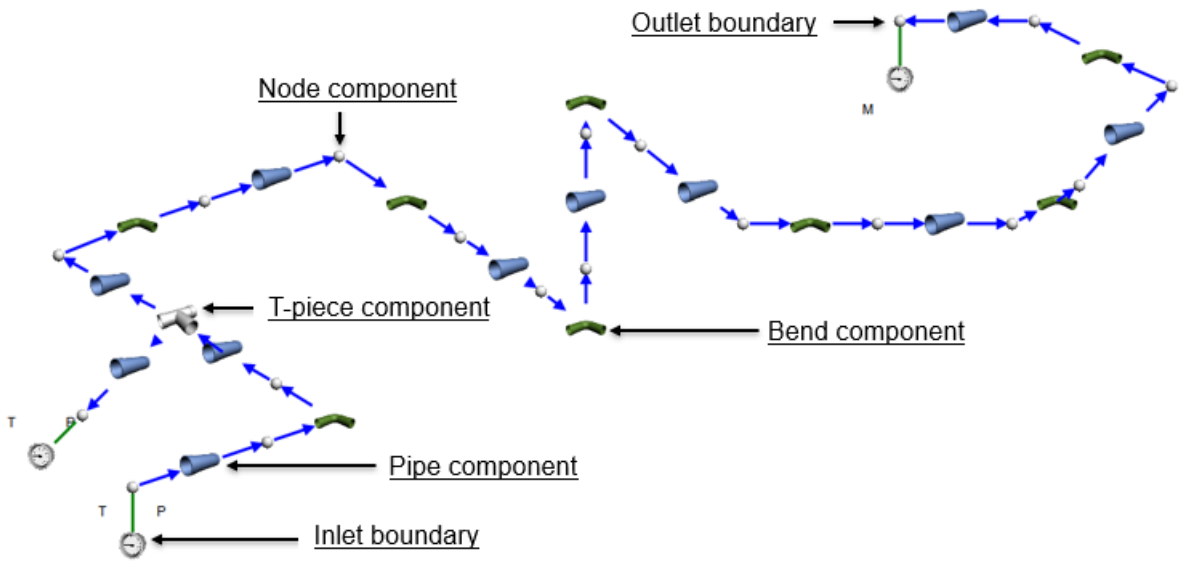

Figure 3.18 Detailed Flownex pipe network

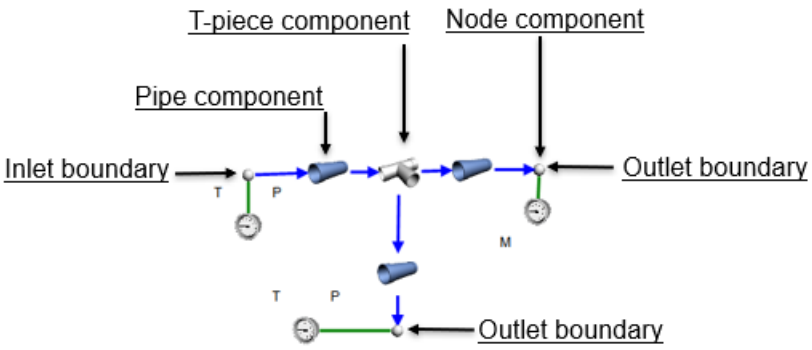

Figure 3.19 Simplified pipe section model

Table 3.12 Detailed vs simplified pipe section model

Outlet value	Detailed model	Simplified model	Error %
Temperature °C	273.2	273.2	0
Pressure bar	159.861	159.854	-0.004

The results shown in Table 3.12 show that the technique used to reduce the amount of Flownex components used when modelling the pipe sections is valid as the error between the two models is practically zero.

3.6 Complete steam generation model

The steam generation model shown in Figure 3.20 consists of the three heat exchanger models shown in sections 3.3 and 3.4, with the connecting piping modelled. The volume of the separator has been modelled with a node for more accurate transient results. The separator in the model does not separate two-phase fluid. This modelling approach was selected because it is stated that only during start-up processes does two-phase fluid reach the separator. Therefore, under normal load conditions two-phase steam is not expected to enter the separator. Figure 3.20 shows the inlets and outlet of the model where the boundary conditions for the model are applied. All the outlets that have not been labelled are pipe connections for emergency drainage and were only added so that the losses in the T-pieces were calculated. There is no flow in these pipe connections, this is achieved by making the diameter ratio for the emergency pipe zero, effectively modelling a closed valve.

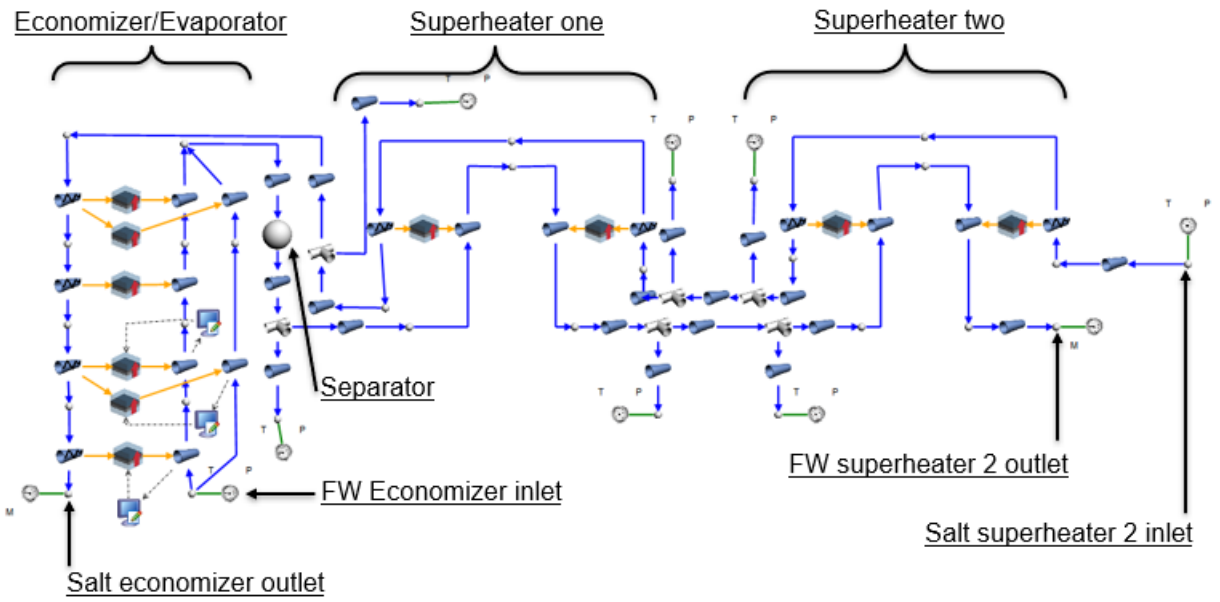

Figure 3.20 Complete steam generation section

From the operating manual provided by Steinmüller, the model can be compared to the results that are expected for the steam generation section. The following parameters are defined for the steam generation section for plant loads of 35%, 100%, and 115%. The pressure and temperature

parameters are applied to the boundary conditions at the inlets of the model. The mass flowrate parameter is applied as a boundary condition at the outlets of the model.

Table 3.13 Steam generation section inlet parameters

Parameter	35% load	100% load	115% load
Salt mass flow (kg/s)	1.45	3.80	4.40
Salt inlet temperature (℃)	580.0	580.0	580.0
FW mass flow (kg/s)	0.25	0.70	0.81
FW inlet pressure (bar)	75.000	160.000	167.000
FW inlet temperature (℃)	260.0	260.0	260.0

The expected outlet conditions from the steam generation section shown in Table 3.14.

Table 3.14 Expected outlet conditions from the steam generation section

Parameter	35% load	100% load	115% load
Salt outlet temperature (℃)	293.0	291.0	294.0
Steam pressure (bar)	70.000	140.000	140.000
Steam temperature(℃)	580.0	563.0	561.0

The complete steam generation system was then simulated at the three different plant loads and the results are shown in Table 3.15. The steady state results for the temperatures were in good agreement. However, the final pressure at the exit of superheater 2 was found to be much lower than expected. In the case of the 100% and 115% loads, the pressure drop was so large that the model could not solve for a pressure, that would result in the correct mass flowrate through the system.

Table 3.15 Original results for the steam generation section when running at expected operating conditions

Parameter	35% load	100% load	115% load
Salt outlet temperature (℃)	324.6	298.1	297.9
Steam pressure (bar)	45.0548	N/A	N/A
Steam temperature (℃)	579.3	580.0	580.0

It was found that, at the design conditions, the exit temperature and quality of the steam at the exit of the evaporator were much higher than expected. The resultant sub element results showed that the boiling point was already occurring in the economizer section when it is only meant to occur in the evaporator section, as shown in Figure 3.21. Due to this, the high velocity steam travelled through the long length of pipe in the economizer/evaporator. This resulted in extremely large pressure drops across the component as shown in Figure 3.21. This indicates that the actual operating conditions for the test facility could be different from what is expected and may, therefore, need to be adjusted.

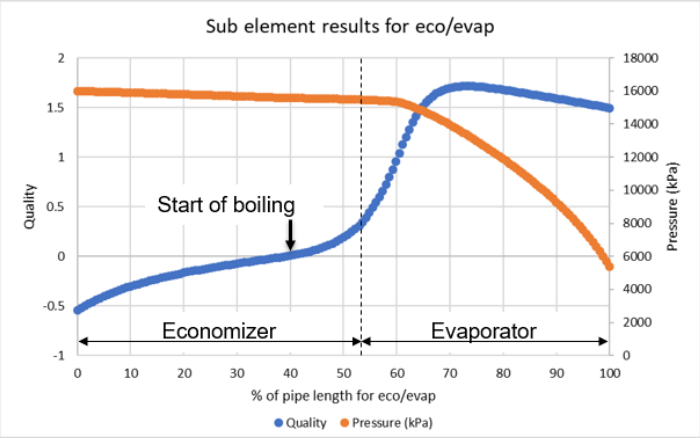

Figure 3.21 Sub element results for design conditions

By conducting a sensitivity analysis where the molten salt mass flowrate was adjusted, a new molten salt mass flowrate could be determined to provide the expected outlet conditions. The sensitivity analysis for the 100% load case is shown in Figure 3.22, the other sensitivity analysis results for the 35% and the 115% are shown in Appendix E.

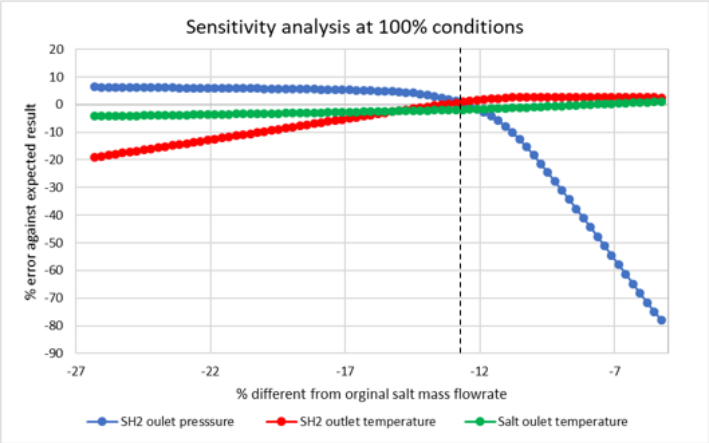

Figure 3.22 100% load sensitivity analysis

For all loads, the sensitivity analysis showed that the salt mass flowrate would have to be reduced to meet the expected outlet conditions. Table 3.16 shows how the model results compare to the expected results when the salt mass flowrate for each load has been reduced.

Table 3.16 New salt mass flowrate and model results for 35%, 100%, and 115% load cases

Parameter	**35% load**		**100% load**		**115% load**	
	Expected	Result	Expected	Result	Expected	Result
Salt mass flowrate (kg/s)	1.45	1.32	3.80	3.30	4.40	3.83
Salt outlet temperature (℃)	293.0	301.5	291.0	285.3	294.0	286.2
Steam pressure (bar)	70.000	68.492	140.000	140.814	140.000	138.657
Steam temperature	580.0	577.5	563.0	564.7	561.0	565.2

3.7 Valves

There are several valves on the test facility. For the cases where enough information was known about the valve the ANSI control valve component available in Flownex was used. The full description of how the ANSI control valve component solves the mass flowrate is described in Appendix A. Table 3.17 shows the inputs entered when using the ANSI control valve.

Table 3.17 ANSI control valve inputs

Input	**Description**
Valve diameter	Diameter of valve opening
Upstream pipes diameter	Diameter of the pipe that it connected upstream
Downstream pipe diameter	Diameter of the pipe that is connected downstream
Valve flow behaviour	Either linear, Equal percentage or use chart options, this determines how the flowrate through the valve changes with valve opening.
C_V	Cv/Kv value at maximum opening.
F_l	Liquid pressure recovery factor can select a constant value or calculate the value from a valve chart.
X_t	Pressure drop ratio factor, can select a constant value or calculate the value from a valve chart.
Valve lift fraction	The opening ratio of the valve ranging from 0-1, 1 means the valve is open, 0 means its closed.

Where there is limited information known about the valve, the pipe component is used. This is done by specifying the orifice diameter ratio. This is a useful modelling technique when little design information is known about a valve. The orifice modelled in the pipe is a flat plate orifice and the solution for the mass flowrate is described in Appendix A. The only input entered, in this case, is the orifice diameter ratio.

3.7.1 Modelling the valves on the test facility

There are several valves on the test facility that are used as control valves to maintain certain parameters. Figure 3.23 shows the valves that are modelled on the test facility and where they are placed. Valve 1 and control valve 6 are modelled using the pipe component where the orifice diameter ratio is specified. All the other control valves and valve 2 are modelled with the ANSI control valve component.

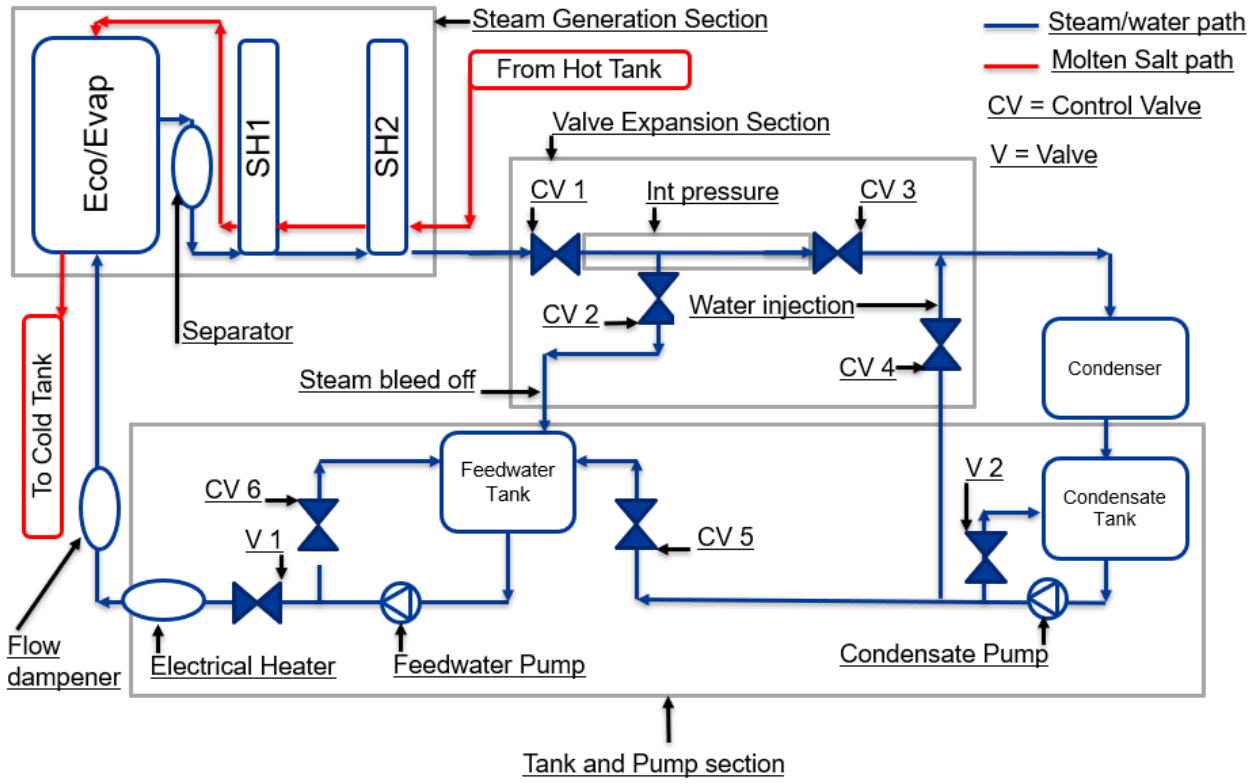

Figure 3.23 Diagram of test facility where valves are shown

Table 3.18 shows all the valves that were modelled with the ANSI valve component and what was entered into the component. These inputs are the valve type, inlet and outlet piping diameters, the valve response, the C_V value, the X_t value and F_l values. These characteristics of the valves were obtained directly from the design documents for each valve. In some cases, the ANSI charts that are available in Flownex directly matched the type of valve specified. In these cases, the values for X_t and F_l were obtained from the graphs which are dependent on the flow characteristics through the valve. In the cases where the ANSI charts available in Flownex did not exactly match the valve specified, the X_t and F_l values were assumed as a constant estimated for that type of valve.

Table 3.18 Valves modelled with the ANSI control value component and inputs

Valve	Type	Inlet diameter, valve diameter, outlet diameter (mm)	Response	C_V	X_t, F_l
Control Valve 1	Angle	25.4, 25.4, 38.1	Linear	4	ANSI2500 chart
Control Valve 2	Angle	29.64, 25.4, 46.48	Linear	1.6	ANSI1500 chart
Control Valve 3	Angle	38.1, 38.1, 44.96	Linear	5	ANSI1500 chart
Control Valve 4	Single Seated	25.4, 17.02, 25.4	Equal %	0.25	0.68, 0.9
Control Valve 5	Single Seated	19.05, 19.05, 19.05	Linear	4	0.68, 0.9
Valve 2	Single Seated	19.05, 19.05, 19.05	Linear	4	0.68, 0.9

Control valve 3 is a unique valve when compared to the other valves in the network. It is classified as a steam conditioning valve, where subcooled water is sprayed into the superheated steam path to reduce the temperature of the steam. This is achieved by having the valve attached to an injector shown in Figure 3.24. For the model developed in Flownex this component is modelled used an ANSI valve, a node and a pipe component. The valve functions as a normal valve, then directly after the valve there is a node where the subcooled water is mixed with the superheated steam. After the node component, the pipe component is used to model the nozzle, this is done by making the pipe the same length as the nozzle and specifying that the pipe has different inlet and outlet diameters. The Flownex model of the steam conditioning valve is shown in Figure 3.25.

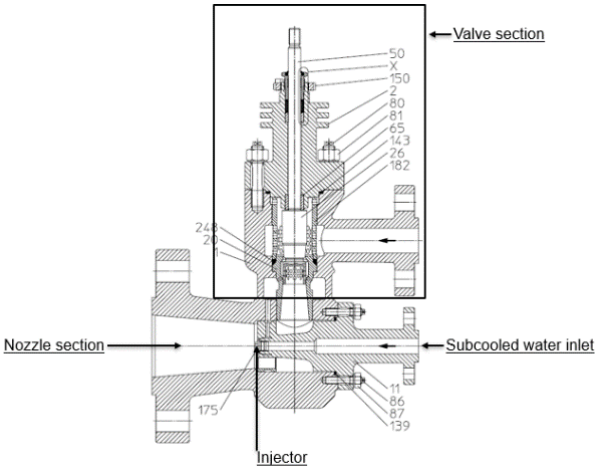

Figure 3.24 Steam conditioning valve drawing (Steinmüller design documents)

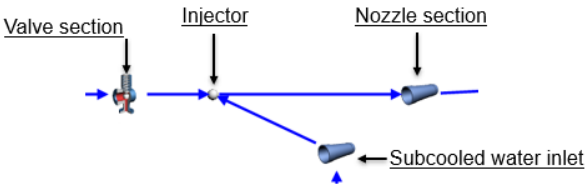

Figure 3.25 Flownex model of the steam conditioning valve

3.8 Controllers

There are multiple controllers on the test facility, controlling either pressure, temperature, mass flowrate or tank level. The majority of the control is via valves on the test facility. The exception being the controller that controls the salt mass flowrate through the steam generation section, this is done by controlling the hot tank pump speed. A basic diagram of the test facility is shown in Figure 3.26 and where these controllers are located. Table 3.19 shows the process value (PV) that is being controlled, the setpoint (SP) and the output.

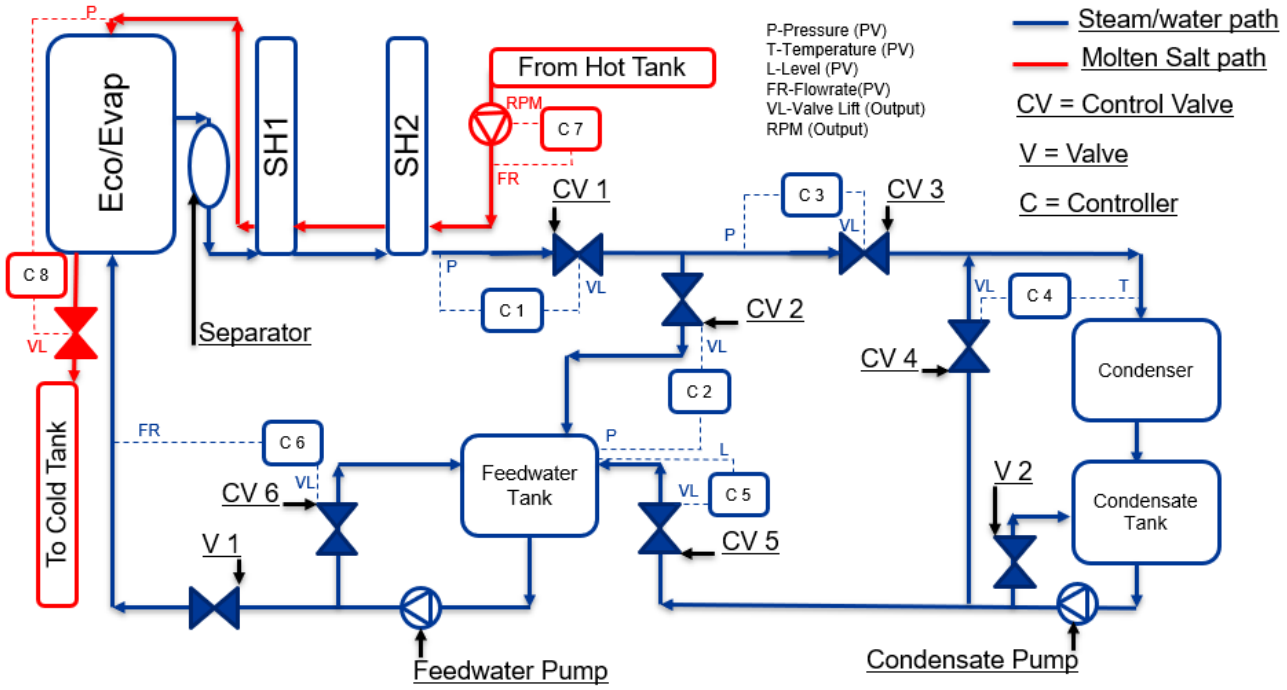

Figure 3.26 Basic control network

Table 3.19 Controllers modelled on the test facility

Controller	Process Value (PV)	Setpoint (SP)	Output
C1	Superheater 2 outlet pressure	Sliding pressure based off Figure 3.27	Valve lift for CV1
C2	Feedwater Tank Pressure	Fixed pressure of 55 bar	Valve lift for CV2
C3	Pressure in front of CV3 (Intermediate P)	Fixed pressure of 65 bar	Valve lift for CV3
C4	Condenser Inlet Temperature	Fixed Temperature of 160 ℃	Valve lift for CV4
C5	Feedwater tank level	Fixed at 0.65 meters	Valve lift for CV5
C6	Feedwater mass flowrate	Dependent on plant load	Valve lift for CV6
C7	Salt mass flowrate through steam gen	Dependent on plant load	Pump RPM
C8	Pressure at the inlet of evaporator	Fixed pressure	Valve lift for control valve before hot tank

As stated in Table 3.19 controller 1 controls the exit pressure of superheater 2. This is a sliding pressure, based on the feedwater mass flowrate through the steam generation system. The graph shown in Figure 3.27 was used to create a script, where the script would change the setpoint of the controller according to the mass flowrate at the inlet of the economizer. Thus, the section of the graph where the pressure increases with respect to flowrate was converted into an equation that was entered into the script. This script can be found in Appendix B**.** The feedwater mass flowrate was measured at the inlet of the economizer because the flowrate is more stable there. Initially, the

mass flowrate was measured at the outlet of superheater 2, but it caused the process value to change too drastically, causing oscillations when running the model.

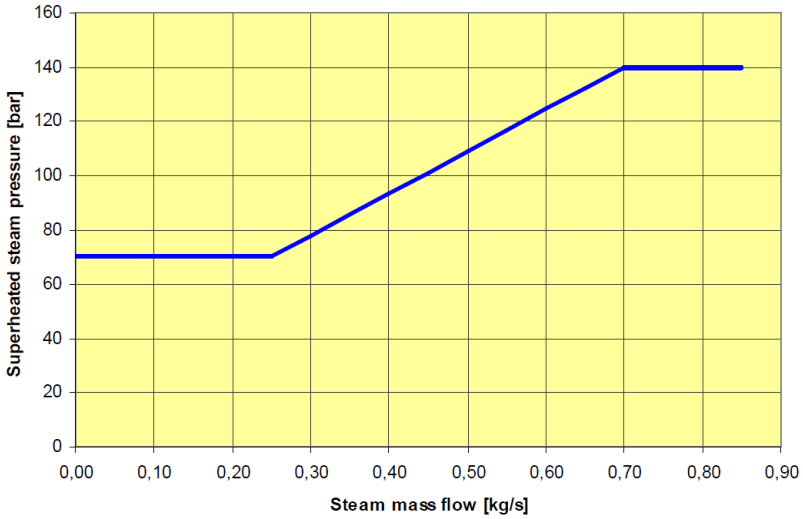

Figure 3.27 Sliding pressure graphs for pressure at the exit of superheater two (Steinmüller design documents)

3.8.1 Flownex control components

The Advanced PID component in Flownex was used to model the controllers. This uses the transfer function shown in equation (3.23) which is a variation of standard transfer function shown in equation (3.24).

$$G_{PID}(s) = K_p\left(1 + \frac{1}{T_i \times s} + \frac{T_d \times s}{d \times s + 1}\right) \tag{3.23}$$

$$G_{PID}(s) = K_p\left(1 + \frac{1}{T_i \times s} + T_d \times s\right) \tag{3.24}$$

The tuning rules applied in this model were defined for the standard transfer function. However, for all controllers the derivative time constant T_d and was set to zero. Therefore, the transfer function that the Advanced PID uses becomes the standard transfer function. The inputs that were changed per controller are shown in Table 3.20.

Table 3.20 Inputs used in advanced controller component

Input	**Description**
SP High Limit	The limit for the setpoint entered.
PV High Limit	The limit for the process value entered.
Auto/Manual	When set to 1 controller is in Auto.
Kp	Proportional term.
Ti	Integral time constant.
Td	Derivative time constant.

Output High Limit	The maximum output the controller can send to the component that is being controlled.
Output Low Limit	The minimum output the controller can send to the component that is being controlled.

The controllers have been modelled without considering certain responses that might exist on the test facility. These responses are any delay that there may be in measuring the process value and any delay due to actuator response. Both these delays have not been modelled as little information is known about the measuring device and the actuator. Thus, for the model developed the process value is transferred by a data transfer link to the controller and the output is transferred by a data transfer link to the component that is being controlled. Figure 3.28 shows the setup of a controller in the Flownex model. Data transfer link 1, takes the process value and inputs it into the process value of the controller. Data transfer link 2 takes the output from the controller and sends it to the component that is trying to control the process value, for example this may be the valve lift fraction.

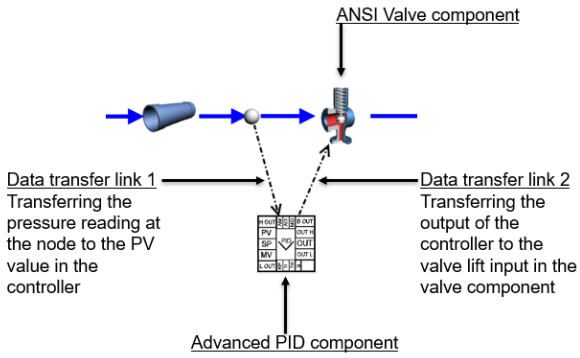

Figure 3.28 Controller setup in Flownex model

For control tuning, one set of control tuning rules could not be followed for all controllers. This is because there are two different responses found for the process value. These two types of responses are classified as self-regulating and non-self-regulating responses and the tuning technique used for these responses is described in section 3.8.2 and 3.8.3 below.

3.8.2 Self-regulating response controller tuning

A self-regulating response is defined that if there is a change in output from its original value, the process value will change from its original value and settle at a new result. When the output is changed back to its original value, the process value will change back to its original value. This self-regulating response is shown in Figure 3.29 where the output is the valve lift and the process value is the flowrate.

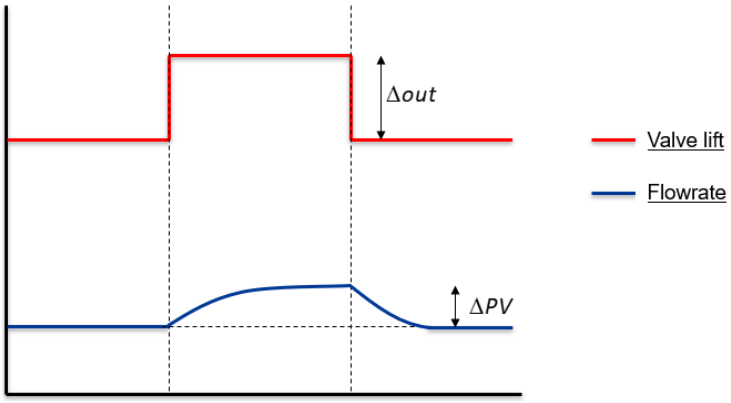

Figure 3.29 Self-regulating response

A 1st order closed loop response tuning technique is used in the model for self-regulating responses. The following steps are followed for control tuning as recommended by ABB services [69].

1. Visual inspection
2. Bump test.
3. Model/Identification
4. Tuning (PID)
5. Validation/testing

These steps were followed for all the controllers modelled on the test facility where a self-regulating response was being controlled. As an example the control tuning for the control valve at the exit of superheater 2 is described below. This control valve is responsible for controlling the pressure at the exit of superheater 2.

Visual inspection

This step in the process applies to real controllers on a plant, where one would inspect the state of the controller, valve, actuator and measurement device. This step is to ensure that there isn't a mechanical problem before trying to tune the controller. In the case for the model developed, this step is not possible, as there would be no mechanical issues for the controller.

Bump test

This step is when the controller is in manual mode and the output of the controller is manually changed (bumped) to another value and the response of the process value is plotted. The results for the bump test for the controller for the superheater 2 exit pressure are shown in Figure 3.30.

Modelling

Modelling is identifying the characteristics that the controller will have to control from the information gathered from the bump test. The three characteristics that are identified are the Δout

being the change in output, the ΔPV being the change in process value and the Δt being the amount of time it takes for the process value to reach steady state. These characteristics are shown in Figure 3.30 from the bump test conducted.

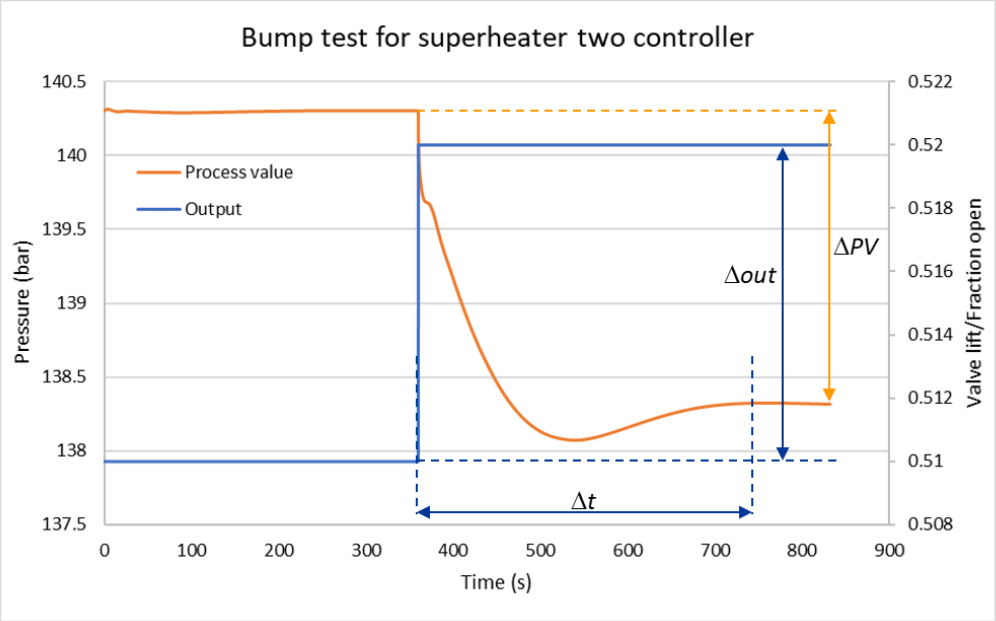

Figure 3.30 Bump test for superheater two controller with modelling parameters

From these three characteristics the following definitions are created; K_Δ shown in equation (3.25) which indicates how much the process value changed for a given change in output, and τ_p is the time constant shown in equation (3.26).

$$K_\Delta = \frac{\Delta PV}{\Delta out} \tag{3.25}$$

$$\tau_p = \frac{\Delta t}{4} \tag{3.26}$$

Table 3.21 shows the parameters identified from the bump test for the pressure controller at the outlet of superheater 2.

Table 3.21 Modelling parameters from bump test for superheater two controller

Parameter	**Result**
Δout (change in output)	0.01 (valve lift)
ΔPV (change in process value)	-1.98 (bar)
Δt (Time taken for process value to settle)	390 (s)
K_Δ (Gain change)	-198.647
τ_p (time constant)	97.5

Tuning

A 1st order response is shown in Figure 3.31. Where the change in setpoint is equal to the change in process value and the response time takes 4 closed loop time constants τ_{CL}.

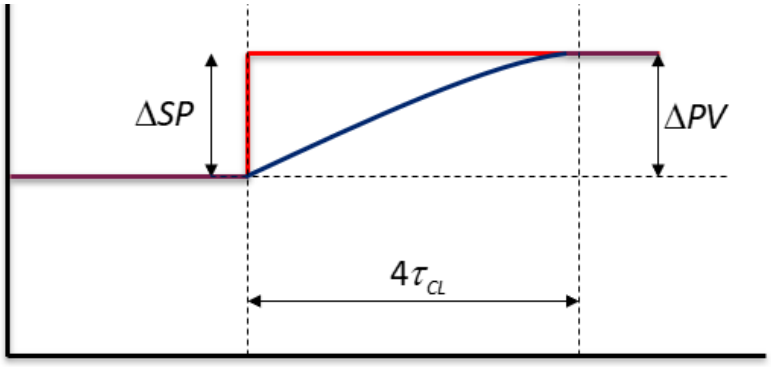

Figure 3.31 First order closed loop response

For the 1st order response the closed loop gain is shown in equation (3.27).

$$K_{CL} = \frac{\Delta PV}{\Delta SP} = 1 \tag{3.27}$$

This gives the following tuning rules for first order closed loop responses:

$$\begin{aligned} K_p &= \frac{1}{K_P \tau_{ratio}} \\ T_I &= \tau_P \\ T_D &= 0 \end{aligned} \tag{3.28}$$

The τ_{ratio} is chosen by the designer and defines the speed of the controller, meaning how long it takes for the controller to get the process value to its setpoint.

$$\tau_{ratio} = \frac{\tau_{CL}}{\tau_P} \tag{3.29}$$

Table 3.22 shows the values for τ_{ratio} that gives slow or fast responses.

Table 3.22 Variables for τ_{ratio}

τ_{ratio}	**Speed**
1	Faster
2	Fast
3	Safe
4	Slow

The tuning rules shown in equations (3.28) are then applied to the parameters from the modelling sections which were identified from the bump test. This then gives the following inputs for the pressure controller at the exit of superheater 2, shown in Table 3.23.

Table 3.23 Controller variables for superheater two pressure controller

K_p	T_i	τ_{ratio}
-0.00168	97.5	3

Validation

For the validation, it is simply testing if the response is the 1st order closed loop response that was tuned for. This is done setting the controller to auto and changing the setpoint and plotting the response of the process value. The time it takes for the process value to reach the setpoint should be roughly equal to equation (3.30).

$$Time = 4 \times \tau_{CL} = 4 \times \tau_{ratio} \times \tau_P \tag{3.30}$$

For the superheater 2 pressure controller, the closed loop response is shown in Figure 3.32. The time it should take for the process value to reach it's setpoint is 1170 seconds, which is marked by the "Time" label on the graph in Figure 3.32. It is clear that the process value is not perfectly at its setpoint, however it is close enough to show that the tuning applied is valid and predictable.

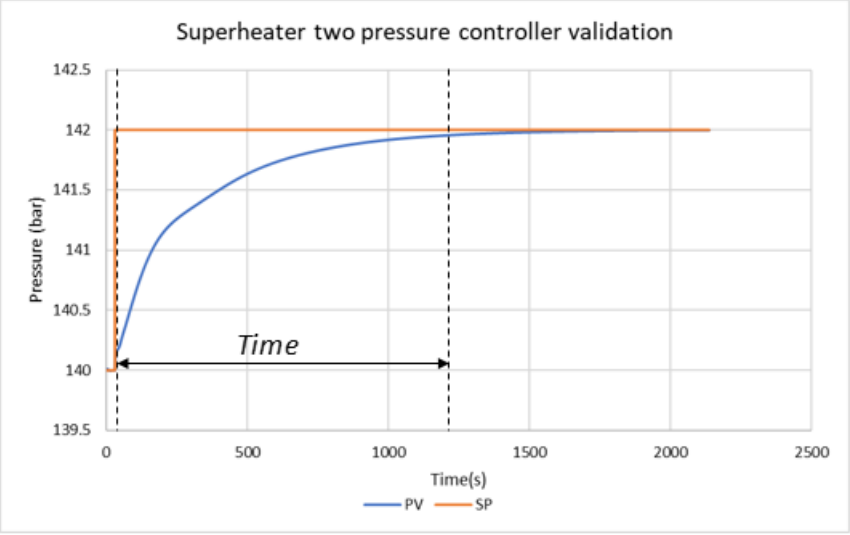

Figure 3.32 Superheater two pressure controller validation

The remainder of the controllers that have a self-regulating response are tuned with the technique described above. Table 3.24 shows the inputs for the controllers that have been tuned with this technique. Appendix F shows the full tuning process for each controller.

Table 3.24 Controller inputs for self-regulating response controllers

Controller	K_p	T_i	τ_{ratio}
Superheater 2 pressure controller (C1)	-0.00168	97.5	3
Intermediate pressure controller (C3)	-0.02	1	1
Condenser inlet temperature controller (C4)	-0.003	2	2
Feedwater mass flowrate controller (C6)	-0.08372	40	3
Salt mass flowrate controller (C7)	85.7219	5	3
Salt exit pressure controller (C8)	-0.002453561	0.75	3

3.8.3 Non-self-regulating tuning

Non-self-regulating responses differ to self-regulating responses because when the output of a controller is changed the response of the process value does not settle at a new value. This type of response is normally associated with tank level tracking. Thus, the tuning technique as described above for self-regulating cannot be used for non-self-regulating responses as the process value would oscillate around its setpoint.

To illustrate how to tune a non-self-regulating response a tank is used as an example. The tank is shown in Figure 3.33 where it has an inlet and an outlet, where the outlet has a fixed mass flowrate, and the inlet is controlled with a control valve being set by a controller.

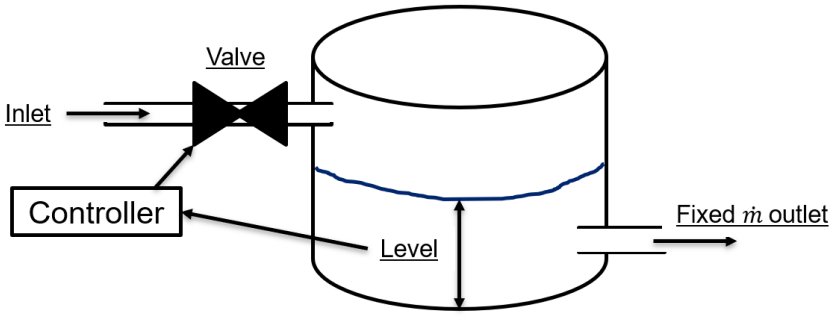

Figure 3.33 Diagram of a tank with a level controller

When there is an increase in the output of the controller, meaning the valve opening ratio increases, the tank level starts to rise. Then the valve goes back to its original position the tank level settles at a new level. This is shown in Figure 3.34.

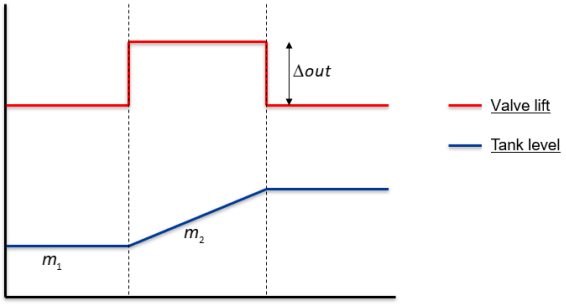

Figure 3.34 Non-self-regulating response illustration

The K_Δ is now defined as the change in slope over the change in output, this is shown in equation (3.31).

$$K_\Delta = \frac{\Delta m = m_2 - m_1}{\Delta out} \tag{3.31}$$

For tanks this definition for K_Δ is convenient as it can be defined by the time it takes to fill the tank, this is shown in equation (3.32).

$$K_\Delta = \frac{1}{T_{Fill}} \tag{3.32}$$

Where T_{Fill} is calculated by knowing the maximum flowrate into the tank and the volume of the tank. Thus, K_Δ can be defined for a tank without doing a bump test.

The next parameter that needs to be defined for tuning a non-self-regulating response is referred to as T_{arrest}. Referring to the tank example, if there is a disturbance in the outlet flow and the outlet flow is now increased. The controller will have to increase the inlet flowrate to try and control tank level. T_{arrest} is defined by the amount of time it takes for the inlet flow (being controlled by the controller) to match the outlet flow, this is shown in Figure 3.35. However, if the flowrates were to stay matched then the tank level would be offset. Thus, the controller must increase the flowrate above the exit flowrate to bring the tank back up to the setpoint (level). Then the controller will have to start decreasing the inlet flowrate until the inlet and the outlet flowrate are matched and the level is at the setpoint, this is illustrated in Figure 3.35. The amount of time it takes for the level to come back to its setpoint is equal to six times the T_{arrest} value.

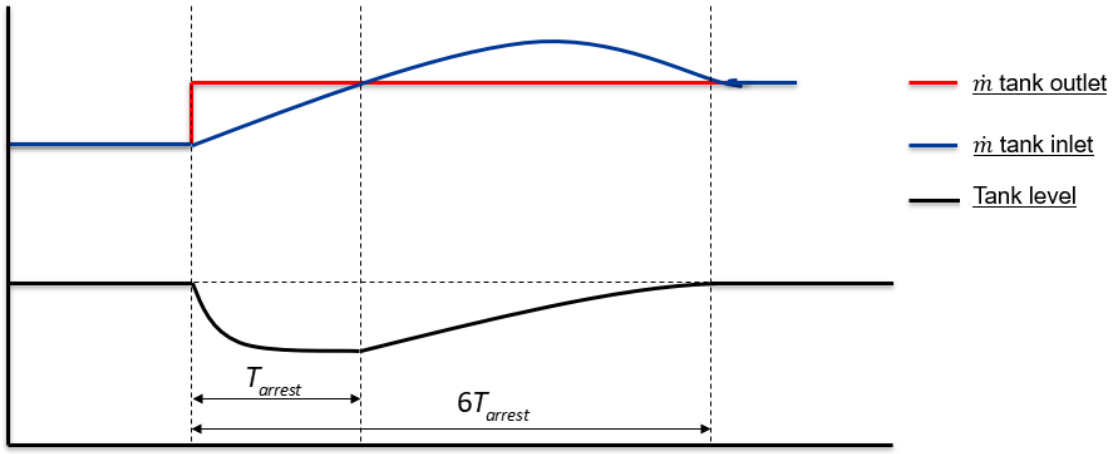

Figure 3.35 Defining Tarrest

The tuning rules are then defined as:

$$K_p = \frac{2}{K_\Delta T_{arrest}} \tag{3.33}$$

$$T_i = 2T_{arrest} \tag{3.34}$$

$$T_d = 0 \tag{3.35}$$

The next process is calculating the arrest time, this is done be creating another parameter called M where T_{arrest} is still defined based on the actual process.

$$M = \frac{T_{Fill}}{T_{arrest}} \tag{3.36}$$

Thus,

$$T_{arrest} = \frac{T_{Fill}}{M} \tag{3.37}$$

Thus T_{arrest} can be defined by selecting a value for M. From the equations defined if 1 is selected for M then the tank would empty before it could recover. Thus, selecting 1 for M can be defined as a very slow response. K_Δ can be redefined in terms of M by substituting equation (3.37) and (3.32) into equation (3.33) and T_i can be redefined in terms of M by substituting equation (3.37) into equation (3.34). Thus, K_Δ and T_i can now be defined in equation (3.38) and equation (3.39).

$$K_p = 2M \tag{3.38}$$

$$T_i = \frac{2T_{Fill}}{M} \tag{3.39}$$

Table 3.25 is used when tuning non-self-regulating responses in the model of the test facility.

Table 3.25 Non-self-regulating response control tuning parameters

Speed	M	T_{arrest}	T_i	K_p
Fast	5	$\frac{T_{Fill}}{M} = \frac{T_{Fill}}{5}$	$\frac{2T_{Fill}}{M} = 2T_{arrest}$	$2M = 10$
	4	$\frac{T_{Fill}}{M} = \frac{T_{Fill}}{4}$	$\frac{2T_{Fill}}{M} = 2T_{arrest}$	$2M = 8$
	3	$\frac{T_{Fill}}{M} = \frac{T_{Fill}}{3}$	$\frac{2T_{Fill}}{M} = 2T_{arrest}$	$2M = 6$
	2	$\frac{T_{Fill}}{M} = \frac{T_{Fill}}{2}$	$\frac{2T_{Fill}}{M} = 2T_{arrest}$	$2M = 4$
Slow	1	$\frac{T_{Fill}}{M} = \frac{T_{Fill}}{1}$	$\frac{2T_{Fill}}{M} = 2T_{arrest}$	$2M = 2$

For the controller that controls the valve lift on the feedwater level control valve, this technique was used to tune the controller. T_{Fill} was calculated as 2237.5 seconds. Thus, Table 3.26 could be generated for the control tuning parameters for the controller.

Table 3.26 Feedwater tank level controller tuning parameters

	M	T_{arrest}	T_i	K_p
Fast	10	223.75	447.5	20
	8	279.6875	559.375	16
	6	372.9167	745.8333	12
	4	559.375	1118.75	8
Slow	2	1118.75	2237.5	4

From Table 3.26 the following values were selected for the controller $K_p = 16$ and $T_i = 559.375$.

The feedwater tank pressure control valve also showed a non-self-regulating response. However, it is not possible to simply calculate T_{Fill}. Thus, the first method described was used, where a bump test was conducted, and the gradients were used to calculated T_{Fill}. Figure 3.36 shows the bump test for the feedwater tank pressure controller.

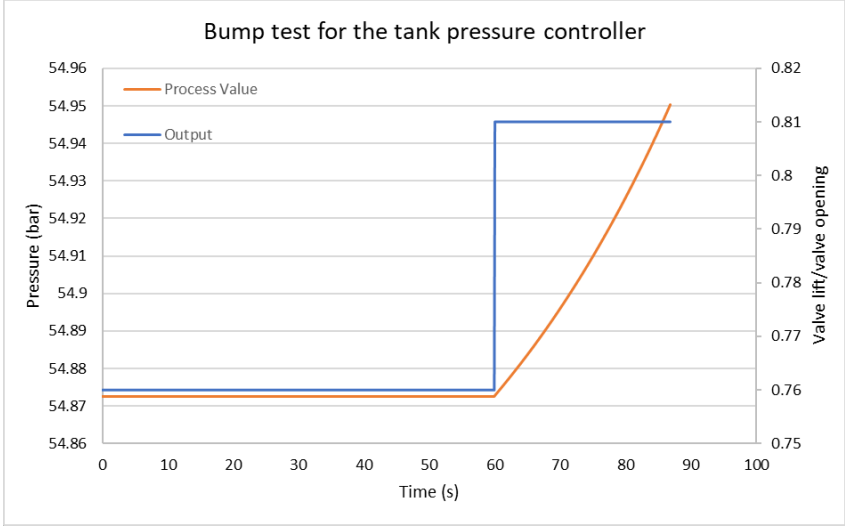

Figure 3.36 Bump test for the feedwater tank pressure controller

The response in the pressure is not a perfectly straight line, thus a gradient for the line was estimated based off its rise over run. This gave the following results to calculate T_{Fill}.

Table 3.27 Calculating Tfill

$m_1 = \frac{rise}{run}$ of process value before step.	$m_2 = \frac{rise}{run}$ of process value after step.	$K_p = \frac{m_1 - m_2}{\Delta out}$	$T_{Fill} = \frac{1}{K_p}$
-4.64E-9	0.00475	0.095	10.53

Table 3.28 was then generated for the feedwater tank pressure controller.

Table 3.28 Controller inputs for feedwater tank pressure controller

	M	Ta	Ti	Kp
Fast	10	1.05309	2.106181	20
	9	1.1701	2.340201	18
	8	1.316363	2.632726	16
	7	1.504415	3.00883	14
	6	1.755151	3.510301	12
	5	2.106181	4.212362	10
	4	2.632726	5.265452	8
	3	3.510301	7.020603	6
	2	5.265452	10.5309	4
Slow	1	10.5309	21.06181	2

In this case the following controller inputs were selected, $K_p = 6$ and $T_i = 7.020603$.

3.9 Steam side tanks

The feedwater tank was modelled using the two-phase tank component shown in Figure 3.37. This component was selected as it's the only component that can track a level in a tank when there are two-phase mixtures. The description of how the level is tracked is described in Appendix A. The inputs for the geometry of the tank were taken from the design documents and drawings for the feedwater tank. These inputs are shown in Table 3.29.

Figure 3.37 Two-phase tank component

Table 3.29 Feedwater tank geometry inputs

Vessel Shape	**Volume** (m^3)	**Diameter** (m)	**Endcap radius** (m)
Cylinder horizontal	1.79	1100	55

For steady state simulations the two-phase tank requires a fixed mass flowrate component attached to the tank in order to solve the correct level. In the complete Flownex model this was control valve 5. This is the control valve that controls the level inside the tank during transient simulations.

The other tank on the water/steam side is the condensate tank, where the tank is filled from the condenser and the water make-up tank. In the final model the tank is not modelled using a tank component. Instead, a node is used, where the pressure and temperature are specified as a boundary value. This means that the node acts as a mass source for the flowrate being drawn by the condensate pump. By specifying the temperature and pressure at the node it is assumed that the condenser will supply the condensate tank with the water at the correct temperature and pressure. Due to there being a water make up tank, the condensate tank should never run out of water, therefore modelling it with a node where the node will always supply the water needed is a valid simplification.

3.10 Water/steam side pump sections

Two pumps have been modelled for the water/steam side. These being the feedwater pump and condensate pump. The feedwater pump is a positive displacement pump and the condensate pump is a centrifugal pump. Both these are variable speed pumps. However, for both the pumps the operating technique used to control the flowrate is the same. This technique is to use a bypass loop which connects to the tank supplying the pump. This is shown in Figure 3.38. In the bypass loop, there is a valve, where the valve would adjust the amount of watering being allowed to flow through

the bypass loop and back into the tank. This is a way of controlling the flowrate from the pump instead of varying pump speed, thus the pump speed is constant.

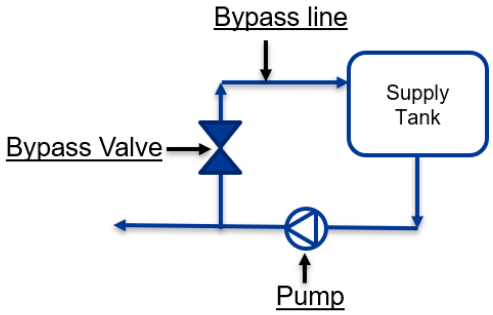

Figure 3.38 Bypass line for pumps on steam side

3.10.1 Condensate pump

The condensate pump is an inline centrifugal pump, which pumps the water from the condensate tank to the feedwater tank. To model this pump the variable speed pump component is used in Flownex, this component is shown in Figure 3.39.

Figure 3.39 Variable speed pump component

The variable speed pump component models the pressure increase over the variable speed pump by interpolating from the pump curves specified for the component. The interpolation scheme selected for this pump is the one based on scaling laws. This scheme works by calculating two possible points on the pump chart using the two closest available pump curves. From these two points, linear interpolation is used to obtain the pump performance of the specified pump speed. The pump charts which were available to input into Flownex are shown in Figure 3.40. These charts are then digitized into a series of points in a table. The digitized pump curves created from Figure 3.40 are shown in Figure 3.41 and Figure 3.42. These tables are then entered as a pump curve into Flownex by creating a custom pump chart.

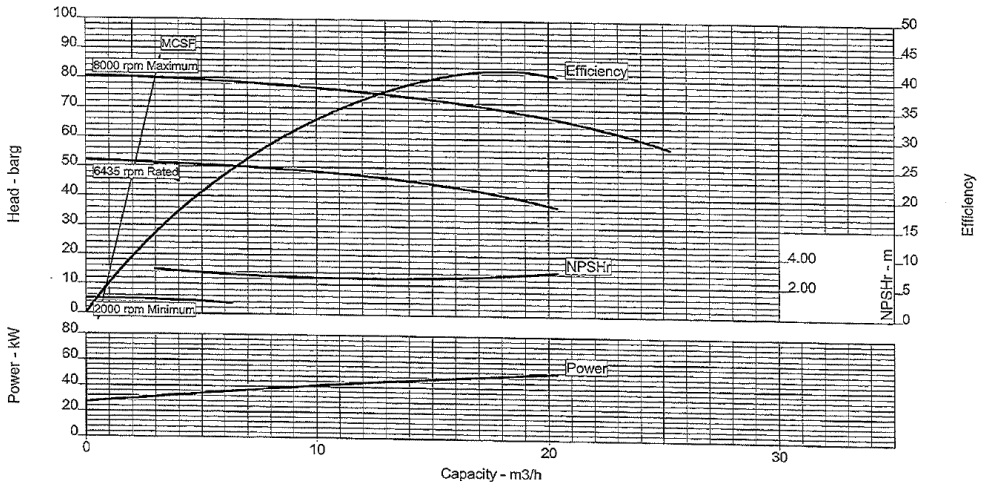

Figure 3.40 Actual condensate pump chart (Steinmüller design documents)

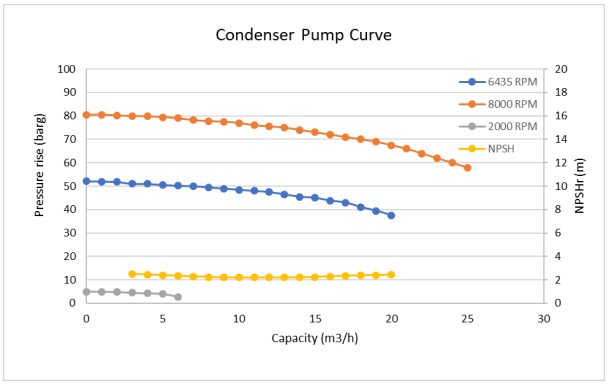

Figure 3.41 Digitized condensate pump chart

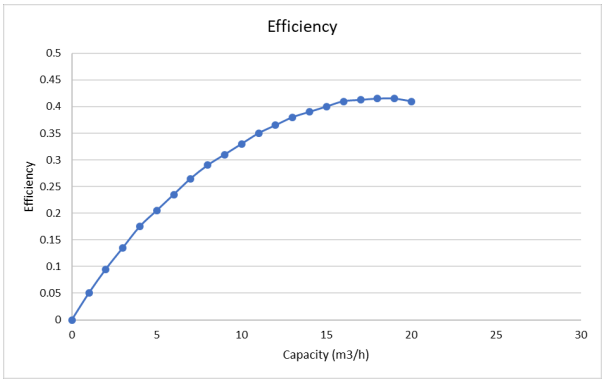

Figure 3.42 Digitized efficiency chart for condensate pump

For the condensate pump the only other input that is entered is the pump speed which is 6435 rpm. The Flownex model of the pump and the valves that control the flowrate is shown in Figure 3.43.

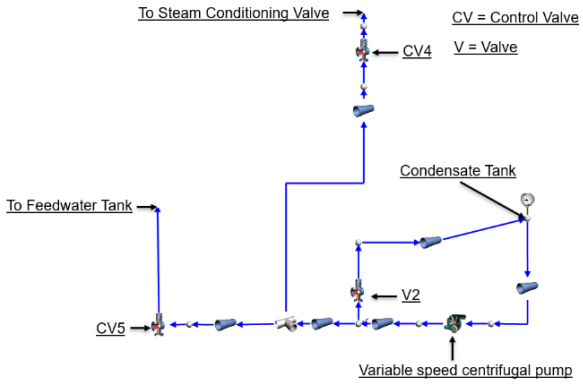

Figure 3.43 Flownex model of condensate pump and feedback loop

The original way the flowrate through the pump was going to be controlled was by using valve 2 as a control valve. However, from running simulations it was found that the valve can be set to a fixed

position having a valve lift position of 0.1. Control valves 4 and 5 then change their opening to control their process values. Thus, it's the opening of control valves 4 and 5 that govern the flowrate through the condensate pump.

3.10.2 Feedwater pump

The feedwater pump on the test facility is a positive displacement pump, where an electric motor turns a crank shaft that moves three plungers (cylinders) to pump the fluid through the pump. The advantage of using a positive displacement pump is that they can produce the same flowrate at a given speed no matter what the outlet pressure of the pump is. The disadvantage is that if the pressure limit is exceeded the pump can be damaged, thus pressure release valves are installed on the pump. The plunger pumping action causes oscillations in the flow compared to the flow produced by centrifugal pumps. These flow oscillations on the test facility are mitigated with a dampener device the dampens out these oscillations in the flow.

To model the positive displacement pump, the Flownex positive displacement pump component is used, shown in Figure 3.44. This Flownex component does not model the flow oscillations typically found on positive displacement pumps. Thus, it is assumed that the flow dampener on the test facility performs its function well enough that there are no or very limited flow oscillations.

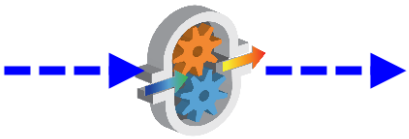

Figure 3.44 Positive displacement pump component

This Flownex positive displacement pump component works off pump curves that can be specified for a given pump. In the case for the positive displacement pump on the test facility, only the characteristic curve for the flowrate vs rotational speed is known and is shown in Figure 3.45. This pump curve is for a pressure rise of 115 bar, there are no other pump curves available to enter into the model. Therefore, it is assumed that for any pressure rise the pump curve is the same.

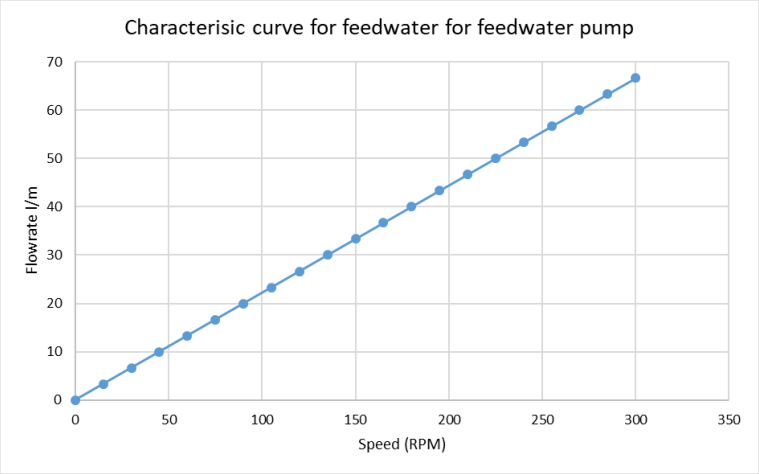

Figure 3.45 Characteristic curve for feedwater pump

This pump curve was entered into Flownex by first digitizing the pump curve into a table, and then inputting that table into Flownex. Where the pump curve is used to model the pump, interpolation is used when the speeds or pressures are different from what is specified in the curve. The pump is run at a constant speed of 291 rpm and the flowrate is controlled through the bypass control valve. The Flownex model for the feedwater pump section is shown in Figure 3.46, where there are two valves downstream of the pump. Both valves are modelled using the pipe component where the orifice diameter ratio is specified. By adjusting either valve the flowrate to the inlet of the economizer can be adjusted. For simplicity, it was decided that valve 1 would have a fixed diameter ratio of 0.37 and control valve six would be controlled to vary the feedwater mass flowrate.

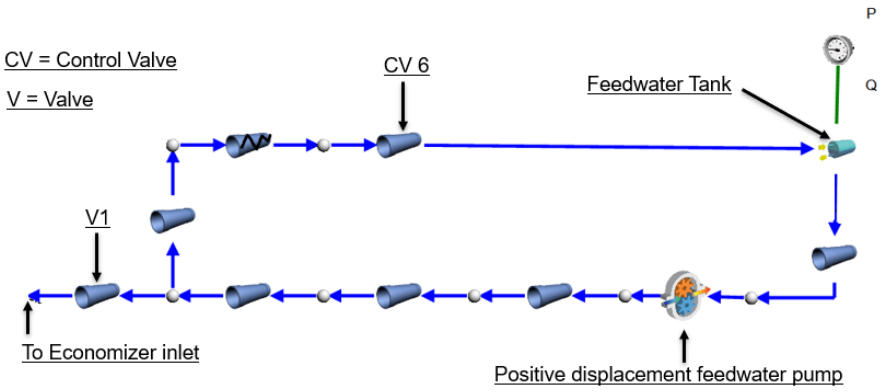

Figure 3.46 Flownex model of feedwater pump and feedback loop

3.11 Salt side tanks and pumps

3.11.1 Salt Tanks

Both the hot and the cold tanks on the test facility are identical in design. Therefore, there is no difference in the model for the hot and cold tank. The tanks are modelled using the open container component in Flownex shown in Figure 3.47. The open container can track level, thus having a dynamic volume variable, calculated using the conservation of mass and energy. The free surface pressure is specified for the open container, the pressure at the inlet of any connecting pipe or pump is calculated using the surface pressure and the head of fluid above the pipe.

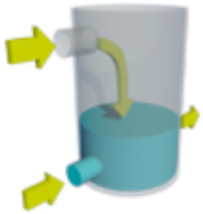

Figure 3.47 Open Container Component

The tanks on the test facility have very similar insulation to the type found on the molten salt tanks on full scale CSP plants. Figure 3.48 shows the amount of insulation around the tanks. From the information gathered in the literature review, the thermal losses in these tanks are assumed to be minimal. It was therefore decided to not model the heat loss to the environment. This decision was made as the model developed only simulated normal plant operation. This means that the longest simulation time the model will run for is about 14 hours. This would result in a minimal temperature drop, especially considering that the hot tank is always being supplied with molten salt at a constant temperature when the solar field is running. Thus, the temperature in the hot tank is fixed at 580 ℃, which is the temperature the salt should be entering the hot tank from the solar field. The temperature of the cold tank is also fixed but at 290 ℃. This was done because the model needed a temperature boundary condition for the steady state solution. For transients, the boundary condition can be removed. The fluctuation in temperature can then be seen if the results are needed. However, for the transient simulations done in this report, the temperature was fixed as there was no solar field attached to this model. The tank is assumed to be at atmospheric pressure thus the free surface pressure was specified as 101 kPa.

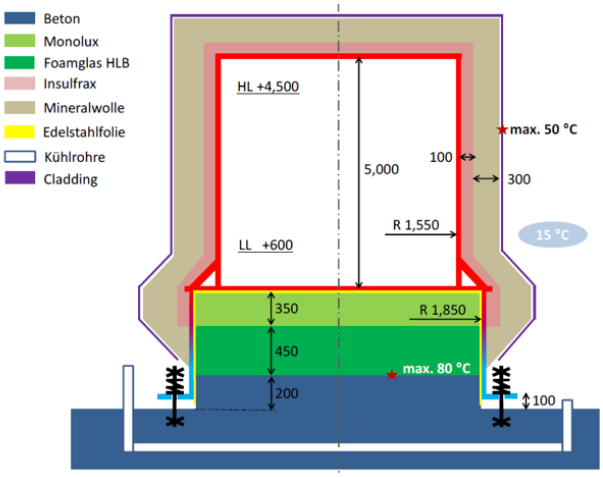

Figure 3.48 Insulation around the molten salt tanks (Steinmüller design documents)

For the steady state simulations and for the starting conditions for transient simulations the level in the molten salt storage tanks had to be specified. These levels were assumed to be the starting levels at the beginning of the day where the hot tank would be at its lowest level and the cold tank at its highest level. The hot tank starting level was estimated to be 0.8 m. This was selected as the low-level alarm goes off at 0.7 m. Thus, 0.8 m was selected to have a safety margin. The cold tank starting level was calculated from knowing the total inventory of the molten salt expected to be supplied to the test facility. From design documentation, the total inventory of molten salt is 27.93 m^3. From estimating that the hot tank has a starting level of 0.8 m, by doing a volume calculation this leaves 21.892 m^3 of salt remaining. Which equates to a starting level of 2.9 m in the cold tank.

The inputs for the open container component are taken directly from the design documents and drawings for the tanks. These inputs are summarized in Table 3.30 below.

Table 3.30 Inputs for molten salt tank models

Tank Level (m)	**Free surface pressure (kPa)**	**Diameter (m)**	**Height(m)**	**Elevation (m)**
Hot tank 0.8 Cold Tank 2.9	101	3.1	5	1.1

3.11.2 Hot tank pump

The pump in the hot tank is a cantilever pump, which is classified as a centrifugal pump. The difference is that instead of the impeller being supported by bearings located near the impeller the impeller is cantilevered from the motor. The pump is installed vertically, thus the motor is on top of the tank and the impeller is submerged in the molten salt and sits at the base of the tank. The drawing for the hot salt pump is shown in Figure 3.49.

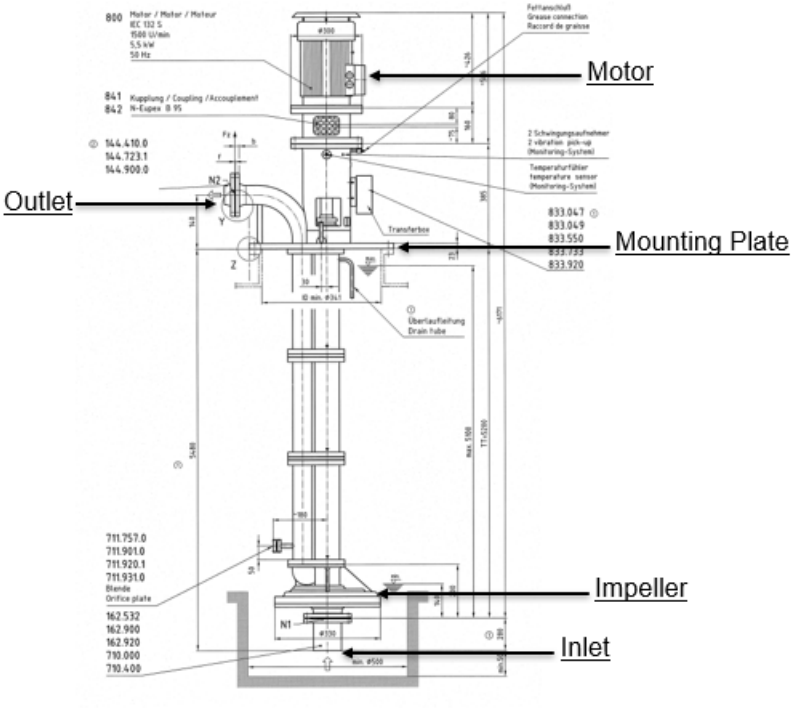

Figure 3.49 Hot Salt Pump (Steinmüller design documents)

Since this pump is a centrifugal pump, the hot salt pump is modelled using the variable speed pump component available in Flownex. The performance curves for the pump were again digitized into a series of points in a table and entered as a custom pump chart into Flownex. These digitized graphs are shown in Figure 3.50 and Figure 3.51.

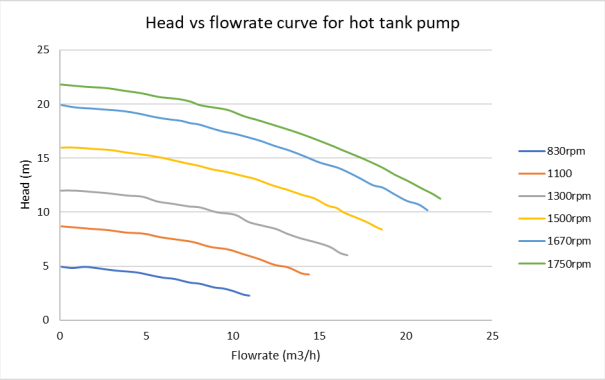

Figure 3.50 Head vs flowrate curve for hot tank pump

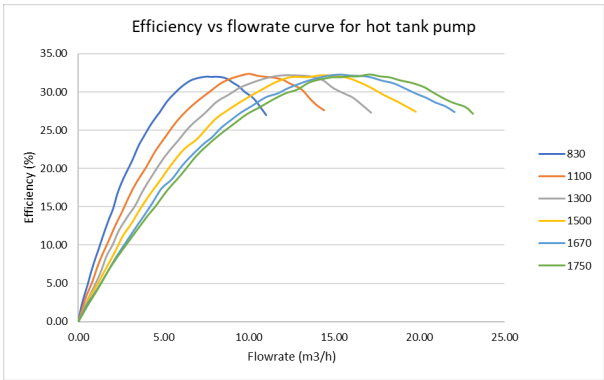

Figure 3.51 Efficiency vs flowrate curve for hot tank pump

3.12 Final model

A complete diagram of the test facility is shown again in Figure 3.52 to compare with the final model developed in Flownex.

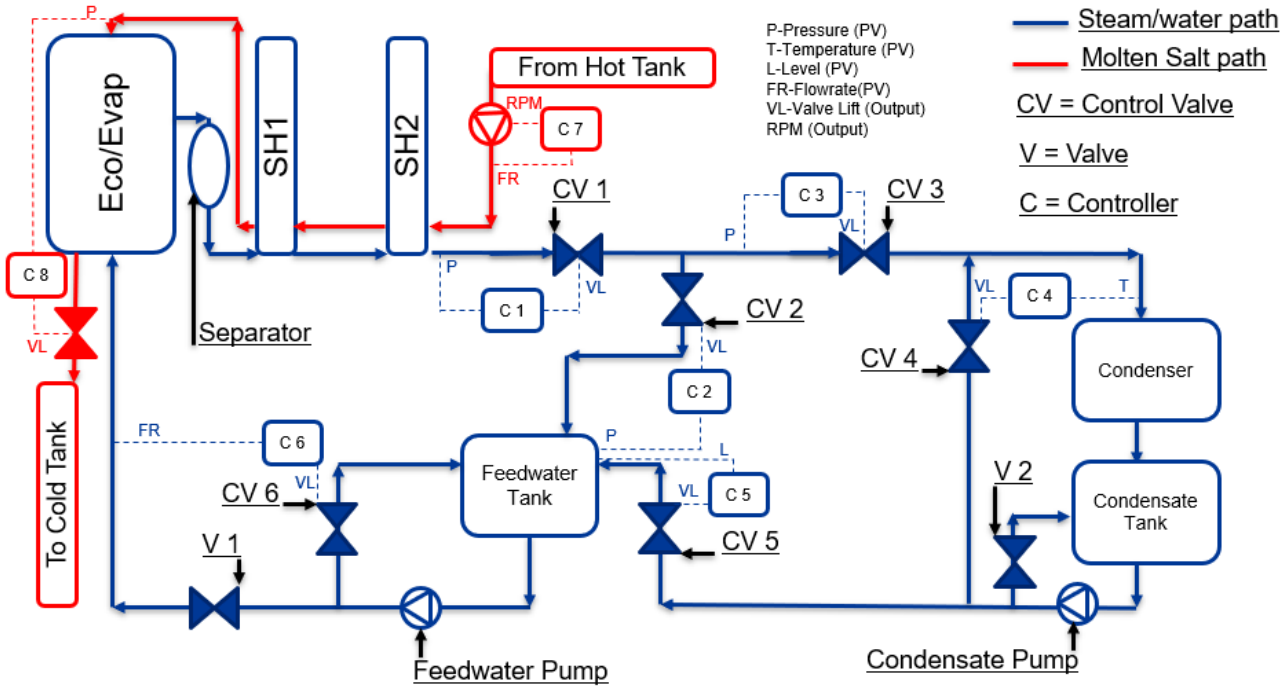

Figure 3.52 Basic diagram of complete steam cycle

The complete Flownex model of the steam cycle with the molten salt storage tanks is shown in Figure 3.53. This complete model was developed from smaller subsection models of the test facility, which included the steam generation section, the valve expansion section and the tank and pump sections. The valve openings and hot salt pump speed were determined from the subsection models, where they were selected so that the results of the subsection models produced the expected conditions. These expected conditions were obtained from the process flow diagram provided by Steinmüller. For a more detailed description of how the complete model was developed refer to Appendix A.

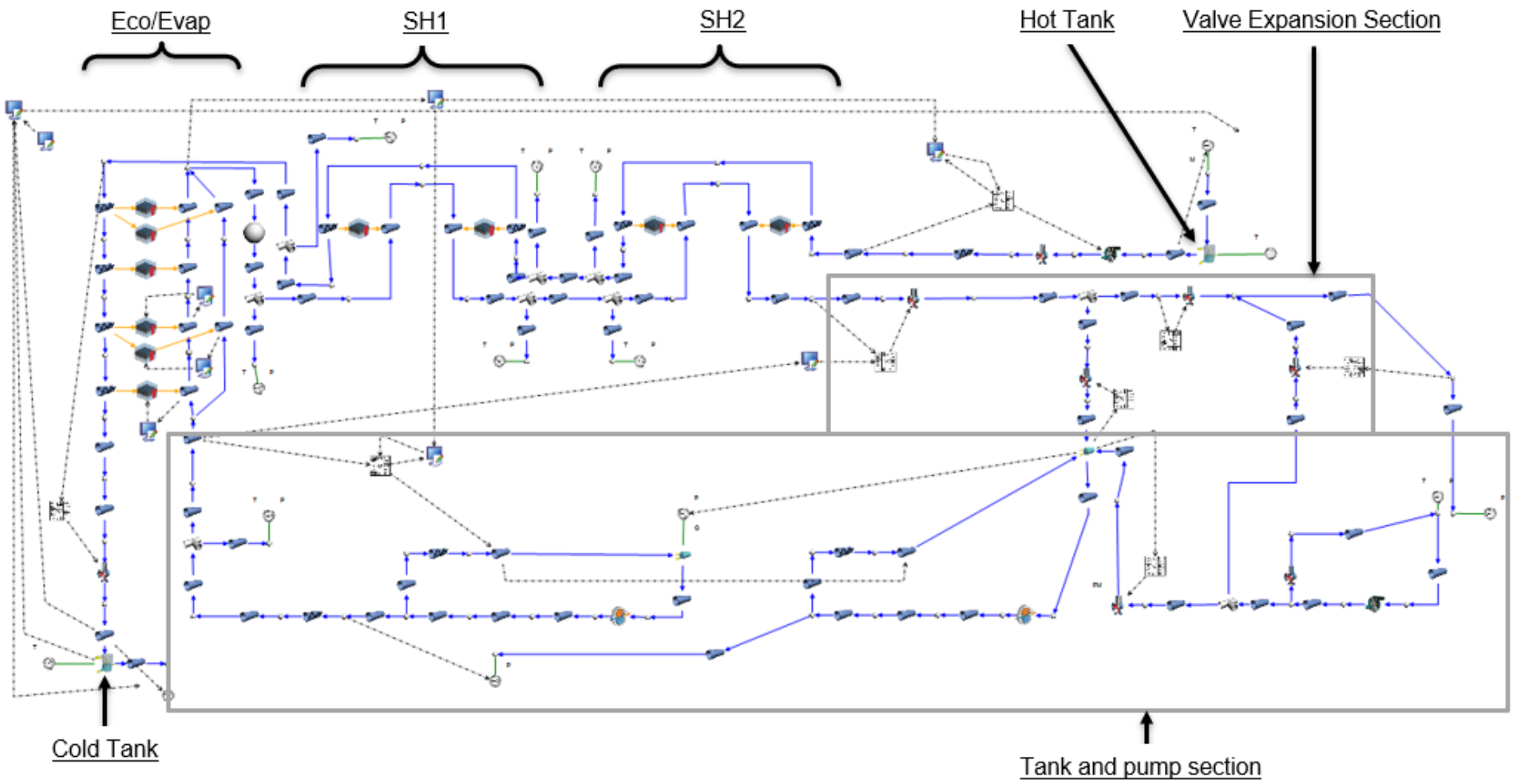

Figure 3.53 Complete Flownex model

The initial steady state solution for the complete model at 100% load did not calculate the exact expected results. This was due to all the subsection models being combined into a single model for the first time. However, a transient simulation was run to let all the controllers converge on their setpoints. After all the controllers had converged the transient simulation was stopped and the steady state simulation run again. This second attempt at the steady state simulation produced the exact steady state results that were expected.

In developing this model, it was not possible to completely close the loop from the feedwater tank to the inlet of the economizer. This was due to Flownex not being able to solve the steady state solution for closed loop systems where two-phase flow is in the network. Instead, it was decided to mirror the feedwater tank, feedwater pump, and bypass loop. This is shown in Figure 3.54.

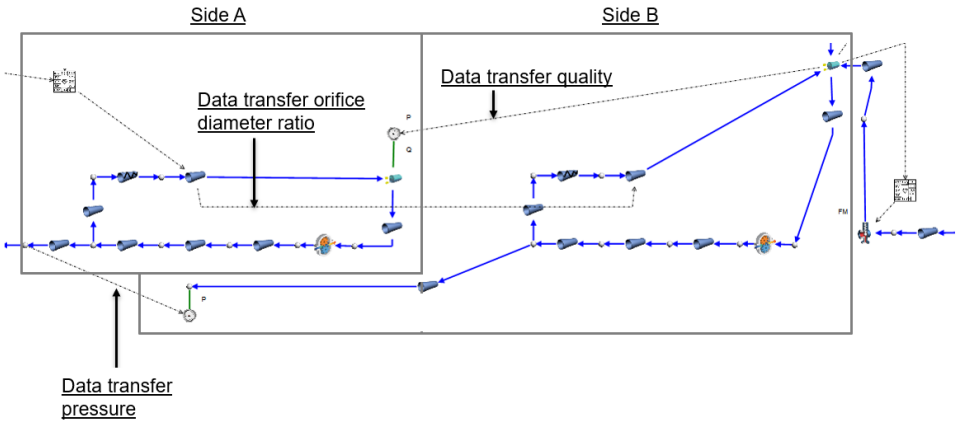

Figure 3.54 Mirrored feedwater pump section

To make this modelling technique as accurate as possible, almost all the parameters being calculated on either side of the model were transferred between the two sections by using data transfer links. These parameters include; The orifice diameter ratio for control valve 6 was transferred from side A to side B. The pressure just after the pump section on side A was transferred to the boundary condition on side B. The quality from the feedwater tank on side B was transferred to the quality boundary condition for the feedwater tank on side A. The only parameter that can be different between these two sides is the pressure in the feedwater tank. However, the pressure is controlled with a control valve on side B, due to the controller is tuning there is practically no fluctuation in pressure in the feedwater tank on side B. Therefore, the pressure in the feedwater tank on side A and B is practically the same leading to both side A and B having the same conditions as each other. This modelling technique essentially closes the loop.

4. Results and discussion

4.1 Steam generation section steady state sensitivity analysis

To simulate the whole model the correct salt mass flowrate through the heat exchangers must be known for the steam generation section to operate as expected. The correct salt mass flowrate was obtained through the sensitivity analysis shown in section 3.6. However, the decision was made to change the salt compound from the classical solar salt specified in the steam generation design documents to the eutectic mixture for the salt compound. This was done since it is more likely to be the salt compound eventually used in the test facility and it will also demonstrate that the model can be used with different salt compounds. Also, the feedwater temperature at the inlet of the economizer is different for the whole steam cycle when compared to the steam generation design documents. Therefore, the salt mass flowrate identified from the sensitivity analysis in section 3.6 could not be assumed and a new sensitivity analysis was conducted. Table 4.1 shows the inlet and outlet conditions specified for the sensitivity analysis conducted for the three load cases.

Table 4.1 Boundary values for steam generation sensitivity analysis

Plant load	Eco inlet (water)	Superheater outlet (water)	Superheater inlet (salt)
35%	270 ℃, 75 bar	0.25 kg/s	580 ℃
100%	270 ℃, 160 bar	0.7 kg/s	580 ℃
115%	270 ℃, 167 bar	0.81 kg/s	580 ℃

The benefits of using the eutectic salt mixture when compared to the classical solar salt are that it has a lower melting temperature, thus reducing the risk of unwanted freezing in the test facility. The eutectic salt mixture was entered into the model by creating a custom single-phase fluid. The fluid properties that were specified are the density, viscosity, conductivity and Cp/Enthalpy. These properties are only dependent on temperature. On average the values of these fluid properties are about 5% lower than the properties specified for the classical solar salt.

The temperature at the inlet of the economizer has changed from what was initially expected because the design documents for the steam generation section used earlier predictions for the temperature. However, from the complete model developed it was found that the temperature is 270 ℃ and not 260 ℃. This is confirmed by the process flow diagram of the complete water/steam cycle provided by Steinmüller.

The sensitivity analysis for the 100% load is shown in Figure 4.1, the sensitivity analysis results for the 35% and the 115% loads are shown in Appendix G.

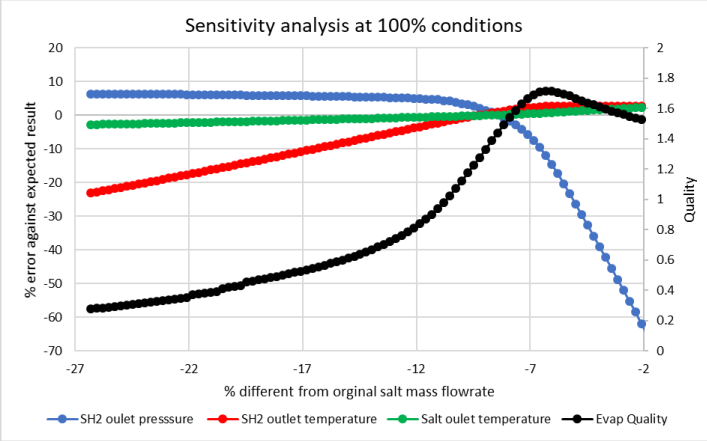

Figure 4.1 Sensitivity analysis results for 100% load with eutectic salt

From the results shown in Figure 4.1 the required salt mass flowrate for the 100% load should be 3.43 kg/s. From the 35% and 115% sensitivity analysis shown in Appendix G the salt mass flowrate should be 1.35 kg/s and 4.02 kg/s respectively.

Table 4.2 shows the required conditions compared to the outlet results from the steam generation model when the salt flowrates are specified to the values shown above.

Table 4.2 Expected outlet conditions vs model results for 35% load case

Plant Load (%)	**Superheater two outlet pressure (bar)**		**Superheater two outlet temperature (℃)**		**Economizer outlet temperature (℃)**	
	Required	Result	Required	Result	Required	Result
35%	70.000	70.253	580.0	575.2	293.0	300.5
100%	140.000	142.716	563.0	559.7	291.0	290.4
115%	140.000	138.073	561.0	565.6	294.0	292.1

An important result from the sensitivity analysis is the quality at the exit of the evaporator. The quality gives an indication as to the boiling conditions inside the economizer/evaporator vessel. If the quality is too high, it means that the boiling point is located to low inside the vessel, which leads to a high pressure drop across the system. If the quality it is too low, the boiling point is located too high in the vessel thus two-phase steam will enter the superheaters. Figure 4.1 shows that the quality at the exit of the evaporator increases gradually for the 100% load case, this is also true for the 115% load. However, for the 35% load case shown in Figure 4.2, the quality is much more responsive to changes in the salt mass flowrate. This shows that at lower load conditions the boiling point is more sensitive to the operating conditions. Thus, there are fewer suitable operating conditions at the lower load.

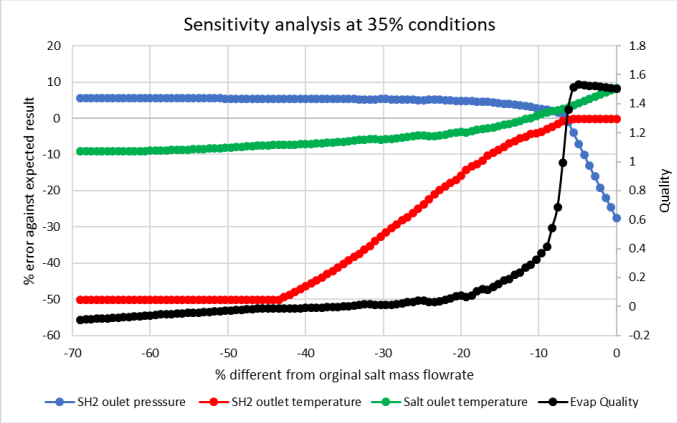

Figure 4.2 Sensitivity analysis results for 35% load with eutectic salt

4.2 Whole day transient results

This section shows the high-level results for how the test facility may respond to given solar conditions over the course of a day. The two cases for the solar conditions are a sunny day and a cloudy day. The start-up and shutdown processes of the test facility are not modelled, and the test facility is initialised at 35% load. The salt is distributed so that the cold tank starts at 60% and the hot tank at 15%.

4.2.1 Solar transient data

Since the HPS2 test facility has not yet been in operation, there is no data available for the HTF flowrates in the actual solar field. Therefore, to investigate the transient operation of the plant, HTF flowrates through the solar field had to be estimated. Powell *et al.* [32] did a study demonstrating the control of a CSP plant with storage. Their strategy was aimed at controlling the temperature at the outlet of the solar field at a constant value. This control strategy is the same as that which will be employed on the HPS2 test facility. Their results showed the flowrates through the solar field on both sunny and cloudy days.

The HTF flowrate results were adjusted to the flowrates that are expected through the solar field on the HPS2 test facility. This was done by normalizing the flowrates reported by Powell *et al.* [32] with the nominal flowrate and then multiplying these with the nominal flowrate through the HPS2 test facility. Thus, Figure 4.3 shows the flowrate of HTF that is flowing from the solar field into the hot tank for the model.

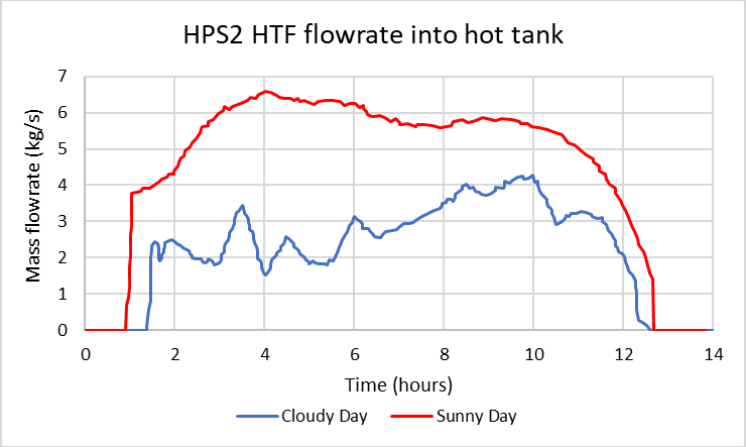

Figure 4.3 HPS2 HTF flowrate into hot tank

This flowrate data is entered into the model via a script that is reading the data from a text file. This script interpolates between points to obtain accurate data for all time steps. The hours on the horizontal axis are not representing the time of day but rather the time since the start of the simulation period.

4.2.2 Sunny day case

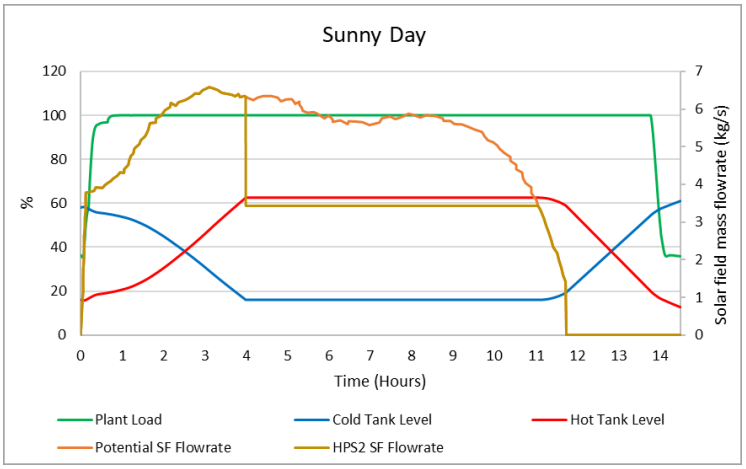

Figure 4.4 Sunny day case transient results

Figure 4.4 shows the results for the sunny day case. The test facility is operated at 35% of the nominal load for the first minute and is then ramped up to 100%. The hot tank was filled to maximum capacity within the first four hours, its maximum capacity is around 60% due to the inventory of salt supplied to the test facility. Since the hot tank is at maximum capacity the flowrate through the solar field had to be reduced to match the molten salt flow rate through the steam generator. The potential flowrate through the solar field is plotted to show how much solar energy is not being used. The thermal storage enabled the test facility to run at 100% for little over two hours when there was no salt flowrate provided to the hot tank from the solar field.

4.2.3 Cloudy day case

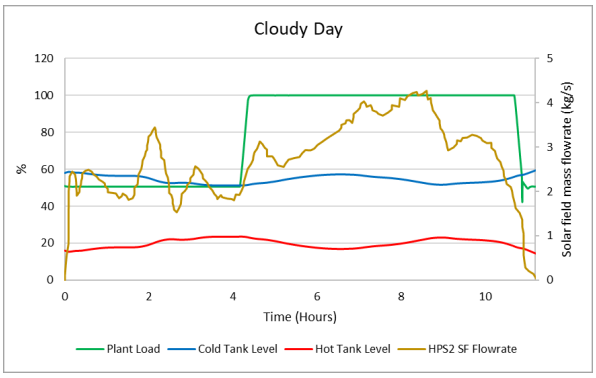

Figure 4.5 Cloudy day transient results operating strategy one

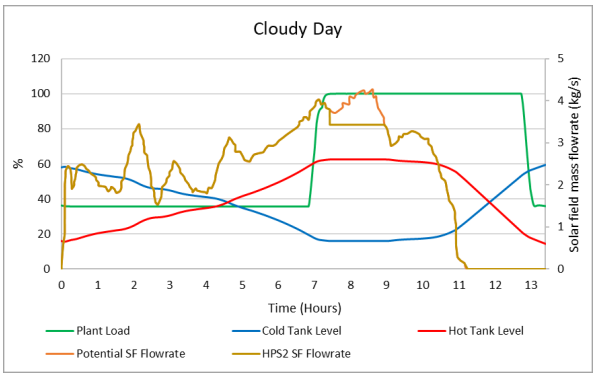

Figure 4.6 Cloudy day transient results operating strategy two

For the cloudy day case, there is significantly less salt flowrate supplied to the hot tank from the solar field. This affects the ability to store molten salt in the hot tank. Figure 4.5 and Figure 4.6 show two different operating strategies for the test facility during the cloudy day conditions.

In Figure 4.5 the operating strategy was to run the test facility at 50% for the first four hours, then ramp up to 100%. This assumes that the operator will have predicted weather conditions for the day. However, using this strategy the levels in the storage tanks could not be increased significantly. Therefore, limited storage was available at the end of the day. Thus, the test facility would have to be shut down soon after the salt flowrate from the solar field was discontinued.

In Figure 4.6 the operating strategy was to run the test facility at its minimum load of 35% until the cold storage tank was approaching its minimum safe value then the load was increased to 100%. This strategy enabled the thermal storage to fill to maximum capacity. Thus, the test facility was able to run at 100% for two hours after solar field shutdown.

For the test facility, these different operating strategies don't make much practical difference. However, in the case of a full scale CSP plant, these two operating strategies can make a difference to revenue depending on what tariff payment system the CSP plant is on. For example, the first strategy selected would suit a flat tariff system. For this tariff system, the plant gets paid the same amount per kWh produced no matter what time of day it is. However, the second strategy used would benefit from a peak tariff system. This is where the plant gets paid more during peak hours.

4.3 Detailed steam cycle transient results

This section shows detailed steam cycle transient results for three different model setups. The first set of results presented are from the whole day results shown in section 4.2. The second set are from the model where a separator has been incorporated into the model. The third set of results

presented are from the model where the load change occurs much more quickly than the whole day results.

Two main controllers are responsible for the plant load namely the feedwater flowrate controller and molten salt flowrate controller. The rate at which the plant load changes is dependent on how fast the setpoints for the feedwater and salt flowrate controllers change. The setpoints are entered in the model via a script, where the rate of change for the setpoint is defined.

In addition to these scripts, there is a script that is aimed at controlling the quality of the steam exiting the evaporator by trying to control either the salt or the feedwater mass flowrate. This script allows the other scripts to run depending on the steam quality at the exit of the evaporator. Having the steam quality equal to one or greater ensures that only single phase superheated steam enters the superheaters. On the real test facility, there is a separator that should stop any vapour reaching the superheaters.

Figure 4.7 shows the completed Flownex model with key points on the test facility highlighted, as well as the three scripts mentioned above. These key points on the test facility are all the points which are referred to when the results in the following sections are presented. Table 4.3 shows what each key point is.

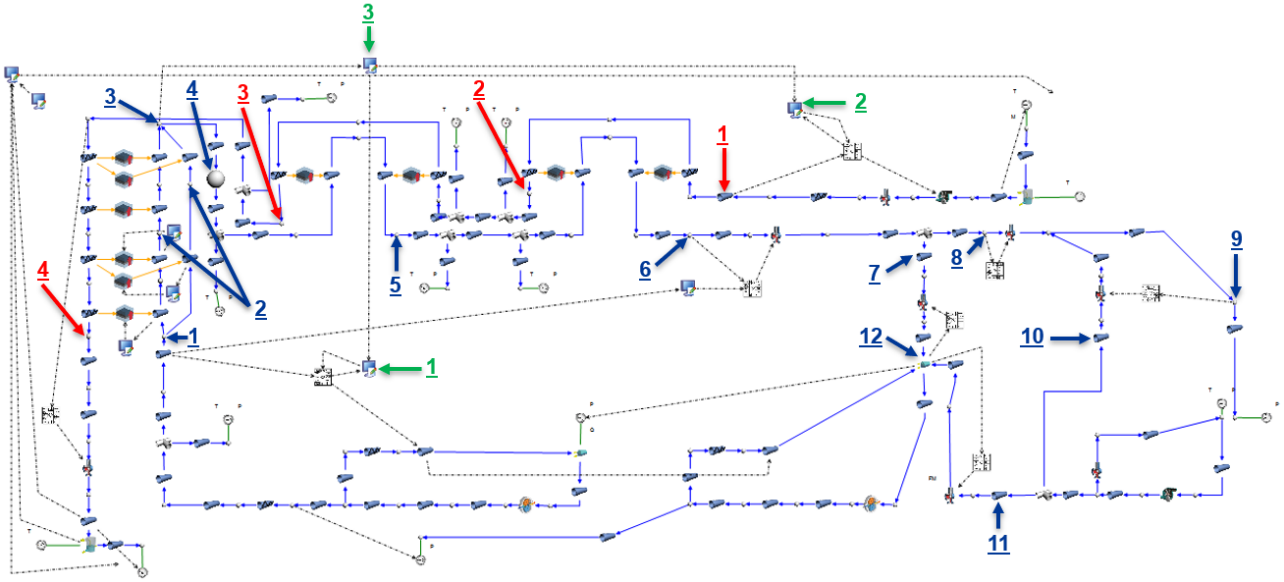

Figure 4.7 Complete Flownex model with key points shown

Table 4.3 Key points in model

	Feedwater/steam side (blue)	Salt side (red)	Scripts (green)
Number	Description		
1	Economizer inlet	Hot tank outlet	Feedwater flowrate setpoint change rate
2	Economizer outlet	Superheater two outlet	Salt flowrate change rate

3	Evaporator outlet	Superheater one outlet	Evap quality control
4	Separator	Economizer outlet	
5	Superheater one outlet		
6	Superheater two outlet		
7	Steam bleed		
8	Intermediate pressure point		
9	Condenser inlet		
10	Spray (Flow to conditioner valve)		
11	Condensate inlet to feedwater tank		
12	Feedwater tank		

4.3.1 Whole day transient results (conservative load change)

This section shows the detailed whole day transient steam cycle results for the 35% - 100% load increase and the 100% - 35% load decrease shown in section 4.2. Since the steam cycle in the test facility is effectively decoupled from the solar field input, there are no noticeable differences between the sunny and cloudy day cases for how the steam cycle increases and decreases plant load. Therefore, the results are not shown individually for the two cases. The feedwater flowrate setpoint rate of change is 0.0005 $^{kg/s}/_{s}$ and the salt flowrate setpoint rate of change is 0.0025 $^{kg/s}/_{s}$. Thus, it takes roughly 15 minutes for the setpoints to change from their 35% value to the 100% value. This load change for this report is referred to as a conservative load change. The rate at which the setpoints change when the load is decreased is the same. According to the design data for the test facility, the separator should not need to be in operation once the plant has gone through its start-up process. Therefore, only the volume of the separator was modelled and not its separating capability.

Flowrate results

Figure 4.8 and Figure 4.9 show the flowrate response at various points in the steam generation for the load increase and decrease. For both the load changes the salt flowrate takes just under 20 minutes to settle. The steam side flowrates for the load increase take 25 minutes to settle while for the load decrease take 35 minutes to settle. This shows that decreasing load takes 10 minutes longer than increasing load. For both the results, the salt flowrate stops increasing or decreasing at various points. This was where the evaporator outlet quality control script stopped the salt flowrate setpoint from changing in order to try and maintain the exit quality around one.

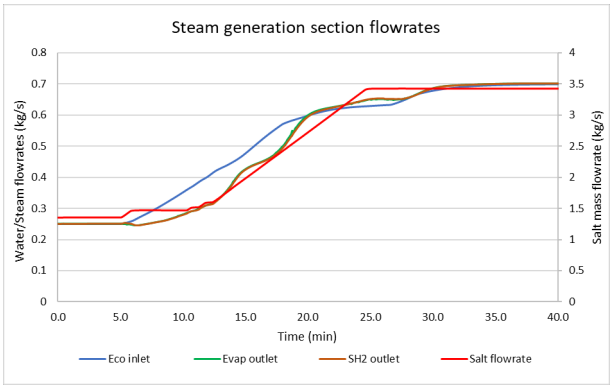

Figure 4.8 Steam generation section flowrate responses, 35%-100% conservative load change

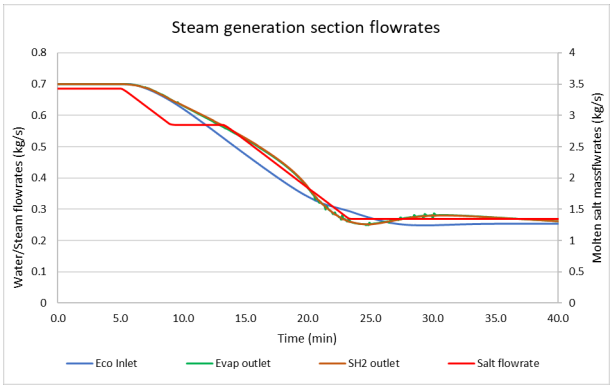

Figure 4.9 Steam generation section flowrate responses, 100%-35% conservative load change

Figure 4.10 and Figure 4.11 show the flowrate response at various points in the expansion valve section for the load increase and decrease. The plant load shown in the figures is calculated from the setpoint of the feedwater mass flowrate controller. For the load increase, the flowrates in this section also settle at their 100% steady state flowrates in roughly 25 minutes. The exception being the feedwater tank inlet, this is being controlled by the feedwater tank level controller. However, for the load decrease, the flowrates take 45 minutes to settle, taking 20 minutes longer than the load increase.

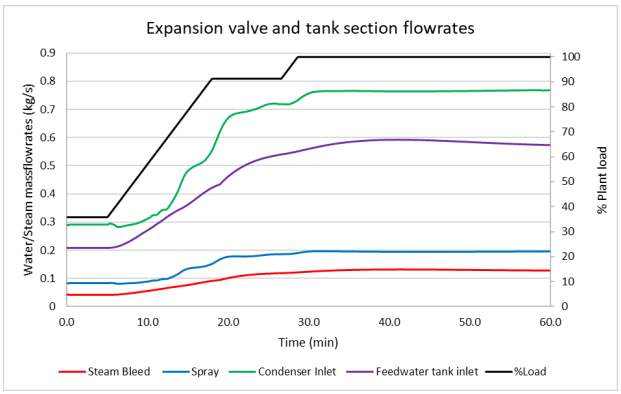

Figure 4.10 Expansion valve and tank section flowrate responses, 35%-100% conservative load change

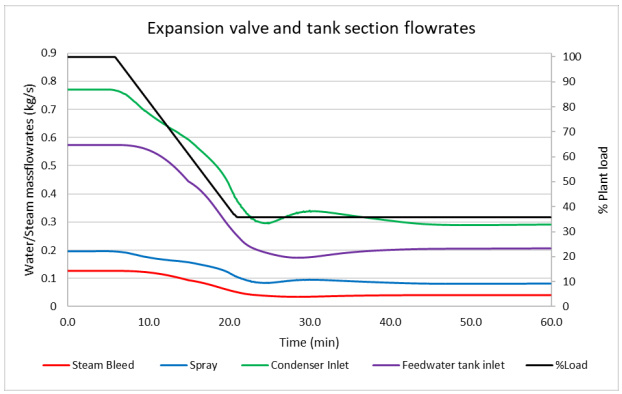

Figure 4.11 Expansion valve and tank section flowrate responses, 100%-35% conservative load change

Pressure results

Figure 4.12 and Figure 4.13 show the pressure responses in the test facility for the 35%-100% load increase and the 100%-35% load decrease.

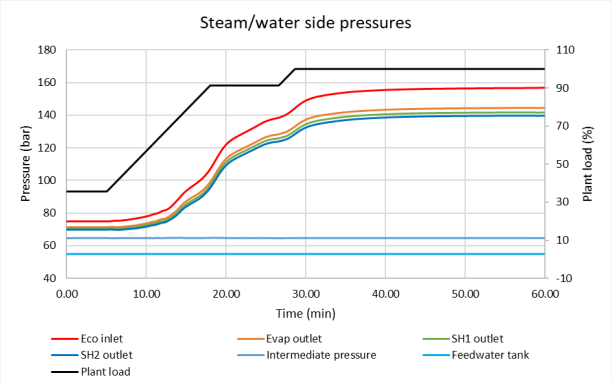

Figure 4.12 Steam/water side pressure responses, 35%-100% conservative load change

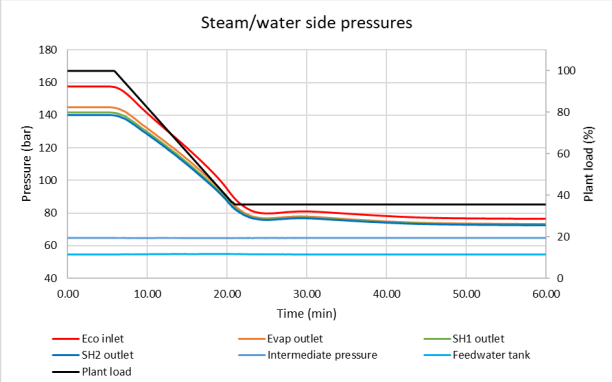

Figure 4.13 Steam/water side pressure responses, 100%-35% conservative load change

For the load increase, the pressures that are changing are almost at their 100% steady state values within 25 minutes. They then take a further 20 minutes to completely reach their 100% steady state values, this is due to the controllers. A similar response is seen when decreasing load where the pressure also takes 45 minutes to fully settle. The intermediate pressure and the feedwater tank pressure do not fluctuate while the plant load is changing load for both results. This shows that these controllers are well tuned to maintain a constant pressure. One can also see how much of a pressure drop exists over the economizer/evaporator compared to the pressure drop over the superheaters. This is primarily due to the two-phase flow in the economizer/evaporator and the difference in design between the economizer/evaporator and the superheaters.

Temperature results

Figure 4.14 and Figure 4.15 show the water/steam side temperature responses around the test facility for the 35%-100% load increase and the 100%-35% load decrease. For the load increase, all the temperatures settle after 25 minutes. While for the load decrease most of the temperatures settle in just over 15 minutes except for the temperature at the exit of superheater 1. The temperature for the condenser inlet and the economizer inlet remains constant throughout both load changes. The temperature at the outlet of superheater 2 remains relatively constant throughout the transient responses, even though the exit temperature for both the evaporator and superheater 1 are fluctuating. To have a constant superheater 2 exit temperature throughout transient conditions was part of the design requirements, and the model proves that this should be achieved. These results also show that at the 100% load the temperature increase across each

superheater is roughly 100 ℃ while at the 35% load the temperature increase over superheater 1 is almost 200 ℃ and for superheater 2 is under 100 ℃.

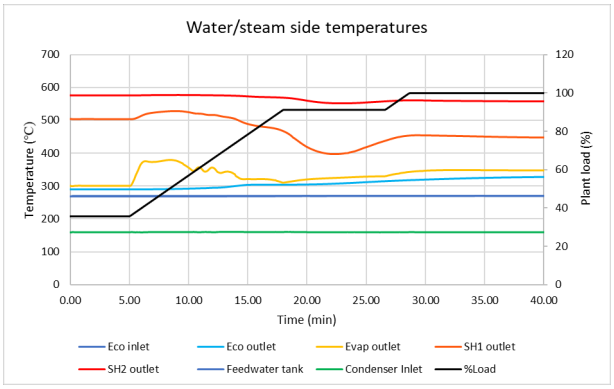

Figure 4.14 Water/steam side temperature responses, 35%-100% conservative load change

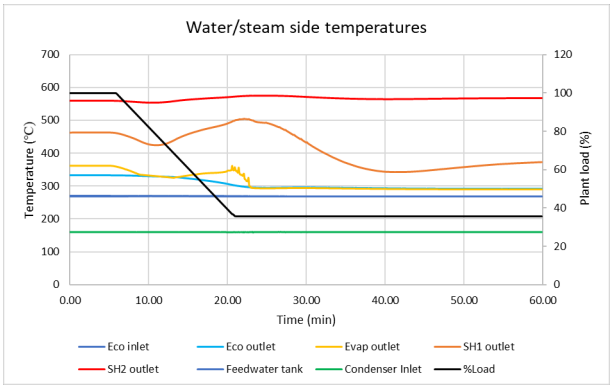

Figure 4.15 Water/steam side temperature responses, 35%-100% conservative load change

Figure 4.16 and Figure 4.17 show the salt temperature response at the outlet of the economizer for increase and decrease in plant load. This is one of the more interesting results from an operator's perspective, as it will be the lowest salt temperature in the test facility. Thus, it is important to understand its temperature response to reduce the risk of unwanted salt freezing. For the load increase, the temperature rapidly decreases about 10 minutes after the load has begun to increase. The temperature does stay above the salt's freezing point and then recovers, taking almost 60 minutes to do so. For the load decrease there is also a fluctuation in temperature, however, in this case, the temperature doesn't decrease so there would be no risk of freezing. The temperature for the decrease in load also takes around 60 minutes to stabilize.

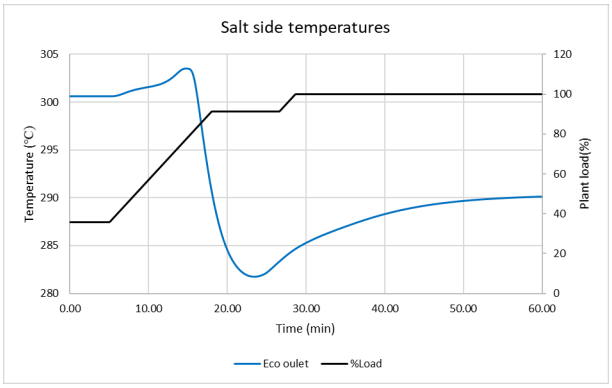

Figure 4.16 Economizer salt exit temperature response, 35%-100% conservative load change

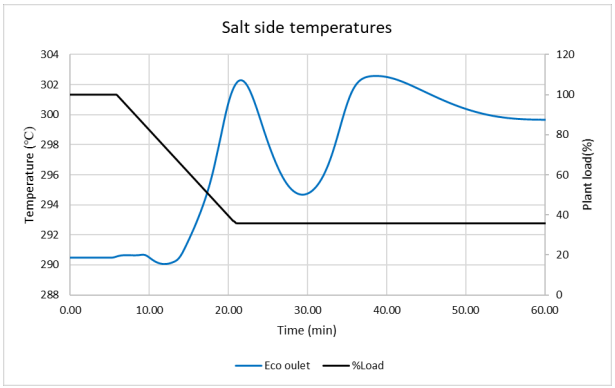

Figure 4.17 Economizer salt exit temperature response, 100%-35% conservative load change

Feedwater tank level results

Figure 4.18 and Figure 4.19 show the results for the feedwater tank level controller for the load increase and decrease.

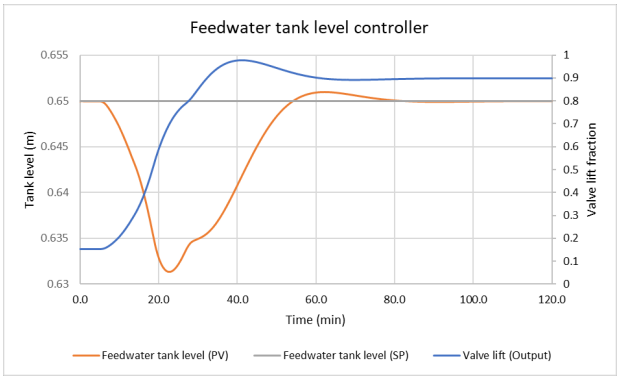

Figure 4.18 Feedwater level controller, 35%-100% conservative load change

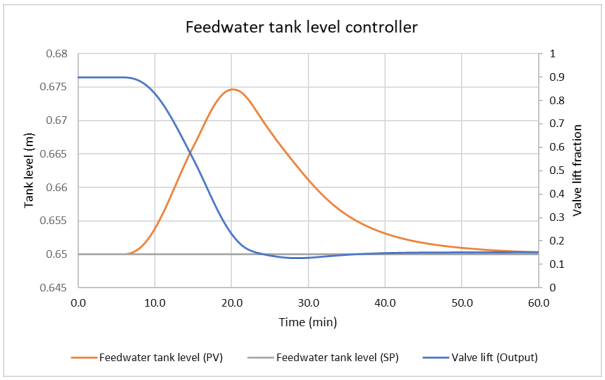

Figure 4.19 Feedwater level controller, 100%-35% conservative load change

For the load increase, the tank level decreases by 0.02 meters and when the load decreases the level increases by 0.025 meters. Both results show that the controller adjusts well to changing conditions and that the level does not fluctuate after the load has finished changing. The feedwater tank takes 75 minutes to settle when the load is increased compared to 55 minutes when the load is decreased. This is the slowest response when compared to the rest of the results around the test facility.

Evaporator steam exit quality

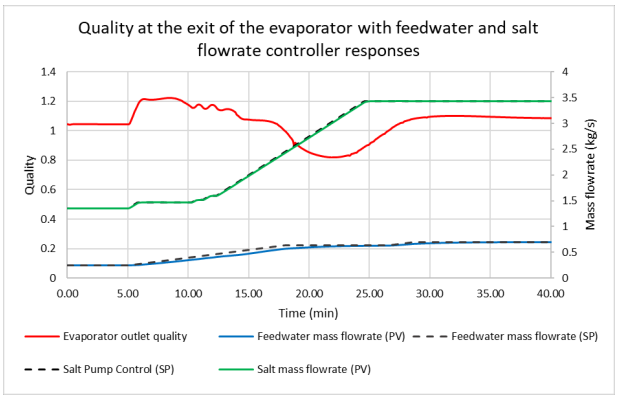

Figure 4.20 Evaporator exit quality results, 35%-100% conservative load change

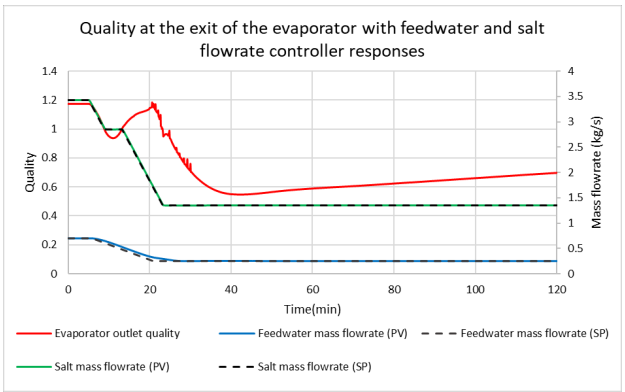

Figure 4.21 Evaporator exit quality results, 100%-35% conservative load change

As stated in the beginning of section 4.3 there is a script that tries to control the steam quality at the exit of the evaporator. Even with this script, the steam quality at the exit of the evaporator is difficult to control. This is shown in Figure 4.20 and Figure 4.21 where the steam quality at the exit of the evaporator is plotted with the setpoints and process values of the feedwater and salt mass flowrate controllers. Where the setpoints in Figure 4.20 and Figure 4.21 stop changing is the point

at which the script has stopped allowing the setpoint to change to try and control the quality. It is clear from both results that the quality fluctuates for both the load changes.

However, the response shown in Figure 4.21 when the load is decreased shows that the quality decreases to a value of 0.6. This decrease occurs after both the feedwater and the salt flowrates have stabilized. The quality then takes 350 minutes to return to a value above one. This shows that when decreasing the plant load the quality at the exit of the evaporator is more difficult to control than when increasing plant load. What is interesting is that from the other results such as the flowrate, temperature, and pressure at the exit of superheater two, it is difficult to tell that the quality at the exit of the evaporator is low. These results show that some other control method would have to be used to try and maintain the exit quality around one. For additional results for this section refer to Appendix G.

4.3.2 Transient results with separator modelled

Since the separator will perform some function if the quality at the exit of the evaporator is not carefully controlled, a basic separator was incorporated into the transient model to see the effect it would have on how the test facility increases and decreases loads. This separator is modelled using a node to model the volume of the separator and a steam trap to model the separating function. The steam trap component used in the model is set to filter out all liquid. This is a very basic model of a separator and it assumes that the separator on the test facility performs perfectly, thus only passing on steam to the superheaters with a quality equal to or greater than one. The script that tries to control the steam quality at the exit of the evaporator is still used in the model. The results presented are primarily focused on the steam generation section as the remainder of the results in the valve expansion section are not as affected by having the separator incorporated into the model. The rate of change for the setpoints in the feedwater and salt flowrate controllers is the same as section 4.3.1 for the conservative load change.

Flowrate results

Figure 4.22 and Figure 4.23 show the flowrate results for the steam generation section for the 35%-100% load increase and the 100%-35% load decrease.

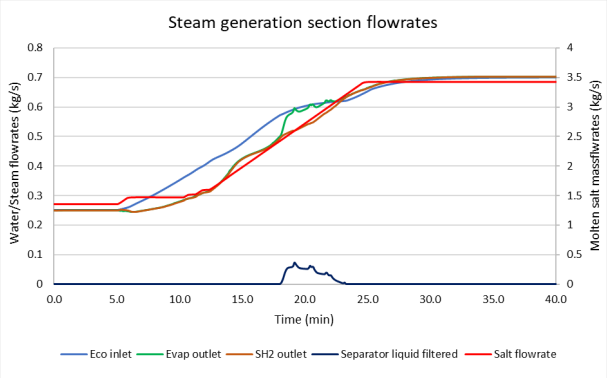

Figure 4.22 Steam generation section flowrates with separator 35%-100% load

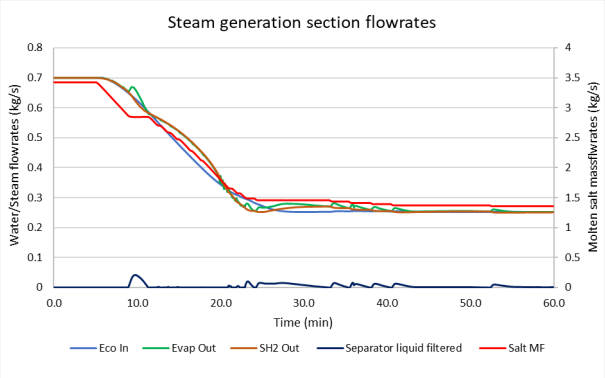

Figure 4.23 Steam generation section flowrates with separator 100%-35% load

When the load is increased, liquid is filtered by the separator for 5 minutes while when the load is decreased liquid is filtered by the separator almost continuously in small amounts. When the results for the model with the separator and without the separator (section 4.3.1) are compared the following can be concluded. For the load increase, the model with the separator reaches the 100% load two minutes faster than the model without the separator. The flowrate at the exit of superheater 2 has fewer fluctuations for the model with the separator. For the load decrease, the model with the separator reaches the 35% load 10 minutes slower. The molten salt flowrate also stops changing multiple times for the model with the separator. This coincides with all the points where the separator starts to separate fluid from the two-phase steam.

Pressure results

The pressure results are not shown as the difference between the model with the separator and without the separator are minimal. The results can be found in Appendix G.

Temperature results

Figure 4.24 and Figure 4.25 show the temperature results for various points on the test facility for the 35%-100 % load increase and the 100%-35% load decrease. When comparing the temperature results for the model with the separator shown in Figure 4.24 and Figure 4.25 with the results from the model without the separator shown in Figure 4.14 and Figure 4.15 the following can be concluded. The superheater 2 exit temperature remains relatively constant throughout the transient conditions with and without the separator. The exit temperature for superheater 1 shows significantly less fluctuation through the load changes with the separator. When decreasing load

there is no fluctuation in temperature at the exit of the evaporator when the separator is modelled. The temperature at the exit of superheater 1 stabilizes at its 35% load significantly faster than the model without the separator.

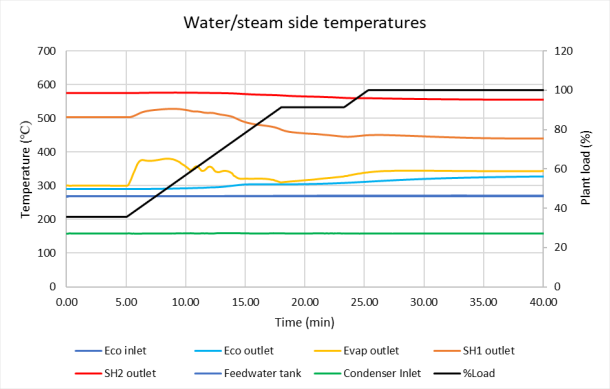

Figure 4.24 water/steam side temperatures with separator 35%-100% load

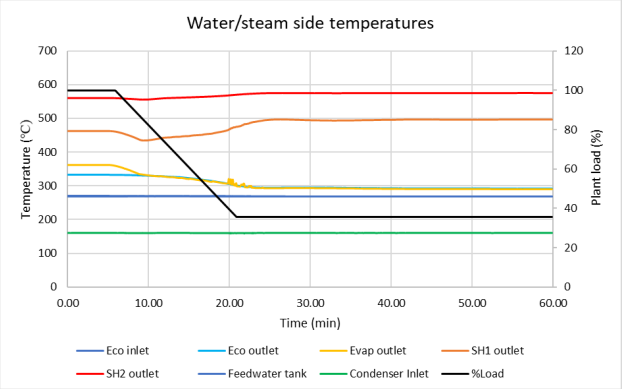

Figure 4.25 water/steam side temperatures with separator 100%-35% load

The results for the temperature of the salt at the exit of the economizer are shown in Appendix G. The separator did not have a significant effect of the salt temperature response for both the increasing load and the decreasing load. However, the amplitude in the fluctuations for the temperature shown in Figure 4.17 when the load is being decreased is less when the separator is incorporated into the model.

4.3.3 Transient results for faster load change

This section shows how the test facility may respond when the rate of load change is increased. The rate of change for the setpoints for the feedwater and salt flowrate controllers is now eight times faster than it was for the results in sections 4.3.1 and 4.3.2. Thus, the feedwater flowrate setpoint rate of change is 0.004 $^{kg/s}/_{s}$ and the salt flowrate setpoint rate of change is 0.02 $^{kg/s}/_{s}$. Thus, it takes the setpoints roughly 1.8 minutes to change from their 35% value to the 100% value. The model used for the faster load change is the same as the one used for the whole day transient results. Thus, only the separator volume is modelled and not its separating capability.

Flowrate results

Figure 4.26 and Figure 4.27 show the results for the flowrates in the steam generation section for the fast increase and decrease in load. When comparing these results to the flowrate results for the conservative load change in section 4.3.1 the amount of time it takes for the flowrates to settle is significantly less. For the increase in plant load, the flowrates settle 13 minutes faster. For the decrease in plant load, all the flowrates settle 10 minutes faster. Again, this shows that even at faster load changes the decrease in plant load takes longer than the increase in plant load. For the

decrease in plant load, the salt mass flowrate had to stop decreasing several times when compared to the conservative load change. This was to try and control the quality at the exit of the evaporator. For both the increase and decrease in plant load the magnitude in the oscillations are greater when the load in increasing faster when compared to the conservative load change.

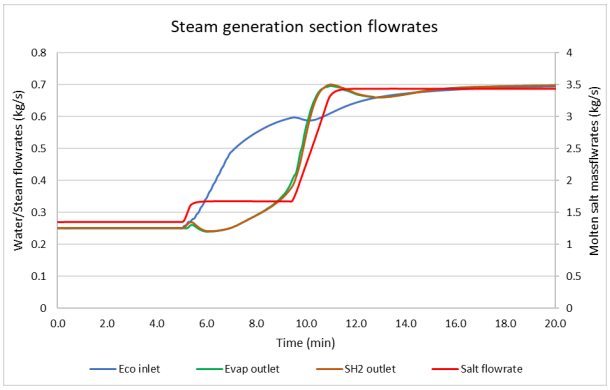

Figure 4.26 Steam generation section flowrate responses for fast load change 35%-100%

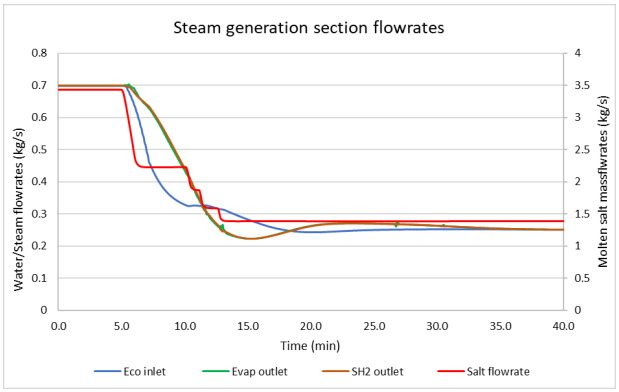

Figure 4.27 Steam generation section flowrate responses for fast load change 100%-35%

The results for the valve expansion section are not reported here but are shown in Appendix G, as the overall trends of increasing the rate of load change are the same. These being that the flowrates settle faster when the load in changed faster, but the oscillations are greater for the faster load change.

Pressure Results

The pressure results for various points around the test facility are shown in Figure 4.28 and Figure 4.29 for the load increase and the load decrease.

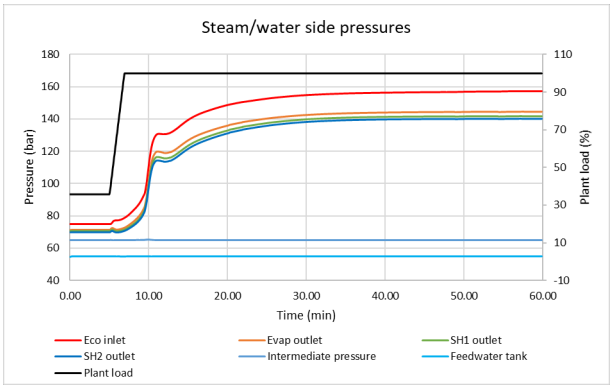

Figure 4.28 Steam/water side pressure responses for fast load change 35%-100% load

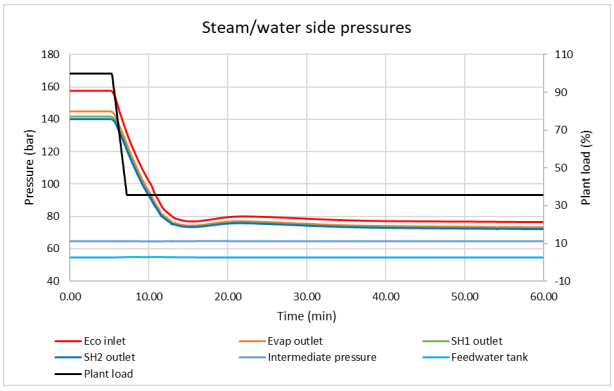

Figure 4.29 Steam/water side pressure responses for fast load change 100%-35% load

The feedwater tank pressure and the intermediate pressure remains constant throughout the faster load change. This shows that the controllers are tuned well even for much faster load changes. For the increase in load, the initial pressure increase is very rapid. However, after the 10 minute mark

the pressure then gradually increases taking 35 minutes to stabilize, which is the same time it takes for the conservative load change. The initial increase in pressure being caused by the increase in flowrate, and then the gradual increase in pressure is the superheater 2 exit pressure controller adjusting the pressure to its setpoint. For the decrease in load, the pressure takes 30 minutes to settle at their 35% steady state values compared to the 40 minutes it takes for the conservative load change.

Temperature Results

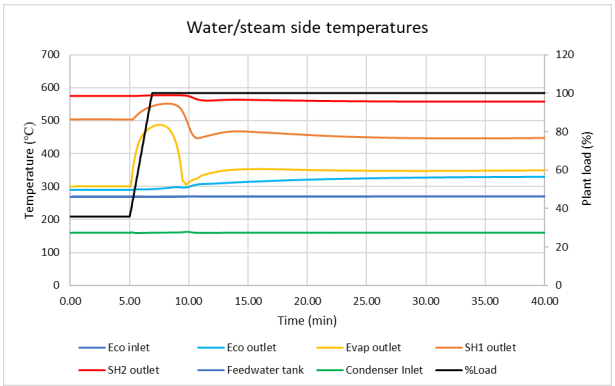

Figure 4.30 Water/steam side temperature responses for fast load change 35%-100% load

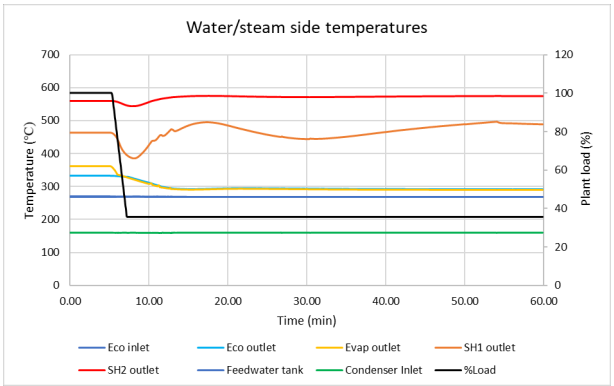

Figure 4.31 Water/steam side temperature responses for fast load change 100%-35% load

Figure 4.30 and Figure 4.31 show the results for the water and steam side temperatures for 35%-100% increase and the 100%-35% decrease in load. The major effect the faster load change is having on the temperature responses is that it is causing greater fluctuations. The most drastic example of this is the evaporator exit temperature in Figure 4.30, where its maximum peak is now 100 ℃ higher than that of the conservative load change in section 4.3.1. Even though the temperature fluctuations are greater, there is still minimal temperature fluctuations at the exit of superheater 2. For the load decrease, the temperature at the exit of the evaporator is more stable compared to the conservative load change.

The results for the salt temperature at the outlet of the economizer is not shown and reported in Appendix G. This is because of the trend for how the salt response is the same for the fast load change and the conservative load change. However, the minimum temperature reached for when the load is increased is higher for the fast load response. This is helpful to know for the operators, as it shows that increasing the rate of load change does not increase the risk of freezing in the test facility.

Feedwater tank results

Figure 4.32 and Figure 4.33 show the feedwater level controller response for the increase in load and the decrease in load.

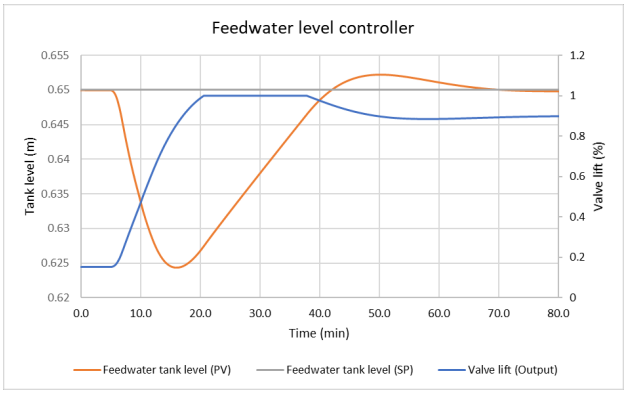

Figure 4.32 Feedwater tank level controller response for fast load change 35%-100% load

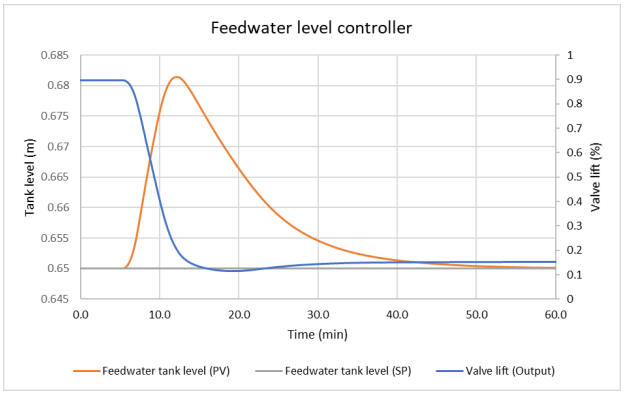

Figure 4.33 Feedwater tank level controller response for fast load change 100%-35% load

The overall trend is the same as the conservative load change where the tank level decreases when the load is increased and the tank level increases when the load is decreased. However, for the faster load change the maximum and minimum levels in the tank are greater. For the load increase, the valve reaches its maximum opening. Thus, the flowrate into the tank reached its maximum and the tank cannot fill any faster. For both cases, the controller can bring the tank level back to its setpoint.

Evaporator quality results

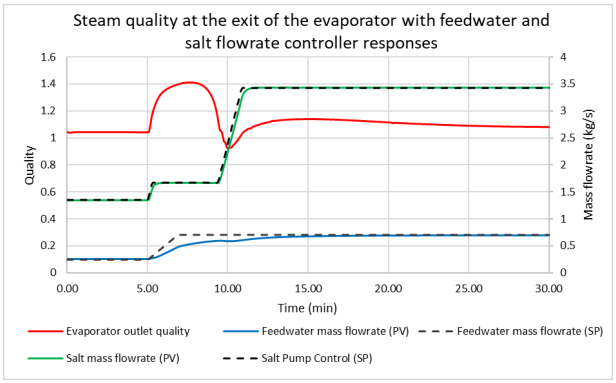

Figure 4.34 Steam quality at the exit of the evaporator for the fast load change 35%-100%

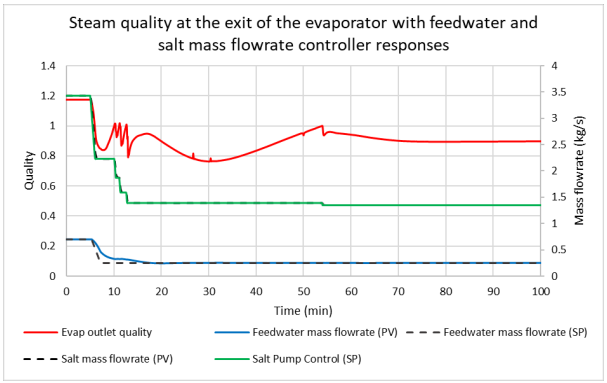

Figure 4.35 Steam quality at the exit of the evaporator for conservative load change 35%-100% load

Figure 4.34 and Figure 4.35 show the response for the quality at the exit of the evaporator with the feedwater and salt flowrate controller responses. For the load increase, the fluctuations in exit quality are greater but the period of time that two-phase steam exits the evaporator is significantly

less than the conservative load change. For the decrease in load the quality still wants to drop, however, the quality now only drops just below 0.8 when compared to the conservative load change where the quality dropped to just below 0.6. It also takes 100 minutes less for the quality to return above one when comparing the fast load change to the conservative load change.

4.3.4 Discussion on faster load change

The effects of increasing the rate of load change have been shown in the results above. However, it is important to understand what the potential limits are for the model developed. The main limit is how fast the flowrate for the feedwater and the salt flowrate through the steam generation system can change. This rate of change is ultimately defined by the script changing the setpoints, and the controllers for the feedwater and the salt flowrates. The script can theoretically change the setpoint at any defined rate. However, for the controllers there is always the same response time for the process value to reach a new setpoint, this was discussed in section 3.8.2.

This means for the salt mass flowrate controller on this model the response time is 60 seconds and for the feedwater mass flowrate controller is 8 minutes. Clearly with the way the feedwater controller is currently tuned the fastest load change would be around 8 minutes. This means that in order to get a faster load change, the controller would have to be tuned for a faster response time.

4.4 Flow distribution in the economizer/evaporator

As discussed in section 3.3, the economizer/evaporator heat exchanger has an inner and an outer coil. From the friction factor used in the model, it was expected that there would be more mass flowrate in the outer coil than the inner coil. This is due to the tighter coil radius causing a higher friction factor when compared to the outer coil. However, from the results shown in Figure 4.36, the outer coil had less mass flowrate.

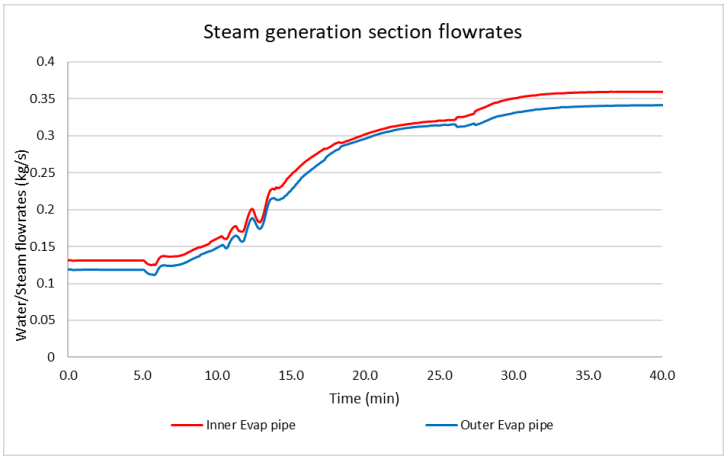

Figure 4.36 Flowrate distribution in the evaporator coils

These results were taken from the conservative load change from 35%-100% load. All the load change results also showed that the inner coil has more flowrate going through it than the outer coil. This result is not due to the friction factors but rather the total heat being transferred to each coil. The results in Figure 4.37 show that there is more heat being transferred to the outer coil than the inner coil. This is because the inner and outer coil have the same length, thus the inner coil starts before the outer coil, this was described in section 3.3. This means that the entire length of the outer coil is exposed to hotter salt than the inner coil. Due to more heat being transferred to the water, it will start to boil first in the outer coil, leading to higher frictional losses because of the higher fluid velocity in the outer coil compared to the inner coil this is shown in Figure 4.38.

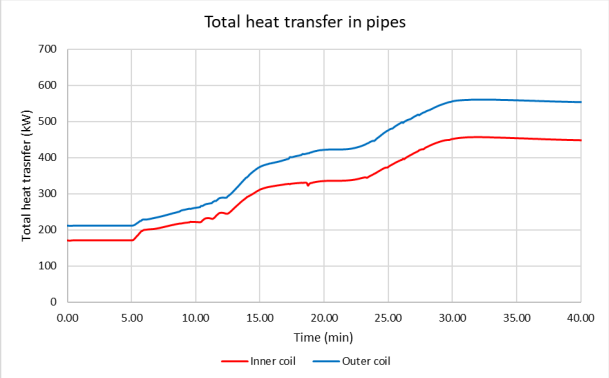

Figure 4.37 Total heat transfer for inner and outer coil

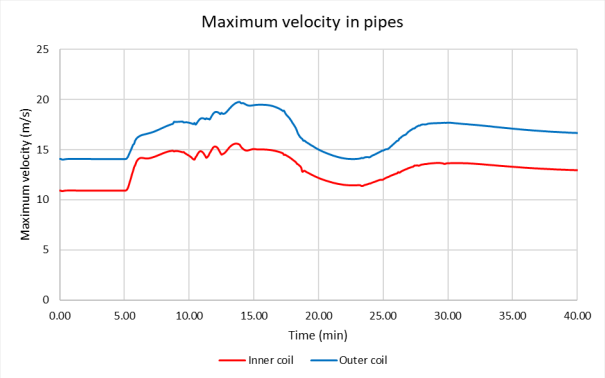

Figure 4.38 Maximum velocity in inner and outer coils

4.5 Investigating static instabilities

This section exists because of the method used when calculating the required valve lift for all the valve components and the pump speed for the hot pump for the steady state solution. This method involved starting from the steady state solution for the 100% load, as stated in section 3.12. The initial solve for the 100% load did not give the exact conditions required. This was because all the valve positions had been selected from separate parts of the model and never run together. Thus, the technique used to get a steady state result that calculated the correct conditions was to run the model in a transient simulation and let the controllers converge on their setpoints. To make sure the controllers had converged on their setpoints, the simulation was run for 2 days simulation time. This resulted in no change to any conditions, which means the transient simulation was modelling a steady state scenario, referred to in this section as a transient steady state. Then the steady state simulation was run again, thus the steady state results gave the exact conditions that were expected. This same approach was then applied to the 35% case. However, unlike the 100% load case, the 35% transient steady state results and the 35% steady state simulation results differ as shown in Table 4.4.

Table 4.4 Transient steady state results vs steady state simulation results for 35% load

Result	Transient steady state	Steady state simulation
Feedwater flowrate	0.25 kg/s	0.26 kg/s
Salt flowrate	1.35 kg/s	1.33 kg/s
Economizer inlet temperature and pressure	270.1 ℃ 74.922 bar	270.1 ℃ 74.389 bar
Superheater two exit temperature and pressure	575.9 ℃ 70.000 bar	559.8 ℃ 71.102 bar
Intermediate pressure	65.000 bar	65.983 bar
Feedwater tank temperature and pressure	270.0 ℃ 55.000 bar	270.1 ℃ 55.1259 bar
Feedwater tank level	0.650 m	0.651 m
Condenser inlet temperature	160.0 ℃	154.19 ℃

The steady state simulation results shown in Table 4.4 shows that the flowrates for the feedwater and salt differ from what was expected from the transient steady state results. What this leads to is two-phase steam exiting the evaporator and going into the superheaters. What is interesting about this result is that even though the flowrates are not at the correct operating conditions for the heat exchangers to operate as designed, the final steam conditions for the exit of superheater 2 are still close to what is required for the 35% load case.

Due to the two-phase boiling in the steam generation system, static instabilities were investigated as the cause of the problem. Static instabilities are typically caused by multiple intersections of the system pressure drop curve and the pump pressure rise curve, as shown in Figure 4.39. What this means is that for the given system there are multiple operating points. In the case of Figure 4.39, the ΔP external would be the pump pressure rise curve and the curve with the "N-shape" is the system pressure drop curve. Having instability problems at low load is consistent with literature from K. Farhadi [62] and M. Colombo et al. [63] due to the lower pressure in the system.

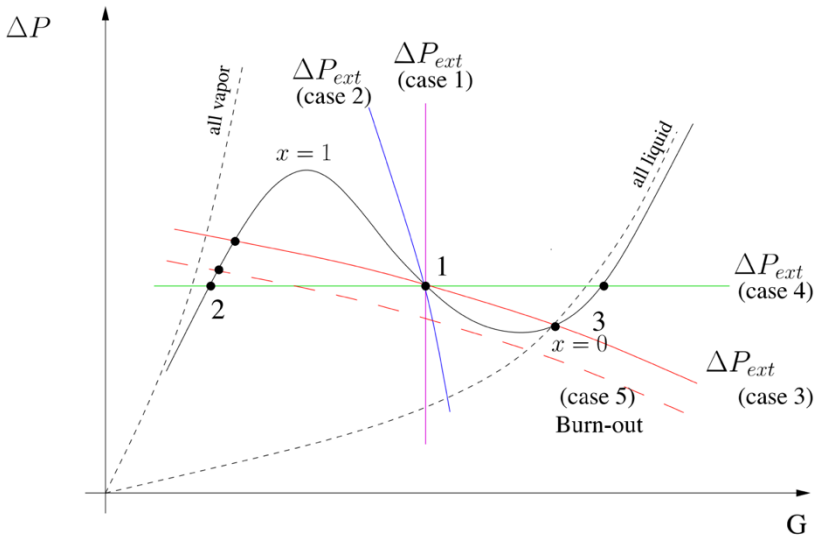

Figure 4.39 Pressure drop vs flow rate curve for a boiling channel [58]

4.5.1 Water/steam side investigation

Static instabilities were investigated on the water/steam side by running a sensitivity analysis. The salt side flowrate was fixed at the expected operating condition defined in section 4.1 at 1.35 kg/s. The feedwater flowrate was then increased from 0.15 kg/s to 0.35 kg/s in increments of 0.002 kg/s, while the system pressure drop was plotted. The system pressure drop is made up of the pressure drop through the economizer/evaporator, the superheaters, and the valve sections. The pressure rise from the pump is plotted against the feedwater flowrate. The results of the sensitivity analysis are shown in Figure 4.40.

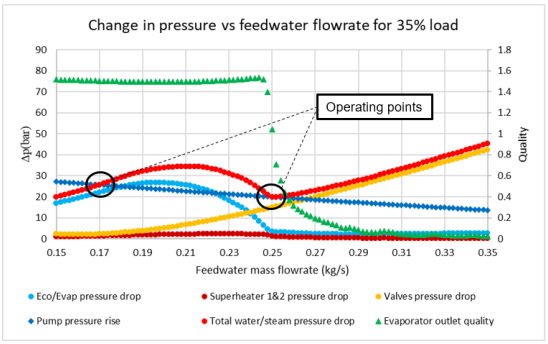

Figure 4.40 Static instability sensitivity analysis for the water/steam side at 35% load

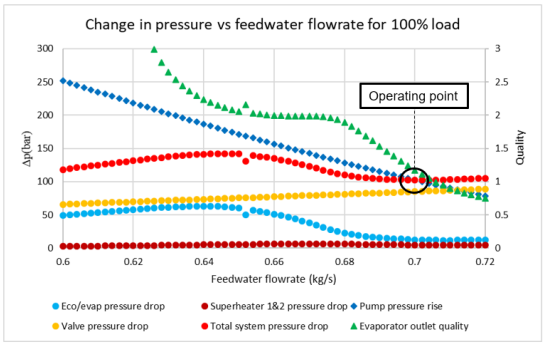

Figure 4.41 Static instability sensitivity analysis for the water/steam side at 100% load

From the results shown in Figure 4.40, there are two points where the pressure rise from the pump can intersect with the pressure drop through the system. Thus, there are potentially two operating points. With the second operating point being the operating point required. However, when comparing the feedwater flowrate of the first operating point shown in Figure 4.40 being 0.17 kg/s, the flowrate doesn't match the flowrate calculated by the steady state simulation in Table 4.4 being 0.257 kg/s. Thus, this potential first operating point is not the source of the problem described. What can also be seen from Figure 4.40 is that the evaporator exit quality drops quickly from superheated conditions to two-phase conditions around the required feedwater mass flowrate. This response is not present in the 100% load case which is shown in Figure 4.41. This indicates that for lower loads the boiling conditions around the required mass flowrates are very sensitive to operating conditions.

The same sensitivity analysis was run again with the salt mass flowrate not fixed but rather governed by the fixed pump speed. This pump speed was determined from the long steady state transient simulation and therefore should give the expected salt mass flowrate when the feedwater mass flowrate 0.25 kg/s.

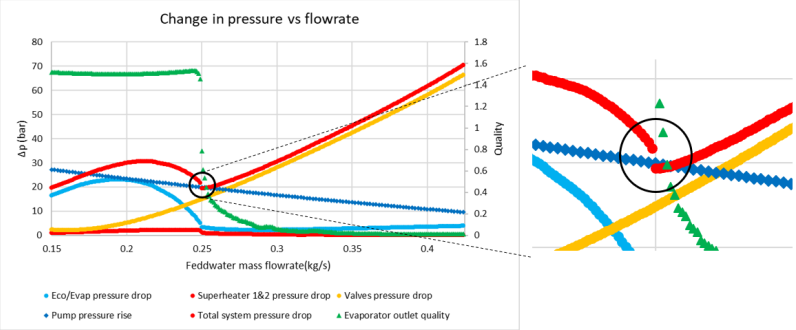

Figure 4.42 Static instability sensitivity analysis for the water/steam side at 35% load with fixed hot tank pump speed

From the results shown in Figure 4.42, there are again two possible operating points. However, the second operating point is not the exact one required as feedwater mass flowrate is now calculated at just above 0.25 kg/s. There is also a discontinuity in the results shown in the right hand zoomed image in Figure 4.42. The discontinuity also exists in the salt mass flowrate as shown in Figure 4.43, which shows the same sensitivity analysis but with the salt mass flowrate reported.

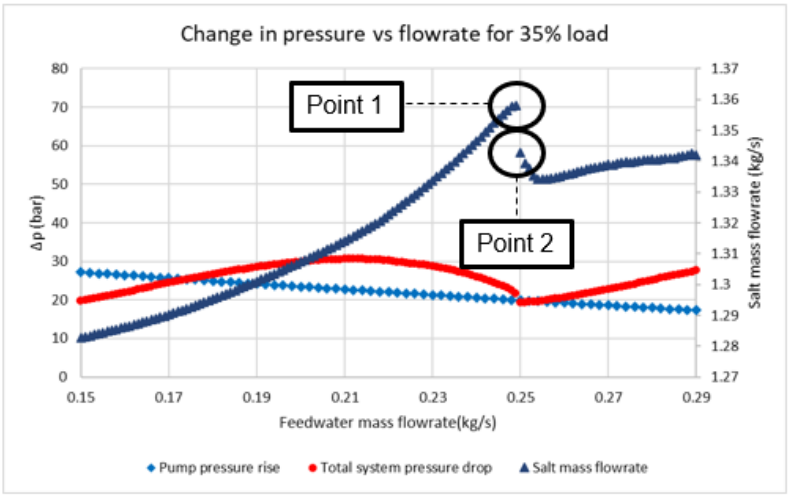

Figure 4.43 Static instability analysis for the water/steam side at 35% load showing salt flowrate

This discontinuity is caused by not having a fixed salt mass flowrate through the system, therefore in the section below the salt side is investigated.

4.5.2 Salt side investigation

The pressure drop characteristics for the salt side were investigated by conducting a sensitivity analysis shown in Figure 4.44 where the salt mass flowrate is increased from 1.25 kg/s to 1.45 kg/s in increments of 0.002 kg/s. The feedwater mass flowrate is fixed at its expected operating condition of 0.25 kg/s. The salt system pressure drop and the salt pump pressure rise are plotted. The hot tank pump speed is fixed on the value calculated by the controller when running the long transient steady state simulation.

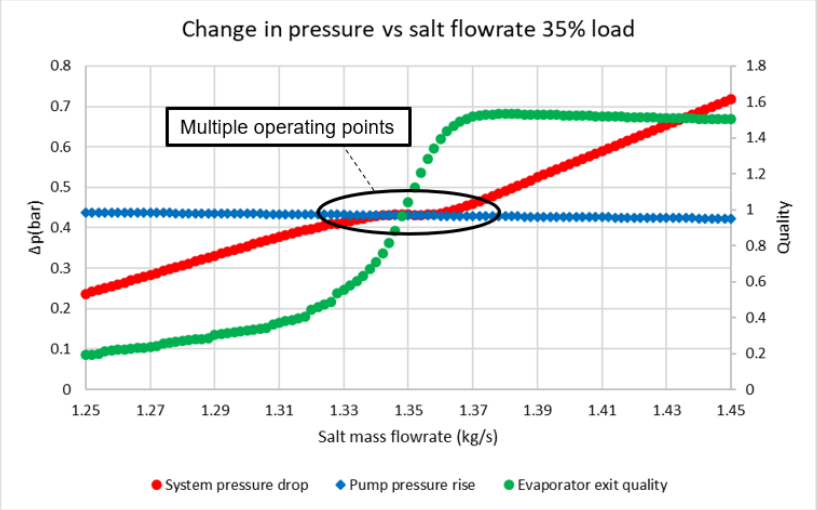

Figure 4.44 Static instability analysis for the salt side at 35% load with fixed feedwater mass flowrate at 0.25 kg/s

From the results shown in Figure 4.44, there are potentially multiple operating points. This appears to be the source of the discontinuity shown in Figure 4.43, which can be described using Figure 4.45 and Figure 4.46. Figure 4.45 shows that the operating point for the salt mass flowrate with the feedwater mass flowrate at 0.249 kg/s is 1.358 kg/s, which correlates to the salt mass flowrate shown at point 1 in Figure 4.43. Figure 4.46 shows that the operating point for the salt mass flowrate with the feedwater mass flowrate at 0.25 kg/s is 1.342 kg/s, which correlates to the salt mass flowrate shown at point 2 in Figure 4.43. Thus, this shows why the discontinuity exists in Figure 4.43. The operating point on the left is first in the region where there are multiple operating conditions.

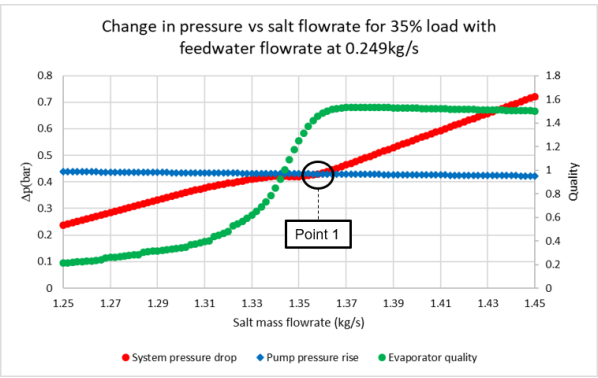

Figure 4.45 Static instability analysis for the salt side at 35% load with fixed feedwater mass flowrate at 0.249 kg/s

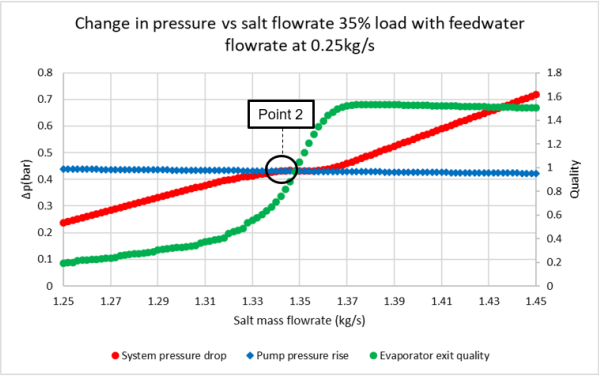

Figure 4.46 Static instability analysis for the salt side at 35% load with fixed feedwater mass flowrate at 0.25 kg/s

The original problem of the transient steady state results not matching the steady state simulation results can now be described. The required feedwater and salt mass flowrate is 0.25 kg/s and 1.35 kg/s to meet the requirements for the 35% load. However, when the steady state solution is solved

there are multiple operating points for the salt side. Therefore, the solution for the salt mass flowrate will converge around point two shown in Figure 4.46. However, having a different salt mass flowrate, the water/steam side of the system no longer converges on the flowrate of 0.25 kg/s and starts to converge on 0.2579 kg/s. This means that the salt side now converges on the salt mass flowrate of 1.332 kg/s as shown in Figure 4.47. This is the cause of the steady state simulation results differing from the transient steady state results. Thus, in the transient simulation, the controllers can maintain the required feedwater and salt flowrates of 0.25 kg/s and 1.35 kg/s respectively. However, during the steady state simulation due to the multiple operating points on the salt side the solver converges on different operating conditions that are not the required ones.

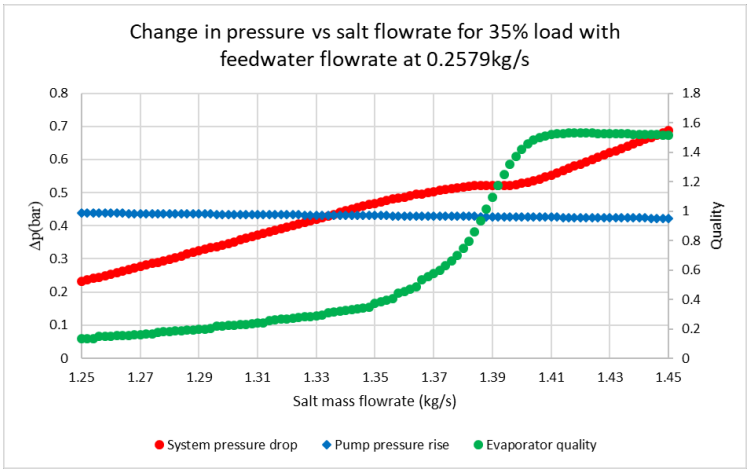

Figure 4.47 Static instability analysis for the salt side at 35% load with fixed feedwater mass flowrate at 0.2579 kg/s

4.5.3 Source of the salt side pressure drop characteristics

Figure 4.48 shows the results of Figure 4.44 on a different scale. This shows the salt side system pressure drop curve looks like the “N-shape” of a boiling system pressure drop curve.

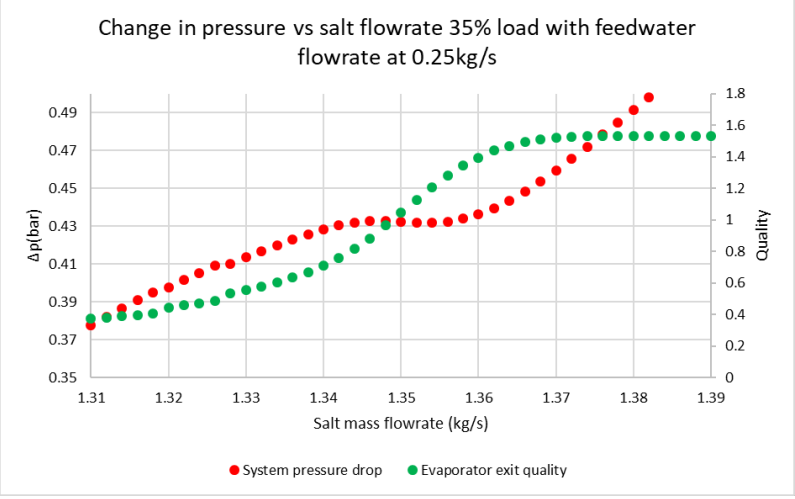

Figure 4.48 Figure 4.44 on a different scale

The molten salt does not change phase in heat exchangers. Thus, this result is not expected as this type of response is only expected to be seen in a two-phase boiling channel. The evaporator exit quality curve shows that the "N-shape" occurs when the quality is increasing rapidly. Thus, there is an interaction between the water/steam side and the salt side when the quality is changing rapidly that is leading to this phenomenon.

There are two main components on the salt side that lead to the pressure drop in the system. The flow resistance component that is used to model the shell side of the heat exchangers and the pipe component that is used to model the pipe networks between components. The pressure drop through each component was analysed to identify which component(s) was responsible for the decrease in pressure drop. Figure 4.49 shows how the salt side is split into eight components. The pressure drop results for each component is shown in Figure 4.50.

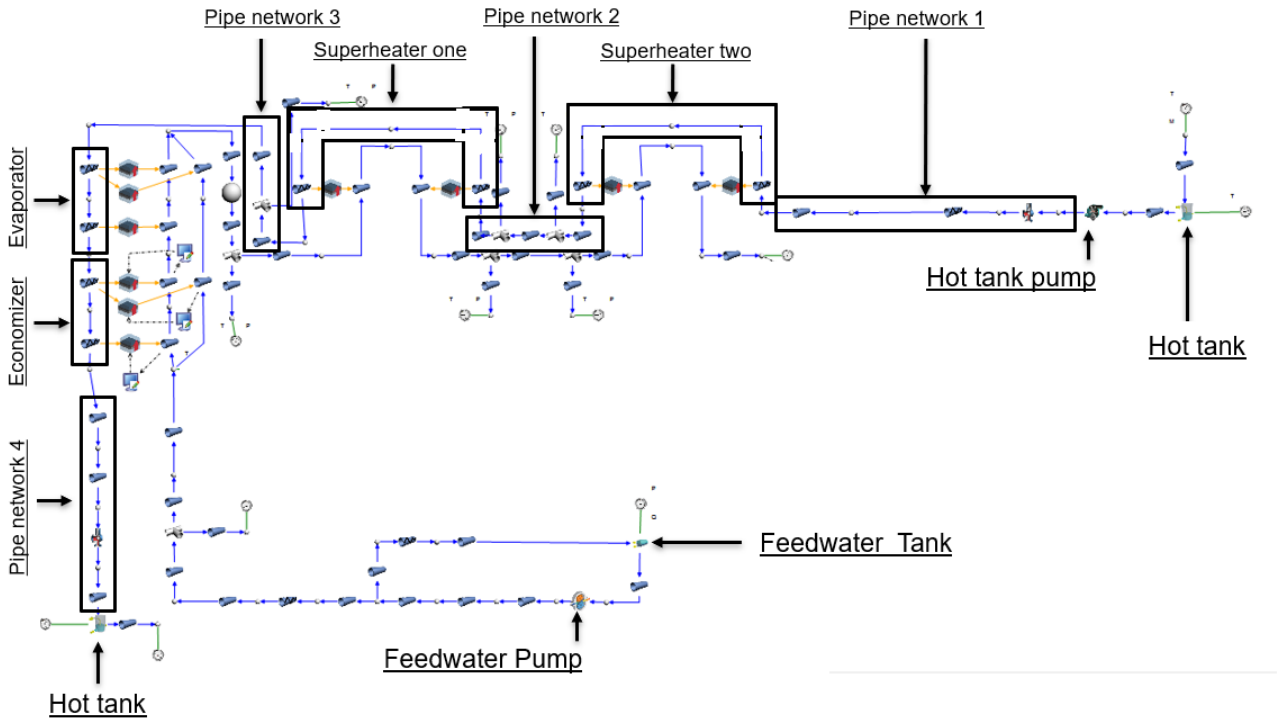

Figure 4.49 Components in the salt side of the steam generation section

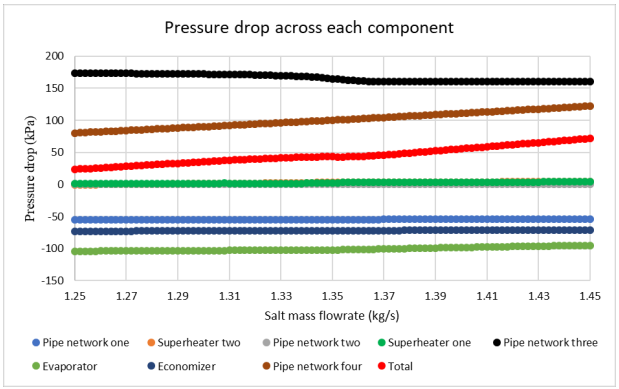

Figure 4.50 Pressure drop across each component on the salt side

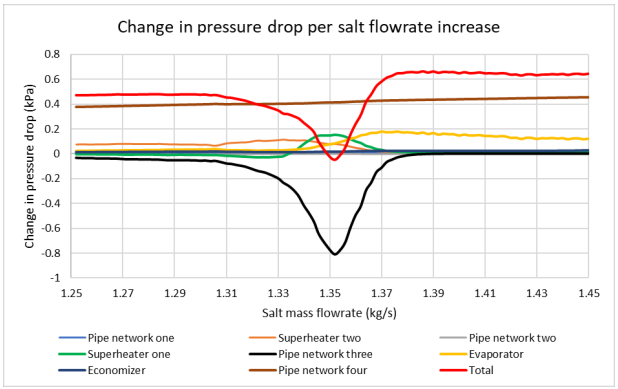

Figure 4.51 Change in pressure drop per salt flowrate increase

It is difficult to see the "N-shape" in Figure 4.50, due to the scale of the pressure drop axis. Figure 4.51 shows the pressure drop results for each component by looking at how much the pressure drop was changing per increase in salt mass flowrate. Pipe network three was identified as the source of the "N-shape" curve because in Figure 4.50 it was the only curve to have a negative slope and from 4.53 it has the largest contribution to the change in pressure drop.

The pressure drop equation for the pipe component consists of a frictional and elevation pressure drop components. Figure 4.52 and Figure 4.53 show that it's the contribution from the elevation pressure drop that is decreasing the pressure drop in the pipe component. Secondly, the elevation pressure loss is decreasing more rapidly when the steam quality at the exit of the evaporator is increasing rapidly show in Figure 4.53.

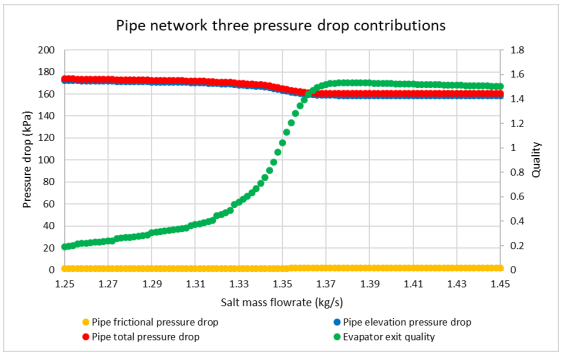

Figure 4.52 Pipe network three pressure drop contributions

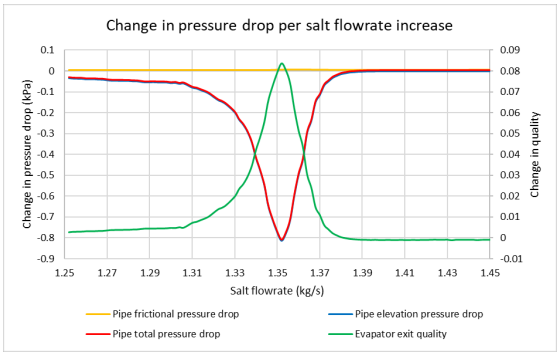

Figure 4.53 Change in pressure drop contributions per salt flowrate increase

Figure 4.54 shows that the decrease in elevation pressure drop is due to the salt density in the pipe decreasing. This is the only property that can affect the elevation pressure drop as the gravitational acceleration, and the change in height remains unchanged.

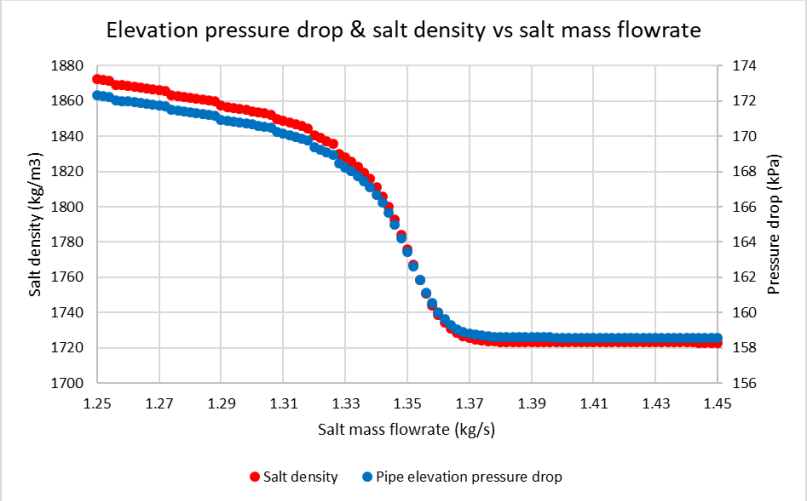

Figure 4.54 Elevation pressure drop & salt density vs salt flowrate for pipe network three

The density of the salt is only dependent on temperature, and the temperature of the salt is dependent on how much heat transfer has occurred in the superheaters before pipe network three. This relationship is shown in Figure 4.55.

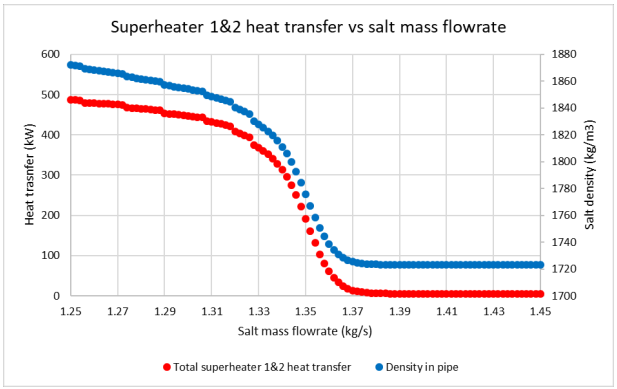

Figure 4.55 Superheater 1&2 total heat transfer vs salt mass flowrate with density change

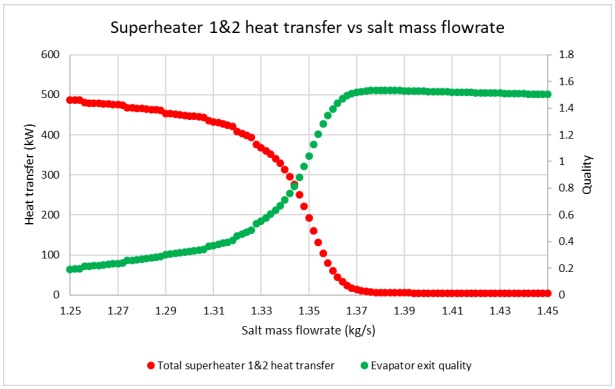

Figure 4.56 Superheater 1&2 total heat transfer vs salt mass flowrate with evaporator exit quality

Figure 4.55 shows that when there is a large amount of heat transfer in the superheaters the density of the salt in pipe network three is high leading to a high pressure drop due to elevation. Figure 4.55 also shows when the heat transfer decreases the density decreases. Figure 4.56 shows the relationship between total heat transfer in superheater 1&2 to the steam quality at the exit of the evaporator. From Figure 4.56 it is shown that when there is low quality two-phase steam entering the superheaters the heat transfer in the superheaters is high and as the quality increases the heat transfer in the superheaters decreases. This is due to the two-phase heat transfer being higher than the single-phase heat transfer. However, the heat transfer is still rapidly decreasing after the steam quality at the exit of the evaporator is greater than one. This can then only be due to the temperature difference between the salt and the steam decreasing rapidly.

Thus, the cause of the decrease in pressure drop has been identified as the rapid decrease in heat transfer in the superheaters due to the rapid increase in the quality of the steam exiting the evaporator. Therefore, the cause of the "N-shape" curve in the pressure drop on the salt side is due to the rapidly changing boiling conditions in the economizer/evaporator for the 35% load conditions.

4.5.4 Separator influence

It is important to note that the results shown in section 4.5 do not consider the effect that the separator will have. Unfortunately incorporating the separator into the steady state model has not been achieved due to steady state solving issues. Thus, the results shown where the evaporator exit quality is below one may not be valid on the real test facility. However, Figure 4.57 shows the results where the quality at the exit of the evaporator is greater than one, these results would not change if the separator is used. These results show that there are still multiple operating points. This is still due to the change in density in pipe network three, which is changing rapidly due to the rapidly changing boiling conditions which occurs at the 35% load conditions.

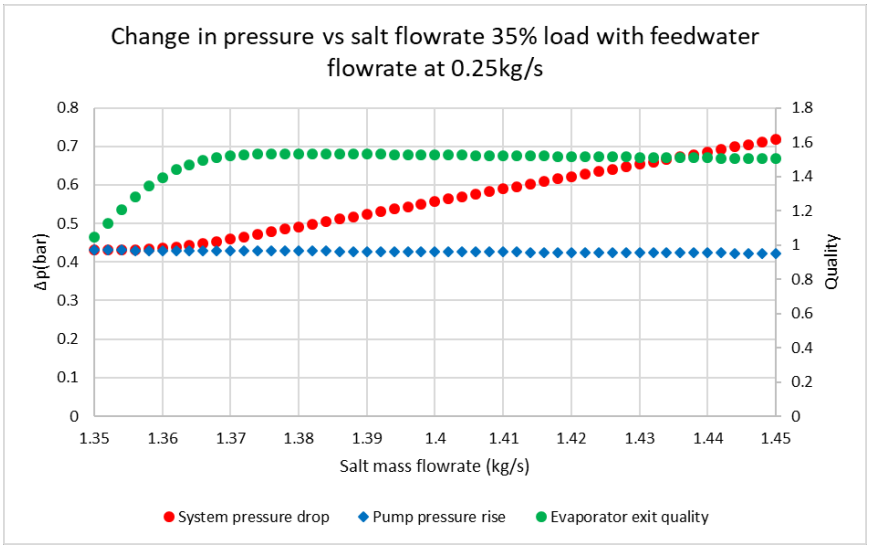

Figure 4.57 Static instability analysis for the salt side at 35% load with fixed feedwater mass flowrate at 0.25 kg/s

5. Summary, conclusions and recommendations

5.1 Summary

The main outcome for this project was to develop a dynamic process model that can model the transient responses of the HPS2 steam cycle. Thus, in order to achieve this outcome, the project entailed the following work:

- A comprehensive literature review of CSP technology, dynamic modelling techniques used in similar systems, characteristics of unique components in the test facility and two-phase instabilities.
- Modelling the water/steam cycle and TES system with the software Flownex, which included the heat exchangers, valve expansion section, controllers, feedwater and salt tanks, and the pumps around the test facility.
- Validating the heat exchanger models against the expected results from the design data.
- Adjusting the expected operating conditions for the salt mass flowrate through the steam generation system to achieve the desired operating requirements.
- Tuning the controllers by performing bump tests and verifying the controller tuning.
- Conducting sensitivity analysis to determine new operating conditions for the salt mass flowrate through the steam generation system when a different salt compound is used.
- Conducting full day simulations with the complete model where transient solar data was entered to simulate sunny and cloudy weather conditions.
- Conducting transient simulations where the load was increased and decreased at different rates.
- Investigating the flow distribution found in the economizer and evaporator.
- Investigating the potential of static instabilities occurring in the steam generation system.

5.2 Conclusions

From the results obtained the following conclusions may be drawn:

- The location of the boiling point is sensitive to the operating conditions and this sensitivity increases at lower loads.
- The steam cycle has stable operating conditions throughout strong solar transient conditions, due to the solar field not being directly connected to the steam cycle.

- The salt temperature at the exit of the evaporator decreases rapidly when the plant load is increased. Plant operators will need to be aware of this response as it's the location where the salt will be at its lowest temperature.
- The quality at the exit of the evaporator is hard to control and has a long recovery time, thus careful operating procedures will have to be implemented on the test facility.
- Due to the difficulty associated with controlling the quality at the exit of the evaporator, the separator may still need to separate fluid after start up conditions when changing loads.
- It will be possible to control the intermediate pressure and the feedwater tank pressure at a constant pressure throughout all transient responses.
- The final exit temperature of superheater 2 remains relatively constant throughout all transient responses, meeting the design requirements.
- Faster load changes result in greater fluctuations in the flowrate, temperature, and pressures around the test facility.
- There is more mass flowrate going through the inner coil than the outer coil in the economizer/evaporator. This disagrees with what is expected, however it was determined that this is due to more heat transfer occurring in the outer coil.
- The potential of a static instability was found for the low load case of 35%. The instability was due to the pressure drop characteristics on the salt side which is an unexpected result.
- The salt side pressure drop characteristics were a result of heat transfer between the steam and the salt being influenced by the steam side conditions.

To conclude the model developed can show the steady state and dynamic responses that the steam cycle in the HPS2 test facility may undergo. This can show the operators what to expect when operating the test facility for the first time. In addition to this, the model can be used for various other case studies that have not been presented in this project, such as temperature fluctuations in the hot tank, different operating strategies and different control tuning etc.

5.3 Recommendations and further model development

It is recommended that the two-phase helical coil pressure drop correlation developed by Colombo et al. [57] be incorporated into the model for the economizer/evaporator. This would lead to even more accurate pressure drop results through this component.

The second recommendation is to model the thermal insulation around the pipes and heat exchangers of the test facility. The main contribution that this would have is that there would be more thermal inertia modelled for transient results.

The third and most important recommendation would be to find a better way to control the quality at the exit of the evaporator. This would help the operators on the real test facility to adopt the same control strategy to limit any risk of two-phase steam reaching the superheaters.

The final recommendation is to model the separator for steady state results. This would lead to more accurate results when running steady state sensitivity analysis where the quality at the exit of the evaporator is below one.

6. List of references

[1] T. Bischof-Niemz, “Statistics of utility-scale solar PV , wind and CSP in South Africa in 2016 CSIR Energy Centre South Africa ’ s Renewable Energy Independent Power Producer Procurement Programme (REIPPPP) started in 2011,” no. April. 2017.

[2] A. Cuellar, “CSP Market Status.” Mott Macdonald, 2017.

[3] A. Castillo and D. F. Gayme, “Grid-scale energy storage applications in renewable energy integration: A survey,” *Energy Convers. Manag.*, vol. 87, pp. 885–894, 2014.

[4] A. S. Pidaparthi, E. P. Dall, J. E. Hoffmann, and F. Dinter, “CSP parabolic trough and power tower performance analysis through the Southern African universities radiometric network (SAURAN) data,” *AIP Conf. Proc.*, vol. 1734, no. May, 2016.

[5] Solar Cell Central, “Concentrated Solar Power.” [Online]. Available: http://solarcellcentral.com/csp_page.html. [Accessed: 23-Jan-2017].

[6] US department of energy, “CSP Systems Analysis.” .

[7] US department of energy, “Linear Concentrator Solar Power Plant Illustration.” .

[8] J. Pacio, C. Singer, T. Wetzel, and R. Uhlig, “Thermodynamic evaluation of liquid metals as heat transfer fluids in concentrated solar power plants,” *Appl. Therm. Eng.*, vol. 60, no. 1–2, pp. 295–302, 2013.

[9] C. K. Ho, “Advances in central receivers for concentrating solar applications,” *Sol. Energy*, vol. 152, pp. 38–56, 2017.

[10] Sargent & Lundy, “Assessment of Parabolic Trough and Power Tower Solar Technology Cost and Performance Forecasts Assessment of Parabolic Trough and Power Tower Solar Technology Cost and Performance Forecasts,” *Rep. No. NREL/SR-550-34440*, no. October, p. 47, 2003.

[11] Solar Energy Industries Association, “Concentrating Solar Power.” [Online]. Available: http://www.seia.org/policy/solar-technology/concentrating-solar-power. [Accessed: 23-Jan-2017].

[12] W. A. K. Al-Maliki, F. Alobaid, R. Starkloff, V. Kez, and B. Epple, “Investigation on the dynamic behaviour of a parabolic trough power plant during strongly cloudy days,” *Appl. Therm. Eng.*, vol. 99, pp. 114–132, 2016.

[13] S. Kuravi, J. Trahan, D. Y. Goswami, M. M. Rahman, and E. K. Stefanakos, “Thermal energy storage technologies and systems for concentrating solar power plants,” *Prog. Energy Combust. Sci.*, vol. 39, no. 4, pp. 285–319, 2013.

[14] S. Millennium, “The parabolic trough power plants Andasol 1 to 3,” *Tech. Sol. Millenn. AG*, pp. 1–26, 2008.

[15] Y. Wang, “Parabolic Trough Power Plant.” [Online]. Available: https://www.mtholyoke.edu/~wang30y/csp/PTPP.html. [Accessed: 24-Jan-2017].

[16] SQM, “Thermo-Solar Salts.” .

[17] J. Deign, “The Trouble with dish stirling CSP.” [Online]. Available: http://analysis.newenergyupdate.com/csp-today/technology/trouble-dish-stirling-csp. [Accessed: 24-Jan-2017].

[18] “Solar Euromed,” 2014. [Online]. Available: http://www.solareuromed.com/en/miroirs-de-fresnel. [Accessed: 24-Jan-2017].

[19] Frenell, “Solar Power on Demand.” pp. 1–66, 2016.

[20] S. Kuravi *et al.*, “Thermal Energy Storage for Concentrating Solar Power Plants,” *Technol. Innov.*, vol. 14, no. 2, pp. 81–91, 2012.

[21] Z. Ravaghi-Ardebili, F. Manenti, N. M. N. Lima, and L. Zuniga, “Study of Direct Thermal Energy Storage Technologies for Effectiveness of Concentrating Solar Power Plants,” *Chem. Eng. Trans.*, vol. 32, pp. 1219–1224, 2013.

[22] X. Xu, K. Vignarooban, B. Xu, K. Hsu, and A. M. Kannan, “Prospects and problems of concentrating solar power technologies for power generation in the desert regions,” *Renew. Sustain. Energy Rev.*, vol. 53, no. January, pp. 1106–1131, 2016.

[23] E. Hakkarainen, T. Sihvonen, and J. Lappalainen, “Dynamic simulation of two concentrated solar power concepts with supercritical CO 2 Brayton cycle,” no. October, 2016.

[24] A. Maccari *et al.*, “Archimede Solar Energy Molten Salt Parabolic Trough Demo Plant: A Step Ahead towards the New Frontiers of CSP,” *Energy Procedia*, vol. 69, no. May 2015, pp. 1643–1651, 2015.

[25] C. Corporation, “Concentrated Solar Power (CSP),” 2017. [Online]. Available: https://www.chiyodacorp.com/en/service/solar-energy/. [Accessed: 29-Jun-2018].

[26] A. Maccari *et al.*, “Archimede Solar Energy Molten Salt Parabolic Trough Demo Plant: A Step Ahead towards the New Frontiers of CSP,” *Energy Procedia*, vol. 69, pp. 1643–1651, 2015.

[27] E. Hakkarainen and L. Kannari, “Dynamic Modelling of Concentrated Solar Field for Thermal Energy Storage Integration,” no. August, 2016.

[28] E. Hakkarainen and M. Tahtinen, “Dynamic modelling and simulation of linear Fresnel solar field model based on molten salt heat transfer fluid,” *AIP Conf. Proc.*, vol. 1734, 2016.

[29] A. G. Fernández, S. Ushak, H. Galleguillos, and F. J. Pérez, “Development of new molten salts with LiNO3 and Ca(NO3)2 for energy storage in CSP plants,” *Appl. Energy*, vol. 119, no. 3, pp. 131–140, 2014.

[30] C. Parrado, A. Marzo, E. Fuentealba, and A. G. Fernández, “2050 LCOE improvement using new molten salts for thermal energy storage in CSP plants,” *Renew. Sustain. Energy Rev.*, vol. 57, pp. 505–514, 2016.

[31] L. Migliari, S. Arena, P. Puddu, and D. Cocco, “Thermo-fluid Dynamic Analysis of a CSP Solar Field Line During Transient Operation,” *Energy Procedia*, vol. 101, no. September, pp. 1167–1174, 2016.

[32] K. M. Powell and T. F. Edgar, “Modeling and control of a solar thermal power plant with thermal energy storage,” *Chem. Eng. Sci.*, vol. 71, pp. 138–145, 2012.

[33] J. P. Rubén M. Montañés*, Johan Windahl° and Marcus Thern¤, “Dynamic Modeling of a Parabolic Trough Solar Thermal Power Plant With Thermal Storage Using Modelica,” vol. 1, 2015.

[34] F. Zaversky, J. García-Barberena, M. Sánchez, and D. Astrain, “Transient molten salt two-tank thermal storage modeling for CSP performance simulations,” *Sol. Energy*, vol. 93, pp. 294–311, 2013.

[35] C. Suárez, A. Iranzo, F. J. Pino, and J. Guerra, “Transient analysis of the cooling process of molten salt thermal storage tanks due to standby heat loss,” *Appl. Energy*, vol. 142, pp. 56–65, 2015.

[36] I. Rodríguez, C. D. Pérez-Segarra, O. Lehmkuhl, and A. Oliva, “Modular object-oriented methodology for the resolution of molten salt storage tanks for CSP plants,” *Appl. Energy*, vol. 109, pp. 402–414, 2013.

[37] A. Rovira, M. J. Montes, M. Valdes, and J. M. Martínez-Val, “Energy management in solar thermal power plants with double thermal storage system and subdivided solar field,” *Appl. Energy*, vol. 88, no. 11, pp. 4055–4066, 2011.

[38] S. Torras, C. D. Pérez-Segarra, I. Rodríguez, J. Rigola, and A. Oliva, “Parametric Study of Two-tank TES Systems for CSP Plants,” *Energy Procedia*, vol. 69, pp. 1049–1058, 2015.

[39] C. Cilliers, “Thermal-fluid simulation of nuclear steam generator performance,” North-West University, 2012.

[40] G. Botha, “Transient modelling of the flow and heat transfer in a once through helical coil steam generator tube for a Small Modular PWR,” North-West University, 2016.

[41] N. V. Hoffer, P. Sabharwall, and N. Anderson, “Modeling a Helical-coil Steam Generator in RELAP5-3D for the Next Generation Nuclear Plant,” no. January, pp. 1–53, 2011.

[42] J. S. Jayakumar, “Helically Coiled Heat Exchangers.pdf,” *Heat Exch. - Basics Des. Appl.*, 2012.

[43] A. M. Fsadni and J. P. M. Whitty, “A review on the two-phase heat transfer characteristics in helically coiled tube heat exchangers,” *Int. J. Heat Mass Transf.*, vol. 95, pp. 551–565, 2016.

[44] A. M. Fsadni and J. P. M. Whitty, “A review on the two-phase pressure drop characteristics in helically coiled tubes,” *Applied Thermal Engineering*. 2016.

[45] L. Zhao, L. Guo, B. Bai, Y. Hou, and X. Zhang, “Convective boiling heat transfer and two-phase flow characteristics inside a small horizontal helically coiled tubing once-through steam generator,” *Int. J. Heat Mass Transf.*, vol. 46, no. 25, pp. 4779–4788, 2003.

[46] J. S. Jayakumar, S. M. Mahajani, J. C. Mandal, P. K. Vijayan, and R. Bhoi, “Experimental and CFD estimation of heat transfer in helically coiled heat exchangers,” *Chem. Eng. Res. Des.*, vol. 86, no. 3, pp. 221–232, 2008.

[47] M. Esch, A. Hurtado, D. Knoche, and W. Tietsch, “Analysis of the influence of different heat transfer correlations for HTR helical coil tube bundle steam generators with the system code TRACE,” *Nucl. Eng. Des.*, vol. 251, pp. 374–380, 2012.

[48] L. Guo, Z. Feng, and X. Chen, “Transient convective heat transfer of steam ± water two-phase ¯ ow in a helical tube under pressure drop type oscillations,” *Most*, vol. 45, pp. 533–542, 2002.

[49] L. Guo, X. Chen, Z. Feng, and B. Bai, “Transie : nt convective heat transfer in a helical coiled

tube with pulsatile fully developed turbulent flow," *Int. J. Heat Mass Transf.*, vol. 41, pp. 2867–2875, 1998.

[50] L. Santini, A. Cioncolini, M. T. Butel, and M. E. Ricotti, "Flow boiling heat transfer in a helically coiled steam generator for nuclear power applications," *Int. J. Heat Mass Transf.*, vol. 92, pp. 91–99, 2016.

[51] E. Rivas and E. Rojas, "Heat transfer correlation between Molten Salts and helical-coil tube bundle Steam Generator," *Int. J. Heat Mass Transf.*, vol. 93, pp. 500–512, 2016.

[52] F. Incropera, T. Bergman, A. Lavine, and D. Dewitt, *Fundamentals of Heat and Mass Transfer*. Joahn Wiley & Sons, 2011.

[53] J. Hart, J. Ellenberger, and P. J. Hamersma, "Single- and two-phase flow through helically coiled tubes," *Chem. Eng. Sci.*, 1988.

[54] C. M. White, "Fluid friction and its relation to heat transfer," *Trans. Inst. chem. Engrs*, vol. 18, pp. 66–86, 1932.

[55] H. Ito, "Friction factors for turbulent flow in curved pipes," *Basic Eng*, pp. 123–134, 1959.

[56] H. Ju, Z. Huang, Y. Xu, B. Duan, and Y. Yu, "Hydraulic performance of small bending radius helical coil-pipe," *J. Nucl. Sci. Technol.*, 2001.

[57] M. Colombo, L. P. M. Colombo, A. Cammi, and M. E. Ricotti, "A scheme of correlation for frictional pressure drop in steam-water two-phase flow in helicoidal tubes," *Chem. Eng. Sci.*, 2015.

[58] L. Guo, Z. Feng, and X. Chen, "An experimental investigation of the frictional pressure drop of steam-water two-phase flow in helical coils," *Int. J. Heat Mass Transf.*, 2001.

[59] A. Owhadi, J. J. Bell, and B. Crain Jr, "Forced convection boiling inside helically-coiled tubes," *Int. J. Heat Mass Transf.*, vol. 11, no. 12, pp. 1779–1793, Dec. 1968.

[60] L. C. Ruspini, C. P. Marcel, and A. Clausse, "Two-phase flow instabilities: A review," *International Journal of Heat and Mass Transfer*. pp. 521–548, 2014.

[61] S. Kakac and B. Bon, "A Review of two-phase flow dynamic instabilities in tube boiling systems," *Int. J. Heat Mass Transf.*, no. 51, pp. 399–433, 2008.

[62] K. Farhadi, "A model for predicting static instability in two-phase flow systems," *Prog. Nucl. Energy*, vol. 51, no. 8, pp. 805–812, 2009.

[63] M. Colombo, A. Cammi, D. Papini, and M. E. Ricotti, "RELAP5/MOD3.3 study on density wave instabilities in single channel and two parallel channels," *Prog. Nucl. Energy*, pp. 15–23, 2012.

[64] D. Papini, M. Colombo, A. Cammi, and M. E. Ricotti, "Experimental and theoretical studies on density wave instabilities in helically coiled tubes," *Int. J. Heat Mass Transf.*, pp. 343–356, 2014.

[65] Flownex Simulation Environment, "Flownex Library Manual." 2016.

[66] Flownex simulation Environment, "Theory Manual." 2016.

[67] D. . GROENEVELD *et al.*, "The 1995 look-up table for critical heat flux in tubes," *Nucl. Eng. Des.*, vol. 163, 1996.

[68] F. Incropera and D. Dewitt, *Fundamentals of heat and mass transfer*, Fourth. 1996.

[69] ABB services, “Tuning A Control Loop - The Knowledge Board,” 2014. .

(Blank Page)

Appendix A. Methodology derivations and explanations

Derivation of governing equations

The governing equations used in Flownex are derived from the conservation laws of mass, momentum and energy. The conservation laws are originally defined in the Lagrangian reference frame. The Lagrangian reference frame is a fixed mass control volume, described as a fluid particle moving from one location to another along a stream line. With this definition, the mass in the control volume is fixed but the volume may change due to density changes. Thus, no fluid can cross the control surfaces. In this reference frame the governing equations of conservation for mass (A.1) , momentum (A.2) and energy (A.3) are as follows:

$$\frac{Dm}{Dt}=0 \qquad \frac{D}{Dt}\int_{CV}\rho dV=0 \quad \text{(A.1)}$$

$$\frac{D(m\vec{V})}{Dt}=\sum\vec{F} \qquad \frac{D}{Dt}\int_{CV}\rho\vec{v}dV=\sum\vec{F} \quad \text{(A.2)}$$

$$\frac{D[m(u+\frac{1}{2}v^2+gz)]}{Dt}=\dot{Q}_H-\dot{W} \qquad \frac{D}{Dt}\int_{CV}\rho(u+\frac{1}{2}v^2+gz)dV=\dot{Q}_H-\dot{W} \quad \text{(A.3)}$$

Where:

$$\frac{D}{Dt}=\frac{\partial}{\partial t}+\vec{v}\cdot\vec{\nabla}$$
$$\vec{\nabla}=(\frac{\partial}{\partial x},\frac{\partial}{\partial y},\frac{\partial}{\partial z})$$

The equations for the conversation of mass, momentum and energy are converted to the Eulerian reference frame. The Eulerian reference frame considers a stationary fixed-volume control volume. In this reference frame fluid can cross the control surfaces, unlike in the Lagrangian reference frame. The conversion of the conservation equations from the Lagrangian to the Eulerian is done by using the Reynolds transport theorem shown in equation (A.4).

$$\frac{DN}{Dt}=\int_{CV}\eta(\rho\vec{v}\cdot d\vec{A})+\frac{\partial}{\partial t}\int_{CV}\rho\eta dV \quad \text{(A.4)}$$

where N denotes a general extensive property and η its intensive counterpart. The conservation equations in this reference frame are shown in equation (A.5) for mass, equation (A.6) for momentum and equation (A.7) for energy.

$(N = m, \eta = 1)$

$$\frac{Dm}{Dt} = \int_{cs} (\rho \vec{v} \cdot d\vec{A}) + \frac{\partial}{\partial t} \int_{cv} \rho dV = 0 \tag{A.5}$$

$(N = m\vec{v}, \eta = \vec{v})$

$$\frac{D(m\vec{v})}{Dt} = \int_{cs} \vec{V}(\rho \vec{v} \cdot d\vec{A}) + \frac{\partial}{\partial t} \int_{cv} \rho \vec{v} dV = \sum \vec{F} \tag{A.6}$$

$(N = me, \eta = e = u + \frac{1}{2}v^2 + gz)$

$$\frac{D(me)}{Dt} = \int_{cs} e(\rho \vec{v} \cdot d\vec{A}) + \frac{\partial}{\partial t} \int_{cv} \rho e dV = \dot{Q}_H - \dot{W} \tag{A.7}$$

The conservation equations are then converted a volume integral and the surface integral into a volume integral by applying the Gauss divergence theorem. The differential form for the conservation of mass is shown in (A.8), the conservation of momentum in (A.9) (where $\vec{T}$ is the stress tensor acting on the control surface and $\vec{B}$ is the body force acting on the fluid inside the control volume) and the conservation of energy in (A.10).

$$\frac{\partial \rho}{\partial t} + \vec{\nabla} \cdot (\rho \vec{v}) = 0 \tag{A.8}$$

$$\frac{\partial \rho \vec{v}}{\partial t} + \vec{\nabla} \cdot (\rho \vec{v} \vec{v}) = \vec{\nabla} \cdot \vec{T} + \vec{B} \tag{A.9}$$

$$\frac{\partial (\rho e)}{\partial t} + \vec{\nabla} \cdot (\rho \vec{v} e) = \dot{Q}_H - \dot{W} \tag{A.10}$$

As stated in section 3.2.1 a one-dimensional approach is used when solving the network. Therefore the conservation equations simplify further to give the one dimensional conservation equations for mass(A.11), momentum (A.12) and energy(A.13).

$$\frac{\partial \rho}{\partial t} + \frac{\partial (\rho v)}{\partial x} = 0 \tag{A.11}$$

$$\rho \frac{\partial v}{\partial t} \rho v \frac{\partial v}{\partial x} = -\frac{\partial p}{\partial x} - \rho g \frac{\partial z}{\partial x} - \frac{f \rho |v| v}{2D} \tag{A.12}$$

$$\frac{\partial (\rho h_0)}{\partial t} - \frac{\partial p}{\partial t} + \frac{\partial (\rho v h_0)}{\partial x} + \rho v \frac{\partial (gz)}{\partial x} = \dot{Q}_H + \dot{W} \tag{A.13}$$

$$Where: h_0 = h + \frac{1}{2}v^2, h = u + pv$$

These are the conservation equations that are solved in the Flownex software and would further simplify when salting only steady state conditions.

Homogeneous two-phase fluid property equations

The fluid properties for the homogeneous two-phase solving approach are evaluated using the following equations: For the velocities equation (A.14), for the average homogeneous void fraction equation (A.15), for the specific volume equation (A.16), for the density equation (A.17), and for the enthalpy equation (A.18).

$$\bar{v}_H = \bar{v}_l = \bar{v}_g \tag{A.14}$$

$$\bar{\alpha}_H = \frac{\rho_l \bar{x}}{\rho_l \bar{x} + \rho_g (1 - \bar{x})} \tag{A.15}$$

$$v_H = v_l \left(1 - \bar{x}\right) + v_g \bar{x} \tag{A.16}$$

$$\rho_H = \frac{(1 - \bar{x})}{\rho_l} + \frac{\bar{x}}{\rho_g} \tag{A.17}$$

$$h_H = h_l (1 - \bar{x}) + h_g \bar{x} \tag{A.18}$$

The mass flow per unit area (mass flux) is given by equation (A.19).

$$G = \rho_H v_H = \left[\rho_l (1 - \overline{\alpha_H}) + \rho_g \overline{\alpha_H} \right] v_H \tag{A.19}$$

Pipe pressure drop equations

The pressure drop through the pipe component is calculated using the Darcy-Weisbach approach with the Swamee and Jain friction factor correlations shown in equation (A.20).

$$f = \frac{0.25}{[\log\{(\frac{\varepsilon}{3.7D}) + \frac{5.74}{\mathrm{Re}^{0.9}}\}]^2} \tag{A.20}$$

The incompressible pressure drop equation for steady state is shown in equation (A.21) and for transient it is shown in equation (A.22). The compressible pressure drop equation for steady state is shown in equation (A.23) and for transient it is shown in equation (A.24).

$$\Delta p_0 = \left(\frac{fL}{D} + \sum K_S + K_R \right) \frac{\rho |v| v}{2} + \rho g \Delta z + \frac{1}{2} K \rho |v| v \tag{A.21}$$

$$\Delta p_0 = \left(\frac{fL}{D} + \sum K_S + K_R \right) \frac{\rho |v| v}{2} + \rho g \Delta z + \frac{1}{2} K \rho |v| v + \rho L \frac{dv}{dt} \tag{A.22}$$

$$\Delta p_0 = \left(\frac{fL}{D} + \sum K_S + \frac{\Delta T_0}{T_0} \right) \frac{p_0 \gamma M^2}{2} + \Delta p_{0r} + \frac{p_0}{p} \left(\rho g \Delta z + \frac{1}{2} K \rho |v| v \right) \tag{A.23}$$

$$\Delta p_0 = \left(\frac{fL}{D} + \sum K_S + \frac{\Delta T_0}{T_0} \right) \frac{p_0 \gamma M^2}{2} + \Delta p_{0r} + \frac{p_0}{p} \left(\rho g \Delta z + \frac{1}{2} K \rho |v| v \right) + \frac{\rho p_0 L}{p} \frac{dv}{dt} \tag{A.24}$$

Flow resistance pressure drop equation derivation

The quadratic pressure drop equation (A.25) is shown again in equation and derived as follows.

$$\Delta p_0 = \frac{|\dot{m}| \dot{m}}{\rho \cdot A_f \cdot A_{sf} \cdot A_0} + \rho g \Delta z \tag{A.25}$$

If the secondary losses across a component are not considered, the pressure drop in equation (A.26) can be used.

$$\Delta p_0 = \left(\frac{fL}{D}\right) \frac{1}{2} \rho v |v| + \rho g \Delta z \tag{A.26}$$

$$\dot{m} = \rho v A$$

$$thus$$

$$v = \frac{\dot{m}}{\rho A}$$

Then Δp_0 becomes:

$$\Delta p_0 = \left(\frac{fL}{D}\right) \frac{1}{2} \frac{|\dot{m}| \dot{m}}{\rho A^2} + \rho g \Delta z \tag{A.27}$$

Thus equation (A.25) is equal to equation (A.26) when:

$$\frac{1}{A_f \cdot A_{sf} \cdot A_0} = \left(\frac{fL}{D}\right) \frac{1}{2A^2}$$

Heat transfer component description

Since radiation heat transfer is not modelled, only the heat transfer for the convection and the conduction is described below.

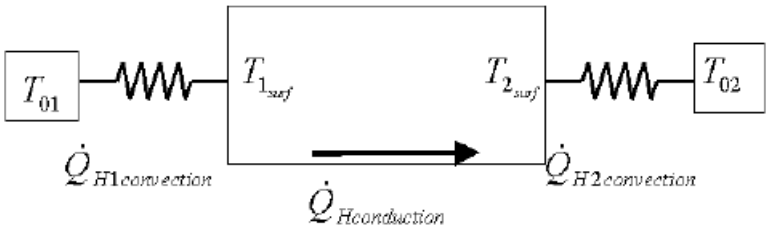

Figure A. 1 Heat trasnfer flow path for convection and conduction [65]

Figure A. 1 shows the heat transfer path of convection and conduction across the composite heat transfer element. The heat transfer for the convection on the shell and tube side is calculated using equation (A.28) and (A.29), and the heat transfer for the conduction is calculated using equation (A.30).

$$\dot{Q}_{H1convection} = \lambda_{01} A_1 (T_{a1} - T_{1surf}) \tag{A.28}$$

$$\dot{Q}_{H2convection} = \lambda_{02} A_2 (T_{2surf} - T_{a2}) \tag{A.29}$$

$$\dot{Q}_{Hconduction} = \frac{kA}{dx} (T_{1surf} - T_{2surf}) \tag{A.30}$$

$$A = \frac{A_1 + A_2}{2}$$

The heat transfer coefficient can be specified as a constant or correlations can be used. The conduction section of the composite heat transfer component can be discretised for a material layer by specifying the number of nodes in the layer as shown in Figure A. 2. In addition to this, multiple layers can be selected to model the conduction across multiple materials. However, for the model developed, the composite heat transfer component is never used to model multiple materials. Two nodes in all the composite heat transfer components were used in the model. This was due to all the heat exchangers having relatively thin wall thicknesses and two nodes were selected instead of three to reduce the overall solving time of the simulation.

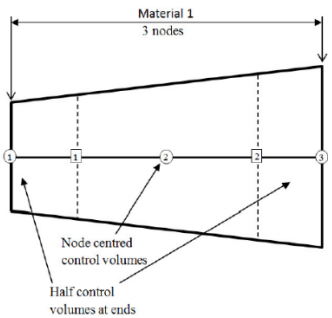

Figure A. 2 Discretised conduction layer in the composite heat transfer element [65]

Two phase heat transfer equations

The standard Dittus-Boelter forced convection heat transfer coefficient is shown in equation (A.31) . This mode of heat transfer is present in both single-phase and two-phase heat transfer flow systems.

$$\lambda_c = 0.023\left(\frac{\lambda}{D}\right)\mathrm{Re}^{0.8}\ \mathrm{Pr}^{n} \tag{A.31}$$

where:

$$n = 0.4\ if\ fluid\ is\ bing\ heated\ and\ 0.3\ if\ fluid\ is\ being\ cooled$$

The heat transfer correlations used in the subcooled boiling and the saturated boiling regions, are applicable to both boiling regions. This entire region is then defined between the onset of Nucleate boiling (ONB) and when the fluid reaches the quality of one or the CHF point. The correlation developed by Sato and Matsumara (1964) is used in this region. The degree of wall superheat where the ONB conditions are satisfied is calculated using equation (A.32)

$$\Delta T_{sat,ONB} = \frac{4\sigma T_{sat} \nu_{fg} \lambda_C}{\lambda_l H_{fg}}\left[1 + \sqrt{1 + \frac{\lambda_l H_{fg} \Delta T_{sub}}{2\sigma T_{sat} \nu_{fg} h_C}}\right] \tag{A.32}$$

where:

$$\Delta T_{sat,ONB} = T_{wall,ONB} - T_{sat}$$

The correlation used for the heat flux at the ONB point is given by equation (A.33).

$$q''_{ONB} = \frac{\lambda_l H_{fg} \Delta T^2_{sat,ONB}}{8\sigma \nu_{fg} T_{sat}} \tag{A.33}$$

Figure A. 3 shows how the heat transfer coefficient changes due to different heat fluxes for a constant mass flow rate. This illustrates how having subcooled boiling increases the heat transfer coefficient when compared to the pure convective boiling that would be defined by equation (A.31). Figure A. 3 also shows how the wall temperature and fluid temperature responds across the boiling regions. At the bottom Figure A. 3, a picture shows what the boiling regions may look like within a pipe.

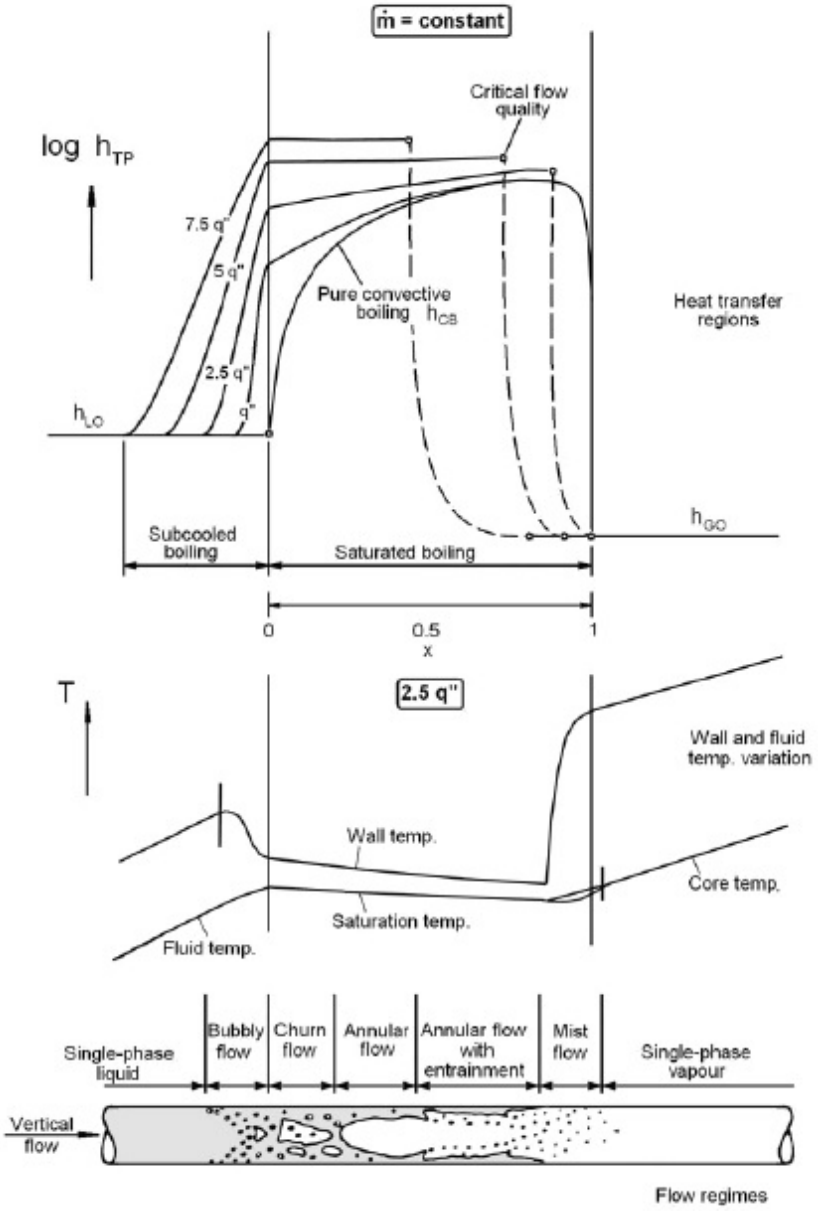

Figure A. 3 Vertical boiling process [66]

As stated, the saturated boiling region is defined up until the fluid quality is equal to one or the CHF point is reached. The CHF point is when the heat flux is raised to such a level that the heated surface can no longer support continuous liquid contact. The CHF point is calculated by using the look-up tables of Groeneveld [67], which determines the CHF point as a function of pressure.

A region referred to as transition boiling is defined between the CHF point and the minimum heat flux (MHF) point. This region consists of unstable nucleate boiling and unstable film boiling. Figure 3.10 shows that a smooth transition exists between the CHF and the minimum heat flux point (MHF). Thus, the heat transfer for this region is calculated using a linear interpolation technique between the CHF and the MHF point. The minimum heat flux point is calculated by using a combination of

the correlation given by Zuber (A.35) and the correlation given by Simon (A.37) [66]. Thus, the minimum heat flux point is defined as the maximum temperature given by the two correlations as shown in equation (A.38).

$$q''_{MFB,1} = 0.09\rho H_{fg}\left(\frac{\sigma}{g(\rho_l-\rho_g)}\right)^{0.25}\left(\frac{g(\rho_l-\rho_g)}{\rho_l-\rho_g}\right)^{0.5} \quad \text{(A.34)}$$

$$T_{MFB,1} = T_{sat} + \frac{q''_{MFB,1}}{\lambda_{film}} \quad \text{(A.35)}$$

$$q''_{MFB.2} = \lambda_{film}(T_{MFB,2} - T_{sat}) \quad \text{(A.36)}$$

$$T_{MFB,2} = 0.13T_{CRIT}\left(\frac{p}{p_{CRIT}}\right) + 0.86T_{CRIT} \quad \text{(A.37)}$$

$$T_{MFB} = \max(T_{MFB,1}, T_{MFB,2}) \quad \text{(A.38)}$$

After the MHF point, film boiling is the next boiling region. This is where the rate of evaporation near the tube wall is high enough to push the remaining liquid away from the wall. The 2003 Groenveld film boiling tables are used to calculate the film boiling heat transfer.

Valve flowrate equations

The incompressible mass flowrate through the control valve is given in equation (A.39).

$$\dot{m} = N_1 F_P F_R C_v \sqrt{\frac{\rho_w\left(p_1 - p_2\right)}{\rho}} \quad \text{(A.39)}$$

Where:

$$N_1 = numerical\ constant\ from\ ANSI\ /\ ISA\ standard\ 75.01-1985(R1995)$$

$$F_P = piping\ geometry\ factor$$

$$F_R = Reynolds\ number\ factor\ from\ ANSI\ /\ ISA\ standard\ 75.01-1985(R1995)$$

$$\rho_w = fuild\ density\ of\ water\ at\ 15.6℃$$

$$p_1 = upstream\ absolute\ pressure$$

$$p_2 = downstream\ absolute\ pressure$$

$$F_p = \frac{1}{\sqrt{1+\frac{\sum K}{N_2}\left(\frac{C_v}{d^2}\right)^2}}$$

$$\sum K = sum\ of\ velocity\ head\ coefficients\ for\ all\ fittings\ attached\ to\ valve$$

$$N_2 = numerical\ constant\ from\ \ ANSI\ /\ \ ISA\ standard\ 75.01 - 1985(R1995)$$

$$d = nominal\ valve\ size$$

In the case of compressible flow, the relationship between the mass flow rate and the pressure drop is much weaker due to the compressible fluid. In this case the mass flowrate through the valve is described with equation (A.40).

$$\dot{m} = F_p C_v N_6 Y \sqrt{x P_1 \rho_1} \tag{A.40}$$

Where:

$$\rho_1 = upstream\ density$$

$$N_6 = numerical\ constant\ from\ ANSI\ /\ \ ISA\ standard\ 75.01 - 1985(R1995)$$

$$Y = 1 - \frac{x}{3F_\gamma x_T}$$

$$x_T = pressure\ drop\ ratio$$

$$F_\gamma = \frac{\gamma}{1.40}$$

$$\gamma = specific\ heat\ ratio$$

$$x = \frac{p_1 - p_2}{p_1}$$

For the two-phase flow condition through the valve, the homogeneous approach is used. This assumes an average density and velocity for the two-phases. These averages are then used in the equations described for single phase flow.

Empirical correction factors are used to account for certain flow characteristics for different valves. The correction factors are F_L, x_T and F_d. F_L is the liquid pressure recovery factor, where there are no fittings taken into account. F_L is defined in equation (A.41). x_T is the pressure drop ratio factor at which compressible flow will start to choke, this is when no fittings are taken into account. F_d is a valve style modifier for incompressible flow to convert geometry of the orifice(s) to an equivalent single flow passage. This is used when there are multiple flow passages such as double seated valves.

$$F_L = \sqrt{\frac{p_1 - p_2}{p_1 - p_{vc}}} \tag{A.41}$$

Flat plate orifice flowrate solving when using a pipe as a valve

The orifice modelled in the pipe is a flat plate orifice, where the equation for the mass flowrate through the orifice is shown in equation (A.42).

$$\dot{m} = \frac{1}{4}\pi d^2 C_d E \sqrt{2\Delta p_r \rho} \tag{A.42}$$

Where:

$$C_d = discharge\ coeffienct$$

$$E = approach\ factor$$

$$d = diameter\ of\ orifice\ throat$$

$$\Delta p_r = static\ pressure\ difference\ accross\ the\ orifice$$

The discharge coefficient is approximated using equation (A.43).

$$C_d = 0.5959 + 0.312\beta^{2.1} - 0.184\beta^8 + 0.0029\beta^{2.5}\left[\frac{10^6}{\mathrm{Re}}\right]^{0.75} + \kappa L_1 \beta^4 \left(1-\beta^4\right)^{-1} - 0.0337 L_2 \beta^3 \tag{A.43}$$

Where:

$$\beta = diameter\ ratio\ \frac{d}{D}$$

$L_1 = \frac{l_1}{D}$ the quotient of the distance of the upstream tapping from the upstream face of the plate divided by the pipe diameter.

$L_2 = \frac{l_2}{D}$ the quotient of the distance of the downstream tapping from the downstream face of the plate divided by the pipe diameter.

$$\kappa = 0.08\ if\ L_1 < 0.4333\ or = 0.039\ if\ L_1 > 0.433$$

The approach factor is defined in equation (A.44).

$$E = \frac{1}{\sqrt{1-\beta^4}} \tag{A.44}$$

Since this flat plat orifice is incorporated into the pipe component, the above equation needs to be defined in the form of a loss coefficient K_R which is defined in equation (A.45).

$$K_R = \frac{\Delta p_{0r}}{\frac{1}{2}\rho v^2} \tag{A.45}$$

This is done by manipulating certain equations, first S is defined in equation (A.46) as the ratio of the total pressure loss to static pressure difference.

$$S = \frac{\Delta p_{0r}}{\Delta p_r} = \frac{1 - C_d E \beta^2}{1 + C_d E \beta^2} \tag{A.46}$$

Then knowing that $\dot{m} = \rho Q$, $V = \frac{Q}{A}$ and $A = \frac{\pi D^2}{4}$ equation (A.42) can be written as equation (A.47)

.

$$\Delta p_{0r} = \frac{S}{C_d^2 E^2 \beta^4} \frac{1}{2} \rho v^2 \tag{A.47}$$

Thus, equation (A.45) can now be written as equation (A.48), where the diameter ratio β is used to define the opening of the valve.

$$K_R = \frac{S}{C_d^2 E^2 \beta^4} \tag{A.48}$$

Two-phase tank level tracking description

Level tracking is achieved by using the quality of the fluid in the tank, where the fraction that is filled with liquid and gas is calculated. The liquid is at the bottom of the tank and the gas at the top of the tank. When connecting pipes to the tank, the level at which the pipes are connected is specified. Thus, it can be determined if the connecting pipes are above or below the liquid level inside the tank. The exact geometry can be specified for the two-phase tank component, being the vessel shape, orientation and volume. Endcaps can also be specified if the tank being modelled has endcaps. To calculate the level for steady state solutions, the quality must be specified which determines the liquid level. The initial pressure is also defined, this is the initial pressure that the solver works off to solve the conditions at the tank. Finally, for the steady state solution a fixed flow element for the two-phase tank must be specified. The solver will then try and maintain the tank level by adjusting the fixed mass flow condition. This is where using the two-phase tank becomes cumbersome, as there is sometimes more than one solution for the fixed flow element to maintain the tank level.

Flownex model development

The final model developed in Flownex was built up in small sections. This was done to make sure each section was performing as expected and if it wasn't then it was easier to find mistakes in a smaller network. A complete diagram of the test facility is shown again in Figure A. 4 as a reference for this section.

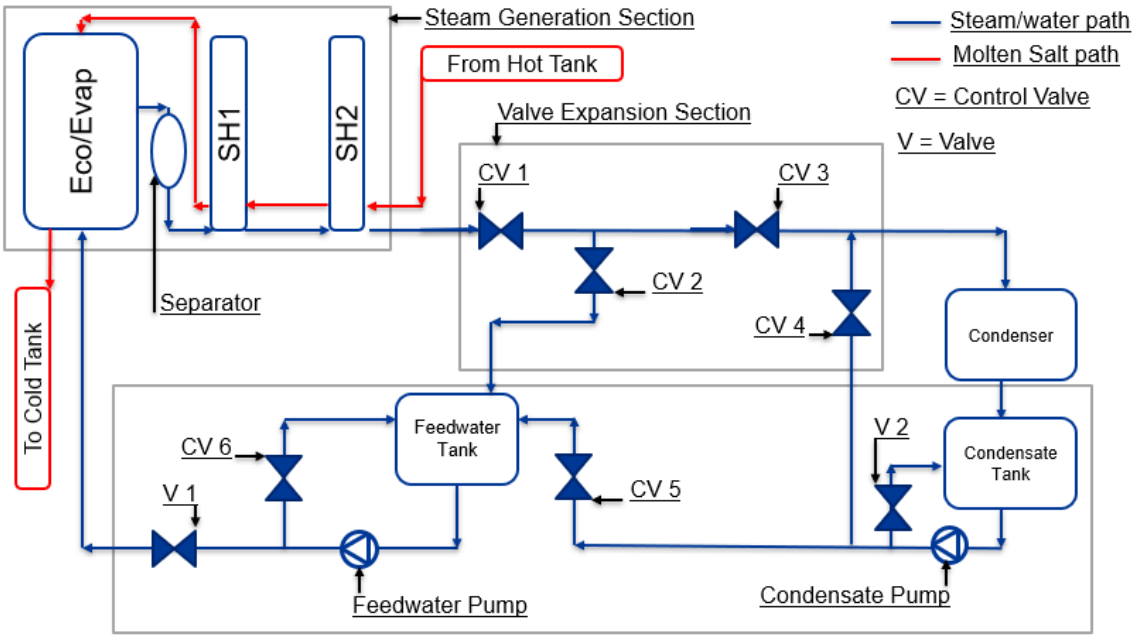

Figure A. 4 Basic diagram of complete steam cycle

First the valve expansion section was developed. This involved having to select the correct valve openings for the valves to achieve the expected conditions at certain points of the test facility. The expected conditions are known from a process flow diagram for the water/steam side provided by Steinmüller. The diagram in Figure A. 5 shows the location of the expected conditions and the sections that were built up to develop the entire model for the valve expansion section. First control valve 1 was added at the exit of superheater two. The valve opening was selected so that the exit pressure of superheater two was 140 bar, this is section 1. The steam generation system was then removed and replaced with a boundary node to develop the rest of the valve expansion section. The pipe network was modelled up until control valve three, with a boundary being placed where the pressure will be controlled by control valve three, this is section 2. Control valve 2 was added with the piping network leading to the valve and from the valve to the feedwater tank. The feedwater tank was initially modelled with a reservoir with the expected inlet and outlet flowrate. This meant that the opening for control valve 3 can be selected to maintain the feedwater tank pressure at 55bar. Control valve 3 was then added to the network and its valve opening was selected so that the pressure in front of the valve is 65 bar, this is section 3. The pipe network around control valve 4 was added as well as control valve 4, this is section 4. The valve opening for control valve 4 could then be selected to maintain the condenser inlet temperature at 160 ℃. Once the valve expansion network was complete, the valve opening for all the control valves were then readjusted to make sure that the correct conditions in the network were being calculated correctly, this is shown in Table A. 1.

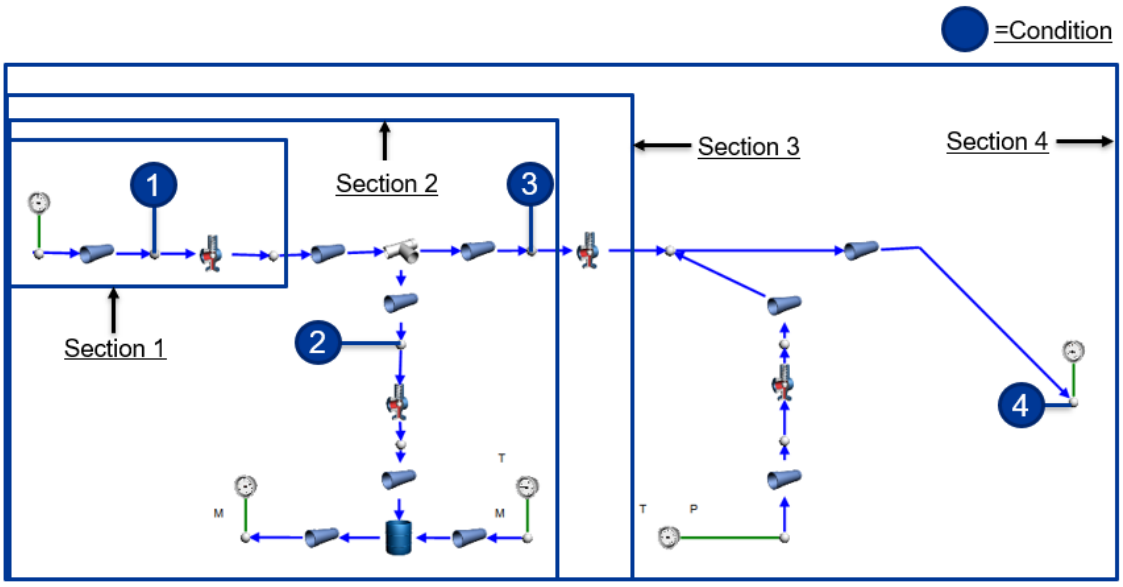

Figure A. 5 Valve expansion section model development

Table A. 1 Expected conditions vs results from valve expansion network

	Pressure(bar)		**Enthalpy(kJ/kg)**		**Mass flowrate(kg/s)**		**Temperature (℃)**	
Condition	Exp	Result	Exp	Result	Exp	Result	Exp	Result
1	140	140.7	3487.5	3486.34	0.7	0.7	560	559.63
2	65	64.72	3487.5	3486.34	0.13	0.13	529.5	529.7
3	65	65.022	3487.5	3486.34	0.57	0.57	529.5	528.91
4	5	5	2767.38	2767.2	0.76	0.77	160	160

Initially the condenser and condensate tank were going to be included in the complete model. Thus, a model was created for the condenser and condensate tank shown in Figure A. 6.

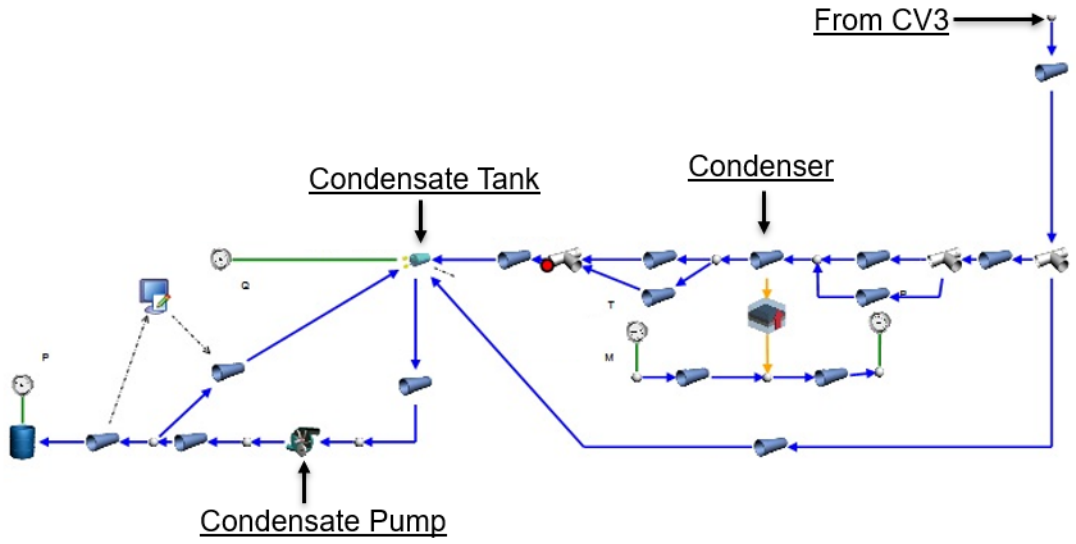

Figure A. 6 Model that was developed for the condenser and condensate tank

However, the decision was made to not model the condenser and condensate tank fully. The condenser was not included in the model because it would add another two-phase region. This would increase the solving time of the model, making it unpractical to use. Since the condenser is just an air-cooled condenser with no unique design it is unlikely that it won't perform as expected. Therefore, the need to model the condenser is not as great as the need to model the heat exchangers in the steam generation section.

The condensate tank was therefore only modelled with a node with the temperature and the pressure fixed as a boundary value. This assumes that the condenser will perform perfectly and that the condensate tank always has water available for the condensate pump to supply the feedwater tank and conditioning valve. Since the feedwater tank has a water makeup tank to supply it with water if the level is to low, the assumption that there is always water available for the feedwater pump is not unrealistic.

After the decision was made to not model the condenser and simplify the condensate tank, the entire model for the valve, tank and pump section could be created. This model is shown in Figure A. 7.

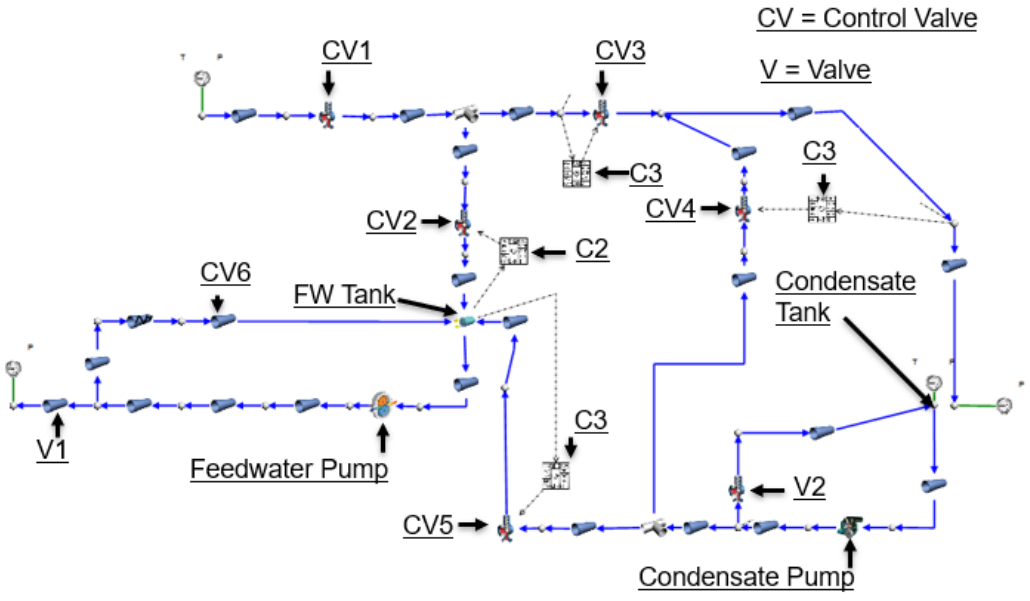

Figure A. 7 Flownex model for valve and tank section

This model now uses a two-phase tank component as the feedwater tank and now connects the tank and pump section to the expansion valve section. The controllers were added to the control valves downstream of the superheater two pressure control valve. The controllers that are shown in Figure A. 7 are also tuned in this network as described in section 3.8. The feedwater positive displacement pump is also added to this network.

The complete steam generation model is further developed to incorporate the hot and cold storage tanks as well as the hot salt pump into the network. The fixed feedwater pump is also added to this network. This is shown in Figure A. 8.

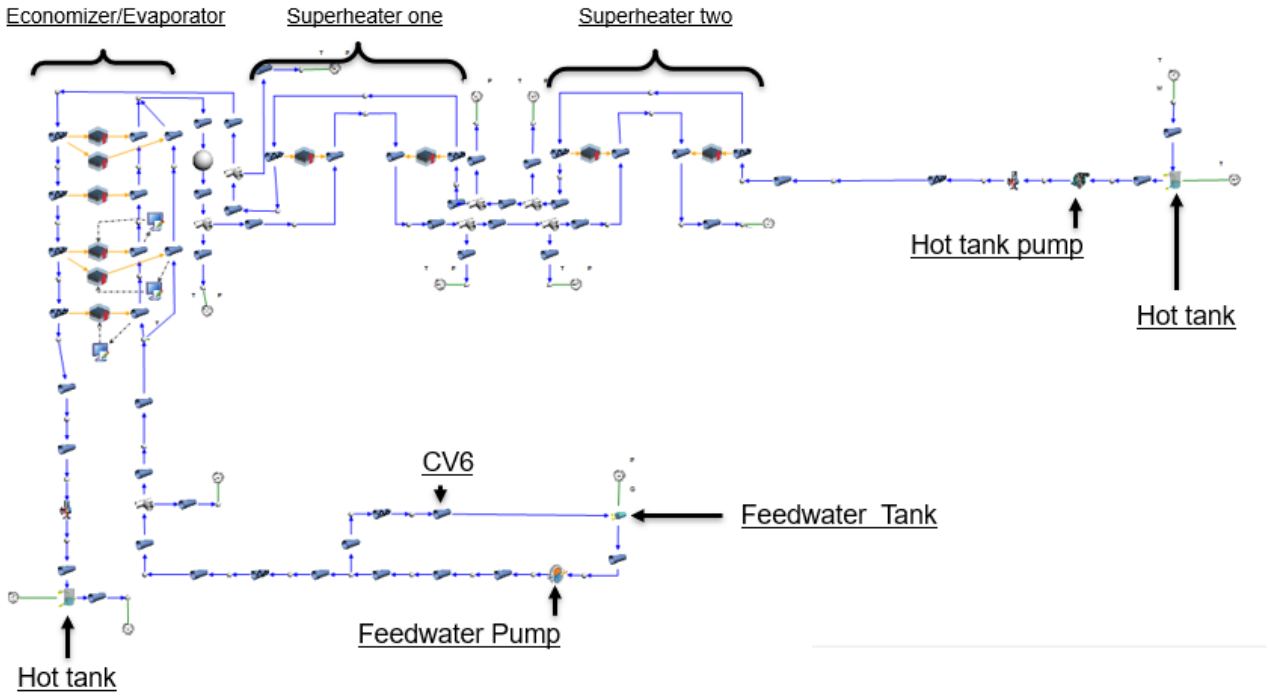

Figure A. 8 Steam generation model with full salt side

From this model the correct pump speed for the hot salt pump can be specified to achieve the salt mass flowrate required at 100% load. The valve lift for the valve that controlled the inlet pressure to the evaporator on the salt side was specified. The orifice diameter ratio for control valve six that controls the feedwater mass flowrate was also specified to obtain the correct feedwater mass flowrate into the economizer.

By combining the model shown in Figure A. 7 and Figure A. 8 the entire model was completed.

Appendix B. Script code

Economizer heat transfer script

```
if(Reynolds>180000)
 {
  C.Value=0.027;
  m.Value=0.8;
  n.Value=0.4;
 }
else
 {
  C.Value=0.328;
  m.Value=0.58;
  n.Value=0.4;
 }
```

Superheater 2 exit pressure script

```
if(Flowrate<0.251)
 {
  PressureSP.Value=70;
 }
else
 {
  if(Flowrate>0.699)
   {
    PressureSP.Value=140;
   }
   else
   {
    PressureSP.Value=(155.56*Flowrate.Value)+31.111;
   }
 }
```

Friction factor script

```
//C#
//Use ParentPipe to access parent pipe
//Index is 0 for non incremented pipes


//Tube Dimensions
double D = ParentPipe.dDiameterInlet.Value;
double e = 3E-05;//surface roughness
double n = Convert.ToDouble(ParentPipe.iNumberOfIncrements.Value);
double Dcoil = 0.555;


// other constants
double pi = Math.PI;
double Re_cr = 20000*Math.Pow((D/Dcoil),0.32); //ito

//Set Values to 0
double Re = 0.0;
double quality = 0.0;
double mass_flux = 0.0;
double FrictionFactor_g = 0.0;
double FrictionFactor_l = 0.0;
double f = 0.0;
double density = 0.0;
double pressure = 0.0;
double De = 0.0;

// 2 Phase Fluid Property Reference
Flownex.DataReferences.Materials.TwoPhaseFluids fluid =
(Flownex.DataReferences.Materials.TwoPhaseFluids)ParentPipe.FluidDataReference.Value;

//Checking if pipe is incremented
if (Index == 0)
  {
    Re = ParentPipe.ReynoldsNumber.Value;
  }
else
  {
    IPS.Increments.IIncrement increment = ParentPipe.GetElementIncrementResult(Index, 0, 0, 0,
IPS.Increments.ShowWhat.ELEMENT);
    Flownex.Increments.ElementIncrementResults subPipe =
(Flownex.Increments.ElementIncrementResults)increment;
    Re = subPipe.ReynoldsNumber.Value;
      quality = subPipe.Quality.Value;
      mass_flux = subPipe.dMassFlux;
      density = subPipe.MeanDensity.Value;
    pressure = subPipe.MeanPressure.Value;
  }
```

```
//Checking Quality
if (quality > 0 && quality < 1)
      {//Two-phase friction factor calculation
        //Liquid and gas properties for the lockart factor
        double enthalpy_liq = fluid.GetEnthalpyFromPressureAndQuality(pressure, 0, "Two Phase
HC2");
        double enthalpy_vap = fluid.GetEnthalpyFromPressureAndQuality(pressure, 1, "Two Phase
HC2");
        double density_liq = fluid.GetDensity(pressure, enthalpy_liq, "Two Phase HC2");
        double density_vap = fluid.GetDensity(pressure, enthalpy_vap, "Two Phase HC2");
        double viscosity_liq = fluid.GetViscosity(pressure, enthalpy_liq, "Two Phase HC2");
        double viscosity_vap = fluid.GetViscosity(pressure, enthalpy_vap, "Two Phase HC2");

        //gas only
        double Re_g = (mass_flux*quality*D)/viscosity_vap;//

        if (Re_g < 2300.0)
                {
                 if (Re_g >= 1.0e-6)
                 FrictionFactor_g = 64.0 / Re_g;
                 else
                 FrictionFactor_g = 64000000.0;
               }
                 else
                 {
                  if (Re_g < 5000)
                  {
                    double f1_g = 64.0 / 2300.0;
                    double y_g = 0.434294 * Math.Log(e / (3.7 * D) + 5.74 / Math.Pow(5000.0, 0.9));
                    double f2_g = 0.25 / (y_g * y_g);
                     FrictionFactor_g = (Re_g - 2300.0) * (f2_g - f1_g) / (5000.0 - 2300.0) + f1_g;
                   }
                   else
                   {
                    double y_g = 0.434294 * Math.Log(e / (3.7 * D) + 5.74 / Math.Pow(Re_g, 0.9));
                    FrictionFactor_g = 0.25 / (y_g * y_g);

                   }
               }


               //Liquid only
               double Re_l = (mass_flux*(1-quality)*D)/viscosity_liq;

               if (Re_l < 2300.0)
                 {
                  if (Re_l >= 1.0e-6)
```

```
                FrictionFactor_l = 64.0 / Re_l;
                else
                FrictionFactor_l = 64000000.0;
            }
              else
              {
               if (Re_l < 5000)
               {
                double f1_l = 64.0 / 2300.0;
                double y_l = 0.434294 * Math.Log(e / (3.7 * D) + 5.74 / Math.Pow(5000.0, 0.9));
                double f2_l = 0.25 / (y_l * y_l);
                 FrictionFactor_l = (Re_l - 2300.0) * (f2_l - f1_l) / (5000.0 - 2300.0) + f1_l;
               }
               else
               {
                double y_l = 0.434294 * Math.Log(e / (3.7 * D) + 5.74 / Math.Pow(Re_l, 0.9));
                FrictionFactor_l = 0.25 / (y_l * y_l);

               }
            }


            //Calculation for Constant C
            double A = (density_vap/density_liq)*Math.Pow((viscosity_liq/viscosity_vap),0.2);
            double ec = Math.E;
            double T = Math.Pow(ec,(-Math.Pow((Math.Log(A,10)+2.5),2)/(2.4-
mass_flux*Math.Pow(10,-4))));
            double F = 28-0.3*Math.Pow(mass_flux,0.5);
            double C = -2+F*T;
            if(C<2)
              {
                C = 2;
              }
            //Calculating equation terms for friction factor
            double A1 = (FrictionFactor_l*Math.Pow(1-quality,2))/density_liq;
            double A2 = C*quality*(1-quality);
            double A3 =
Math.Pow((FrictionFactor_l*FrictionFactor_g)/(density_liq*density_vap),0.5);
            double A4 = (FrictionFactor_g*Math.Pow(quality,2))/density_vap;

        FrictionFactor = density*(A1+A2*A3+A4);
    }
    else
    {//single-phase friction factor calculation
    De = Re*Math.Pow((D/Dcoil),0.5);
        if (De < 11.6) //laminar friction factor
            {
```

```
            if (Re >= 1.0e-6)
            {
            FrictionFactor = 64.0 / Re;
        }
            else
            {
            FrictionFactor = 64000000.0;
        }
       }
         if (De>11.6 && Re<Re_cr) //laminar with big vortex friction factor
            {
               f = 64/Re;
               FrictionFactor = f*(1+0.015*Math.Pow(Re,0.75)*Math.Pow((D/Dcoil),0.4));

            }
         if(De>11.6 && Re>Re_cr) //Turbulent friction factor
         {
            if (Re < 5000)
             {
              double f1 = 64.0 / 2300.0;
              double y = 0.434294 * Math.Log(e / (3.7 * D) + 5.74 / Math.Pow(5000.0, 0.9));
              double f2 = 0.25 / (y * y);
               f = (Re - 2300.0) * (f2 - f1) / (5000.0 - 2300.0) + f1;
             }
           else
             {
              double y = 0.434294 * Math.Log(e / (3.7 * D) + 5.74 / Math.Pow(Re, 0.9));
              f = 0.25 / (y * y);
             }
           FrictionFactor = f*(1+0.11*Math.Pow(Re,0.23)*Math.Pow((D/Dcoil),0.14));
        }
}
```

Appendix C. Mesh independent studies

Economizer/Evaporator mesh independent studies

Figure C. 1 shows the results for the single coil region of the economizer, where the heat transfer is shown to be independent when the number of increments is greater than 6. Figure C. 2 shows the results of the double coil region of the economizer where the heat transfer is shown to be independent when the number of increments is greater than 40.

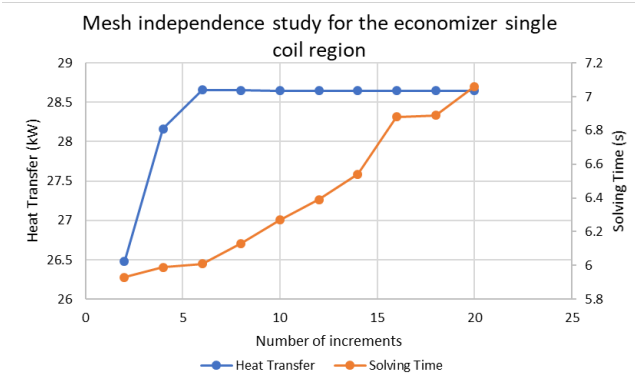

Figure C. 1 Mesh independence study for the single coil region of the economizer

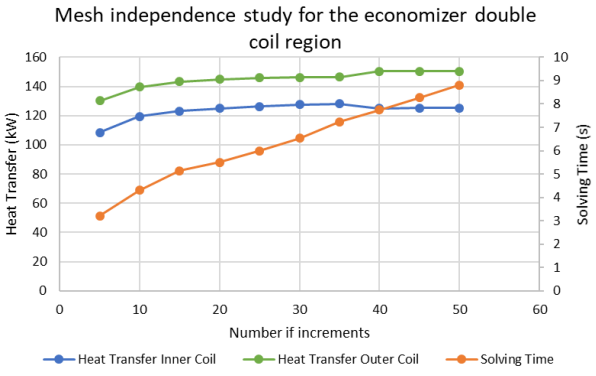

Figure C. 2 Mesh independence study for the double coil region of the economizer

Figure C. 3 shows the results of the single coil region of the evaporator, where the heat transfer becomes independent when the number of increments is greater than four. Figure C. 4 shows the results of the double coil region of the evaporator, where the heat transfer becomes independent when the number of increments is greater than 60.

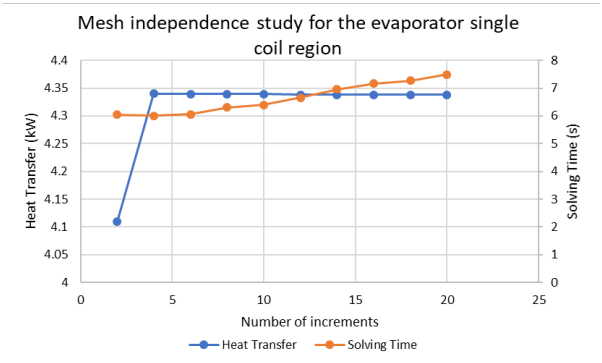

Figure C. 3 Mesh independence study for the single coil region of the evaporator

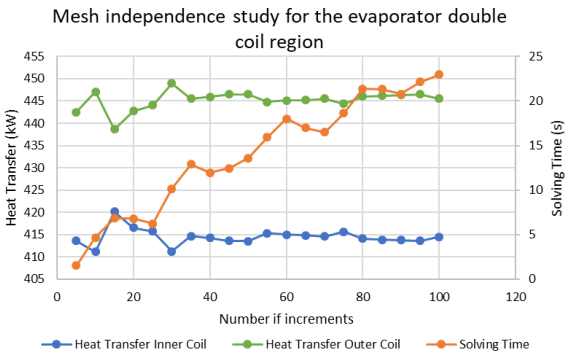

Figure C. 4 Mesh independence study for the double coil region of the evaporator

Superheater 1 and 2 mesh independent studies

Figure C. 5 and Figure C. 6 show the independence studies done for superheater 1 and 2 respectively. All the pipe and flow resistance components have the same amount of increments per heat exchanger.

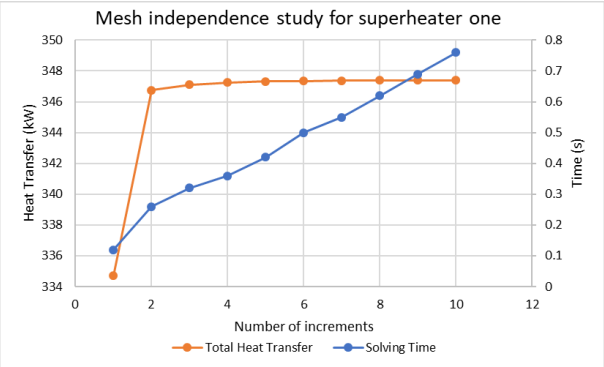

Figure C. 5 Mesh independence study for superheater 1

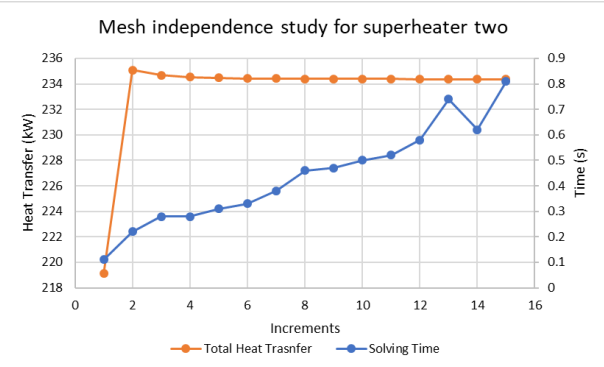

Figure C. 6 Mesh independence study for superheater 2

The results for superheater 1 shown in Figure C. 5 shows that the heat transfer calculated started to converge from 4 increments onwards. The results for superheater 2 shown in Figure C. 6 shows that the heat transfer calculated started to converge from six increments onwards.

Appendix D. Inputs for components

Inputs for components used for the economizer and evaporator

Table D. 1 Flow resistance component inputs for shell side of helical coil heat exchanger

Shell side component	Flow admittance factor	Volume	Increments
Economizer and evaporator single coil region	3.1×10^{-6}	Specified from design document.	10
Economizer and evaporator double coil region	3.1×10^{-7}	Specified from design document.	75

Table D. 2 Eco/Evap tube side pipe component inputs

Tube side component	Pipe length	Diameter	Friction factors	Number of Increments	K values
Economizer Inner coil single coil region	11.166% of the specified length for economizer	As specified in design documentation	Equations (3.8), (3.9),(3.11)and (3.17) with $\varepsilon = 30\mu m$	10	0
Economizer Inner coil double coil region	88.834% of the specified length for economizer	As specified in design documentation	Equations (3.8), (3.9),(3.11)and (3.17) with $\varepsilon = 30\mu m$	75	0
Economizer Outer coil	As specified in design documentation	As specified in design documentation	Equations (3.8), (3.9),(3.11)and (3.17) with $\varepsilon = 30\mu m$	75	0
Evaporator Inner coil single coil region	11.596% of the specified length for evaporator	As specified in design documentation	Equations (3.8), (3.9),(3.11)and (3.17) with $\varepsilon = 30\mu m$	10	0
Economizer Inner coil double coil region	88.404% of the specified length for evaporator	As specified in design documentation	Equations (3.8), (3.9),(3.11)and (3.17) with $\varepsilon = 30\mu m$	75	0
Economizer outer coil	As specified in design documentation	As specified in design documentation	Equations (3.8), (3.9),(3.11)and (3.17) with $\varepsilon = 30\mu m$	75	0

Table D. 3 Conduction inputs for composite heat transfer component

Heat transfer component	Wall thickness	Material	Number of nodes	Flow configuration
All composite heat transfer components	As specified from design documents	As specified from design documents	2	Counter

Table D. 4 Composite heat transfer inputs for shell side convection

Heat transfer component	Convection area	Heat transfer correlation	Cross sectional flow area	Hydraulic diameter
Economizer single coil region	Outside area of tubes	Flow over single cylinder equation (3.18), $C_1 = 0.193, m = 0.618$	Adjusted using equation (3.21)	Calculated from known internal geometry
Economizer double coil region	Outside area of tubes	Flow over tube banks equation (3.18), $C_1 = 0.27, m = 0.63$	Adjusted using equation (3.21)	Calculated from known internal geometry
Evaporator single coil region	Outside area of tubes	Flow over single cylinder equation (3.18), $C_1 = 0.193, m = 0.618$	Adjusted using equation (3.21)	Calculated from known internal geometry
Evaporator double coil region	Outside area of tubes	Flow over tube banks equation (3.18), $C_1 = 0.27, m = 0.63$	Adjusted using equation (3.21)	Calculated from known internal geometry

Table D. 5 Composite heat transfer inputs for tube side convection

Heat transfer component	Convection area	Heat transfer correlation	Cross sectional flow area	Hydraulic diameter
Economizer single coil region	Calculated from pipe component	Equation (3.7), Re<180,000 Equation (3.6) Re>180,000	Calculated from pipe component	
Economizer double coil region	Calculated from pipe component	Equation (3.7), Re<180,000 Equation (3.6) Re>180,000	Calculated from pipe component	
Evaporator single coil region	Calculated from pipe component	Equation (3.6)	Calculated from pipe component	
Evaporator double coil region	Calculated from pipe component	Equation (3.6)	Calculated from pipe component	

Inputs for components used for the superheater 1 and 2

Table D. 6 Flow resistance component inputs for shell side of superheaters 1&2

Shell side component	Flow admittance factor	Volume	Increments
Superheater 1	6×10^{-7}	Specified from design document.	4
Superheater 2	6×10^{-7}	Specified from design document.	8

Table D. 7 Pipe component inputs for superheaters 1&2

Tube side component	Pipe length	Diameter	Friction factors	Number of Increments	K values
Superheater 1, pipe 1	Specified from design documentation.	As specified in design documentation	Darcy Weisbach $\varepsilon = 30\mu m$	4	0.79
Superheater 1, pipe 2	Specified from design documentation.	As specified in design documentation	Darcy Weisbach $\varepsilon = 30\mu m$	4	1.29
Superheater 2, pipe 1	Specified from design documentation.	As specified in design documentation	Darcy Weisbach $\varepsilon = 30\mu m$	8	0.79
Superheater 2, pipe 2	Specified from design documentation.	As specified in design documentation	Darcy Weisbach $\varepsilon = 30\mu m$	8	1.29

Table D. 8 Conduction inputs for composite heat transfer component

Heat transfer component	Wall thickness	Material	Number of nodes	Flow configuration
All composite heat transfer components	As specified from design documents	As specified from design documents	2	Counter

Table D. 9 Composite heat transfer inputs for shell side convection

Heat transfer component	Convection area	Heat transfer correlation	Cross sectional flow area	Hydraulic diameter
Superheater 1	Outside area of tubes	Shell side single phase heat transfer equation (3.22),	As specified from design documentation	Calculated from known internal geometry
Superheater 2	Outside area of tubes	Shell side single phase heat transfer equation (3.22),	As specified from design documentation	Calculated from known internal geometry

Table D. 10 Composite heat transfer inputs for tube side convection

Heat transfer component	Convection area	Heat transfer correlation	Cross sectional flow area	Hydraulic diameter
Superheater 1	Calculated from pipe component	Dittus-boelter equation (3.6)	Calculated from pipe component	
Superheater 2	Calculated from pipe component	Dittus-boelter equation (3.6)	Calculated from pipe component	

Appendix E. 35% and 115% sensitivity analysis for steam generation using solar salt

Figure E. 1 and Figure E. 2 show the sensitivity analysis done for the steam generation system when solar salt is used as the salt compound. The results in Figure E. 1 show that the salt mass flowrate would have to be adjusted by about 10% to reach the expected operating requirements for the 35% load. Figure E. 2 shows that the salt mass flowrate would have to be adjusted by about 12% to reach the expected operating requirements for the 115% load.

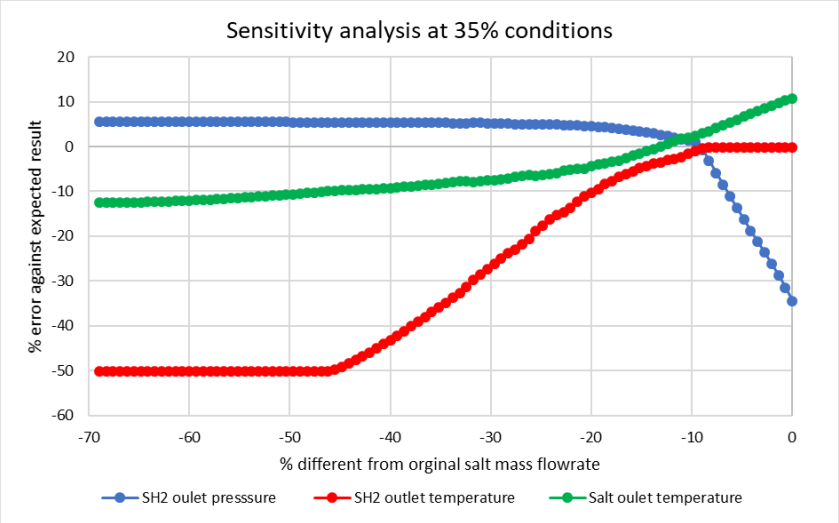

Figure E. 1 35% load sensitivity analysis

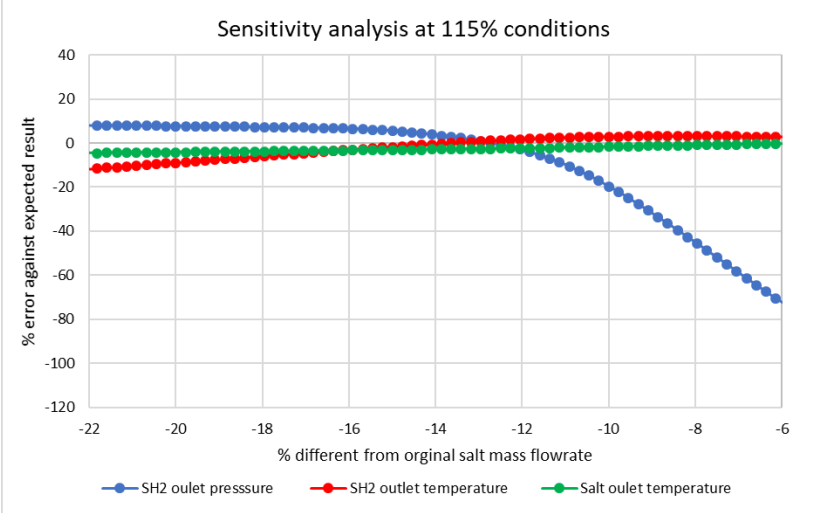

Figure E. 2 115% load sensitivity analysis

Appendix F. Controller Tuning

Intermediate pressure controller (C3)

Bump test:

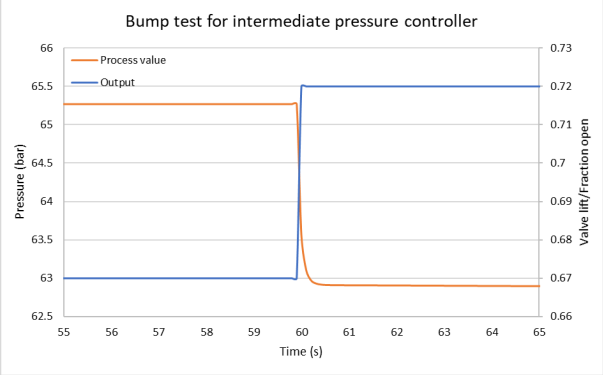

Figure F. 1 Controller C3 bump test

Modelling parameters:

Parameter	**Result**
Δout (change in output)	0.05 (valve lift)
ΔPV (change in process value)	-2.36995 (bar)
Δt (Time taken for process value to settle)	4(s)
K_{Δ} (Gain change)	-47.4
τ_p (Closed loop time constant)	1

Tuning:

K_p	T_i	τ_{ratio}
-0.02	1	1

Validation:

$$Time = 4 \times \tau_{CL} = 4 \times \tau_{ratio} \times \tau_P = 4s$$

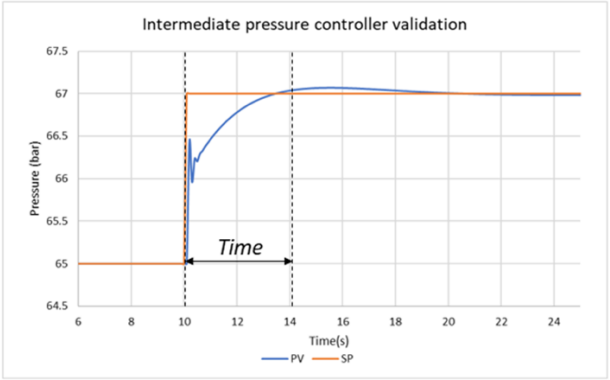

Figure F. 2 Controller C3 validation

Condenser inlet temperature controller (C4)

Bump test:

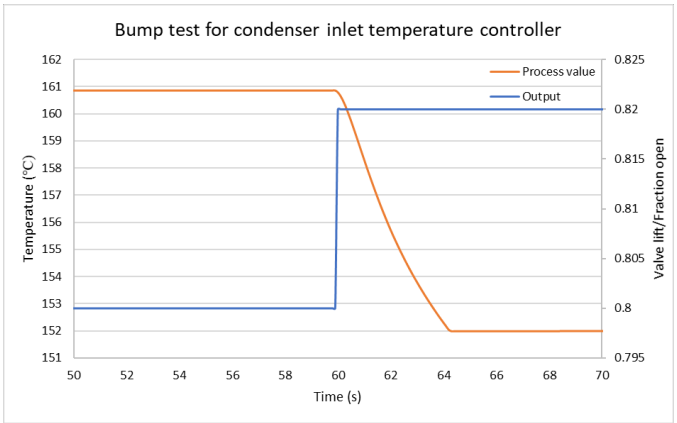

Figure F. 3 Controller C4 bump test

Modelling parameters:

Parameter	**Result**
Δout (change in output)	0.05 (valve lift)
ΔPV (change in process value)	8.87 (℃)
Δt (Time taken for process value to settle)	7.2(s)
K_{Δ} (Gain change)	177.31
τ_p (Closed loop time constant)	1.8

Tuning:

K_p	T_i	τ_{ratio}
-0.003	2	2

Validation:

$$Time = 4 \times \tau_{CL} = 4 \times \tau_{ratio} \times \tau_P = 14.4s$$

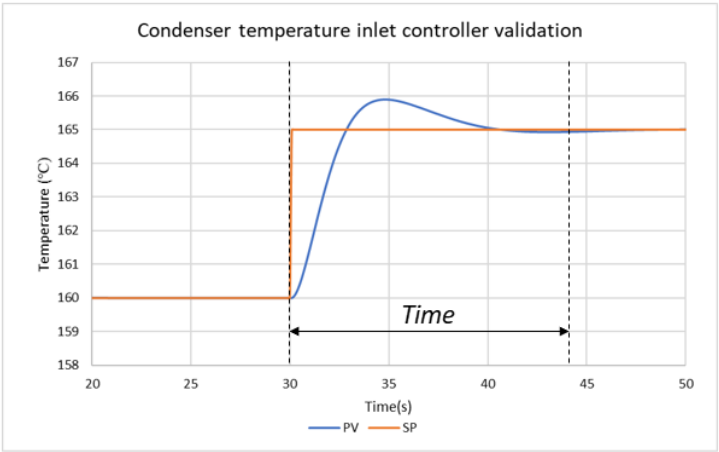

Figure F. 4 Controller C4 validation

Feedwater mass flowrate controller (C6)

Bump test:

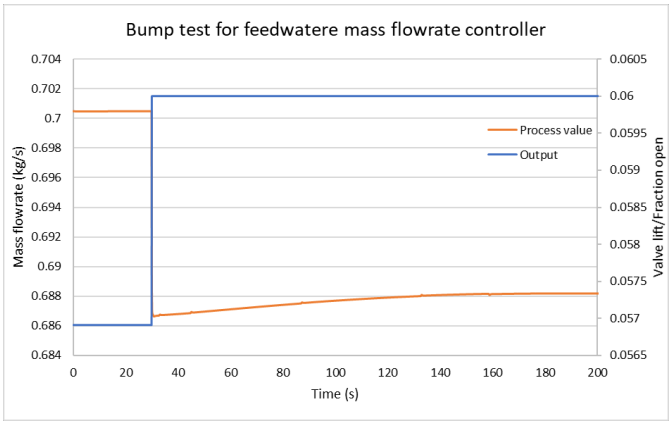

Figure F. 5 Controller C6 bump test

Modelling parameters:

Parameter	**Result**
Δout (change in output)	0.003 (valve lift)
ΔPV (change in process value)	-0.012 (kg/s)
Δt (Time taken for process value to settle)	160(s)
K_{Δ} (Gain change)	-3.98
τ_p (Closed loop time constant)	40

Tuning:

K_p	T_i	τ_{ratio}
-0.08372	40	3

Validation:

$$Time = 4 \times \tau_{CL} = 4 \times \tau_{ratio} \times \tau_P = 480s$$

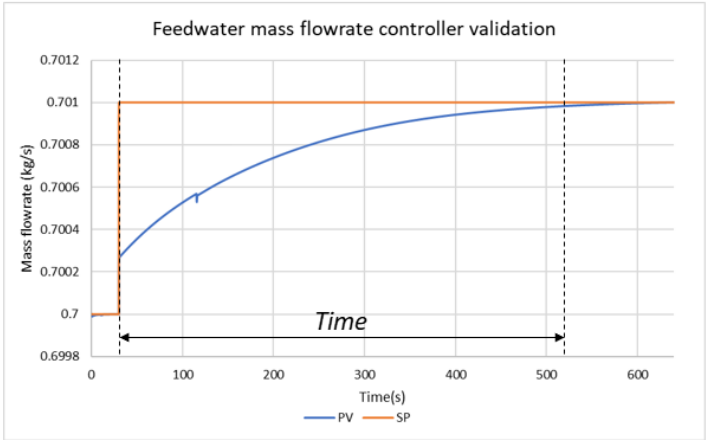

Figure F. 6 Controller C6 validation

Salt mass flowrate controller (C7)

Bump test:

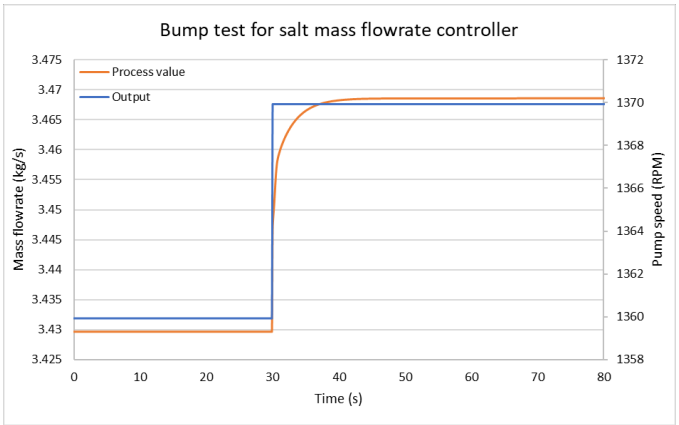

Figure F. 7 Controller C7 bump test

Modelling parameters:

Parameter	**Result**
Δout (change in output)	10(RPM)
ΔPV (change in process value)	0.038 (kg/s)
Δt (Time taken for process value to settle)	20(s)
K_{Δ} (Gain change)	0.0038
τ_p (Closed loop time constant)	5

Tuning:

K_p	T_i	τ_{ratio}
85.7219	5	3

Validation:

$$Time = 4 \times \tau_{CL} = 4 \times \tau_{ratio} \times \tau_P = 60s$$

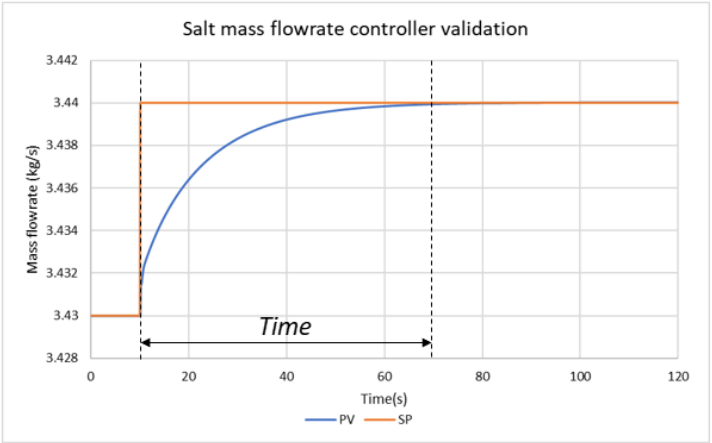

Figure F. 8 Controller C7 validation

Salt exit pressure controller (C8)

Bump test:

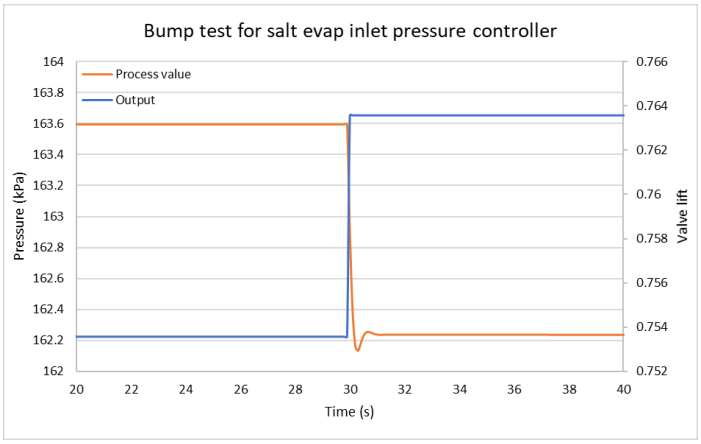

Figure F. 9 Controller C8 bump test

Modelling parameters:

Parameter	**Result**
Δout (change in output)	0.01(valve lift)
ΔPV (change in process value)	-1.36(kPa)
Δt (Time taken for process value to settle)	3(s)
K_{Δ} (Gain change)	-135.857
τ_p (Closed loop time constant)	0.75

Tuning:

K_p	T_i	τ_{ratio}
-0.002453561	0.75	3

Validation:

$$Time = 4 \times \tau_{CL} = 4 \times \tau_{ratio} \times \tau_P = 9s$$

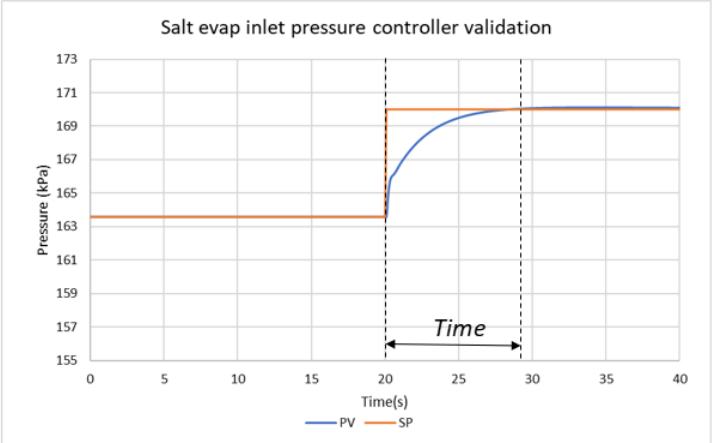

Figure F. 10 Controller C8 validation

Appendix G. Additional results

35% and 115% sensitivity analysis for eutectic salt compound

Figure G. 1 and Figure G. 2 show the sensitivity analysis done for the steam generation system when eutectic salt is used as the salt compound. The results in Figure G. 1 show that the salt mass flowrate would have to be adjusted by about 8% to reach the expected operating requirements for the 35% load. Figure G. 2 shows that the salt mass flowrate would have to be adjusted by about 10% to reach the expected operating requirements for the 115% load.

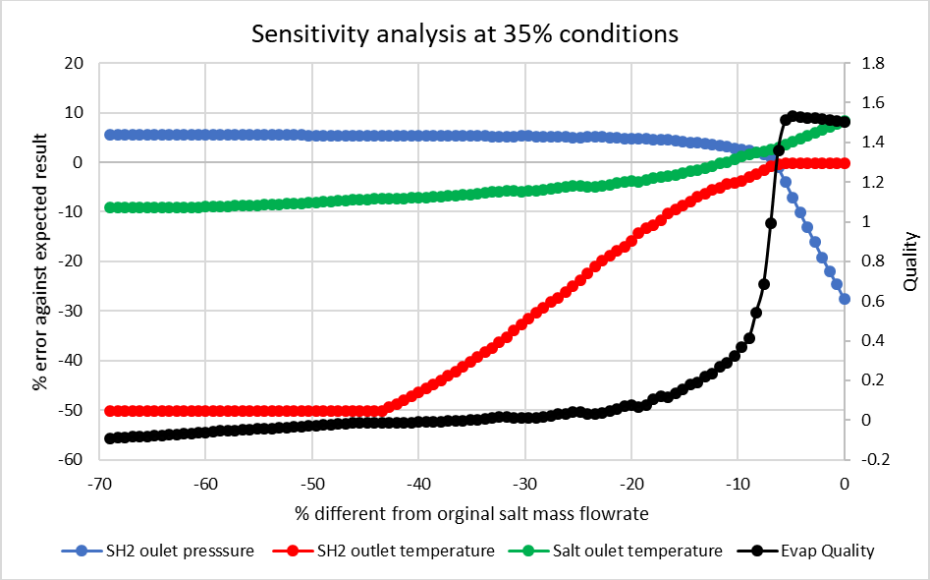

Figure G. 1 Sensitivity analysis for 35% load with eutectic salt

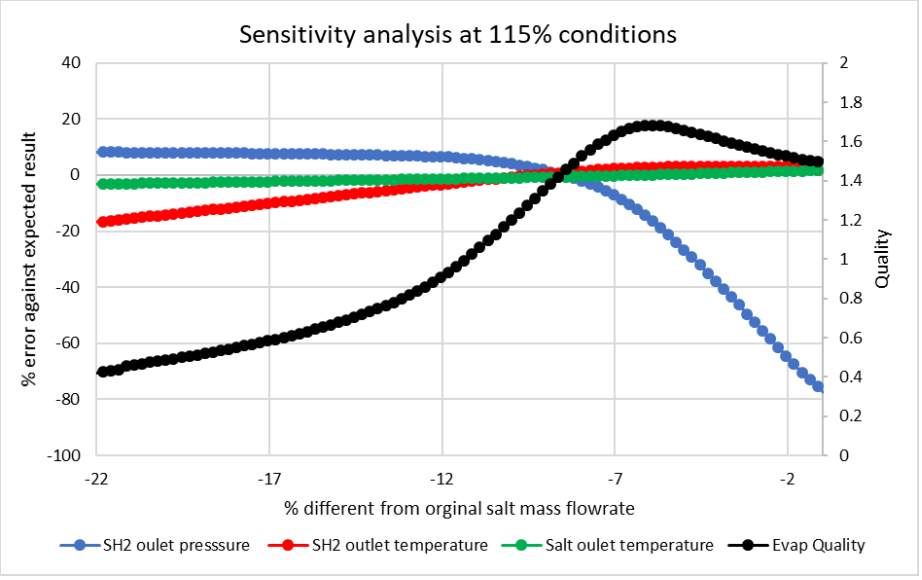

Figure G. 2 Sensitivity analysis for 115% load with eutectic salt

Additional results for the conservative load change described section 4.3.1

The graphs below show additional transient results when the load is changed from 35%-100% load.

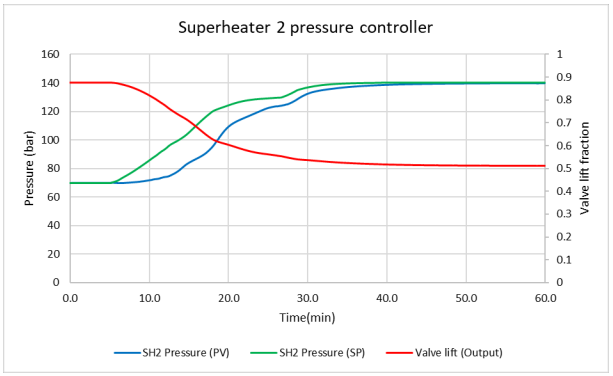

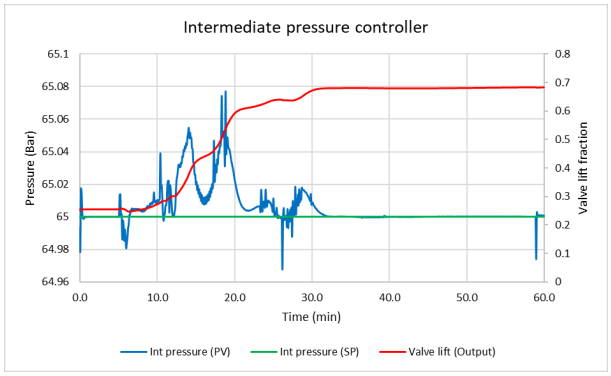

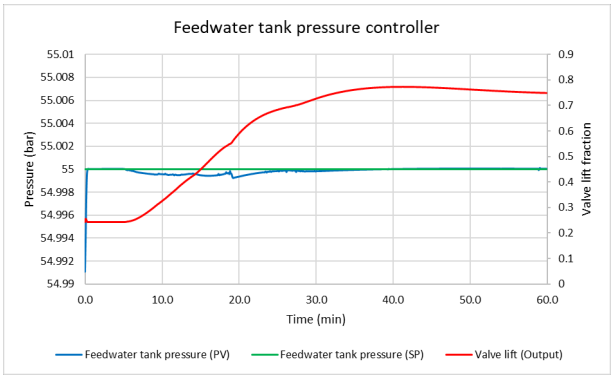

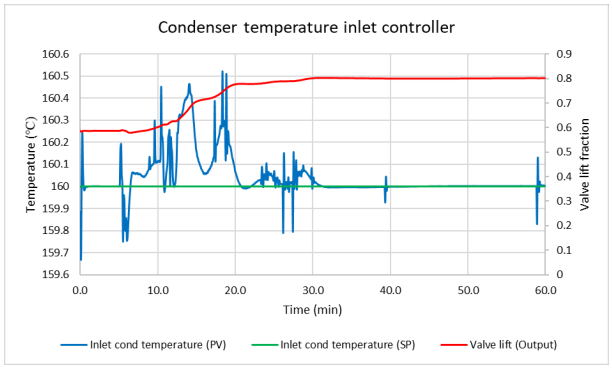

The graphs below show additional transient results when the load is changing from 100%-35% load.

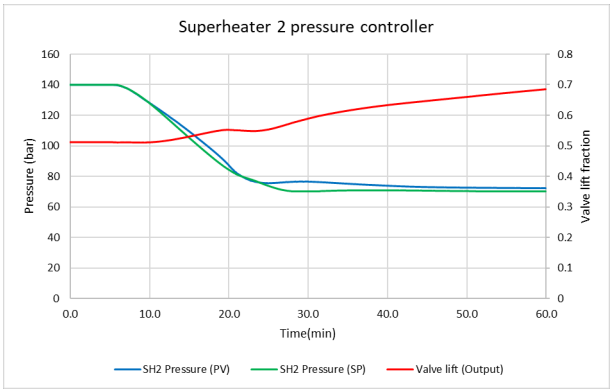

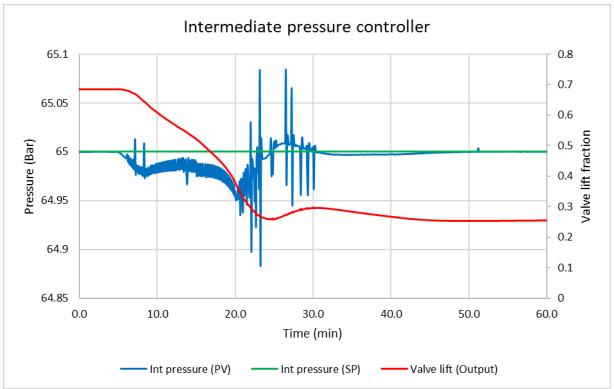

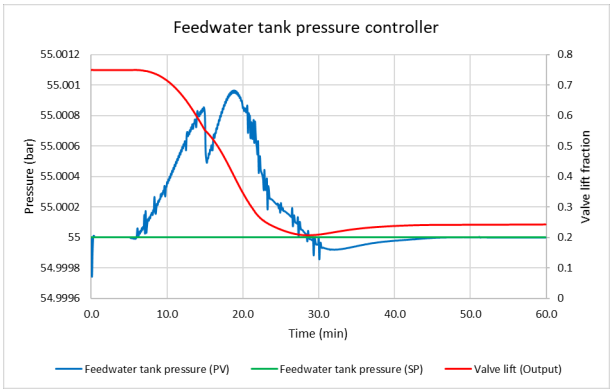

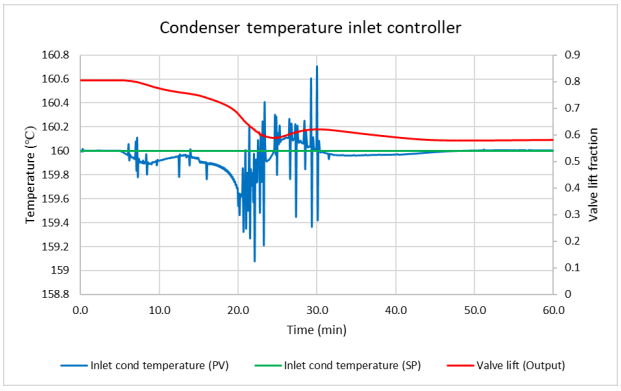

Additional results for conservative load change with separator as described in section 4.3.2

The graphs below and on the next page show the additional transient results for when the load is changing from 35%-100% load.

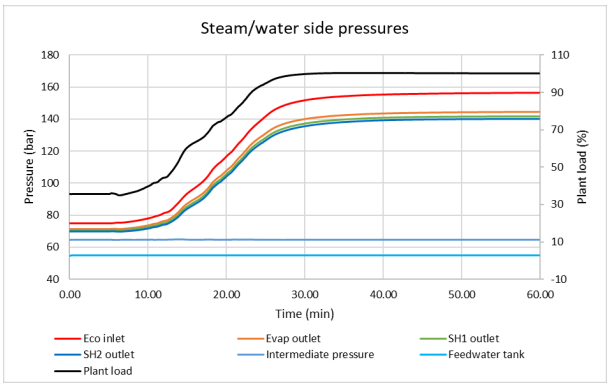

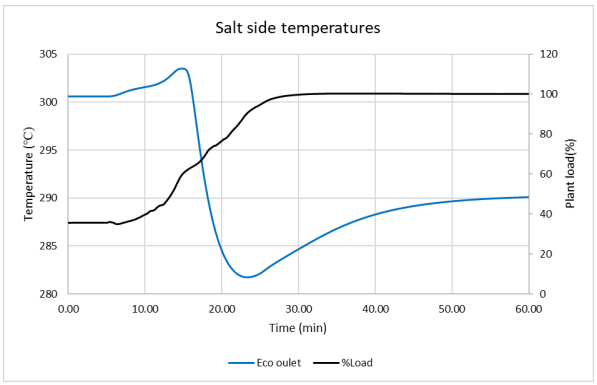

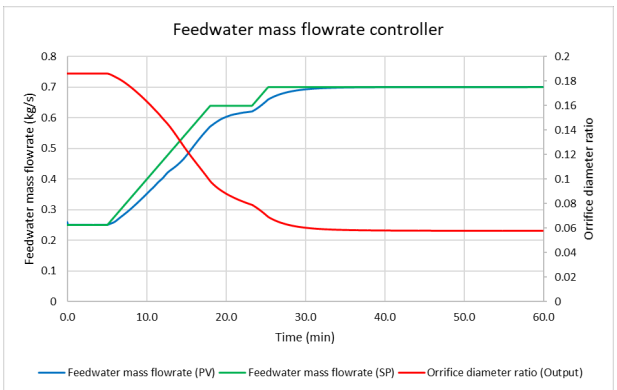

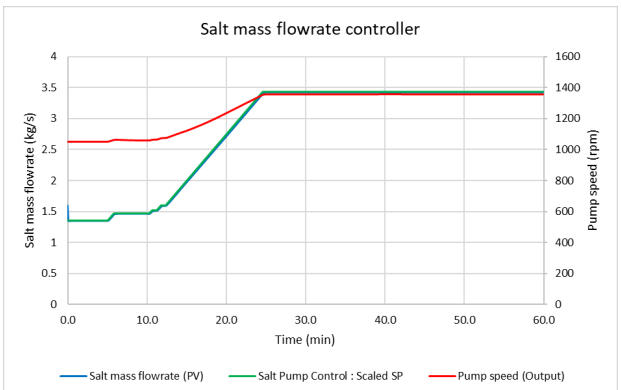

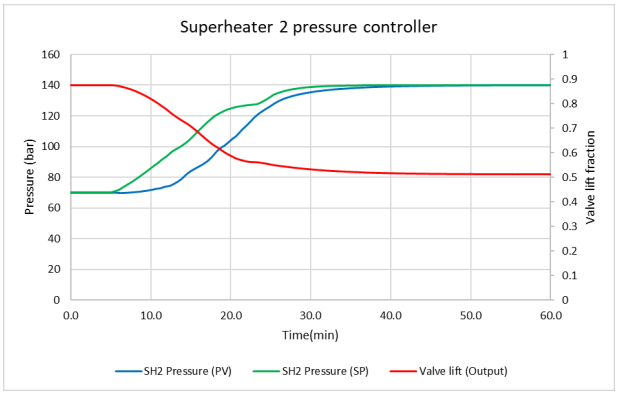
Superheater 2 pressure controller
Pressure (bar)
Valve lift fraction
Time(min)
SH2 Pressure (PV)
SH2 Pressure (SP)
Valve lift (Output)

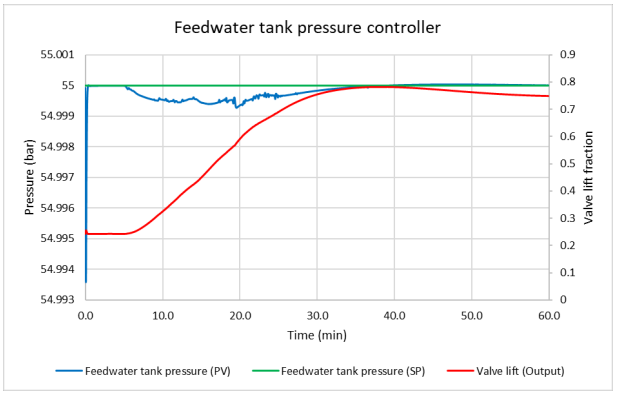
Feedwater tank pressure controller
Pressure (bar)
Valve lift fraction
Time (min)
Feedwater tank pressure (PV)
Feedwater tank pressure (SP)
Valve lift (Output)

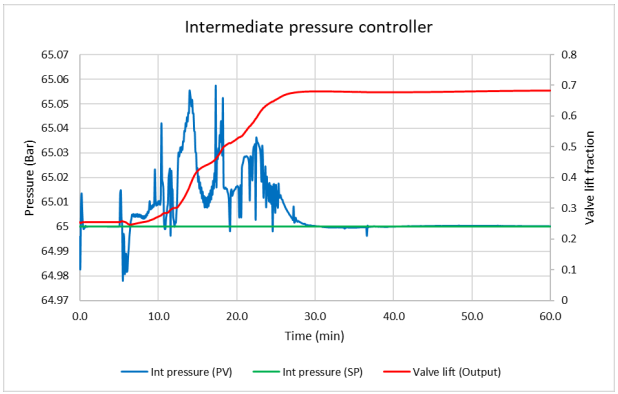
Intermediate pressure controller
Pressure (Bar)
Valve lift fraction
Time (min)
Int pressure (PV)
Int pressure (SP)
Valve lift (Output)

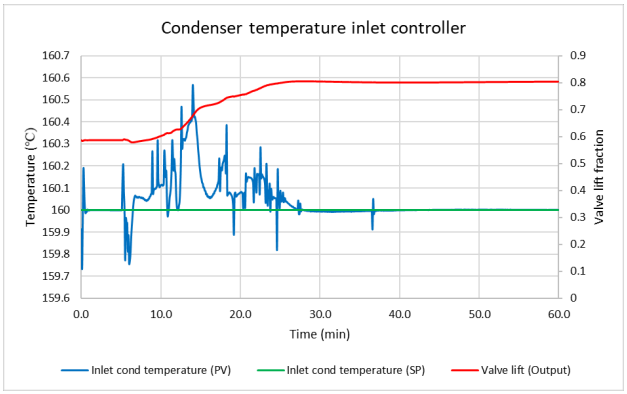
Condenser temperature inlet controller
Temperature (°C)
Valve lift fraction
Time (min)
Inlet cond temperature (PV)
Inlet cond temperature (SP)
Valve lift (Output)

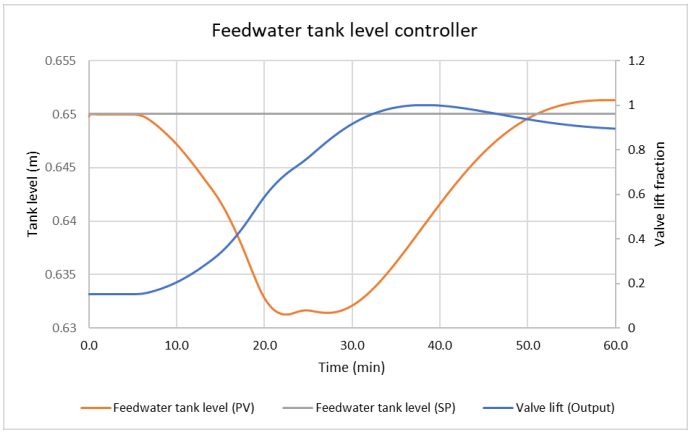
Feedwater tank level controller
Tank level (m)
Valve lift fraction
Time (min)
Feedwater tank level (PV)
Feedwater tank level (SP)
Valve lift (Output)

The graphs below and on the next page show the additional transient results for when the load is changing from 100%-35% load.

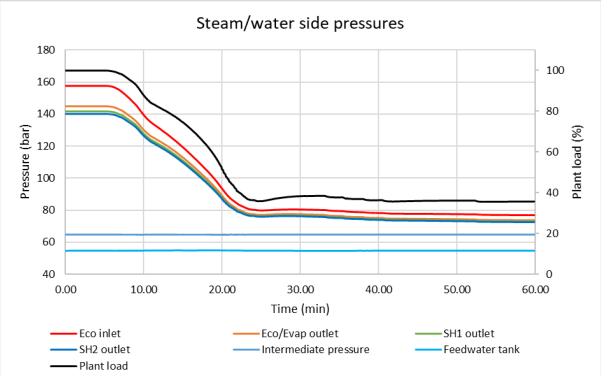

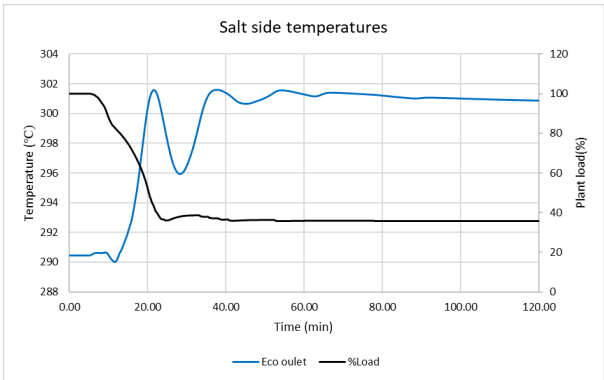

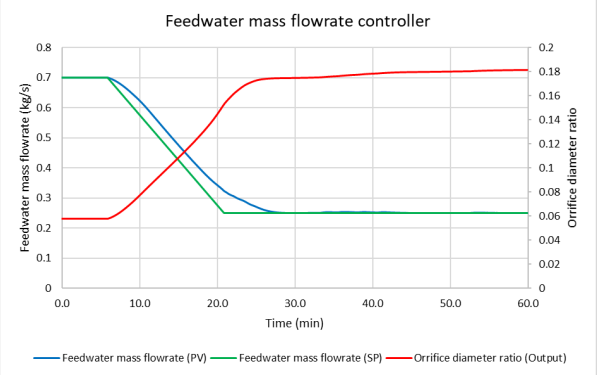

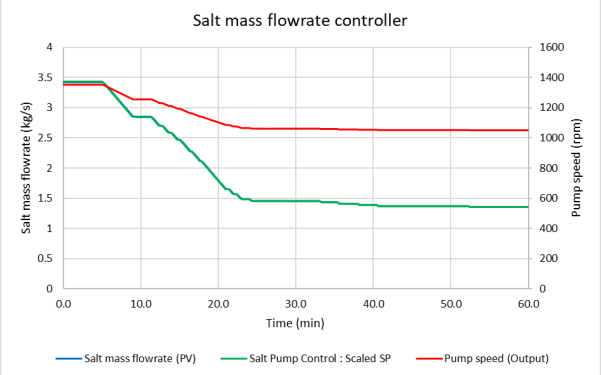

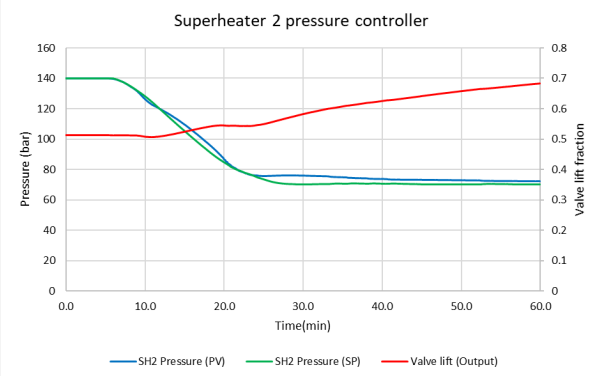

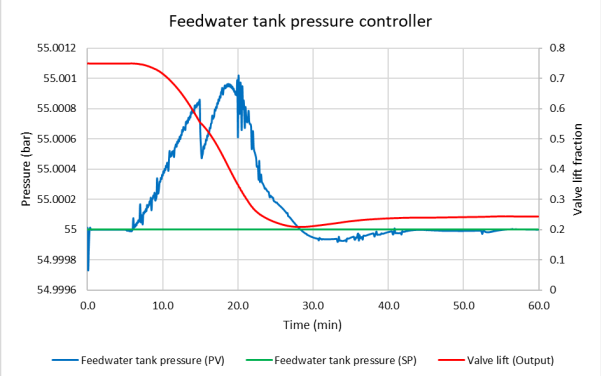

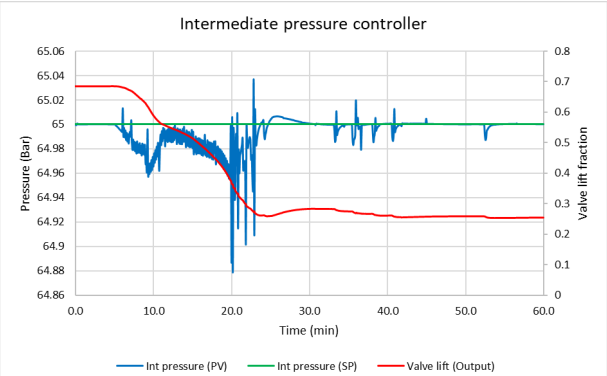

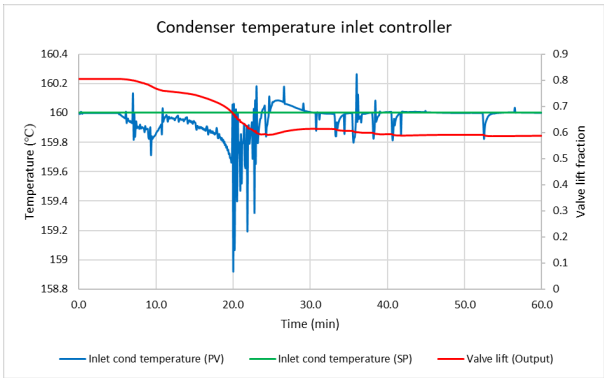

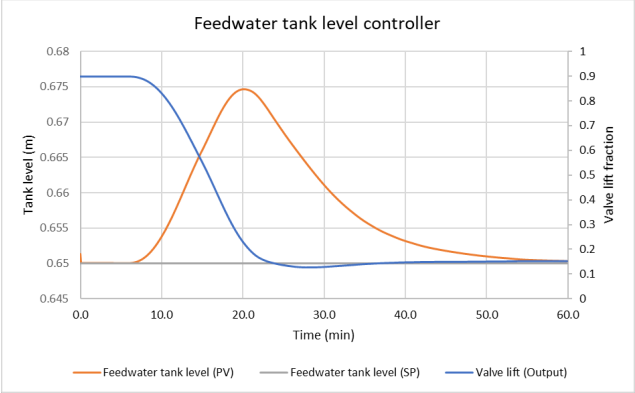

Additional results for fast load change as described in section 4.3.3

The graphs below and on the next page show additional transient results when the load is changed from 35%-100% load.

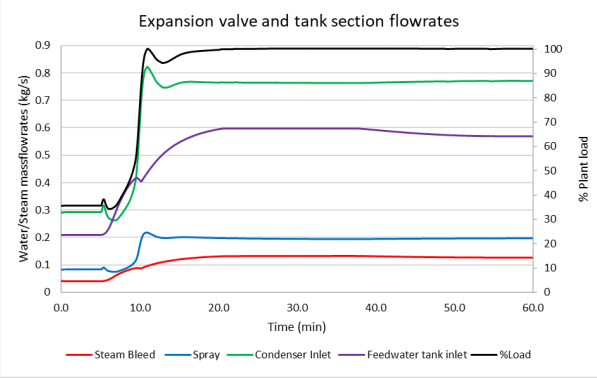

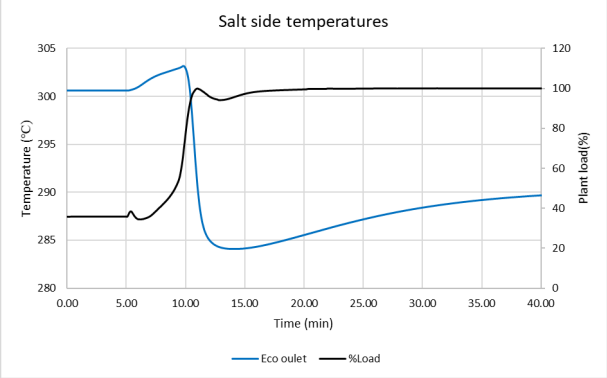

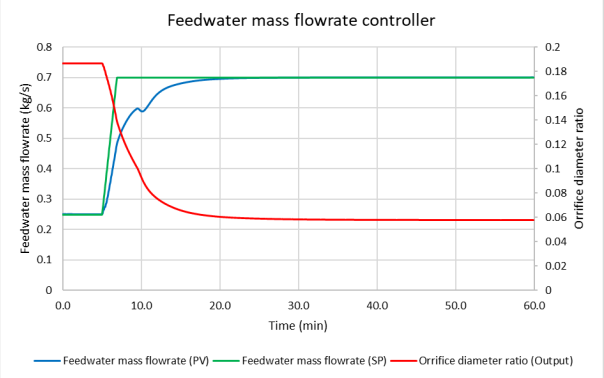

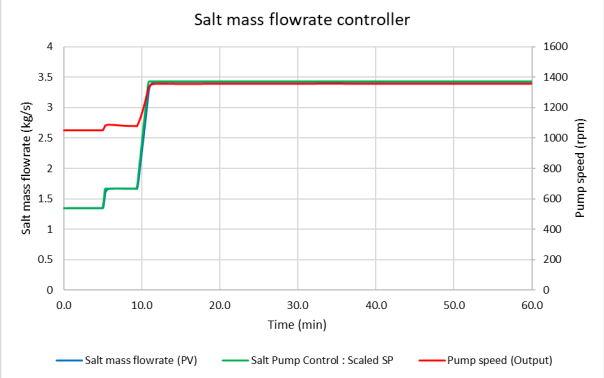

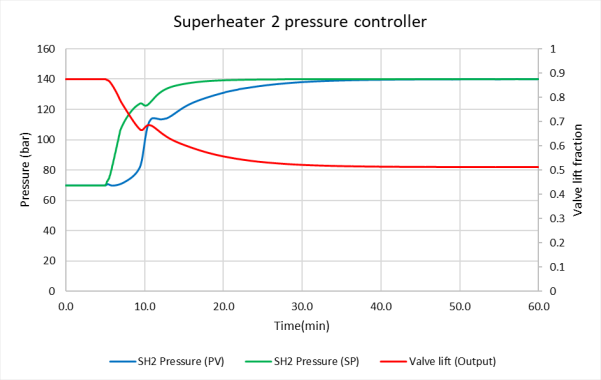

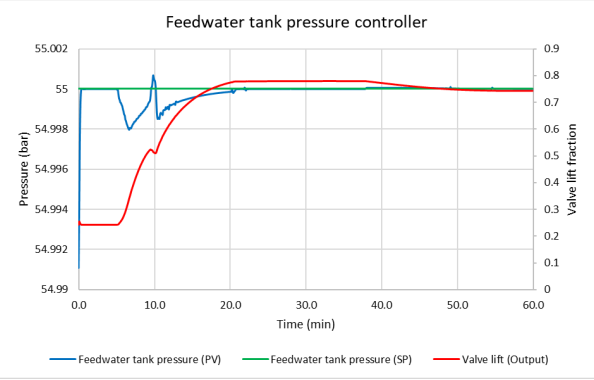

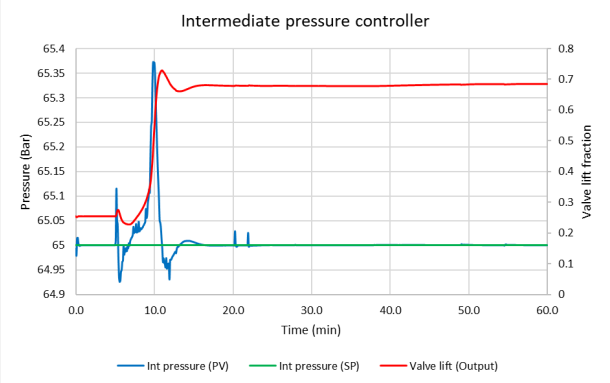

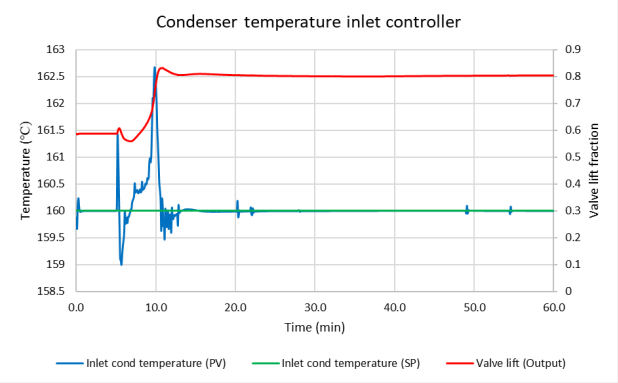

The graphs below and on the next page show additional transient results when the load is changed from 100%-35% load.

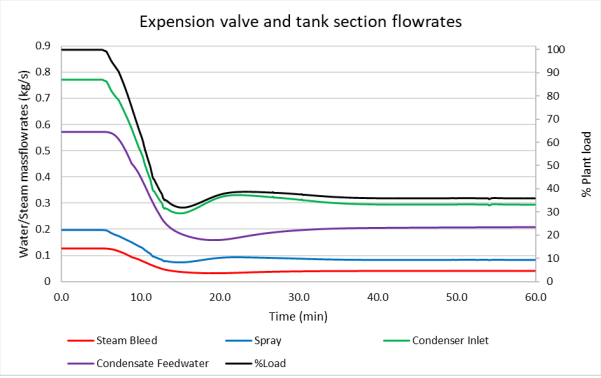

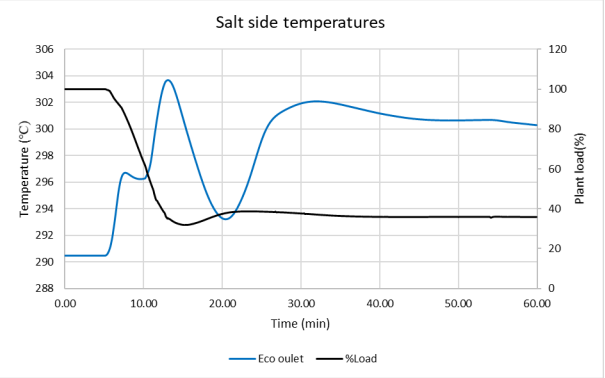

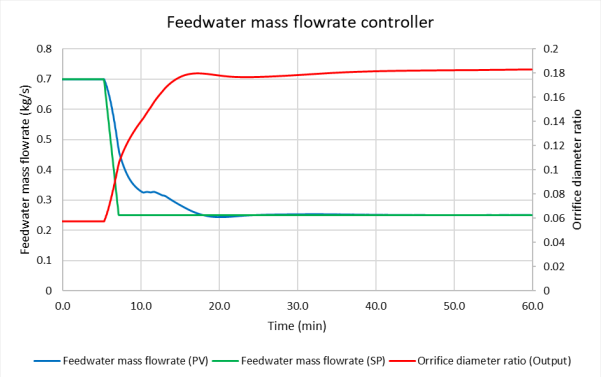
Feedwater mass flowrate controller
Feedwater mass flowrate (kg/s)
Orrifice diameter ratio
Time (min)
Feedwater mass flowrate (PV)
Feedwater mass flowrate (SP)
Orrifice diameter ratio (Output)

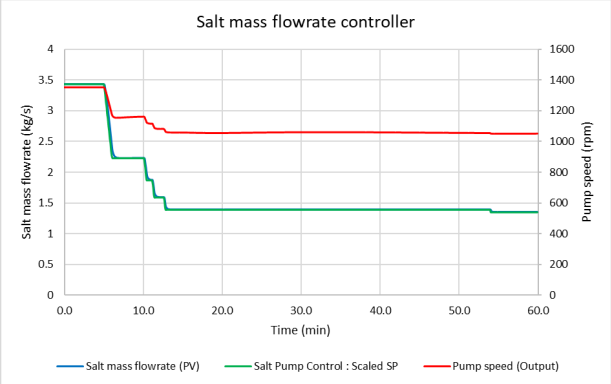
Salt mass flowrate controller
Salt mass flowrate (kg/s)
Pump speed (rpm)
Time (min)
Salt mass flowrate (PV)
Salt Pump Control : Scaled SP
Pump speed (Output)

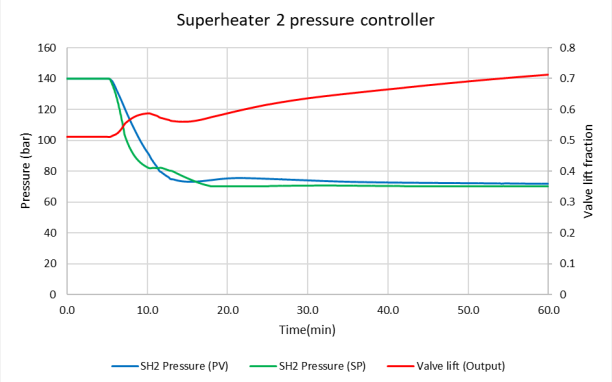
Superheater 2 pressure controller
Pressure (bar)
Valve lift fraction
Time(min)
SH2 Pressure (PV)
SH2 Pressure (SP)
Valve lift (Output)

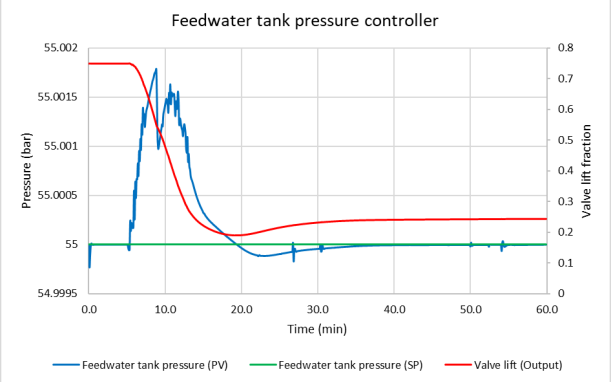
Feedwater tank pressure controller
Pressure (bar)
Valve lift fraction
Time (min)
Feedwater tank pressure (PV)
Feedwater tank pressure (SP)
Valve lift (Output)

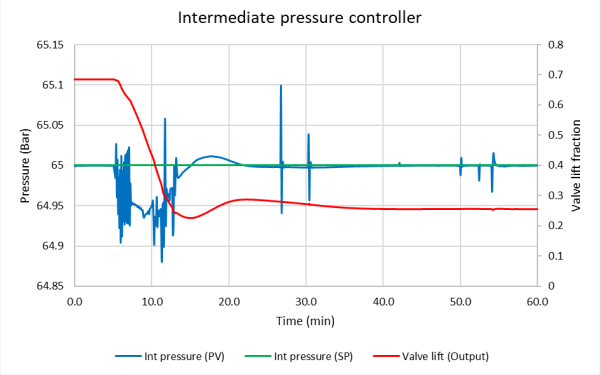
Intermediate pressure controller
Pressure (Bar)
Valve lift fraction
Time (min)
Int pressure (PV)
Int pressure (SP)
Valve lift (Output)

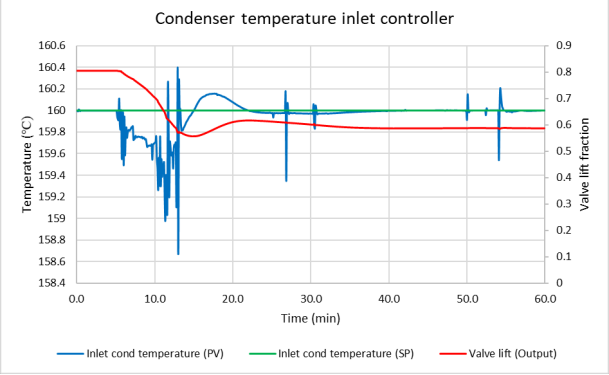
Condenser temperature inlet controller
Temperature (°C)
Valve lift fraction
Time (min)
Inlet cond temperature (PV)
Inlet cond temperature (SP)
Valve lift (Output)

(End blank page)